

AIR-COUPLED ULTRASONIC TESTING OF MATERIALS

by

William Matthew David Wright

submitted for a

Ph.D. in Engineering

to the

University of Warwick

describing research conducted in the

Department of Engineering

Submitted in March 1996

Table of Contents

	Page no.
Table of contents	i
List of Figures and Tables	vii
Acknowledgements	xxiv
Declaration	xxv
Summary	xxvi

Chapter 1: Introduction and overview of non-contact ultrasonics

1.1	Introduction	1
1.2	Types of sound wave	2
1.3	Some properties of sound waves	4
1.4	Conventional ultrasonic testing	7
1.5	Non-contact methods	9
1.5.1	Laser generation of ultrasound	9
1.5.2	Laser detection of ultrasound	14
1.5.3	Non-contact transducers	17
1.6	Air-coupled transducers	20
1.6.1	Piezoelectric air-coupled devices	20
1.6.2	Capacitance air-coupled devices	23
1.7	Outline of the thesis	25
1.8	References	27

**Chapter 2: Studies of laser-generated ultrasound using an
air-coupled micromachined silicon capacitance
transducer**

2.1	Introduction	33
2.1.1	Micromachined devices	33
2.1.2	Construction of the micromachined silicon air-coupled transducer	35
2.1.3	Advantages of using laser generated ultrasound	37
2.2	Studies of laser generated through transmission waveforms	39
2.2.1	Characterising the air-coupled capacitance transducer	39
2.3	Studies of laser generated surface (Rayleigh) and plate (Lamb) waves	51
2.3.1	Detection of Rayleigh waves	51
2.3.2	Detection of Lamb waves	55
2.4	Discussion	59
2.5	Conclusions	61
2.6	References	62

Chapter 3: Air-coupled 1-3 connectivity piezocomposite transducers

3.1	Introduction	65
3.2	The manufacture of resonant (narrow bandwidth) devices	65

3.2.1	Characterising the prototype resonant devices	67
3.2.2	Results using the resonant devices	70
3.3	Advancements in transducer design	74
3.3.1	Characterising the wideband piezocomposite device	77
3.3.2	Comparison of the broadband piezoelectric and capacitance air transducers	77
3.4	Through thickness waveforms in composite materials	81
3.4.1	The composite materials	82
3.5	C-scanning of defects using bulk waves	87
3.6	Discussion	96
3.7	Conclusions	97
3.8	References	98

Chapter 4: Air-coupled capacitance transducers with metal backplates

4.1	Introduction	101
4.1.1	Air-coupled capacitance transducers	101
4.1.2	Theoretical frequency response	103
4.1.3	Construction of the transducers	104
4.2	Manufacture of random metallic backplates by grinding and polishing	105
4.2.1	Experimental technique	107
4.2.2	The effects of backplate surface properties	110

4.2.3	The effects of polymer film thickness	116
4.2.4	The effects of applied bias voltage	119
4.2.5	Repeatability between 'identical' devices	124
4.2.6	Comparison with the theoretical frequency response	128
4.3	Manufacture of metallic backplates by chemical etching	130
4.3.1	Experimental technique	137
4.3.2	The effects of the hole dimensions	138
4.4	Discussion	140
4.5	Conclusions	142
4.6	References	143

Chapter 5: Thickness estimation using air-coupled Lamb waves

5.1	Introduction	147
5.1.2	A brief history of Lamb waves	147
5.2	An overview of Lamb wave theory	149
5.3	Extracting the dispersion relations from Lamb wave data	155
5.4	Calculation of theoretical curves	156
5.5	Trial experiments using a contact detector	158
5.6	Experiments using the air-coupled detector	165
5.6.1	Group velocity dispersion curves	167
5.6.2	Extracting the sheet thickness from the group velocity dispersion curves	170
5.6.3	Phase velocity dispersion curves	174

5.6.4	Extracting the sheet thickness from the phase velocity dispersion curves	176
5.7	Entirely air-coupled experiments	178
5.8	Discussion	180
5.9	Conclusions	181
5.10	References	182

Chapter 6: Materials testing using an air-coupled source and receiver

6.1	Introduction	187
6.1.1	Entirely air-coupled ultrasonics	187
6.2	Through thickness experiments	190
6.2.1	Results in CFRP composite materials	192
6.2.2	Results in other materials	197
6.3	C-scanning of defects	203
6.4	Lamb waves in composite and polymer plates	210
6.5	Conclusions	213
6.6	References	214

Chapter 7: Air-coupled Lamb wave tomography

7.1	Introduction	216
7.1.1	Different tomographic reconstruction techniques	216

7.2	Tomographic reconstruction using Fourier analysis	218
7.2.1	The Projection Theorem	220
7.2.2	Filtered back projection	221
7.3	Equipment and experimental technique	225
7.4	Results using the laser source and the capacitance receiver	228
7.5	Results using the air-coupled capacitance transducer source	236
7.6	Conclusions	245
7.7	References	246
Chapter 8:	Conclusions	
8.1	Conclusions	250
Bibliography		254
Publications arising from the work in this thesis		254
Appendix A: Equipment specifications		256
Appendix B: FORTRAN program listings		257

List of Figures and Tables

- Figure 1.1(a): Particle motion for a longitudinal wave.
- Figure 1.1(b): Particle motion for a shear wave.
- Figure 1.1(c): Particle motion for a Rayleigh wave. The elliptical motion becomes more circular and reduces in amplitude with depth.
- Figure 1.2(a): Snell's law for a wave travelling across the interface between two different materials, with velocity c_B greater than c_A .
- Figure 1.2(b): Mode conversion of a longitudinal wave at a material interface into shear S and longitudinal L wave components, with velocity c_A greater than c_B . The angle of incidence i equals the angle of reflection r_L for the longitudinal wave.
- Figure 1.3(a): Construction of a typical piezoelectric transducer.
- Figure 1.3(b): Different transducer techniques.
- Figure 1.4(a): Laser generation of ultrasound by the thermoelastic mechanism.
- Figure 1.4(b): Theoretical displacement waveform for a thermoelastic source, with longitudinal L and shear S components. Adapted from Scruby and Drain [21].
- Figure 1.5(a): Laser generation of ultrasound using the ablation mechanism.
- Figure 1.5(b): Theoretical displacement waveform for an ablative source, with longitudinal L and shear S components. Adapted from Scruby and Drain [21].
- Figure 1.6(a): Laser generation of ultrasound using the air breakdown mechanism.
- Figure 1.6(b): Theoretical displacement waveform for an air breakdown source, with

longitudinal L and shear S components. Adapted from Edwards *et. al.* [20].

- Figure 1.7(a): The basic Michelson interferometer.
- Figure 1.7(b): The resonant optical cavity of a Fabry-Pérot confocal interferometer.
- Figure 1.7(c): The knife edge detector or beam deflector.
- Figure 1.8(a): A longitudinal wave EMAT.
- Figure 1.8(b): A shear wave EMAT.
- Figure 1.9: A capacitance transducer using air or a solid dielectric between the polished electrode and the conducting sample.
- Table 1.1: Acoustical properties of some transducer materials [9,10].
- Figure 1.10: Different connectivity composites, with the piezoelectric material shown shaded.
- Figure 1.11: Operation of the capacitance devices. The sizes of the polymer film and the backplate features are greatly exaggerated for clarity.
- Figure 2.1: Detail of the micromachined silicon backplate.
- Figure 2.2(a): Through transmission in air using two air-coupled transducers. Values shown are approximate fractions of the original energy.
- Figure 2.2(b): Improved through transmission using a laser source. Values shown are approximate fractions of the original energy.
- Figure 2.3(a): Schematic diagram of the experimental apparatus.
- Figure 2.3(b): The contact capacitance device used for comparison.
- Figure 2.4(a): Longitudinal wave through 86.0mm aluminium detected by the contact transducer.

- Figure 2.4(b): Frequency spectrum of Figure 2.4(a).
- Figure 2.5(a): Longitudinal arrival through 86.0mm aluminium detected using the air-coupled micromachined capacitance device.
- Figure 2.5(b): Frequency spectrum of the waveform in Figure 2.5(a).
- Figure 2.6(a): Waveform through 12.8mm of aluminium detected using the contact transducer, showing the surface displacement.
- Figure 2.6(b): Waveform through 12.8mm of aluminium, detected using the micromachined air-coupled capacitance transducer.
- Figure 2.6(c): Waveform in Figure 2.6(a) 'filtered' over the range of frequencies shown in Figure 2.5(b).
- Figure 2.6(d): Contact capacitance transducer waveform after differentiation, showing the velocity of the surface.
- Figure 2.7(a): Signals obtained using an increasing optical power density, detected using the contact device.
- Figure 2.7(b): Signals obtained using an increasing optical power density, detected using the micromachined air-coupled capacitance transducer.
- Figure 2.8(a): Typical laser generated waveform in 10mm thick steel, detected using the air-coupled capacitance transducer.
- Figure 2.8(b): Typical laser generated waveform in 25mm thick Perspex, detected using the air-coupled capacitance transducer.
- Figure 2.9(a): Apparatus for detecting Rayleigh waves.
- Figure 2.9(b): Apparatus for detecting Lamb waves.
- Figure 2.10(a): Surface waves in aluminium detected by the contact transducer.
- Figure 2.10(b): Surface waves in aluminium at an angle of 0° , detected using the

air-coupled capacitance transducer.

Figure 2.10(c): Surface waves in aluminium at an angle of 3° , detected using the air-coupled capacitance transducer.

Figure 2.10(d): Surface waves in aluminium at an angle of 6° , detected using the air-coupled capacitance transducer.

Figure 2.11: Lamb waves in a 0.69mm thick aluminium sheet, detected using the contact device after propagating 50mm in the sample.

Figure 2.12(a): Lamb waves in a 0.69mm thick aluminium sheet, detected using the air-coupled capacitance transducer at an angle of 2° .

Figure 2.12(b): Lamb waves in a 0.69mm thick aluminium sheet, detected using the air-coupled capacitance transducer at an angle of 5° .

Figure 2.12(c): Lamb waves in a 0.69mm thick aluminium sheet, detected using the air-coupled capacitance transducer at an angle of 10° .

Figure 2.12(d): Lamb waves in a 0.69mm thick aluminium sheet, detected using the air-coupled capacitance transducer at an angle of 15° .

Figure 2.12(e): Lamb waves in a 0.69mm thick aluminium sheet, detected using the air-coupled capacitance transducer at an angle of 20° .

Figure 2.13: Lamb waves in a 1.5mm thick perspex sheet, detected using the air-coupled capacitance transducer at an angle of 12° .

Figure 3.1: The 1-3 connectivity composite transducer.

Table 3.1: Properties of the prototype devices, courtesy of the University of Strathclyde [4].

Figure 3.2: Schematic diagram of experimental apparatus.

- Figure 3.3(a): Waveform through 86mm of aluminium using the contact capacitance device, with longitudinal arrivals $L1$ and $L2$, and shear arrival S .
- Figure 3.3(b): Frequency spectrum of the first longitudinal arrival in Figure 3.3(a).
- Figure 3.4(a): Waveform through 86mm of aluminium using the low frequency damped device, showing longitudinal (L) and shear (S) wave arrivals.
- Figure 3.4(b): Waveform through 86mm of aluminium using the low frequency undamped device, showing longitudinal (L) and shear (S) wave arrivals.
- Figure 3.4(c): Waveform through 86mm of aluminium using the high frequency device, again showing longitudinal (L) and shear (S) wave arrivals.
- Figure 3.5(a): Frequency spectrum of the first longitudinal arrival in Figure 3.4(a).
- Figure 3.5(b): Frequency spectrum of the first longitudinal arrival in Figure 3.4(b).
- Figure 3.5(c): Frequency spectrum of the first longitudinal arrival in Figure 3.4(c).
- Figure 3.6(a): Response of the contact capacitance device to a waveform in 19.8mm of aluminium, with longitudinal (L), shear (S) and mode converted shear (M) arrivals.
- Figure 3.6(b): Response of the low frequency damped device to a waveform in 19.8mm of aluminium.
- Figure 3.6(c): Response of the low frequency undamped device to a waveform in 19.8mm of aluminium.
- Figure 3.6(d): Response of the high frequency device to the waveform in 19.8mm of aluminium.
- Figure 3.7(a): Waveform through 86mm of aluminium using the wide bandwidth device, showing longitudinal (L) and shear (S) wave arrivals.

- Figure 3.7(b): Frequency spectrum of first longitudinal arrival in Figure 3.7(a).
- Figure 3.7(c): Response of the wide bandwidth device to the waveform in 19.8mm of aluminium.
- Figure 3.8(a): A comparison of the longitudinal arrivals in 86.0mm aluminium for the wideband capacitance and 1-3 connectivity piezocomposite air-coupled transducers.
- Figure 3.8(b): A comparison of the frequency spectra of the two waveforms shown in Figure 3.8(a).
- Figure 3.9: Waveforms in (a) 8-ply (1.1mm thick), (b) 24-ply (3.3mm thick) and (c) 40-ply (5.5mm thick) quasi-isotropic CFRP composite plates.
- Figure 3.10: Frequency spectra of differentiated waveforms in Figure 3.9.
- Figure 3.11: Waveforms through (a) 4.25mm thick pultruded U-channel and (b) 9.8mm thick pultruded I-beam composites.
- Figure 3.12: Frequency spectra of the differentiated waveforms in Figure 3.11.
- Figure 3.13: The C-scanning apparatus.
- Figure 3.14: Waveforms from a typical scan, with (a) a delamination and (b) no delamination between source and receiver.
- Figure 3.15(a): Image of a 25mm square delamination in 16-ply (3.2mm thick) CFRP, produced using signal amplitude. Grey scale is in mV.
- Figure 3.15(b): Image of a 12mm square delamination in 16-ply (3.2mm thick) CFRP, found using signal amplitude. Grey scale is in mV.
- Figure 3.15(c): Image of a 6mm square delamination in 16-ply (3.2mm thick) CFRP, found using signal amplitude. Grey scale is in mV.
- Figure 3.16: Image of a 10mm diameter flat recess machined to a depth of 3.2mm

into a 32-ply (4.4mm thick) cross-ply CFRP plate. Grey scale is in mV.

Figure 3.17(a): Image of a 10mm diameter flat recess machined 1mm into a 9.8mm thick pultruded GRP plate, found using signal amplitude. Grey scale is in mV.

Figure 3.17(b): Image of a 10mm diameter flat recess machined 1mm into a 9.8mm thick pultruded GRP plate, found using time shift of first arrival. Grey scale is in μ s.

Figure 3.17(c): Image of a 10mm diameter flat recess machined 1mm into a 9.8mm thick pultruded GRP plate, found using FFT amplitude. Grey scale is arbitrary.

Figure 3.17(d): Image of a 10mm diameter flat recess machined 1mm into a 9.8mm thick pultruded GRP plate, found using frequency shift. Grey scale is in kHz.

Figure 3.18(a): Image of a 5mm diameter recess 1mm deep in a 9.8mm thick pultruded GRP plate, found using signal amplitude. Grey scale is in mV.

Figure 3.18(b): Image of a 5mm diameter recess 1mm deep in a 9.8mm thick pultruded GRP plate, found using FFT amplitude. Grey scale is arbitrary.

Figure 4.1: Construction of the air transducers.

Table 4.1: Grinding and polishing parameters for brass [24].

Table 4.2: Selected surface properties for each backplate.

- Figure 4.2: The capacitive decoupling circuit.
- Figure 4.3: Schematic diagram of the experimental apparatus.
- Figure 4.4(a): Typical air-coupled waveform using the silicon transducer source, received by the #1200 backplate filmed with 6 μ m Mylar.
- Figure 4.4(b): Frequency spectrum of Figure 4.4(a).
- Figure 4.5(a): Comparison of frequency spectra for all brass backplates, showing their relative sensitivity.
- Figure 4.5(b): Comparison of normalised frequency spectra for all brass backplates, showing their relative bandwidth.
- Figure 4.6: Plot of bandwidth against sensitivity for all brass backplates.
- Figure 4.7(a): Plot of 3dB bandwidth against $1/\sqrt{R_a}$.
- Figure 4.7(b): Plot of relative sensitivity against $1/\sqrt{R_a}$.
- Figure 4.7(c): Plot of centre 3dB frequency against $1/\sqrt{R_a}$.
- Figure 4.8: Plot of relative sensitivity against $1/\sqrt{S_m}$.
- Figure 4.9(a): Frequency response using different Kapton polyimide films.
- Figure 4.9(b): Frequency response using different Mylar polyethylene terephthalate (PET) films.
- Figure 4.10(a): Plot of inverse square root of film thickness against 3dB bandwidth.
- Figure 4.10(b): Plot of inverse square root of film thickness against upper, lower and centre 3dB frequencies.
- Figure 4.10(c): Plot of film thickness against sensitivity.
- Figure 4.11(a): Change in frequency response of the #1200 backplate filmed with 12.5 μ m Kapton when the bias voltage is increased up to 1000V d.c.
- Figure 4.11(b): Change in frequency response of the #1200 backplate filmed with

7.6 μ m Kapton when the bias voltage is increased up to 1000V d.c.

- Figure 4.12(a): A plot of 3dB bandwidth against bias voltage for both the 7.6 μ m and 12.5 μ m Kapton films.
- Figure 4.12(b): Plot of sensitivity against bias voltage for both the 7.6 μ m and 12.5 μ m Kapton films.
- Figure 4.13(a): Plot of upper, lower and centre 3dB frequencies against bias voltage for the 7.6 μ m Kapton film.
- Figure 4.13(b): Plot of upper, lower and centre 3dB frequencies against bias voltage for the 12.5 μ m Kapton film.
- Figure 4.14(a): Received waveforms for three ‘identical’ devices.
- Figure 4.14(b): Frequency spectra for the three ‘identical’ devices.
- Figure 4.15(a): Beam plot for transducer ‘a’.
- Figure 4.15(b): Beam plot for transducer ‘b’.
- Figure 4.15(c): Beam plot for transducer ‘c’.
- Table 4.3: Values of constants for theoretical frequency response.
- Table 4.4: Theoretical resonant frequencies and measured frequency response for a 6.0 μ m film calculated using different surface properties.
- Table 4.5: Predicted transducer frequencies and measured frequency response for a #1200 backplate and various films.
- Table 4.6: Polishing parameters for copper [24].
- Table 4.7: Surface properties for the copper backplates.
- Table 4.8: Hole dimensions on the photolithography masks.
- Figure 4.16: Etched backplates (a) with photoresist for the 30x60 mask, and without photoresist for (b) the 30x60 and (c) the 40x60 mask sizes.

Scale 1mm:6.85 μ m

- Figure 4.16: Etched backplates with the photoresist removed for (d) the 40x80, (e) the 20x40 and (f) the 10x20 mask sizes. Scale 1mm:6.85 μ m
- Table 4.9: Mask and hole dimensions for each of the copper backplates.
- Figure 4.17(a): Talysurf profile for 1mm across the 40x80 backplate.
- Figure 4.17(b): Talysurf profile for a single hole on the 40x80 backplate.
- Table 4.10: Backplate surface parameters.
- Figure 4.18(a): Frequency spectra for all the copper backplates, showing their relative sensitivity.
- Figure 4.18(b): Normalised frequency spectra for all the copper backplates, showing their relative bandwidth.
- Figure 4.19: Plot of sensitivity against bandwidth for the copper backplates.
- Figure 5.1: Plate surface motion for (a) asymmetric and (b) symmetric Lamb waves.
- Figure 5.2: The interference of two waves of slightly different frequencies f_1 and f_2 , travelling at phase velocities c_{p1} and c_{p2} , to produce a modulation of frequency f_g travelling at a group velocity c_g .
- Figure 5.3: Phase velocity dispersion curves for the first four asymmetric and symmetric Lamb wave modes in aluminium.
- Figure 5.4: Group velocity dispersion curves for the first four asymmetric and symmetric Lamb wave modes in aluminium.
- Figure 5.5: Formation of (a) zero order modes from surface waves, and (b) higher order modes from standing waves.

- Figure 5.6: Schematic diagram of experimental equipment.
- Figure 5.7(a): Multimode Lamb waves in a 1.2mm aluminium plate, detected using the contact capacitance device.
- Figure 5.7(b): Frequency spectrum of Figure 5.7(a).
- Table 5.1: Theoretical cut off frequencies in a 1.2mm thick plate of aluminium.
- Figure 5.8: a_0 group velocity in a 1.2mm aluminium plate, found using zero crossing technique and a contact capacitance transducer - theory vs. experiment.
- Figure 5.9(a): Uncorrected phase information from the contact capacitance transducer waveform in a 1.2mm aluminium sheet.
- Figure 5.9(b): Corrected phase information from the contact capacitance transducer waveform in a 1.2mm aluminium sheet.
- Figure 5.10: a_0 phase velocity in a 1.2mm aluminium plate, found using the FFT phase reconstruction technique and a contact capacitance transducer - theory vs. experiment.
- Figure 5.11: A selection of air-coupled Lamb waves in 1.2mm aluminium at transducer-plate angles of 0° to 25° .
- Figure 5.12: Using a difference technique, where X is the known propagation length in the sample, A is the unknown propagation length in the air gap, and dX is the change in the sample propagation path.
- Figure 5.13: Group velocity dispersion curve for a 1.2mm aluminium plate, found using the zero crossing technique.
- Figure 5.14: Group velocity dispersion curve for a 0.85mm brass plate, found using the zero crossing technique.

- Figure 5.15: Group velocity dispersion curve for a 1.18mm steel plate, found using the zero crossing technique.
- Table 5.2: Physical constants and the calculated sheet velocities c_s .
- Figure 5.16(a): Best fit line through origin and first part of curve for the square of the group velocity in a 1.2mm aluminium plate. Gradient of best fit is $41.39\text{m}^2\text{s}^{-3}$.
- Figure 5.16(b): Best fit line through origin and first part of curve for the square of the group velocity in a 0.85mm brass plate. Gradient of best fit is $16.8\text{m}^2\text{s}^{-3}$.
- Figure 5.16(c): Best fit line through origin and first part of curve for the square of the group velocity in a 1.2mm mild steel plate. Gradient of best fit is $42.33\text{m}^2\text{s}^{-3}$.
- Table 5.3: Comparison of measured and estimated thickness.
- Figure 5.17: Phase velocity dispersion curve for a 0.69mm aluminium plate, found using the FFT reconstruction technique.
- Figure 5.18: Phase velocity dispersion curve for a 0.254mm (0.010") steel shim, found using the FFT reconstruction technique.
- Table 5.4: Nominal thickness, estimated thickness and percentage difference.
- Figure 5.19(a): A typical Lamb wave in 0.254mm brass shim.
- Figure 5.19(b): The fast Fourier Transform (FFT) of Figure 5.19(a).
- Figure 5.20: Schematic diagram of apparatus for entirely air-coupled testing using Lamb waves.
- Figure 5.21: Phase velocity dispersion curve for a 0.69mm aluminium plate, obtained using air-coupled source and receiver.

- Figure 6.1: Transmission through a thin layer half a wavelength thick.
- Figure 6.2: Apparatus for through thickness experiments and C-scanning.
- Figure 6.3(a): Waveform through a 30mm air gap.
- Figure 6.3(b): Frequency spectrum of Figure 6.3(a).
- Figure 6.4(a): Waveform obtained through a 16-ply (2.2mm thick) cross-ply CFRP composite plate.
- Figure 6.4(b): Frequency spectrum of Figure 6.4(a)
- Figure 6.5(a): Waveform obtained through a 16-ply (2.2mm thick) unidirectional CFRP composite plate.
- Figure 6.5(b): Frequency spectrum of Figure 6.5(a).
- Figure 6.6(a): Waveforms in 8-ply, 24-ply and 40-ply quasi-isotropic CFRP plates.
- Figure 6.6(b): Frequency spectra of waveforms in Figure 6.6(a).
- Figure 6.7: Waveform through a 120-ply (17.5mm thick) unidirectional CFRP plate.
- Figure 6.8(a): Waveforms through 4.0mm and 9.8mm thick pultruded glass fibre reinforced polymer composite.
- Figure 6.8(b): Frequency spectra of the waveforms in Figure 6.8(a).
- Figure 6.9(a): Waveforms through 1.5mm, 6.0mm and 26.5mm thick perspex (polymethylmethacrylate).
- Figure 6.9(b): Frequency spectra of waveforms in 1.5mm and 6.0mm thick perspex.
- Figure 6.10(a): Waveform through 25mm of expanded polyurethane foam (solid line), and signal through air gap only (dashed line, scaled by 10^{-2} for presentation purposes).

- Figure 6.10(b): Waveform through 12mm of expanded polyurethane foam (solid line),
and through the air gap only (dashed line to same scale).
- Figure 6.11(a): Waveform through 12.9mm thick aluminium, showing longitudinal
arrivals *L*, shear wave arrival *S* and its mode conversions *M*.
- Figure 6.11(b): Waveform through 6.0mm thick aluminium.
- Figure 6.12(a): Waveform through a defect free area of a 16-ply unidirectional CFRP
composite plate.
- Figure 6.12(b): Waveform through a delaminated area of a 16-ply unidirectional
CFRP composite plate.
- Figure 6.13(a): Image of a 25mm square Teflon delamination in a 16-ply (2.2mm
thick) CFRP composite plate. Grey scale is in mV.
- Figure 6.13(b): Image of a 12.5mm square Teflon delamination in a 16-ply (2.2mm
thick) CFRP composite plate. Grey scale is in mV.
- Figure 6.13(c): Image of a 6.25mm square Teflon delamination in a 16-ply (2.2mm
thick) CFRP composite plate. Grey scale is in mV.
- Figure 6.13(d): Image of a delamination caused by a 5mm diameter impact in a
6.35mm thick CFRP cross-ply composite plate. Grey scale is in mV.
- Figure 6.14(a): Image of a defect 10mm diameter by 1mm deep machined into a
9.8mm thick pultruded composite plate. Grey scale is in mV.
- Figure 6.14(b): Image of a defect 5mm diameter by 2mm deep machined into a 9.8mm
thick pultruded composite plate. Grey scale is in mV.
- Figure 6.15(a): Signal amplitude image of an 8mm diameter recess machined halfway
into a 0.7mm thick aluminium plate. Grey scale is in mV.
- Figure 6.15(b): Change in time of arrival image of an 8mm diameter recess machined

halfway into a 0.7mm thick aluminium plate. Grey scale is in μs .

Figure 6.16(a): Lamb wave in a 1mm thick perspex sheet, propagating over a distance of 50mm through the plate.

Figure 6.16(b): Lamb wave in a 8-ply (1.1mm thick) quasi-isotropic CFRP composite.

Figure 6.17(a): Lamb wave in 8-ply (1.1mm thick) unidirectional CFRP composite, travelling 50mm parallel to the principle fibre axis.

Figure 6.17(b): Lamb wave in 8-ply (1.1mm thick) unidirectional CFRP composite, travelling 50mm perpendicularly to the principle fibre axis.

Figure 7.1(a): Schematic diagram of the sampling geometry.

Figure 7.1(b): The rotated co-ordinate system.

Figure 7.2(a): The data points in a polar grid.

Figure 7.2(b): The data points in a Cartesian grid.

Figure 7.3(a): Schematic diagram of the experimental apparatus with the pulsed laser source and air-coupled receiver.

Figure 7.3(b): Schematic diagram of experimental apparatus using a pair of capacitance transducers for an entirely air-coupled system.

Figure 7.4(a): Typical Lamb wave in 0.69mm thick aluminium sheet using the laser source.

Figure 7.4(b): Frequency spectrum of Figure 7.4(a).

Figure 7.5(a): Attenuation image in $\text{dB}\cdot\text{mm}^{-1}$ for a 5mm hole through a 0.69mm thick aluminium sheet, obtained using signal amplitude.

Figure 7.5(b): Image of shift in centroid frequency in kHz for the 5mm hole through a 0.69mm thick aluminium sheet.

- Figure 7.6(a): A typical Lamb wave in 1mm thick perspex (PMMA).
- Figure 7.6(b): The frequency spectrum of Figure 7.6(a).
- Figure 7.7(a): Attenuation image in $\text{dB} \cdot \text{mm}^{-1}$ for a 5mm hole through a 1mm thick sheet of perspex (PMMA).
- Figure 7.7(b): Slowness image in $\mu\text{s} \cdot \text{mm}^{-1}$ found using the cross correlated time of flight for a 5mm diameter hole through a 1mm sheet of perspex (PMMA).
- Figure 7.7(c): Image of the shift in centroid frequency in kHz of a 5mm hole through a 1mm thick sheet of perspex (PMMA).
- Figure 7.8: Image of the shift in centroid frequency in kHz of a 10mm diameter recess machined in a 32 ply (4.4mm) cross ply CFRP composite plate.
- Figure 7.9(a): Attenuation image in $\text{dB} \cdot \text{mm}^{-1}$ of a 1" (25.4mm) square delamination in a 16 ply (2.2mm) unidirectional CFRP composite plate.
- Figure 7.9(b): Slowness image in $\mu\text{s} \cdot \text{mm}^{-1}$ of a 1" (25.4mm) square delamination in a 16 ply (2.2mm) unidirectional CFRP composite plate.
- Figure 7.10(a): A typical Lamb wave in a 0.69mm aluminium sheet, obtained using the pair of air-coupled transducers.
- Figure 7.10(b): The frequency spectrum of Figure 7.10(a).
- Figure 7.11(a): Attenuation image in $\text{dB} \cdot \text{mm}^{-1}$ of an 8mm diameter recess machined halfway through a 0.69mm thick aluminium sheet.
- Figure 7.11(b): Slowness image in $\mu\text{s} \cdot \text{mm}^{-1}$ for an 8mm diameter recess machined halfway through a 0.69mm thick aluminium plate.
- Figure 7.11(c): Image of the shift in centroid frequency in kHz for an 8mm diameter recess machined halfway through a 0.69mm thick aluminium plate.

- Figure 7.12(a): A typical Lamb wave in 1mm perspex (PMMA), obtained using the pair of air-coupled transducers.
- Figure 7.12(b): The frequency spectrum of Figure 7.12(a).
- Figure 7.13(a): Attenuation image in $\text{dB}\cdot\text{mm}^{-1}$ of a 5mm hole through a 1mm thick sheet of perspex (PMMA).
- Figure 7.13(b): Slowness image in $\mu\text{s}\cdot\text{mm}^{-1}$ of the 5mm hole through a 1mm thick sheet of perspex (PMMA).
- Figure 7.13(c): Image of shift in centroid frequency in kHz of the 5mm hole through a 1mm thick sheet of perspex (PMMA).
- Figure 7.14(a): Image of shift in centroid frequency in kHz of a 10mm diameter recess in a 16 ply (2.2mm) cross ply CFRP plate.
- Figure 7.14(b): Attenuation image in $\text{dB}\cdot\text{mm}^{-1}$ of a 1mm by 10mm slot in a 0.69mm thick aluminium sheet, off centre by 10mm in the horizontal direction.
- Figure 7.15(a): Attenuation image in $\text{dB}\cdot\text{mm}^{-1}$ of a 10mm hole (centre) and a 5mm hole (offset by 20mm in both directions) through a 0.69mm thick aluminium sheet.
- Figure 7.15(b): Image of shift in centroid frequency in kHz of a 10mm hole (centre) and a 5mm hole (offset by 20mm in both directions) through a 0.69mm thick aluminium sheet.

Acknowledgements

I would first like to thank Professor David Hutchins, for without his excellent supervision, endless encouragement and formidable insight, this thesis would never have been completed. I would also like to thank Duncan Billson and Lawrence Scudder for their help and guidance throughout the work, and to Andy Bashford, Andy Pardoe and Craig McIntyre for their companionship. I must also thank David Schindel for providing the micromachined devices used extensively in this work, and Dion Jansen for the use of his tomography reconstruction theory and program.

My thanks also go to all the staff in the Department of Engineering who have given their assistance, and I apologise for not naming them all individually. Special thanks, however, go to Steve Wallace and all the technicians in the INRG workshops, Dave Robinson for help with the Talysurf, Frank Courtney for his guidance on etching and photolithography, and Viola Kading for the backplate polishing and photography.

Finally, I would like to thank my family for their endless support and patience, and to everyone at Warwick University Mountaineering Club for helping me escape every now and then.

Declaration

The work described in this thesis was conducted by the author, except where stated otherwise, in the Department of Engineering between October 1991 and February 1996. No part of this work has been previously submitted by the author to the University of Warwick or any other academic institution for admission to a higher degree. All publications to date arising from this thesis are listed after the bibliography.

W.M.D. Wright, 23rd February, 1996.

Summary

This thesis describes how air-coupled ultrasound was used to test metals, polymers and fibre reinforced composite materials. A micromachined silicon air-coupled capacitance transducer was characterised using laser-generated ultrasound and a contact capacitance probe, and found to approximate the surface displacement of the sample with a bandwidth of up to 2MHz. This device was then used to detect laser-generated bulk waves, surface waves and Lamb waves travelling in solid materials. Alternative air-coupled transducers made from 1-3 piezocomposites were similarly evaluated. A 1.2MHz piezocomposite transducer with a 1.6MHz bandwidth was used to measure longitudinal velocities in fibre reinforced composites from 1.1mm to 9.8mm thick in through-transmission with a laser source, and to produce C-scan images of delaminations up to 25mm square, and machined defects up to 10mm in diameter. Air-coupled capacitance transducers with roughened, polished, and chemically etched metal backplates were manufactured, and the effects of surface roughness, polymer film thickness from 5 μ m to 25 μ m, and bias voltages to 1000V were investigated and found to be consistent with previous work. The thickness of metal sheets 0.08mm to 1.2mm thick was estimated to within 5% using air-coupled Lamb waves, by reconstructing the velocity dispersion curves and comparing them to theoretical curves calculated by a FORTRAN program. A pair of air-coupled capacitance transducers was used to measure the longitudinal wave velocity in polymers up to 25mm thick, fibre reinforced composites up to 17mm thick and aluminium up to 12mm thick, using entirely air-coupled through-thickness waves. C-scan images of delaminations up to 25mm square and machined defects up to 10mm diameter were also obtained using this system. Finally, air-coupled capacitance transducers were used to reconstruct tomographic images of delaminations and machined defects in thin plates, using Lamb waves and a filtered back projection algorithm, with varying success depending on their size, shape and location.

Chapter 1: Introduction and overview of non-contact ultrasonics

1.1 Introduction

To most people, sound is simply something with which we communicate, or listen to in the form of music. However, elsewhere in the animal kingdom, it has long been realised that certain creatures such as bats [1,2] use sound to navigate, locate food and even stun their prey. These natural phenomena have since been copied by scientists and engineers to produce SONAR [3], object recognition [4] and robot guidance systems [5-6]. Sound waves are mechanical vibrations which may travel through solids, liquids and gases, at frequencies in Hertz (Hz) given by:

$$f = \frac{c}{\lambda} \quad \{1.1\}$$

where f is the given frequency, c is the velocity of the wave in the material, and λ is the wavelength. At frequencies above 20kHz, sound waves are no longer audible and are said to be ultrasonic. Perhaps the most well-known uses of high frequency sound are medical [7], with applications ranging from imaging of the foetus and heart, to more direct surgical procedures. The use of sound in engineering has been less well publicised. Applications may range from non-destructive testing with a simple tap test [8], to materials evaluation, thickness measurement, and defect detection and characterisation [9].

This introductory chapter will explain briefly some of the properties of ultrasonic wave propagation, and a few of the more conventional ways in which it is used in engineering. Some of the associated problems with these techniques will be highlighted, and some of the methods by which they may be overcome will be discussed. An outline of this thesis will then be given.

1.2 Types of sound wave

There are several different types of sound wave [9-11]. If the particles of material vibrate in the same direction as the propagation of the wave, as shown schematically in Figure 1.1(a), then alternating areas of compressed and rarefied particles are formed and a longitudinal or compression wave is said to exist. Longitudinal waves may be supported in solids, liquids and gases. If the material particles vibrate perpendicularly to the direction of wave motion, as shown schematically in Figure 1.1(b), then a shear or transverse wave is said to exist. Shear waves do not propagate in most liquids and gases, which are unable to support shear forces. The longitudinal wave velocity c_L may be calculated from the elastic constants of the material by the following formula:

$$c_L = \sqrt{\frac{E(1-\sigma)}{\rho(1+\sigma)(1-2\sigma)}} \quad \{1.2\}$$

and similarly for the shear wave velocity c_S :

$$c_S = \sqrt{\frac{E}{2\rho(1+\sigma)}} \quad \{1.3\}$$

where E is Young's modulus of elasticity, ρ is the density and σ the Poisson's ratio for the material. The two velocities are also linked by the relation:

$$c_S = c_L \sqrt{\frac{1-3\sigma}{2(1-\sigma)}} \quad \{1.4\}$$

When a sound wave travels along the surface of a thick sample of material, and the particle motion is an ellipse as shown in Figure 1.1(c), a surface or Rayleigh wave [12,13] exists. The surface motion is not sinusoidal, and the particle motion decreases in amplitude and becomes more circular with depth. The frequency of Rayleigh waves

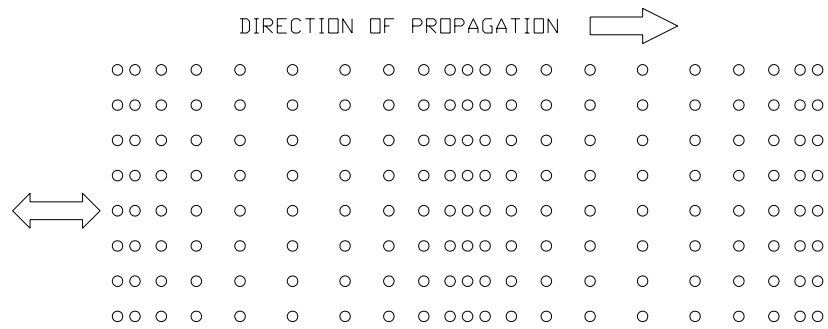


Figure 1.1(a): Particle motion for a longitudinal wave.

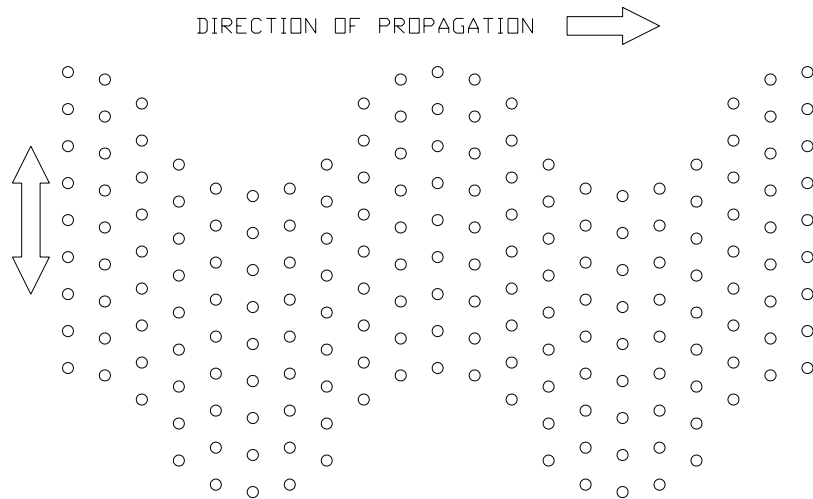


Figure 1.1(b): Particle motion for a shear wave.

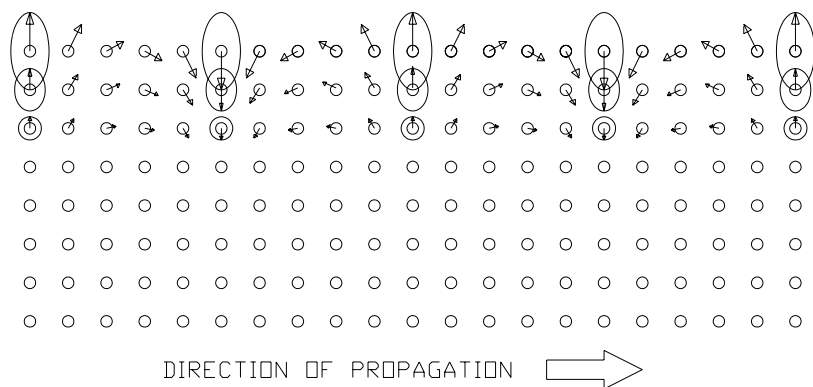


Figure 1.1(c): Particle motion for a Rayleigh wave. The elliptical motion becomes more circular and reduces in amplitude with depth.

determines how far into the material they penetrate, and this is usually to the order of one wavelength. Plate or Lamb waves [12,13] occur when the two surfaces of a plate are sufficiently close together to prevent the propagation of pure surface waves. These guided waves are highly complex and will be discussed in greater detail in a later chapter. Other less commonly used waves are Love waves and Stoneley waves, and as they are not used in this work will not be discussed here.

1.3 Some properties of sound waves

Sound waves are affected by discontinuities in the medium in which they propagate [9-11,14,15]. When a wave crosses a boundary between two materials which have different velocities, at any angle other than normal incidence, as shown schematically in Figure 1.2(a), then the wave is refracted and the angle at which it propagates in the second material differs to the angle in the first. The relationship between angle and velocity is known as Snell's law, given by:

$$\frac{\sin \alpha}{\sin \beta} = \frac{c_A}{c_B} \quad \{1.5\}$$

where A and B denote the two different materials, and α and β the two angles.

At a boundary between two different materials, some of the incident acoustic energy will be reflected, and some will be refracted or transmitted across the interface. These quantities may be determined using the acoustic impedance Z , given by:

$$Z = \rho \cdot c_n \quad \{1.6\}$$

where ρ is the density and c_n the acoustic velocity in the material. The coefficient of reflection R may be found using:

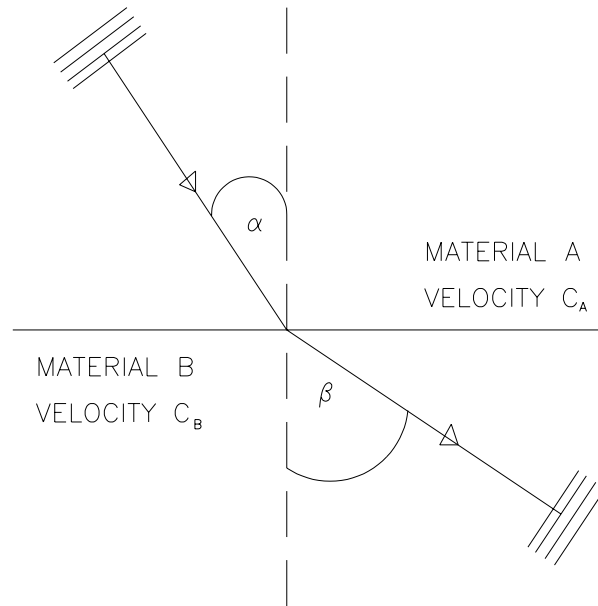


Figure 1.2(a): Snell's law for a wave travelling across the interface between two different materials, with velocity c_B greater than c_A .

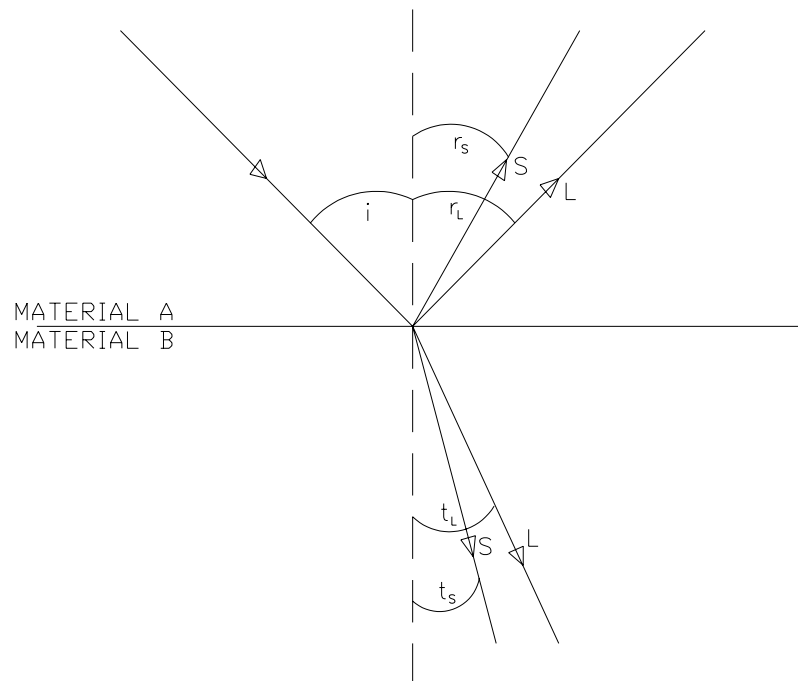


Figure 1.2(b): Mode conversion of a longitudinal wave at a material interface into shear S and longitudinal L wave components, with velocity c_A greater than c_B . The angle of incidence i equals the angle of reflection r_L for the longitudinal wave.

$$R = \left(\frac{Z_1 - Z_2}{Z_1 + Z_2} \right)^2 \quad \{1.7\}$$

and the transmission coefficient T by:

$$T = \frac{4Z_1Z_2}{(Z_1 + Z_2)^2} \quad \{1.8\}$$

This interface may also cause mode conversions of both the reflected and refracted waves, as shown schematically in Figure 1.2(b) for a compression wave, where the angle of incidence i equals the angle of reflection r_L . This also occurs for shear waves.

Another important wave phenomenon which occurs when a wave interacts with a discontinuity in the medium is diffraction. These effects are most prominent when the size of the discontinuity is not very large when compared to the wavelength.

As sound travels through most media, the signal is attenuated, i.e. it loses energy in the form of heat due to a variety of mechanisms, including scattering due to the effects of microstructure. This attenuation α is a complicated function of frequency, material grain size, grain orientation, and other material properties such as anisotropy, and so a convenient quantity may be measured in decibels, using the ratio of acoustic powers given by the relation:

$$\alpha = 10 \log_{10} \left(\frac{P_1}{P_2} \right) \quad \{1.9\}$$

or the ratio of amplitudes:

$$\alpha = 20 \log_{10} \left(\frac{A_1}{A_2} \right) \quad \{1.10\}$$

The principles outlined here are intended only for reference purposes throughout the thesis, and a general introduction to some of the more commonly used formulae. For a more detailed description of these and other wave phenomena, the

reader is directed to any of the numerous works available on general optics and wave theory [16].

1.4 Conventional ultrasonic testing

The use of sound to test engineering materials involves many different techniques and applications, and most use some form of ultrasonic piezoelectric contact probe [9,10,17]. These consist of a thin disc of a piezoelectric material, such as quartz or lead-zirconate-titanate (PZT) with a metallised electrode on each face, attached to a block of backing material. The construction of a typical piezoelectric transducer is shown schematically in Figure 1.3(a). To generate ultrasonic waves, a voltage is applied across these electrodes which causes the disc to vibrate due to the piezoelectric effect. When acting as a receiver, an ultrasonic wave causing motion of one of the faces of the piezoelectric element will produce a charge which may be detected by a suitable amplifier. The majority of most conventional ultrasonic flaw detectors and thickness gauges use piezoelectric transducers.

The transducers may be used in a number of different ways, the most common being shown in Figure 1.3(b). When a single transducer is used as both a source and receiver, this is known as pulse-echo. By employing two separate transducers, one as a source and the other as a receiver, techniques such as pitch-catch (both transducers on the same side of the sample) and through transmission (transducers on opposite sides of the sample) may be used.

There are many different designs of piezoelectric transducer, which are usually governed by the type of ultrasonic wave required. Longitudinal (compression) waves

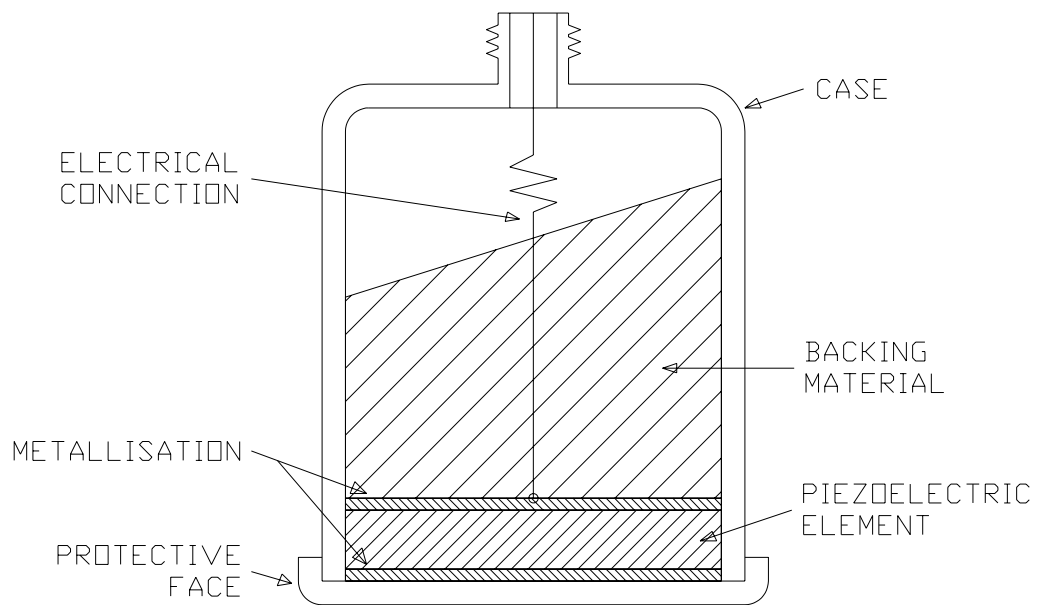


Figure 1.3(a): Construction of a typical piezoelectric transducer.

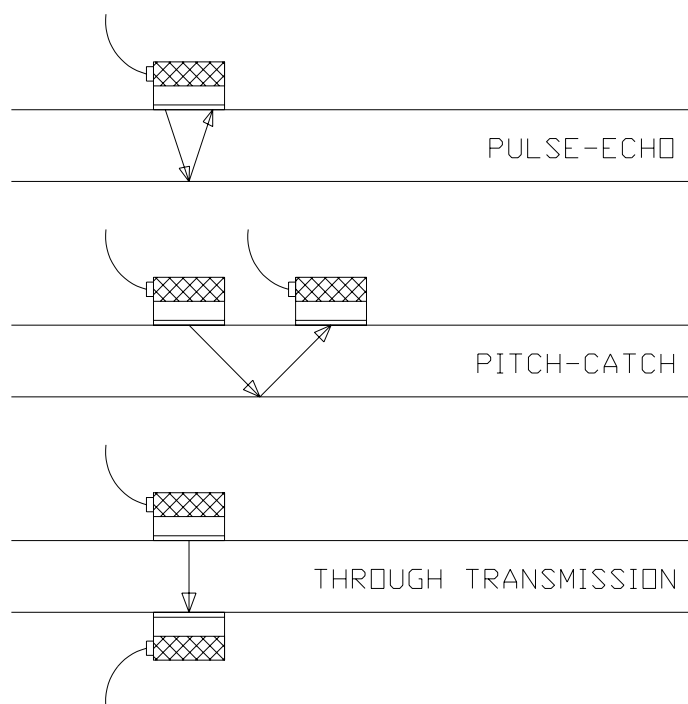


Figure 1.4(b): Different transducer techniques.

and shear (transverse) waves may be easily generated by selecting a piezoelectric element with the correct orientation. A transducer may have more than one element, so that a single transducer may be used in pitch-catch rather than pulse-echo. By the addition of a wedge at the correct angle, a variety of surface (Rayleigh) and plate (Lamb) waves may be used in the sample under test. Focused transducers may be similarly constructed by the addition of a suitable lens, or by using a curved piezoelectric element.

1.5 Non-contact methods

To couple these vibrations into the material under examination, some form of fluid couplant is usually used, or complete immersion in a water bath. This is the major limitation of conventional ultrasonic probes, and there are many situations and applications where contact with the specimen is undesirable, for example when the sample is at elevated temperature, is moving rapidly in a production process, or the material itself is toxic or radioactive. Many materials themselves are unsuitable for use with fluid couplants, as they may be highly absorbent or easily corroded. Fortunately there are methods of ultrasonic transduction which do not require couplants or contact with the test material, and these will be described in the next sections.

1.5.1 Laser generation of ultrasound

The use of pulsed lasers as sources of ultrasound has been well documented by several authors [18-21], and will be described here as the technique is used

extensively throughout this thesis. When the surface of a sample is irradiated by a pulsed laser, generation of ultrasonic transients may occur by one of three mechanisms, determined by the optical power density and surface conditions. If the power density is low (typically less than 10^7W/cm^2), the absorption of radiation causes rapid localised heating of the sample, making the irradiated area expand and generate a stress (sound) wave which propagates through the medium, as shown in Figure 1.4(a). Since the majority of the stresses are transverse, i.e. in the plane of the sample surface, this mechanism produces predominantly shear waves and is known as thermoelastic generation. The corresponding surface displacement waveform is shown in Figure 1.4(b), and consists of a small longitudinal component L , followed by a larger step like shear wave arrival at S .

If the optical power density is increased (typically 10^7W/cm^2 to 10^9W/cm^2), the absorption of radiation causes a thin layer of the sample to vaporise or ablate. This removal of material produces stresses normal to the sample surface by momentum transfer, and so longitudinal waves are preferentially produced, as shown in Figure 1.5(a). This method of generation is known as ablation, and may be used in conjunction with a layer of fluid or a constraining layer such as a glass cover slip to enhance the longitudinal wave component. The corresponding surface displacement waveform is shown in Figure 1.5(b), with now a much larger longitudinal transient L , followed by a smaller shear step S . If the optical power density is increased further, the vaporised material absorbs more energy and ionises into a plasma close to the sample surface. The energy of the ions within the plasma, and hence the momentum transfer into the sample, will increase with power density until the plasma shields the surface from the incoming radiation, and no further gain in ultrasonic signal amplitude is obtained. The interaction of the incoming laser pulse with the plasma is extremely

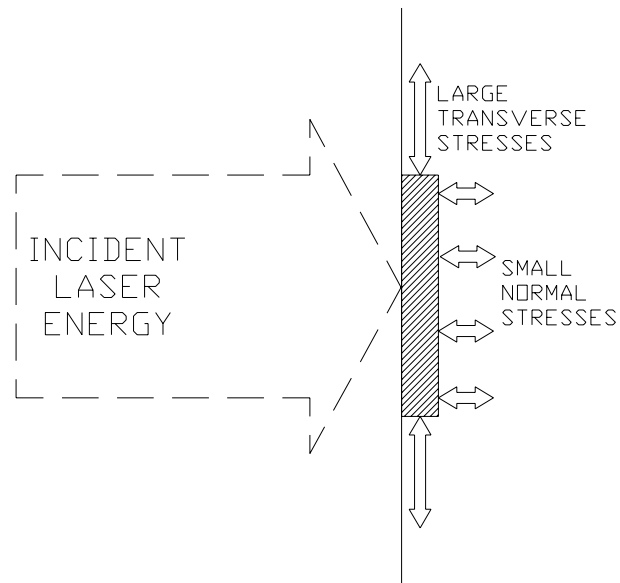


Figure 1.4(a): Laser generation of ultrasound by the thermoelastic mechanism.

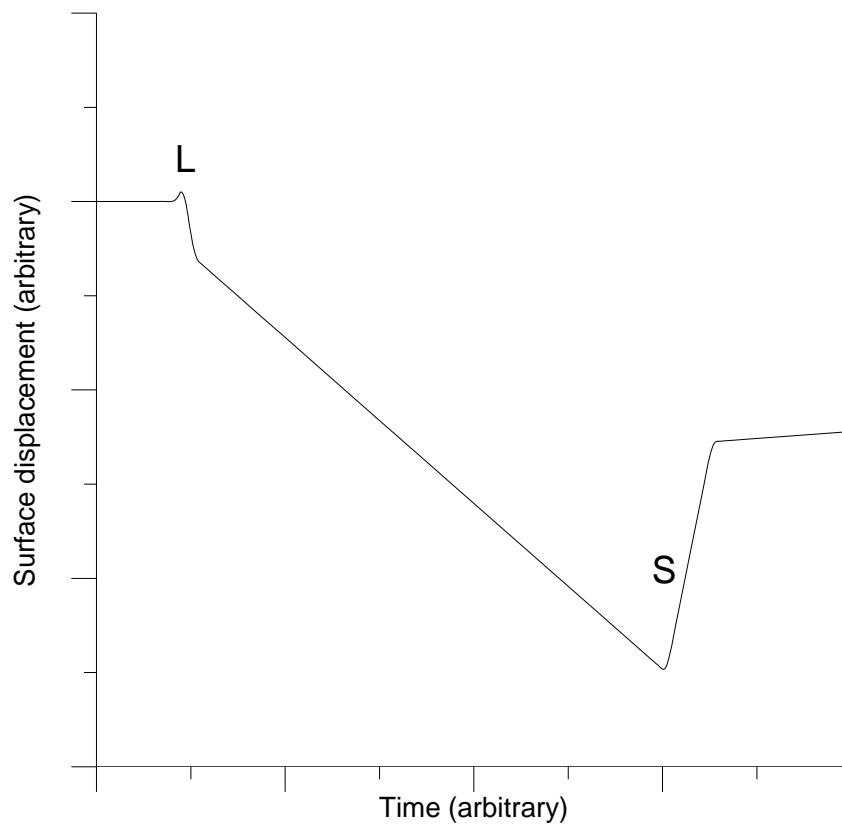


Figure 1.4(b): Theoretical displacement waveform for a thermoelastic source, with longitudinal L and shear S components. Adapted from Scruby and Drain [21].

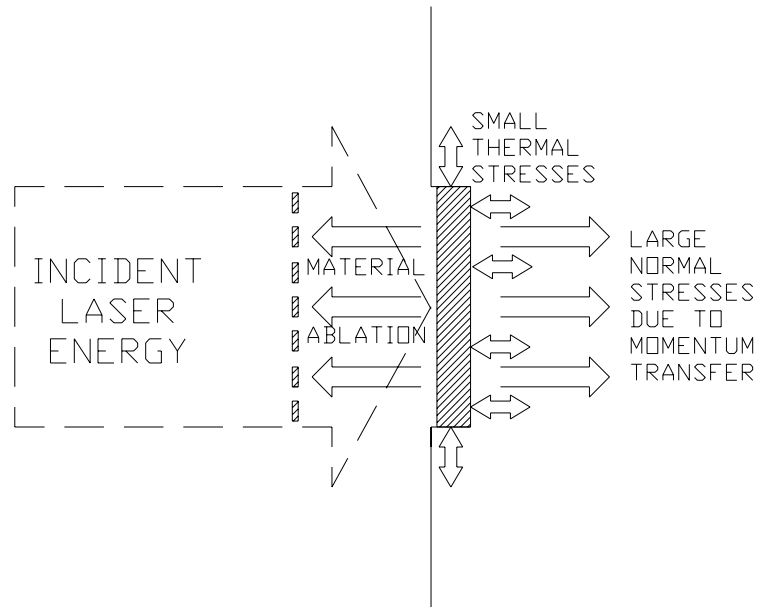


Figure 1.5(a): Laser generation of ultrasound using the ablation mechanism.

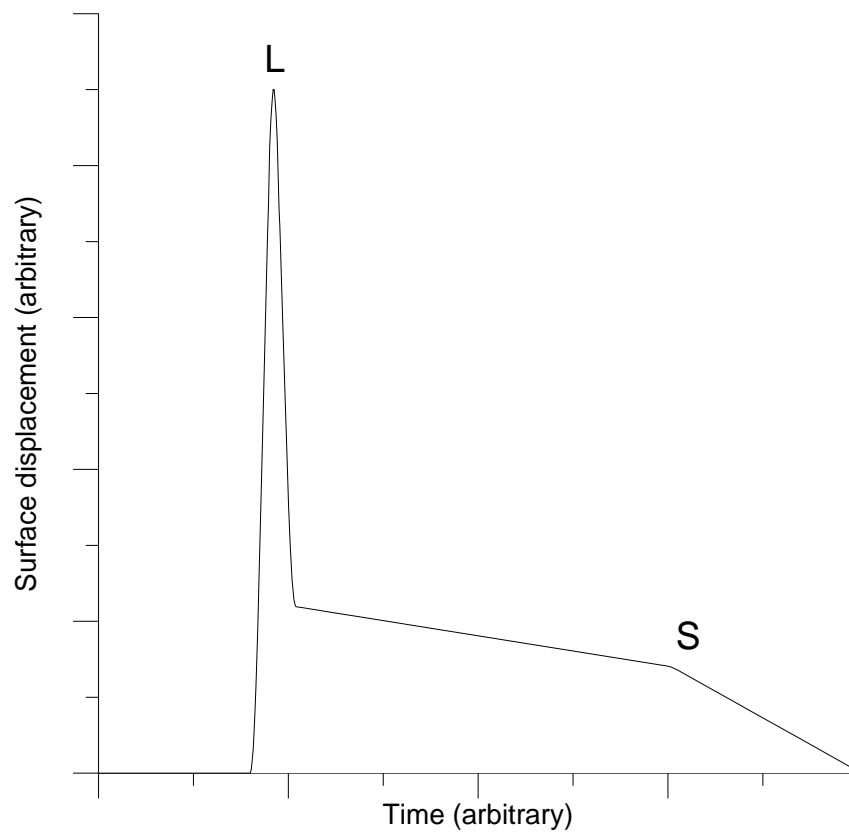


Figure 1.5(b): Theoretical displacement waveform for an ablative source, with longitudinal L and shear S components. Adapted from Scruby and Drain [21].

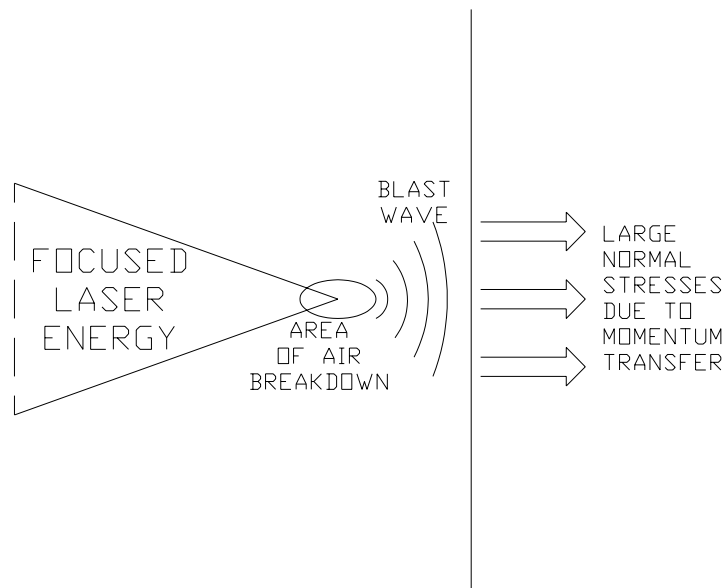


Figure 1.6(a): Laser generation of ultrasound using the air breakdown mechanism.

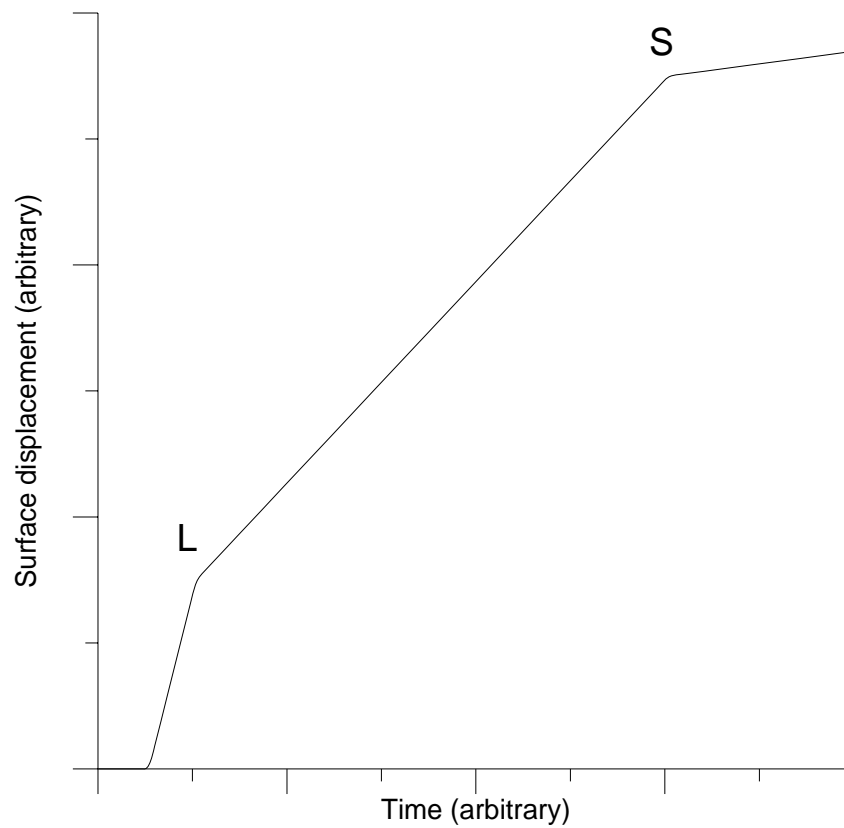


Figure 1.6(b): Theoretical displacement waveform for an air breakdown source, with longitudinal L and shear S components. Adapted from Edwards *et. al.* [20]

complex [22], as various in-plasma detonation waves may be produced, and is outside the scope of this study.

An alternative to this technique is to focus the incoming laser pulse to a point some distance in front of the sample, and use a sufficiently high optical power to ionise the air. This air breakdown source [20] produces a blast wave which imparts momentum into the sample, and will preferentially generate longitudinal transients, as shown in Figure 1.6(a), with the corresponding surface displacement waveform shown in Figure 1.6(b).

1.5.2 Laser detection of ultrasound

Lasers have been used as detectors of displacement and surface motion for many years [21,23-26], the most common type is probably the interferometer. Many different designs are available, but the types most commonly used are (a) those that measure displacement, by interfering the light returned from a surface (by reflection or scattering) with a reference beam, and (b) those that operate as an optical spectrometer to detect frequency shifts in the light returned from a surface, and hence act as velocity detectors.

Most displacement interferometers are based on the Michelson interferometer, shown schematically in Figure 1.7(a). The light source, usually a helium-neon (HeNe) or argon-ion (Ar^+) laser, is split into two beams, one of which goes to a static reference mirror, the other to the surface under scrutiny which is moving due to the influence of an ultrasonic wave. The two reflected beams are then recombined and sent to a photodiode or some other optical detector. The intensity of the light received

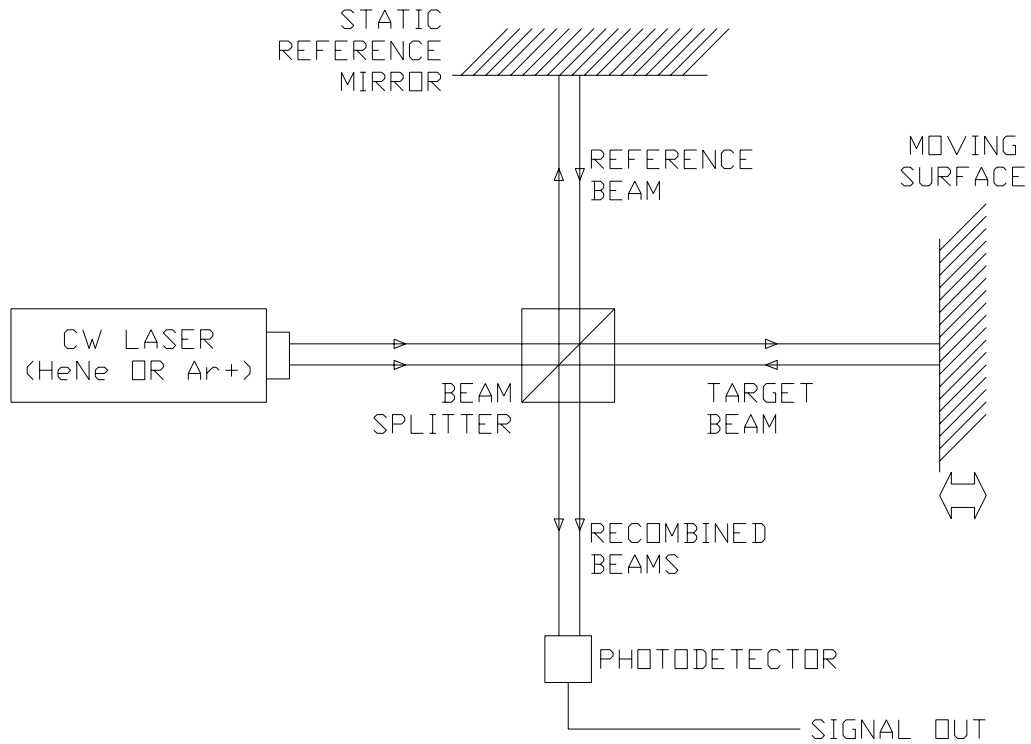


Figure 1.7(a): The basic Michelson interferometer.

is dependent upon the phase difference between the reference and returned beam, which is determined by the change in path lengths caused by motion of the surface. If the range of surface motion is less than one wavelength, then the light intensity may be measured directly, otherwise some form of counter is used to determine the number of wavelengths moved.

The most common of the second type of device is the Fabry-Pérot interferometer, which relies on the interference of multiple reflections of the light returned from a sample to detect small changes in the frequency of this light due to Doppler shift. The device uses a resonant optical cavity, shown schematically in Figure 1.7(b), which consists of two parallel partially reflecting mirrors. This cavity

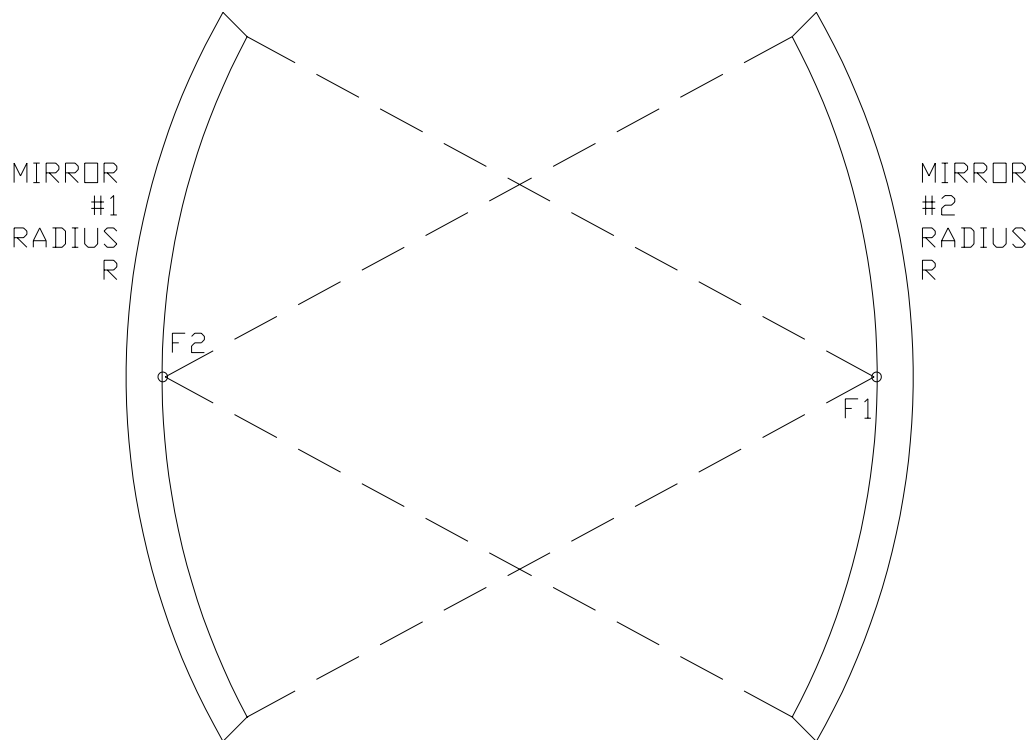


Figure 1.7(b): The resonant optical cavity of a Fabry-Pérot confocal interferometer.

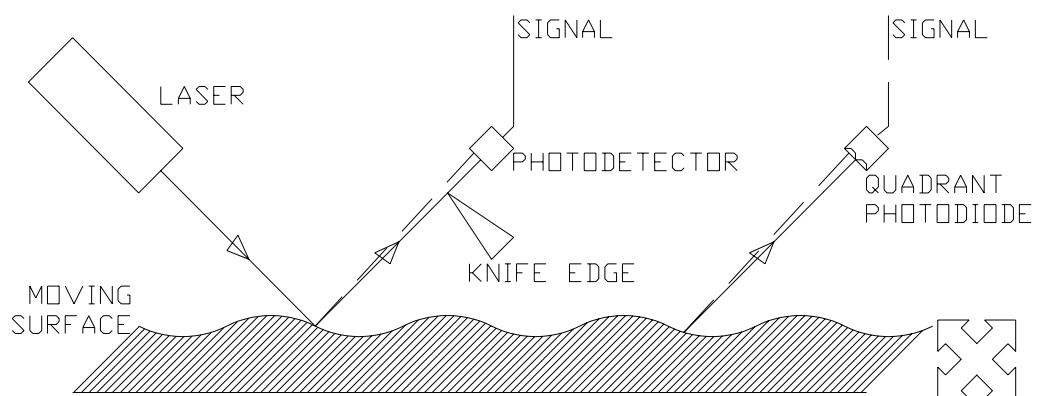


Figure 1.7(c): The knife edge detector or beam deflector.

transmits most light when all the reflections are in phase, i.e. when there is an integer number of wavelengths separating the mirrors. Any slight shift in frequency (caused by motion of the sample surface) will cause the light intensity from the cavity to change proportionally to the velocity of this motion. By using two identical curved mirrors, separated exactly by their radius of curvature, the device is known as confocal and is very insensitive to its orientation with the sample, and so is more practical.

Other forms of optical detector include the beam deflector and knife edge detector, shown schematically in Figure 1.7(c). Motion of the sample surface will shift the position of the reflected beam, so that either the amount of light detected past a knife edge is varied, or the position of the beam on, say, a quadrant photodiode connected to a differential amplifier is changed. This form of detector is most sensitive to tilt of the surface under examination.

All laser based detectors have some significant limitations, however. Most require good optical reflectivity from the surface under examination, and as real samples tend to be optically rough, some form of surface preparation is required, and this is not always practical. Most of the interferometers also require precise alignment, a stable working environment, and (particularly the confocal Fabry-Pérot) can be expensive due to the optical components required.

1.5.3 Non-contact transducers

There are several different non-contact transducers available with which a laser based source or detector of ultrasound may be replaced. The electromagnetic acoustic transducer (EMAT) [27,28] consists of a radio frequency (r.f.) coil in a static magnetic field which permeates into the sample, as shown in Figure 1.8. When acting

as a receiver, an ultrasonic wave reaching the surface of the sample causes motion M of the surface in the magnetic field B , generating an eddy current I which is picked up by the coil. Generation is simply a reverse of this process, i.e. passing a current through the coil to produce an ultrasonic wave. Both longitudinal and shear wave EMATs may be constructed, as shown schematically in Figures 1.8(a) and 1.8(b) respectively, by changing the orientation of the magnetic field with respect to the coil.

Another type of non-contact device is the capacitance transducer [17] (not to be confused with the air-coupled capacitance detectors to be described later), and may be used as both a source and detector of ultrasound. A polished flat electrode is placed in close proximity to the surface of the sample which acts as the other electrode of a capacitor, shown schematically in Figure 1.9. A bias voltage of typically a few hundred volts is applied between the two electrodes. When used as a detector, an ultrasonic wave causing motion of the sample surface will cause the electrode gap to change, and thus the capacitance and charge on the two electrodes. This may be detected by using a suitable charge sensitive amplifier. Often a thin polymer film is used as the dielectric, instead of an air gap, producing a pseudo-contact device which is easier to set up.

Both EMATs and this form of capacitance transducer have two significant limitations. They require an electrically conducting sample, and so cannot be used on most polymers and other non-conducting materials without preparation of the sample surface with some form of conducting layer. They also require small stand-off distances from the test specimen, typically a few mm for EMATs and a few μm for the capacitance transducers.

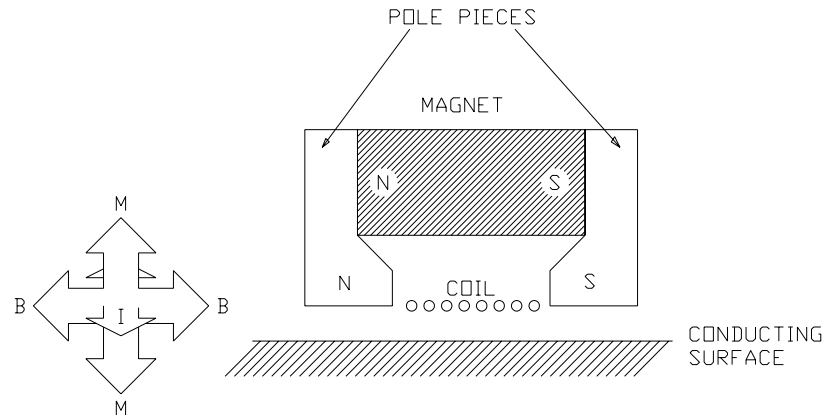


Figure 1.8(a): A longitudinal wave EMAT.

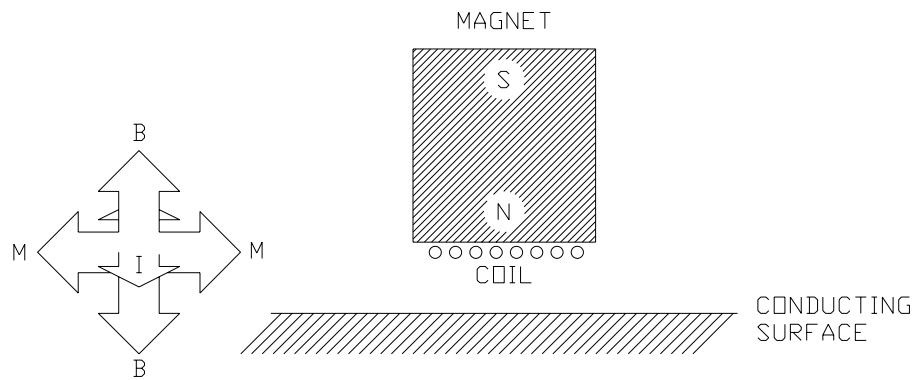


Figure 1.8(b): A shear wave EMAT.

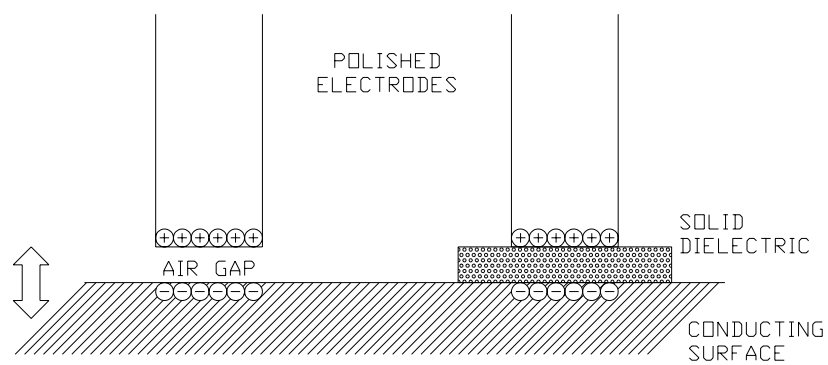


Figure 1.9: A capacitance transducer using air or a solid dielectric between the polished electrode and the conducting sample.

1.6 Air-coupled transducers

There has been much recent interest in the use of transducers that use air as their coupling medium, as the restrictions associated with other devices do not occur. Initially these devices were in the form of high frequency microphones [29], but in general could not operate at frequencies in excess of 200-300 kHz. New designs [30], however, can operate well into the MHz range. Air-coupled transducers may be classified into two distinct groups, piezoelectric and capacitance (or electrostatic).

1.6.1 Piezoelectric air-coupled devices

Whilst being suited for direct coupling to a solid or liquid, most standard piezoelectric transducers are inefficient when used with air as the coupling medium. However, some success has been achieved using high powered driving circuitry and amplifiers [31-32]. This inefficiency is due to the large impedance mismatch between the air and the piezoelectric element. Using equations {1.6} and {1.8}, the impedance, transmission coefficient and other acoustic properties are shown in Table 1.1 [9,10]. It can be seen that the majority of the acoustic energy is not transmitted and so the efficiency of these devices in air is low. There are, however, several mechanisms by which this efficiency may be improved. A metal membrane attached to a 200kHz piezoelectric element has been used [33] to increase the coupling into air. Layers of different material may also be attached to the front face of the transducer, which match the device to air [34], ideally with an acoustic impedance Z_L of:

Material	ρ (kg.m ⁻³)	c_L (m.s ⁻¹)	Z (kg.m ⁻³ .s ⁻¹)	T_{water}	T_{air}
PZT-5	7700	3800	29.3 x10 ⁶	183.6 x 10 ⁻³	5.6 x 10 ⁻⁵
BT	5300	5200	27.6 x10 ⁶	193.8 x 10 ⁻³	6.0 x 10 ⁻⁵
Quartz	2650	5740	15.2 x10 ⁶	323.7 x 10 ⁻³	10.9 x 10 ⁻⁵
PVDF	1760	2000	3.5 x10 ⁶	834.2 x 10 ⁻³	46.9 x 10 ⁻⁵
Water (@20°C)	1000	1483	1.5 x10 ⁶	1.0	111.3 x 10 ⁻⁵
Air (@20°C)	1.2	344	413.8	1.1 x 10 ⁻³	1.0

Table 1.1: Acoustical properties of some transducer materials [9,10].

$$Z_L = \sqrt{Z_1 \cdot Z_2} \quad \{1.11\}$$

where Z_1 and Z_2 are the impedances of air and the piezoelectric element respectively. These layers should be a quarter wavelength thick at the frequency of interest, and they therefore reduce the overall bandwidth of the device. Materials such as Lucite [35], silicone rubber [36], epoxy resin [37], aerogel [38] and ‘solid air’ (compacted tiny air-filled spheres) [39] have been used, or a combination of different layers [40]. There has also been limited success when using air at very high pressure as the coupling medium, with conventional piezoelectric devices, high gain amplifiers and high powered driving circuitry [41]. Another method to improve the impedance mismatch is to use a piezoelectric polymer which has an acoustic impedance closer to that of air to construct the element, such as polyvinylidene difluoride (PVDF) [42-44], or a copolymer [45].

Another technique is to modify conventional piezoceramic elements so that their impedance is reduced, and thus their efficiency increased. These so called

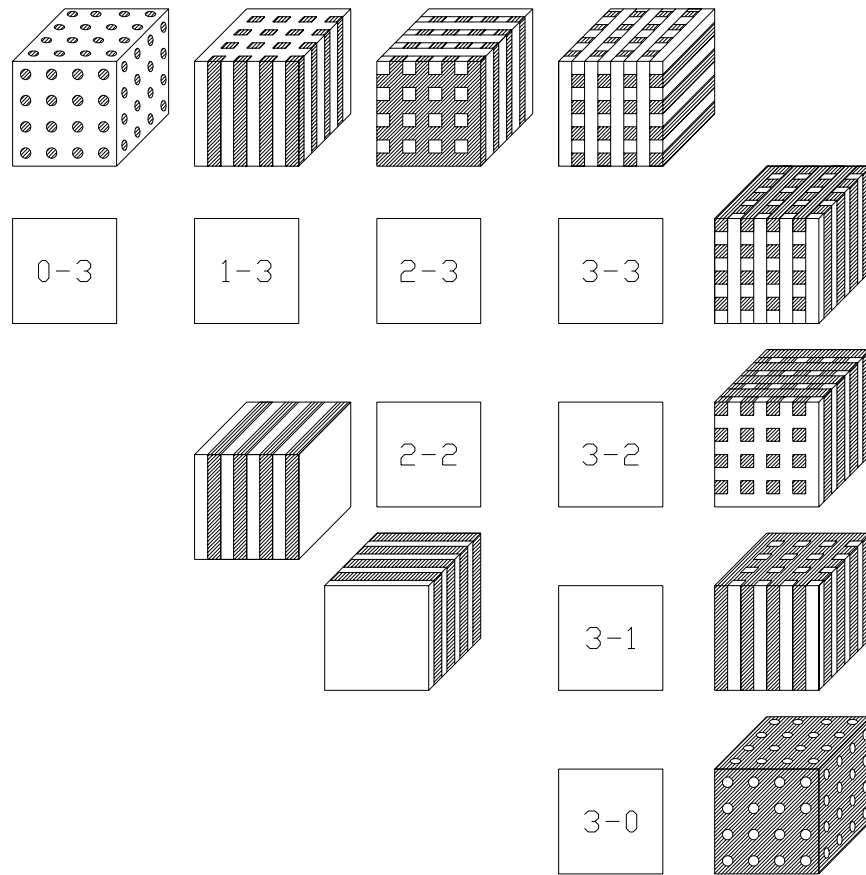


Figure 1.10: Different connectivity composites, with the piezoelectric material shown shaded.

piezocomposite materials are usually made from PZT and a filler material such as epoxy resin. Piezocomposite materials have different properties depending on how the material is modified, and are described in terms of the number of directions of mechanical connectivity for both materials [46]. The different connectivities and composite structures to which they apply are shown schematically in Figure 1.10. Typical piezocomposite materials are 2-2 connectivity (alternate layers of ceramic and filler) [47], and 1-3 connectivity (ceramic rods in a filler matrix). Perhaps the

most widely used piezocomposite material is 1-3 connectivity composite [35,48-53], which is usually manufactured by the ‘slice and fill’ process [54], whereby slots are machined into a disc of the required piezoceramic, and then filled with epoxy to reduce the density and acoustic velocity of the material, and hence the impedance of the element. The composite is then machined to an element of the required shape and thickness for the frequency of interest. More recently, investigations into other processing methods for piezocomposites have been performed [55], such as the injection moulding of the piezoceramic into the required shape without the need for machining.

1.6.2 Capacitance air-coupled devices

Electrostatic or capacitance transducers for operation in air [56] consist of a contoured conducting backplate, over which a flexible dielectric film is placed. This film is usually metallised so that a capacitor is created which has one rigid and one flexible electrode. This type of device is shown schematically in Figure 1.11. Acting as a receiver, a bias voltage is usually applied between the film and backplate electrodes. An ultrasonic wave striking the film will cause it to vibrate, varying the air gap behind it and thus the capacitance of the device. Variations in the charge on the two electrodes may then be detected using a suitable charge sensitive amplifier. Acting as ultrasonic generators, an alternating voltage applied to the device will cause the charge on the electrodes to vary, and the dielectric film to move and produce an ultrasonic wave in the surrounding air.

The majority of work to date concerning electrostatic air transducers has been on different designs of contoured backplate. Traditionally, these have been

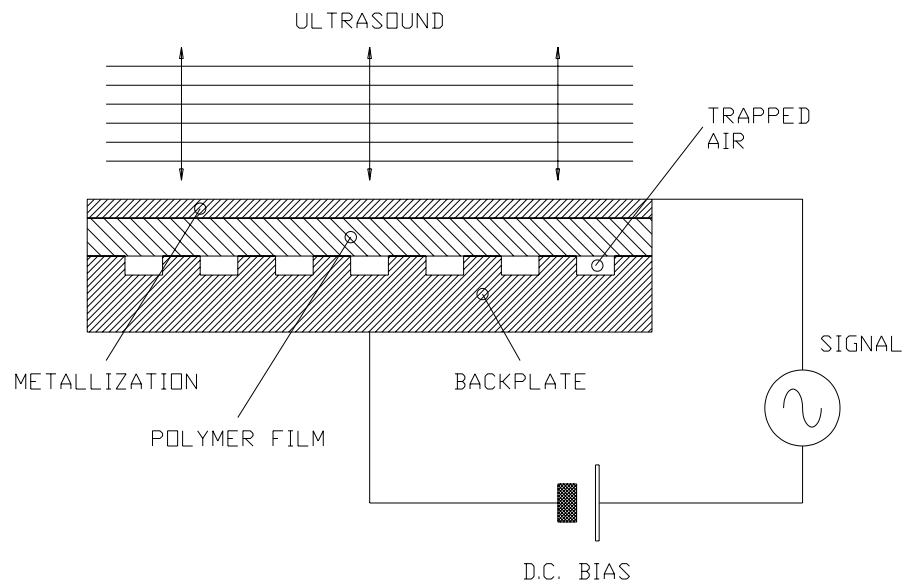


Figure 1.11: Operation of the capacitance devices. The sizes of the polymer film and backplate features are greatly exaggerated for clarity.

manufactured by machining grooves in metal, by shot blasting to give a random surface profile, or some other mechanical roughening process. However, these techniques produce low frequency transducers, typically less than 200kHz, and which have poor reproducibility between devices. More recent work has investigated smooth and polished backplates, which give transducers which operate well into the MHz frequency range, but again pose reproducibility problems. Some success has been achieved in alleviating this problem by micromachining the backplate out of silicon [57,58], using standard integrated circuit manufacturing techniques. This allows precise sub-micrometer control of the backplate surface, and thus the reproducibility between devices. These devices will be discussed in greater detail in a later chapter.

1.7 Outline of the thesis

The work described in this thesis was driven by the recent advances in air-coupled transducer technology, in that there seemed to be a lack of application of air-coupled ultrasonics to existing practical situations. It was thus felt that this area of work would present many interesting opportunities for research.

In Chapter 2, a capacitance or electrostatic device which used a backplate micromachined from silicon was investigated. Laser generated ultrasound was used to help characterise the device, and a more comprehensive study of laser generated waveforms was performed. In Chapter 3, a range of piezoelectric air-coupled transducers were evaluated in a similar fashion. These devices were 1-3 connectivity composite designs, manufactured specifically as receivers. A novel instrumentation system was developed, which used a pulsed laser as a source and an air-coupled piezoelectric receiver. This preserved the non-contact nature of the experiments and assisted in the characterisation of the devices. Details of the transducer construction will be given, along with sample waveforms in aluminium and a comparison with a standard pseudo-contacting displacement transducer, before extensive experimental work in composite materials is presented.

In Chapter 4, a series of air-coupled capacitance devices with metallic backplates were manufactured, and different methods of producing the backplates (roughening, polishing and chemical etching) were evaluated. The effects of film thickness and applied bias voltage were also investigated. Some of the devices were designed to be used as sources, and so the practicalities of entirely air-coupled ultrasonics were investigated. In Chapter 5, air-coupled Lamb waves were used to estimate the thickness of thin metal plates and shim, using entirely non-contact

ultrasonics. The Lamb waves were either generated by the laser, or by an air-coupled capacitance transducer. A computer program was written in FORTRAN to calculate the theoretical dispersion curves in isotropic materials, and then two techniques were employed to extract the dispersion relations and sample thickness data from the air-coupled waveforms.

Chapter 6 presents details of how an entirely air-coupled ultrasonic system was used to test a variety of materials, including pultruded glass-fibre reinforced polymer (GRP) and carbon fibre reinforced polymer (CFRP) composites. This work used a pair of silicon backplate air-coupled capacitance transducers, one as a source and one as a receiver of ultrasound, to characterise samples using through transmission of bulk waves and the propagation of Lamb waves. Waveforms were also obtained in other materials such as perspex, expanded polyurethane foam and aluminium. A variety of machined and delamination defects in these materials were evaluated with a C-scanning technique which again used entirely air-coupled ultrasound.

Finally, another application of air-coupled ultrasonics was investigated in Chapter 7. A pair of the micromachined silicon air-coupled capacitance transducers was used to produce images of a variety of defects in thin plates using tomographic reconstruction. In this technique, a sequence of regularly spaced ultrasonic waveforms was used to build up a series of different views or projections through a defect at different angles. A filtered back projection algorithm was then used to reconstruct a cross sectional image of the defects.

1.8 References

- [1] S. Schmidt, 'Evidence for a spectral basis of texture perception in bat sonar', *Nature* **331**, 617-619 (1988)
- [2] N. Suga, 'Biosonar and neural computation in bats', *Scientific American* **June 1990**, 34-41 (1990)
- [3] S. Stergiopoulos and A.T. Ashley, 'Sonar system technology', *IEEE Journal of Oceanic Engineering* **18**, (IEEE, New York, 1993)
- [4] M. Lach and H. Embert, 'An acoustic sensor system for object recognition', *Sensors and Actuators A* **25-27**, 541-547 (1991)
- [5] W.S.H. Munro, S. Pomeroy, M. Rafiq, H.R. Williams, M.D. Wybrow and C. Wykes, 'Ultrasonic vehicle guidance transducer', *Ultrasonics* **28**, 350-354 (1990)
- [6] P. Kleinschmidt and V. Mágori, 'Ultrasonic robotic sensors for exact short range distance measurement', *Proc. 1985 IEEE Ultrason. Symp.* 457-462 (1985)
- [7] C.R. Hill (ed.), *Physical principles of medical ultrasonics*, (Ellis Horwood Ltd., Chichester, 1986)
- [8] E.P. Papadakis, 'Ultrasonic impulse-induced-resonance utilising damping for adhesive disbond detection', *Mat. Eval.* **36**, 37-40 (1978)
- [9] J. Krautkrämer and H. Krautkrämer, *Ultrasonic testing of Materials*, 4th edition, (Springer-Verlag, Berlin, 1990)
- [10] R. Halmshaw, *Non-destructive testing*, (Edward Arnold, London, 1987)
- [11] J. Blitz, *Fundamentals of Ultrasonics*, 2nd edition, (Butterworths, London, 1967)

- [12] J.D. Achenbach, *Wave propagation in elastic solids*, (Elsevier Science Publishers, Netherlands, 1990)
- [13] I.A. Viktorov, *Rayleigh and Lamb waves - Physical theory and applications*, (Plenum, New York, 1967)
- [14] B.A. Auld, *Acoustic fields and waves in solids: Volume II*, (John Wiley Sons, New York, 1973)
- [15] G.S. Kino, *Acoustic waves*, (Prentice Hall, Englewood Cliffs NJ, 1987)
- [16] F.A. Jenkins and H.E. White, *Fundamentals of optics*, 4th edition, (McGraw-Hill Book Co., Singapore, 1981)
- [17] W. Sachse and N.N. Hsu, 'Ultrasonic transducers for materials testing and their characterisation', in *Physical Acoustics - Principles and Methods*, eds. W.P. Mason and R.N. Thurston, (Academic, New York, 1979), Vol. XIV, pp277-406
- [18] R.M. White, 'Generation of elastic waves by transient surface heating', *J. Appl. Phys.* **34**, 3559-3567 (1963)
- [19] D.A. Hutchins, 'Ultrasonic generation by pulsed lasers', in *Physical Acoustics - Principles and Methods*, eds. W.P. Mason and R.N. Thurston, (Academic, New York, 1988), Vol. XVIII, pp21-123
- [20] C. Edwards, G.S. Taylor and S.B. Palmer, 'Ultrasonic generation with a pulsed TEA CO₂ laser', *J. Phys. D: Appl. Phys.* **22**, 1266-1270 (1989)
- [21] C.B. Scruby and L.E. Drain, *Laser ultrasonics - techniques and applications*, (Adam Hilger, Bristol, 1990)
- [22] M. von Allmen, *Laser-beam interactions with materials - physical principles and applications*, (Springer-Verlag, Berlin, 1987)

- [23] W.H. Steel, *Interferometry*, eds. A. Herzenberg and J.M. Ziman, (Cambridge University Press, Cambridge, 1967)
- [24] J.-P. Monchalin, 'Optical detection of ultrasound', *IEEE Trans. Ultrason., Ferroelec., Freq. Contr.* **UFFC-33**, 485-499 (1986)
- [25] R. Jones and C. Wykes, *Holographic and speckle interferometry - a discussion of the theory, practice and application of the techniques*, (Cambridge University Press, Cambridge, 1989)
- [26] J.W. Wagner, 'Optical detection of ultrasound', in *Physical Acoustics - Principles and methods*, eds. W.P. Mason and R.N. Thurston, (Academic, New York, 1990), Vol. XIX, pp201-266
- [27] H.M. Frost, 'Electromagnetic ultrasonic transducers: principles, practice and applications', in *Physical Acoustics - Principles and methods*, eds. W.P. Mason and R.N. Thurston, (Academic, New York, 1979), Vol. XIV, pp179-276
- [28] R.B. Thompson, 'Physical properties of measurements with EMAT transducers', in *Physical Acoustics - Principles and methods*, eds. R.N. Thurston and A.D. Pierce, (Academic, New York, 1990), Vol. XIX, pp157-200
- [29] W. Kuhl, G.R. Schodder and F.-K. Schröder, 'Condenser transmitters and microphones with solid dielectric for airborne ultrasonics', *Acustica* **4**, 519-532 (1954)
- [30] W. Manthey, N. Kroemer and V. Mágori, 'Ultrasonic transducers and transducer arrays for applications in air', *Meas. Sci. Techn.* **3**, 249-261 (1992)
- [31] D.E. Chimenti and C.M. Fortunko, 'Characterization of composite prepreg with gas-coupled ultrasonics', *Ultrasonics* **32**, 261-264 (1994)

- [32] A.J. Rogovsky, 'Development and application of ultrasonic dry-contact and air-contact C-scan systems for non-destructive evaluation of aerospace composites', *Mat. Eval.* **49**, 1491-1497 (1991)
- [33] M. Babic, 'A 200-kHz ultrasonic transducer coupled to the air with a radiating membrane', *IEEE Trans. Ultrason. Ferroelec. Freq. Contr.* **UFFC-38**, 252-255 (1991)
- [34] L.C. Lynnworth, 'Ultrasonic impedance matching from solids to gases', *IEEE Trans. Sonics, Ultrason.* **SU-12**, 37-48 (1965)
- [35] T.R. Gururaja, W.A. Schultze, L.E. Cross, R.E. Newnham, B.A. Auld and Y.J. Wang, 'Piezoelectric composite materials for ultrasonic transducer applications. Part I: Resonant modes of vibration of PZT rod-polymer composites', *IEEE Trans. Son. Ultrason.* **SU 32**, 481-498 (1985)
- [36] J.D. Fox, B.T. Khuri-Yakub and G.S. Kino, 'High-frequency acoustic wave measurements in air', *Proc. IEEE 1983 Ultrason. Symp.*, Vol.1, 581-584 (1983)
- [37] J.D. Fox, B.T. Khuri-Yakub and G.S. Kino, 'Acoustic resonator transducer for operation in air', *Elec. Lett.* **21**, 694-696 (1985)
- [38] O. Krauß, R. Gerlach and J. Fricke, 'Experimental and theoretical investigations of SiO₂-aerogel matched piezo-transducers', *Ultrason.* **32**, 217-222 (1994)
- [39] M. Teshigawara, F. Shibata and H. Teramoto, 'High resolution (0.2mm) and fast response (2ms) range finder for industrial use in air', *Proc. 1989 IEEE Ultrason. Symp.*, 639-642 (1989)
- [40] M. Tone, T. Yano and A. Fukumoto, 'High-frequency ultrasonic transducer operating in air', *Japan. J. Appl. Phys.* **23**, L436-L438 (1984)
- [41] C.M. Fortunko, R.E. Schramm, C.M. Teller, G.M. Light, J.D. McColskey, W.P. Dubé and M.C. Renken, 'Pulse-echo gas-coupled ultrasonic crack

- detection and thickness gaging', *Proc. Rev. Quant. Nondest. Eval.* Vol. 14A and 14B, Ch. 312, 951-958 (1995)
- [42] H. Kawai, 'The piezoelectricity of poly(vinylidene fluoride)', *Japan. J. Appl. Phys.* **8**, 975-976 (1969)
- [43] M. Platte, 'PVDF ultrasonic transducers for ultrasonic testing', *Ferroelectrics* **115**, 229-246 (1991)
- [44] W. Manthey, N. Kroemer and V. Mágori, 'Ultrasonic transducers and transducer arrays for applications in air', *Meas. Sci. Technol.* **3**, 249-261 (1992)
- [45] H. Ohigashi, K. Koga, M. Susuki and T. Nakamishi, 'Piezoelectric and ferroelectric properties of P(VDF-TrFE) copolymers and their application to ultrasonic transducers', *Ferroelectrics* **60**, 263-276 (1984)
- [46] R.E. Newnham, D.P. Skinner and L.E. Cross, 'Connectivity and piezoelectric-pyroelectric composites', *Mat. Res. Bull.* **13**, 525-536 (1978)
- [47] T. Möckl, V. Mágori and C. Eccardt, 'Sandwich-layer transducer - a versatile design for ultrasonic transducers operating in air', *Sensors and Actuators A* **21-23**, 687-692 (1990)
- [48] W.A. Smith and B.A. Auld, 'Modelling 1-3 composite piezoelectric: thickness mode oscillations', *IEEE Trans. Ultrason. Ferroelec. Freq. Contr.* **UFFC-38**, 40-47 (1991)
- [49] T.R. Gururaja, W.A. Schulze, L.E. Cross and R.E. Newnham, 'Piezoelectric composite materials for ultrasonic transducer applications. Part II: Evaluation of ultrasonic medical applications', *IEEE Trans. Son. Ultrason.* **SU 32**, 499-513 (1985)
- [50] M.I. Haller and B.T. Khuri-Yakub, 'Micromachined 1-3 composites for ultrasonic air transducers', *Rev. Sci. Instrum.* **65**, 2095-2098 (1994)

- [51] J.A. Hossack and G. Hayward, 'Finite-element analysis of 1-3 composite transducers', *IEEE Trans. Ultrason. Ferroelec. Freq. Contr.* **UFFC 38**, 618-629 (1991)
- [52] G. Hayward, A. Gachagan, R. Hamilton, D.A. Hutchins and W.M.D. Wright, 'Ceramic-epoxy composite transducers for non-contact ultrasonic applications', *SPIE Symp. 1992*, Vol. 1733, 49-56 (1992)
- [53] G. Hayward and J.A. Hossack, 'Unidimensional modeling of 1-3 composite transducers', *J. Acoust. Soc. Am.* **88**, 599-608 (1990)
- [54] H.P. Savakus, K.A. Klicker and R.E. Newnham, 'PZT-epoxy piezoelectric transducer: a simplified fabrication procedure', *Mat. Res. Bull.* **16**, 677-680 (1981)
- [55] V.F. Janis and A. Safari, 'Overview of fine-scale piezoelectric ceramic/polymer composite processing', *J. Am. Ceram. Soc.* **78**, 2945-2955 (1995)
- [56] H. Carr, W.S.H. Munro, M. Rafiq and C. Wykes, 'Developments in capacitive transducers', *Nondest. Test. Eval.* **10**, 3-14 (1992)
- [57] K. Suzuki, K. Higuchi and H. Tanigawa, 'A silicon electrostatic ultrasonic transducer', *IEEE Trans. Ultrason., Ferroelec., Freq. Contr.* **UFFC-36**, 620-627 (1989)
- [58] D.W. Schindel, D.A. Hutchins, L. Zou and M. Sayer, 'Capacitance devices for the controlled generation of airborne ultrasonic fields', *Proc. IEEE 1992 Ultrason. Symp.*, 843-846 (1992)

Chapter 2: Studies of laser-generated ultrasound using an air-coupled micromachined silicon capacitance transducer

2.1 Introduction

The work to be described in this chapter will investigate the detection of laser-generated ultrasound in solid materials, using an air-coupled capacitance transducer. These devices are usually made with metal backplates [1-4], and a more detailed review will be given in Chapter 4. However, some of the problems concerning capacitance devices for operation in air are lack of repeatability between devices, and difficulty in producing identical surfaces for the backplate electrodes. In an attempt to have more control over the surface properties of the backplate than are available by mechanical machining techniques, integrated circuit manufacturing techniques have been used to manufacture devices from silicon.

In the next section, a review of micromachined capacitance transducers will be given, followed by construction details of the devices used in this study. The following sections will then use laser-generated longitudinal waves in aluminium to characterise the transducer, before a more detailed study of the various ultrasonic waves from a laser source is conducted. The air-coupled waveforms will be compared to those obtained from a capacitance transducer mentioned earlier in Chapter 1, which uses the sample as one electrode.

2.1.1 Micromachined devices

Several different transducer designs using micromachined silicon have been investigated. Suzuki *et al.* [5] developed devices which operated up to at least 500kHz, by using photolithographic techniques to etch an array of square holes into a silicon wafer using ammonia solution. The conducting surface of the backplate was

produced by covering the pitted silicon with a $1\mu\text{m}$ layer of aluminium from an electron gun. The dielectric layer was formed from SiO_2 by chemical vapour deposition (CVD), so that the insulating layer followed the contours of the surface. The polymer membrane used was metallised $12\mu\text{m}$ polyester, with the metallised side facing inwards so that the polymer film did not act as part of the dielectric. It was shown that the hole dimensions had an effect on the low frequency response and the sensitivity of the devices.

Other work by Schindel *et al.* [6-10] examined devices whose backplates consisted of a regular array of circular pits, with only the polymer membrane and air trapped behind it acting as the dielectric. The work to be described in this and subsequent chapters used one or more of these devices and they will therefore be described in more detail in the next section.

An alternative to etching silicon was attempted by Anderson *et al.* [11], where polyamide ridges were deposited using photolithographic techniques onto a polished aluminium surface, and a $5\mu\text{m}$ metallised polyethylene terephthalate (PET) membrane used as the other electrode. The device relied on a well defined air gap between the $2.75\mu\text{m}$ high polymer ridges and the backplate surface. Thus the surface properties of the aluminium were not of great importance, rather the tension of the membrane, as the dominant mechanism of operation was flexing of the PET membrane. Measuring the tension of polymer films used in capacitance devices has proved to be difficult.

The micromachined devices mentioned so far all used metallised flexible polymer membranes as one electrode. This technique, however, allows for the inclusion of unwanted particles between membrane and backplate during assembly of the device. This may seriously effect the frequency response and operation of the transducer, especially if the particles are of a similar size to the backplate surface

features. Kühnel and Hess [12] produced a range of devices entirely by micromachining, using two separate silicon components. The first was a backplate electrode with either grooves 10-12 μm deep or holes 35-40 μm deep, the second was a membrane of silicon nitride 150nm thick. These devices were only 0.8mm square, and operated at frequencies up to 20kHz. Haller and Khuri-Yakub [13] also manufactured transducers using only micromachining, from a single piece of silicon. A layer of silicon oxide was etched away beneath another layer of silicon nitride which acted as the membrane electrode once it had been metallised with gold. Small pillars of the etched SiO_2 layer remained to support the membrane. These resonant devices operated at frequencies of 1.8MHz and 4.5MHz, although more recently a 9.2MHz device has been reported by the same authors [14].

The work described so far has concentrated mainly on the manufacture of the devices themselves, rather than applications using air-coupled ultrasound [15]. The experiments described in this chapter were the first to use a pulsed laser and a capacitance air-coupled detector for non-contact ultrasonics, and the results have been published [16].

2.1.2 Construction of the micromachined silicon air-coupled transducer

The transducer used in this work is one of the air-coupled capacitance type devices mentioned earlier in Chapter 1, made by David Schindel at the Department of Physics, Queens University Canada. The construction detail of the transducer is shown schematically in Figure 2.1, and was manufactured as follows [10]. A polished (110)

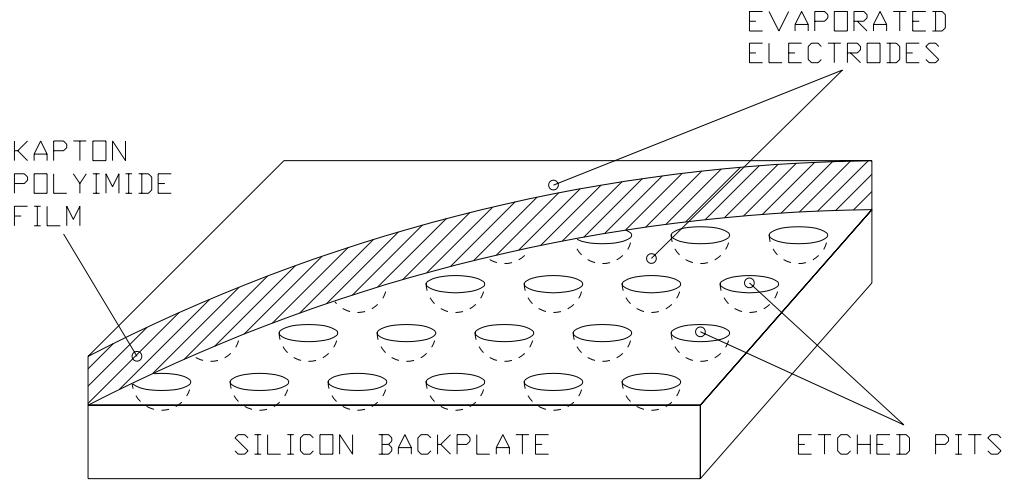


Figure 2.1: Detail of the micromachined silicon backplate.

silicon wafer was coated with masking layers of silicon nitride and silicon oxide, plus a layer of photoresist. The photoresist was exposed using photolithographic techniques through a mask consisting of a uniform grid of $40\mu\text{m}$ diameter holes, with the hole centres $80\mu\text{m}$ apart. The silicon oxide circles were then removed using a hydrofluoric acid etch, and the silicon nitride circles etched with phosphoric acid. The silicon substrate was finally etched with potassium hydroxide, to a self limiting depth of $18\mu\text{m}$. The contoured backplate was then coated with 1000\AA of gold to make a conducting surface. The dielectric and upper electrode consisted of a $7.6\mu\text{m}$ Kapton polyimide membrane, metallized on the outer side with aluminium. This prototype device had an active area of $10\times 7\text{mm}$.

2.1.3 Advantages of using laser-generated ultrasound

The mismatch of acoustic impedances between solid materials and air is probably the main reason why air-coupled ultrasonic applications appear to have been restricted to areas such as range finding, surface profiling and object recognition, where the reflection from a solid/air interface is used. If, however, it is required to couple ultrasound into a solid material, e.g. for material characterisation, then the situation is more problematic. The intensity transmission coefficient, as given by equations {1.6} and {1.8} in Chapter 1, is of the order of 10^{-4} for an interface between most solid materials and air. With such low efficiencies, materials testing using purely air-coupled ultrasound is therefore difficult, but not impossible as will be shown later in Chapters 5, 6 and 7. Consider the scenario shown schematically in Figure 2.2(a), in which ultrasound is generated in air, passes through a solid material e.g. aluminium, and then detected in air on the opposite side. Only a tiny fraction (10^{-8}) of the original acoustic energy is transmitted through both air/solid interfaces to reach the receiver. This assumes that the two interfaces are considered separately, although more energy may be available for samples of a certain thickness if a resonance is produced. Now consider the second scenario, shown schematically in Figure 2.2(b), in which the ultrasound is generated directly in the solid using a pulsed laser. One of the interfaces with air has effectively been removed, so that the energy reaching the receiver could increase by a factor of 10^4 , making material characterisation in air more feasible. In addition, a single laser source is able to generate a variety of different wave types in the same material, without the need for mode conversion techniques.

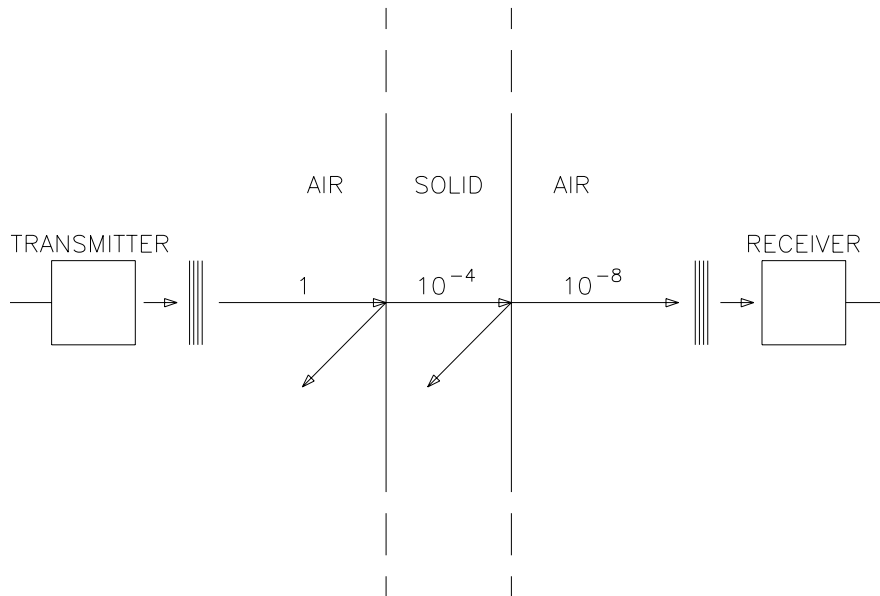


Figure 2.2(a): Through transmission in air using two air-coupled transducers. Values shown are approximate fractions of the original energy.

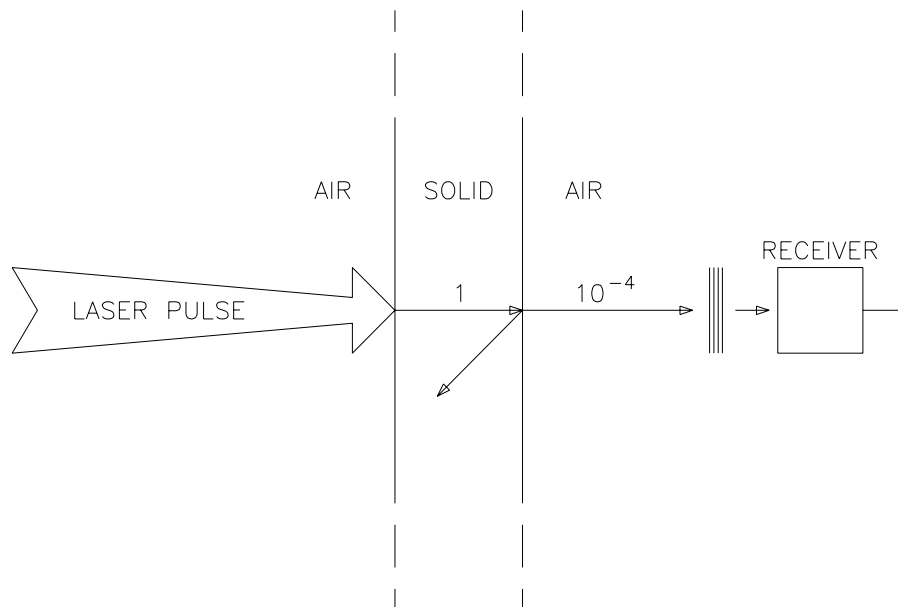


Figure 2.2(b): Improved through transmission using a laser source. Values shown are approximate fractions of the original energy.

2.2 Studies of laser-generated through transmission waveforms

Experiments were performed to detect laser-generated waveforms in a variety of solid materials, using the equipment shown schematically in Figure 2.3(a). Ultrasound was generated in the samples using a Lumonics ‘Mini-Q’ Q-switched Nd:YAG laser, operating at a wavelength of 1064nm in the near infra-red spectrum, and delivering pulses of 4ns duration with a maximum energy of 120mJ per pulse. The beam was directed onto the sample using various optics to give an ablative source approximately 2mm in diameter. Signals were then detected by the air-coupled device, to which a 100V d.c. bias was applied via a Cooknell CA6/C charge amplifier with SU2/C power supply. The resultant time domain waveforms were captured using a Tektronix 540 TDS digital oscilloscope, and transferred to an IBM PS/2 Model 30 286 PC via an IEEE-488/GPIB interface for storage and analysis. For more detailed equipment specifications, see Appendix A. Unless stated otherwise, the air gap between sample and transducer was 10mm, although larger separations were possible.

2.2.1 Characterising the air-coupled capacitance transducer

To provide some form of calibration waveform against which to compare the air-coupled devices, a contact capacitance probe was also used to detect the laser-generated ultrasound for the same generation conditions. This is shown schematically in Figure 2.3(b), and consisted of a steel sphere, in an insulated case, used as one electrode of a capacitor with the other electrode being the sample itself. Note that due to the use of a spherical electrode, tilt of this device is not critical, and

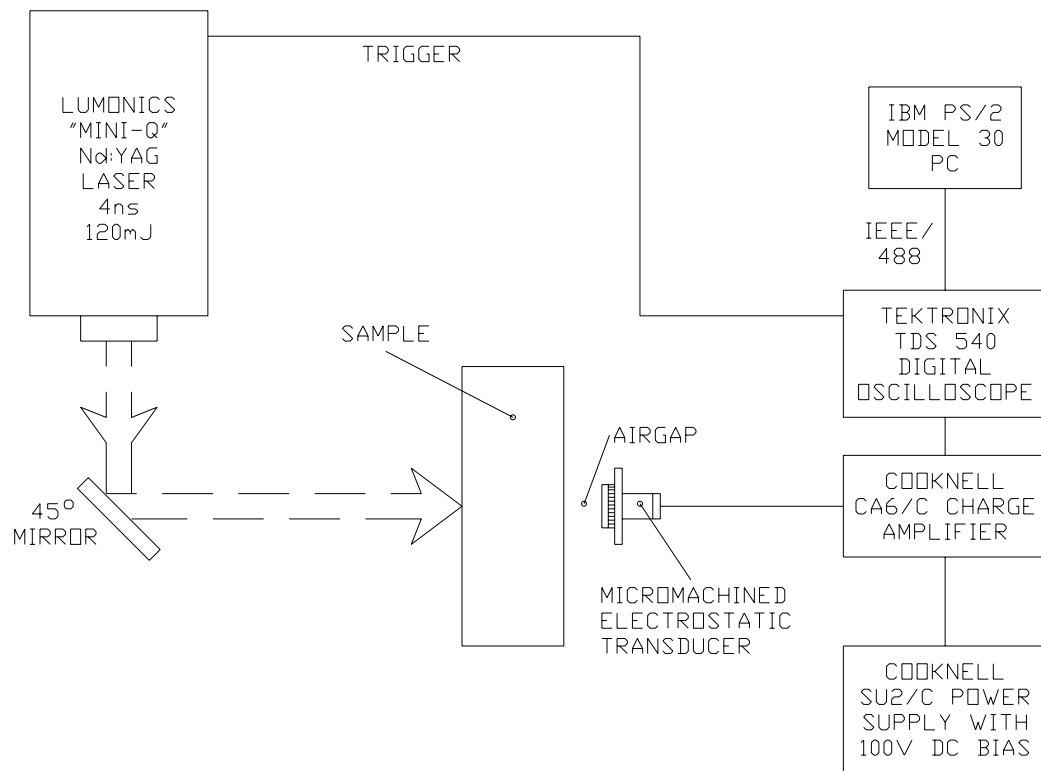


Figure 2.3(a): Schematic diagram of the experimental apparatus.

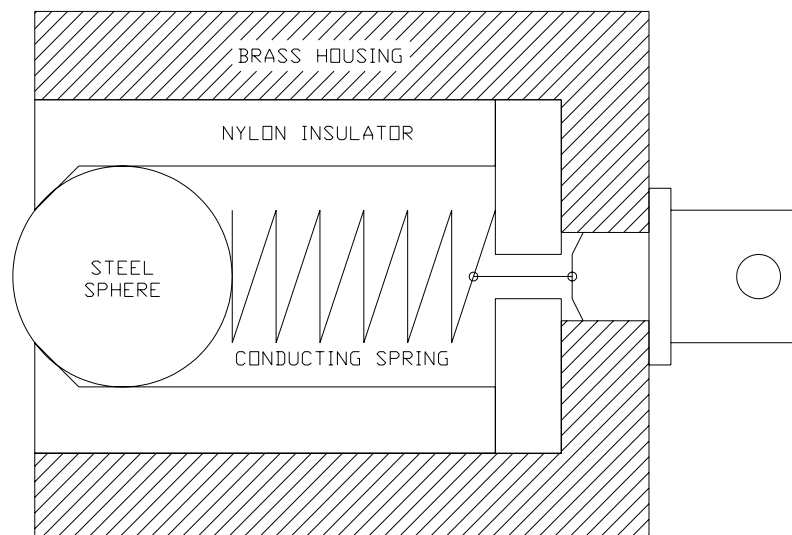


Figure 2.3(b): The contact capacitance device used for comparison.

acts as a point receiver at most angles. A film of polymer 5 μ m thick was used as a dielectric between the two electrodes, and a bias voltage of 100V was applied between the sphere and the sample. This type of device is a well characterised displacement sensor [17], and gives a linear response (to within 0.5%) up to frequencies of at least 30MHz. The same amplifier, bias unit and waveform storage facilities were used with both transducers.

The first experiments compared the signals detected by the silicon electrostatic transducer to those detected by the contacting capacitance device for normal displacement of an aluminium surface caused by bulk wave propagation. The surface motion recorded in an 86.0mm thick aluminium sample is shown in Figure 2.4(a) for an ablative source, detected by the contact device and showing the longitudinal arrival only. 128 averages were used to reduce the level of background noise. This thickness of aluminium was chosen so that the longitudinal and shear waves were well separated in time, to allow the transducers to reach an equilibrium state between echoes. The waveform has the characteristic sharp monopolar longitudinal arrival associated with a laser-generated ablative source, shown earlier in Figure 1.5(b) in Chapter 1. To illustrate the bandwidth present in this signal, a fast Fourier transform (FFT) of the waveform is shown in Figure 2.4(b), which indicates that the device was broadband up to a frequency of 10MHz, which was the upper frequency limit of the charge amplifier. The effects of the higher frequencies are reduced due to attenuation in the sample and diffraction. The corresponding waveform for the electrostatic air transducer, the result of just 16 signal averages, is shown in Figure 2.5(a), with the FFT of the longitudinal arrival in Figure 2.5(b). This indicates that the air transducer had a much narrower bandwidth, with a reduced response at both low and high frequencies when compared to the contact device. This may be attributed in part to the attenuation in air of high

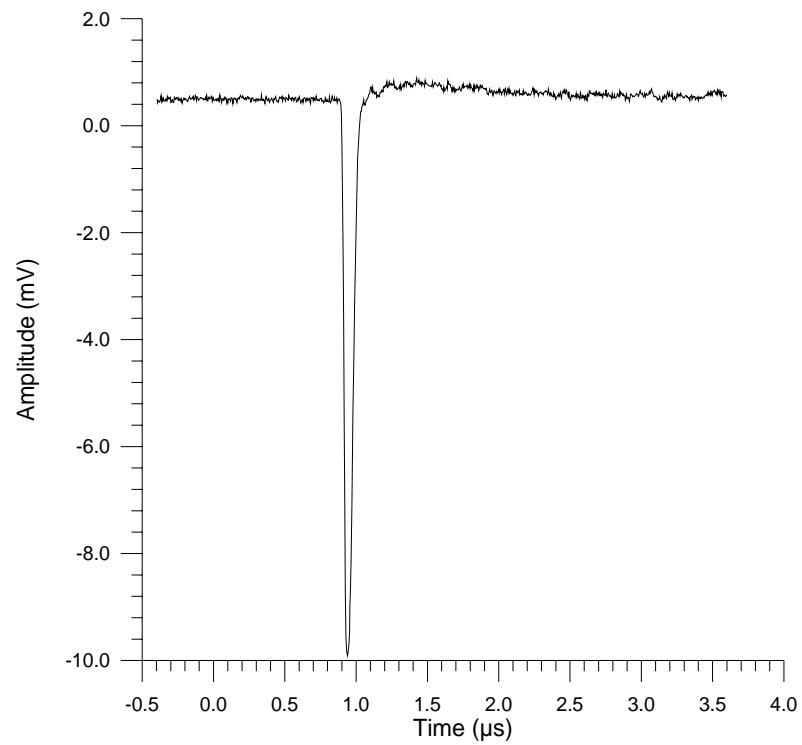


Figure 2.4(a): Longitudinal wave through 86.0mm aluminium detected by the contact transducer.

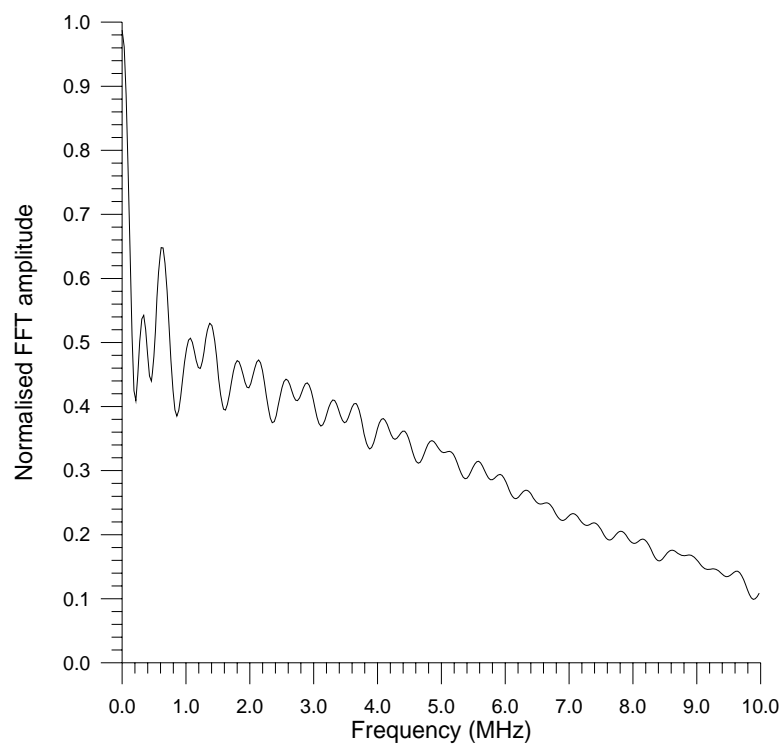


Figure 2.4(b): Frequency spectrum of Figure 2.4(a).

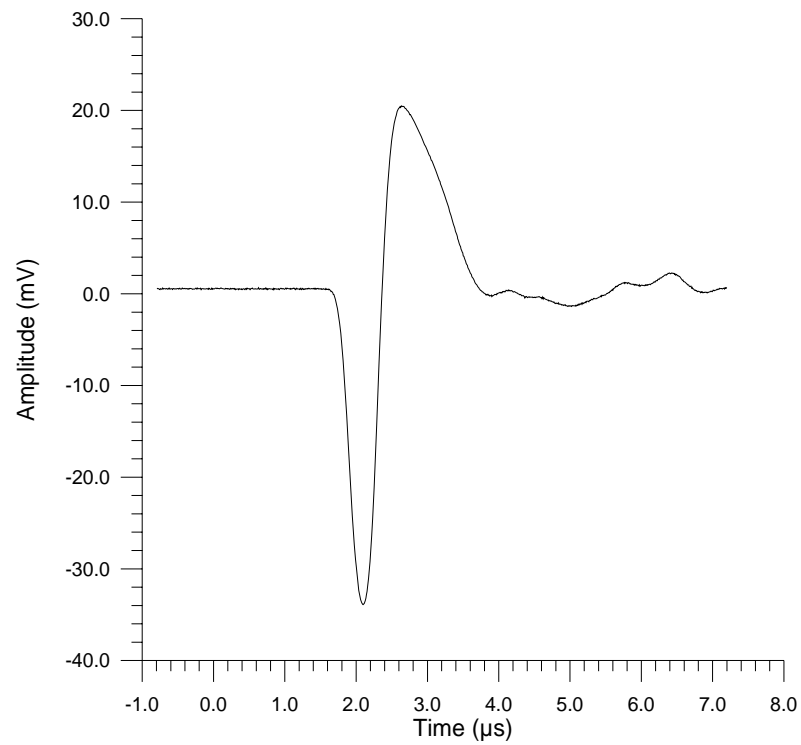


Figure 2.5(a): Longitudinal arrival through 86.0mm aluminium detected using the air-coupled micromachined capacitance device.

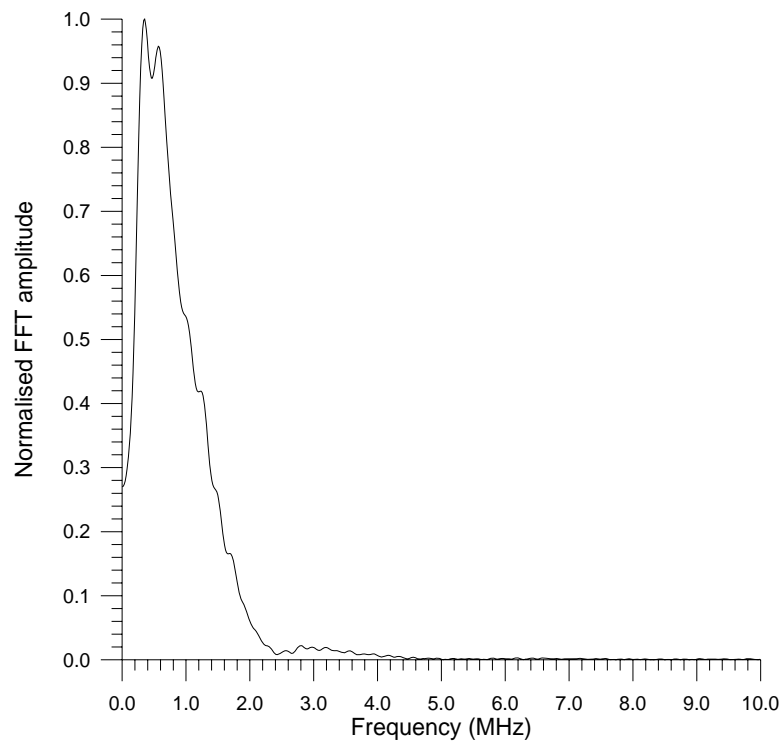


Figure 2.5(b): Frequency spectrum of the waveform in Figure 2.5(a).

frequencies, the different characteristics of the transducer, and the larger active area of the air-coupled device, as the contact transducer is effectively a point receiver. In addition, the applied bias voltage was restricted to 100V by the charge amplifier, and so the recommended 400V could not be used [10] to obtain a wider bandwidth.

A more typical waveform with multiple reflections in a thinner (12.8mm) sample of aluminium is shown in Figure 2.6(a) for the contact device. *L1*, *L2* etc. are the longitudinal wave arrivals, with a shear wave arrival at *S*. The features at *M1*, *M2* etc. are the longitudinal mode conversions of the first shear wave arrival at *S*, and *R* is a reflection from the edge of the sample. Figure 2.6(b) shows the corresponding signal received by the air-coupled transducer, and all the major features in the contact transducer waveform (*L1*, *S*, *M1* etc.) have been detected.

The signal in Figure 2.5(a) is the response of the air-coupled device to what is essentially a delta function from the laser, and so the spectrum in Figure 2.5(b) may be thought of as the overall frequency response of the device. If the FFT of the contact device waveform of Figure 2.6(a) is multiplied by the normalised ‘response’ spectrum in Figure 2.5(b), and the result inverse Fourier transformed, the waveform shown in Figure 2.6(c) is produced. This is effectively the broadband displacement waveform of Figure 2.6(a) filtered over the narrower frequency range detected by the air-coupled transducer. Figure 2.6(d) shows the differentiation of the displacement waveform Figure 2.6(a), and thus describing the velocity of the surface. A comparison of Figures 2.6(b) and (c) shows a degree of similarity, with all the main features (*L1*, *S*, *M1* etc.) clearly visible. It could therefore be assumed that the air-coupled device operated as a sensor which gave a good representation of the displacement of the sample surface, but with a reduced bandwidth.

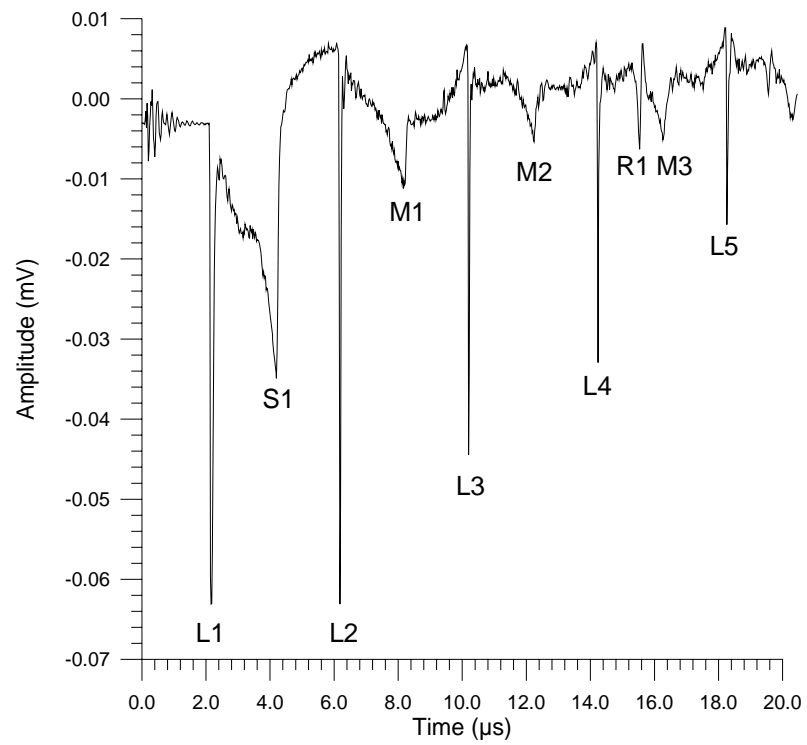


Figure 2.6(a): Waveform through 12.8mm of aluminium detected using the contact transducer, showing the surface displacement.

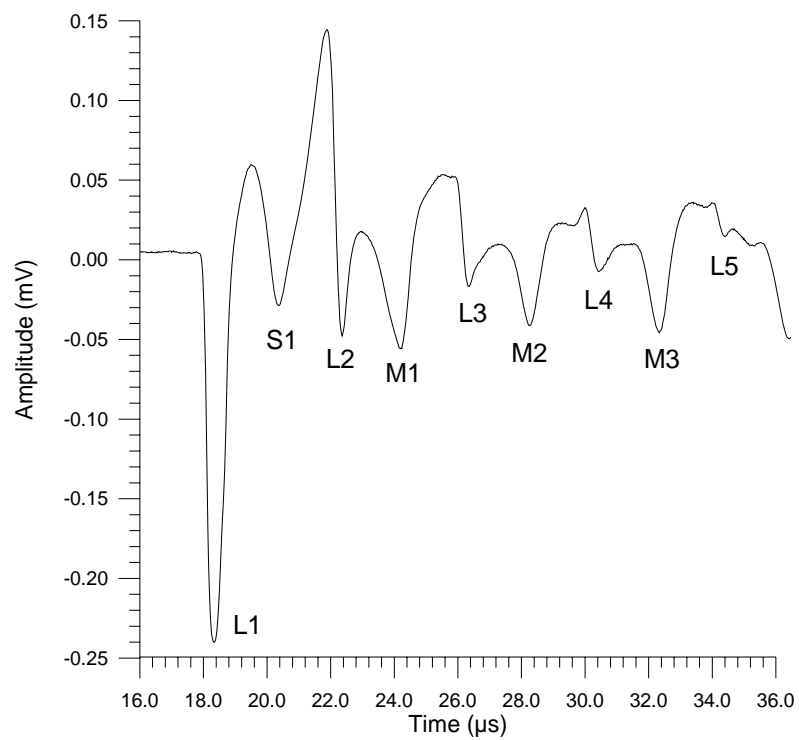


Figure 2.6(b): Waveform through 12.8mm of aluminium, detected using the micromachined air-coupled capacitance transducer.

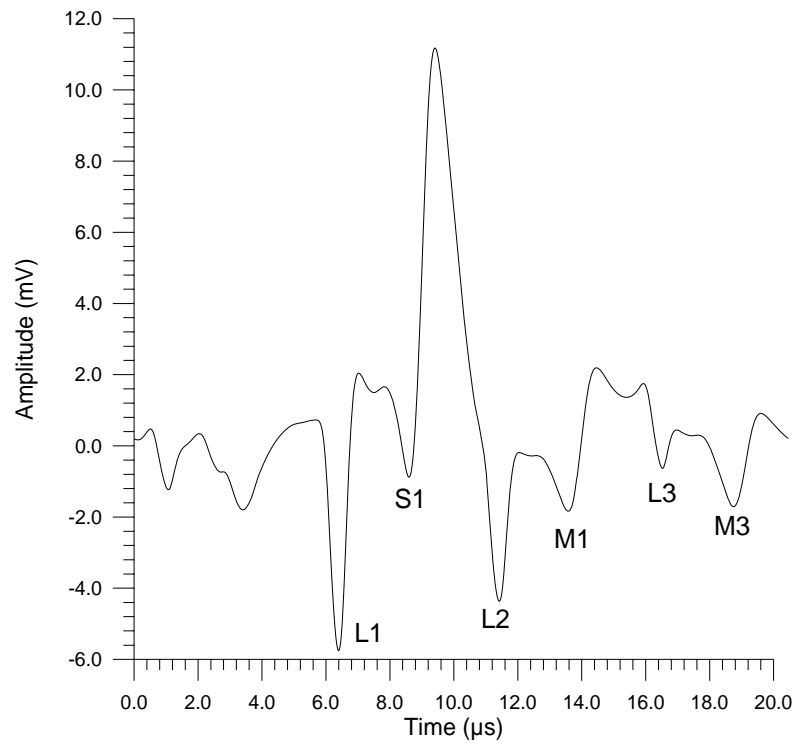


Figure 2.6(c): Waveform in Figure 2.6(a) 'filtered' over the range of frequencies shown in Figure 2.5(b).

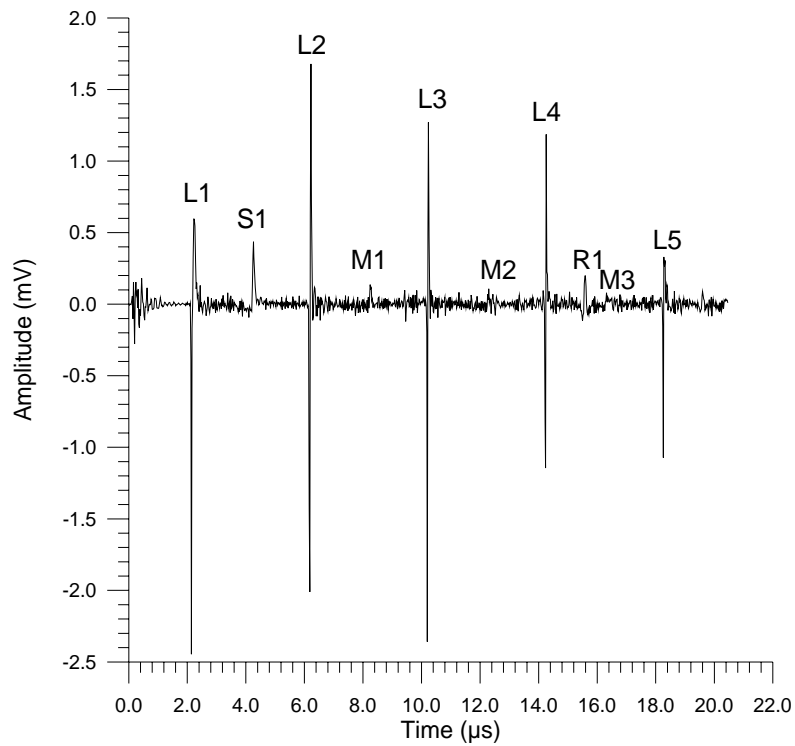


Figure 2.6(d): Contact capacitance transducer waveform after differentiation, showing the velocity of the surface.

Another experiment was conducted in which the optical power density at the aluminium surface was gradually increased, so that the generation mechanism changed from thermoelastic expansion to ablation. A selection of waveforms is presented in Figure 2.7 for (a) the contact device and (b) the air-coupled transducer. Again, there is good correlation between the two devices. The step like shear arrival *SI* is present in most waveforms and optical densities, and the monopolar longitudinal arrival *L1* and echo *L2* increasingly dominate the signal as the source becomes more ablative.

The combination of a laser source and an air-coupled receiver may be used to test many different materials. Similar waveforms to those shown in Figures 2.6 for aluminium were also obtained in samples of brass and steel, with slight variations in waveform shape which may be attributed to the differences in microstructure, elastic properties and thermal characteristics of the materials. A typical signal in 10mm of steel is shown in Figure 2.8(a), where it can be seen that the shear wave *SI* is far less prominent when compared to Figure 2.6(b). Waveforms were also obtained in samples of perspex (polymethylmethacrylate) by replacing the Nd:YAG laser with a Lumonics ‘Lasermark’ series Model 630 CO₂ TEA (Transversely Excited at Atmospheric pressure) laser, which had a pulse duration of 100ns and a maximum energy of 8J. This laser operated at a wavelength of 10.6μm in the far infra-red spectrum, where absorption in this polymer, which readily transmits visible and near infra-red light, is high. A typical signal in a 25mm thick sample is shown in Figure 2.8(b), where the shear step *SI* is the dominant feature. The generation mechanism was predominantly thermoelastic, due to the improved absorption at this wavelength.

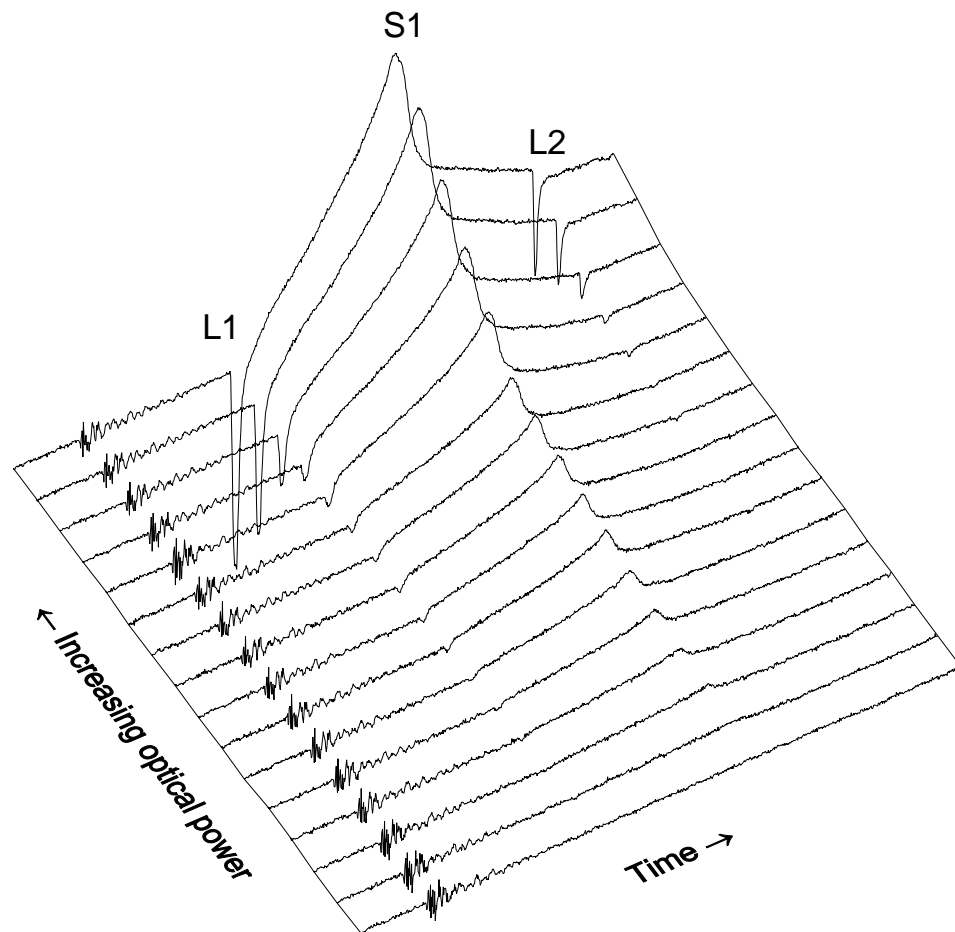


Figure 2.7(a): Signals obtained using an increasing optical power density, detected using the contact device.

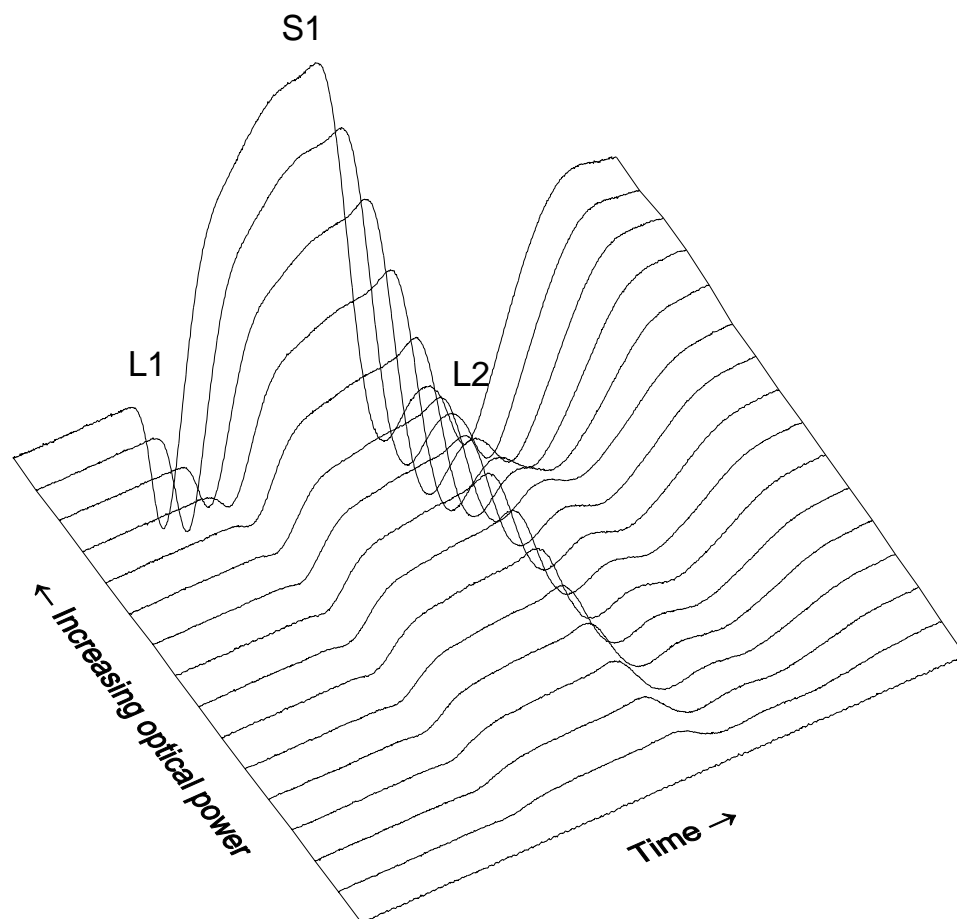


Figure 2.7(b): Signals obtained using an increasing optical power density, detected using the micromachined air-coupled capacitance transducer.

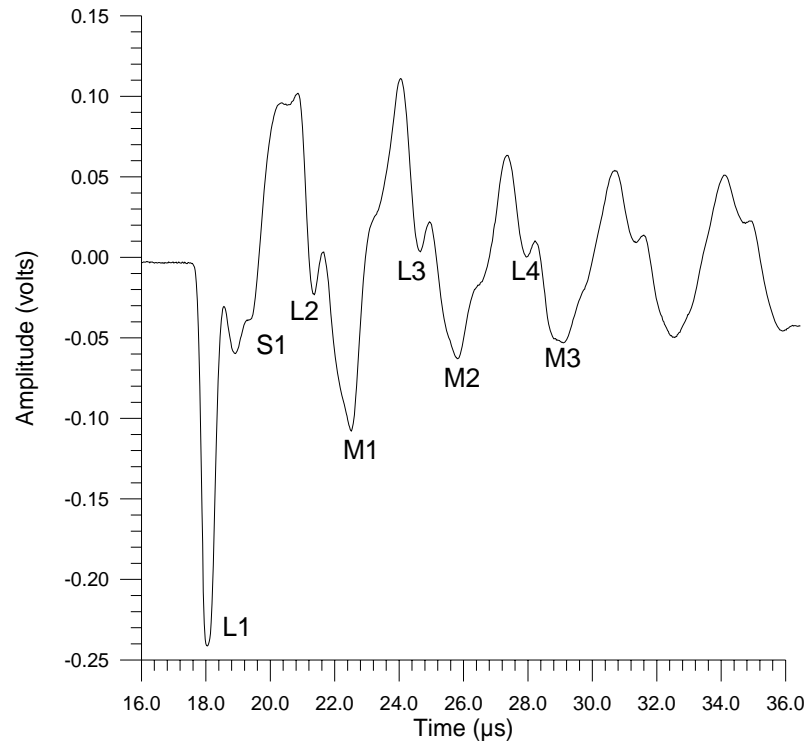


Figure 2.8(a): Typical laser-generated waveform in 10mm thick steel, detected using the air-coupled capacitance transducer.

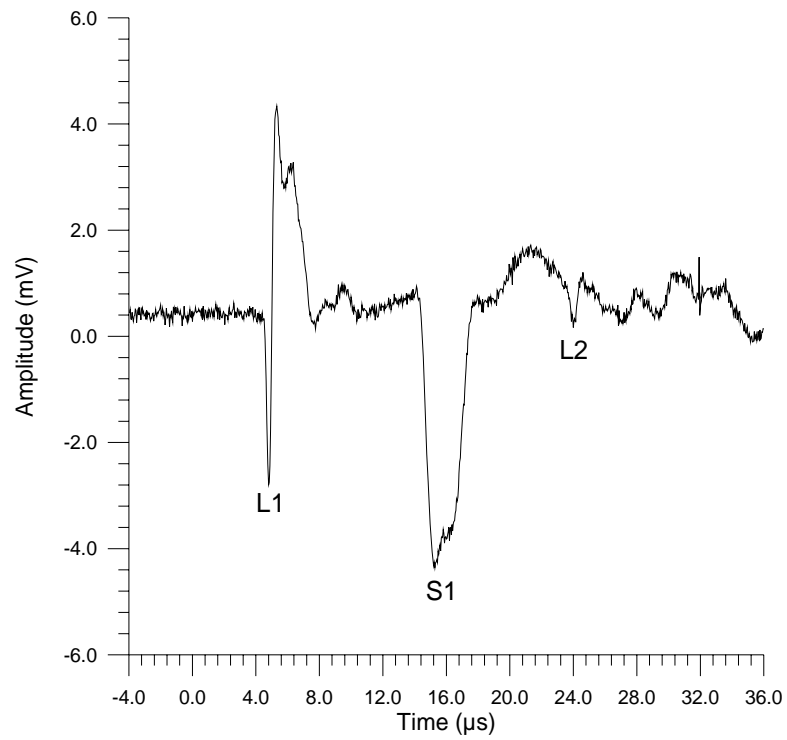


Figure 2.8(b): Typical laser-generated waveform in 25mm thick Perspex, detected using the air-coupled capacitance transducer.

2.3 Studies of laser-generated surface (Rayleigh) and plate (Lamb) waves

As stated earlier, surface waves (Rayleigh waves) were also generated by the laser source at a solid surface simultaneously with bulk modes. The apparatus used to detect these signals was identical to that for the bulk waves, except that the transducer was moved to the same side of the sample as the laser source, and displaced by 50mm, as shown schematically in Figure 2.9(a). Lamb waves could also be detected in thin plates, using the arrangement shown in Figure 2.9(b), again with the transducer 50mm from the laser source. The different wave types radiate from the sample into air at different angles depending on their velocity, as defined by Snell's Law (equation {1.5}, Chapter 1). Hence detection of different features by the air transducer was optimised by varying θ , which was the angle the transducer made with the surface of the sample. The contact capacitance transducer could measure simultaneously all the different features which caused motion of the sample surface, due to the spherical electrode as mentioned earlier in Section 2.2.1.

2.3.1 Detection of Rayleigh waves

The surface waveform detected by the contact capacitance device on a sample of aluminium 86mm thick is shown in Figure 2.10(a), and may be explained as follows. The initial feature *E* was the electrical feedthrough from the laser and was effectively trigger noise, feature *S* was a surface skimming longitudinal wave, feature *R* was the Rayleigh wave travelling at slightly less than the bulk shear wave velocity, and feature *L* was the first longitudinal wave echo within the thickness of the test block.

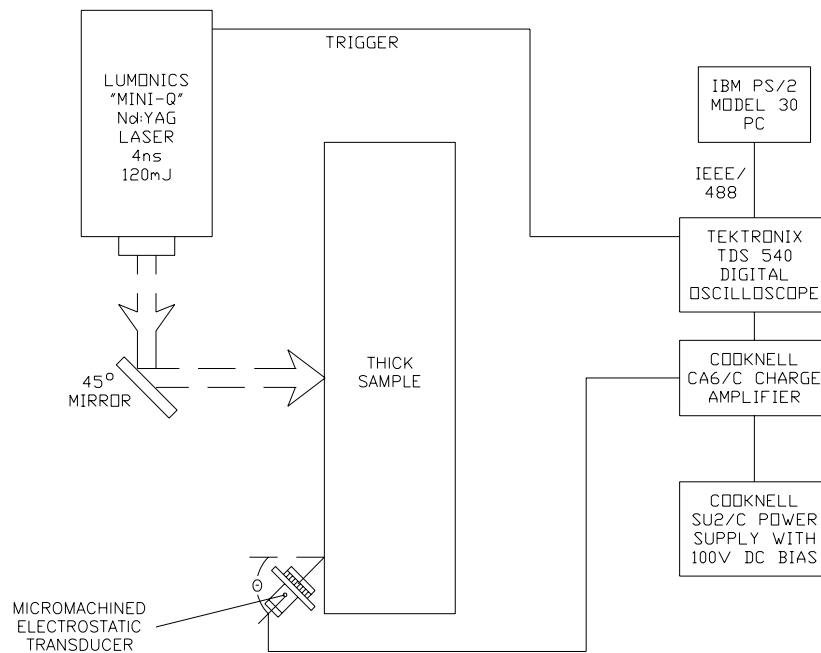


Figure 2.9(a): Apparatus for detecting Rayleigh waves.

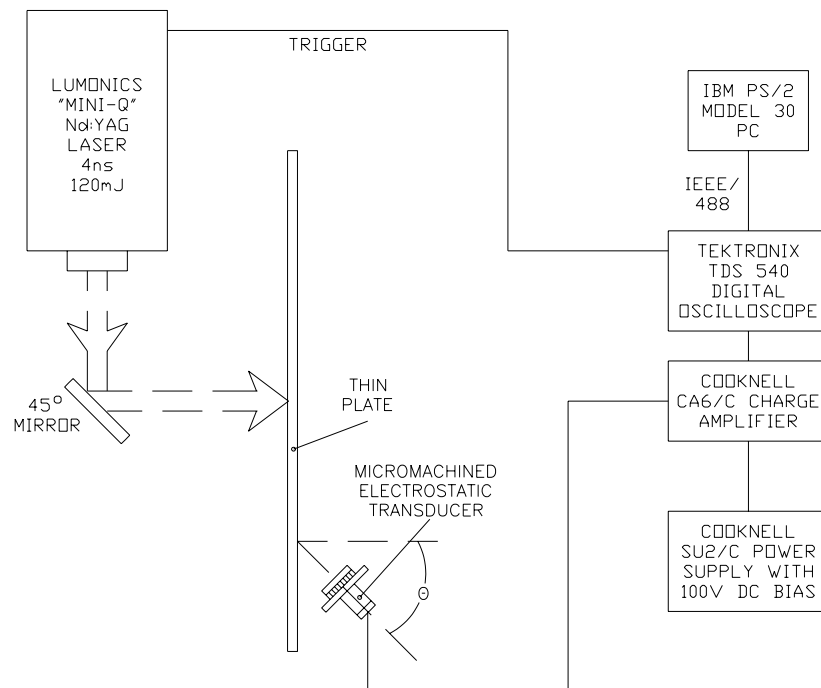


Figure 2.9(b): Apparatus for detecting Lamb waves.

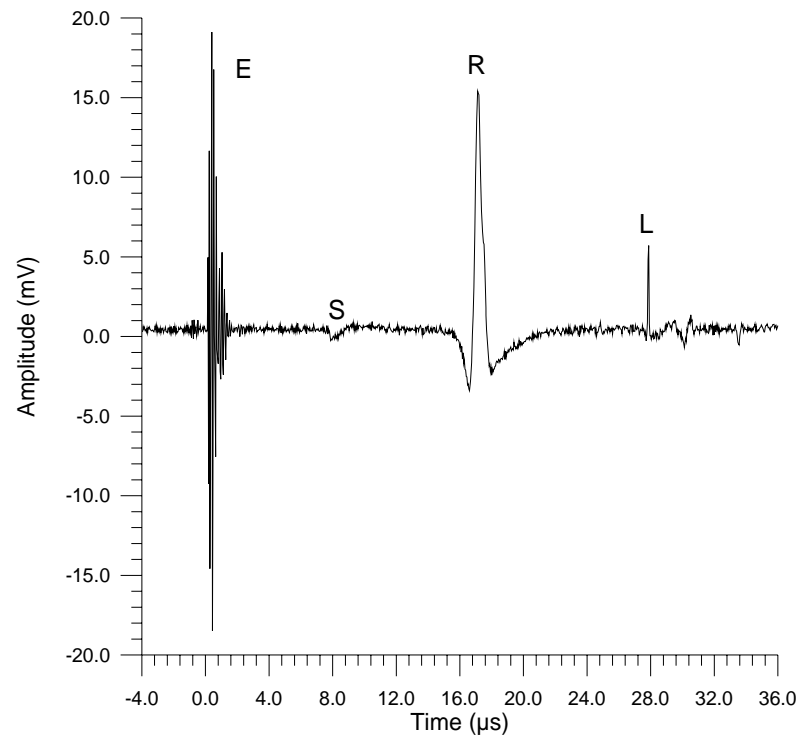


Figure 2.10(a): Surface waves in aluminium detected by the contact transducer.

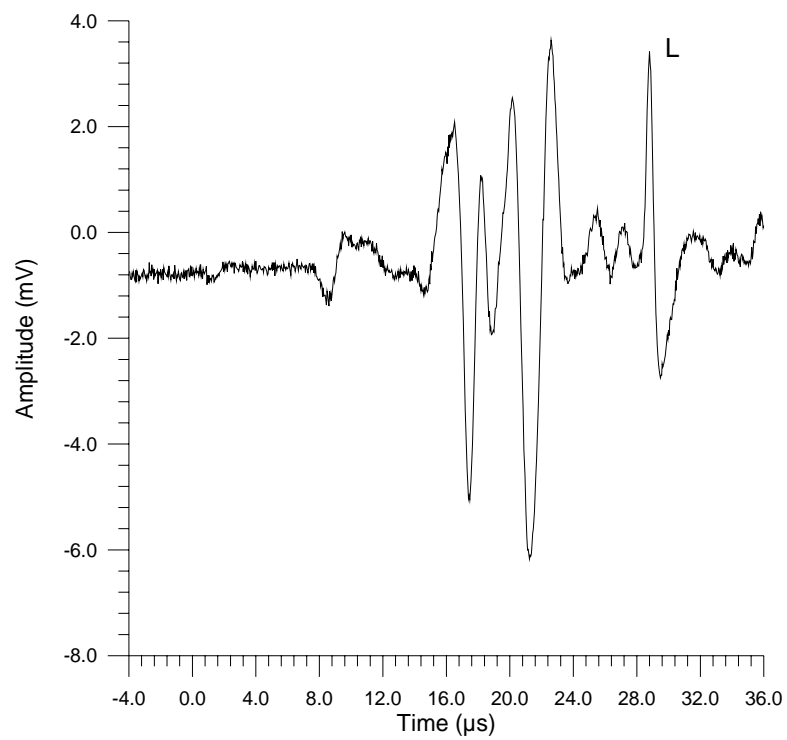


Figure 2.10(b): Surface waves in aluminium at an angle of 0° , detected using the air-coupled capacitance transducer.

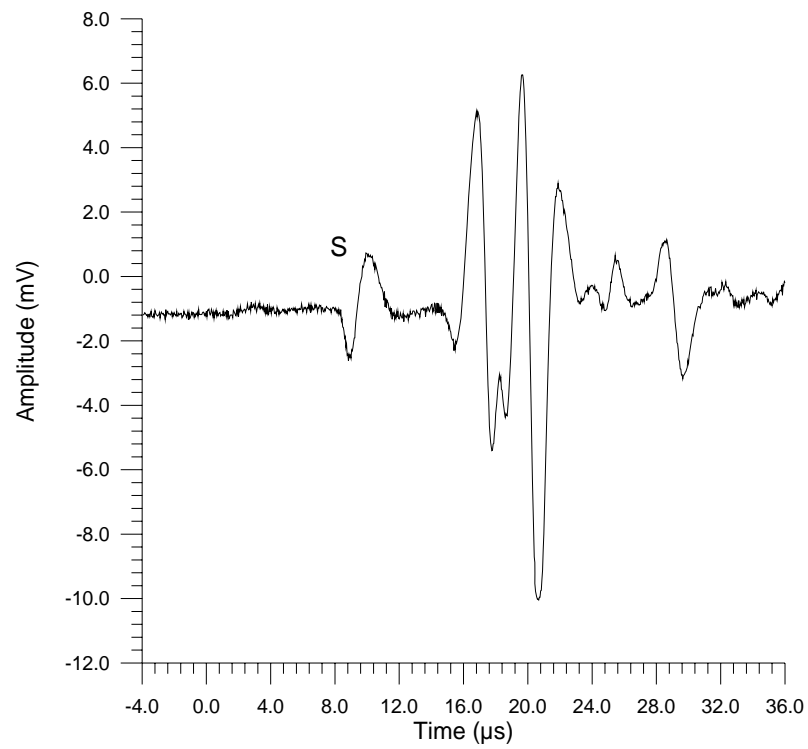


Figure 2.10(c): Surface waves in aluminium at an angle of 3°, detected using the air-coupled capacitance transducer.

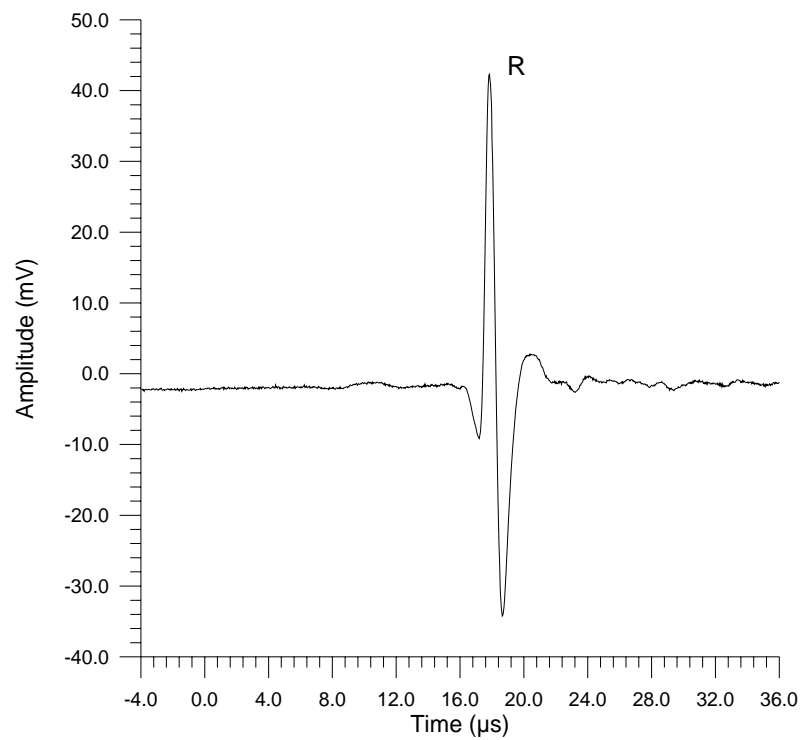


Figure 2.10(d): Surface waves in aluminium at an angle of 6°, detected using the air-coupled capacitance transducer.

The experiment was then repeated using the air-coupled capacitance transducer, with results for various angles of θ shown optimised in Figure 2.10 for (b) the longitudinal reflection L at $\theta=0^\circ$, (c) the surface skimming longitudinal wave S at $\theta=3^\circ$, and (d) the Rayleigh wave R at $\theta=6^\circ$.

2.3.2 Detection of Lamb waves

A plate of aluminium 0.69mm thick was used as the sample, and a typical normal displacement waveform is shown in Figure 2.11, detected using the contact capacitance probe. The symmetric s modes and asymmetric a modes are clearly visible, and show some dispersion due to the thickness of the plate and the range of frequencies present, particularly for the a_0 mode. Some higher order modes are also present.

By replacing the contact device with the micromachined air-coupled transducer, the various Lamb wave modes could also be detected in air. A selection of waveforms at different angles of the detector is shown in Figure 2.12(a) to (e). At $\theta=2^\circ$, the symmetric mode is clearly visible, but reduces in amplitude at $\theta=5^\circ$, and is not visible at all at $\theta=10^\circ$. This was expected, as the s_0 mode in thin plates has a velocity approaching the shear velocity (approximately the longitudinal velocity in the material), and hence will radiate into air at small angles. The higher frequency asymmetric vibrations become more prominent at $\theta=5-10^\circ$, and at larger angles the frequency content of this asymmetric mode clearly decreases.

Lamb waves could also be generated and detected in a 1.5mm thick sheet of perspex, using the CO₂ laser described earlier as a source of ultrasound. A typical

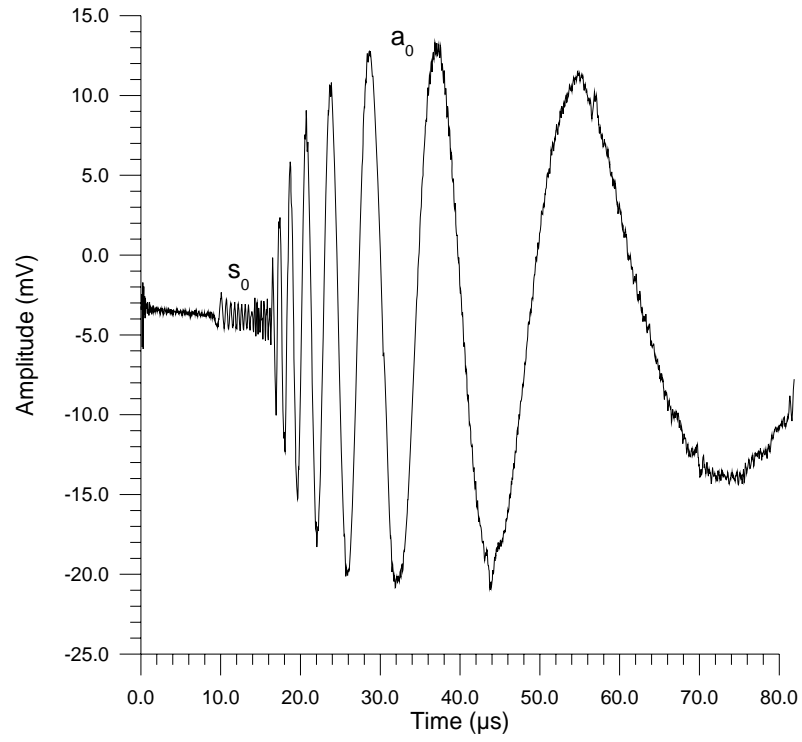


Figure 2.11: Lamb waves in a 0.69mm thick aluminium sheet, detected using the contact device after propagating 50mm in the sample.

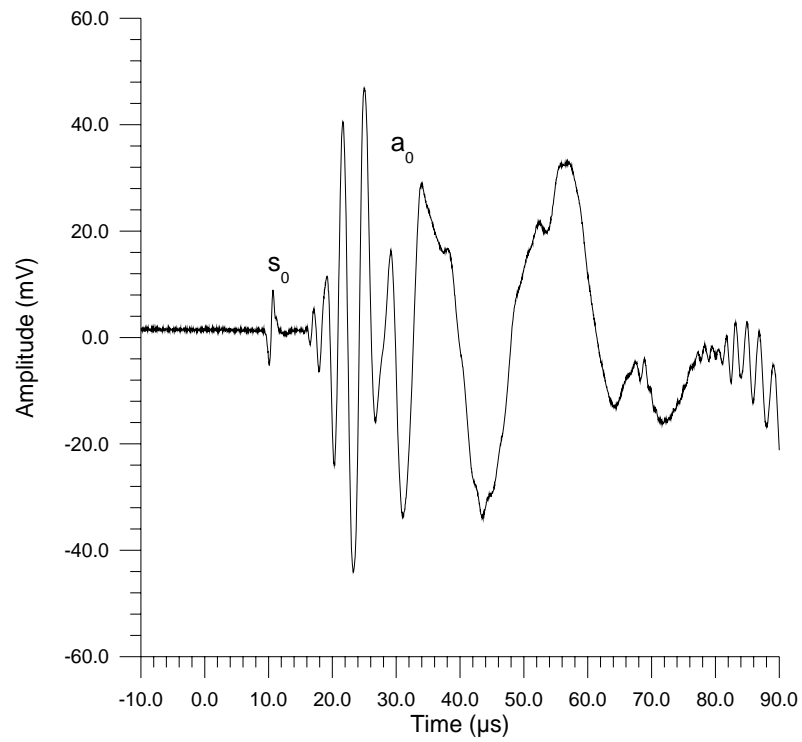


Figure 2.12(a): Lamb waves in a 0.69mm thick aluminium sheet, detected using the air-coupled capacitance transducer at an angle of 2° .

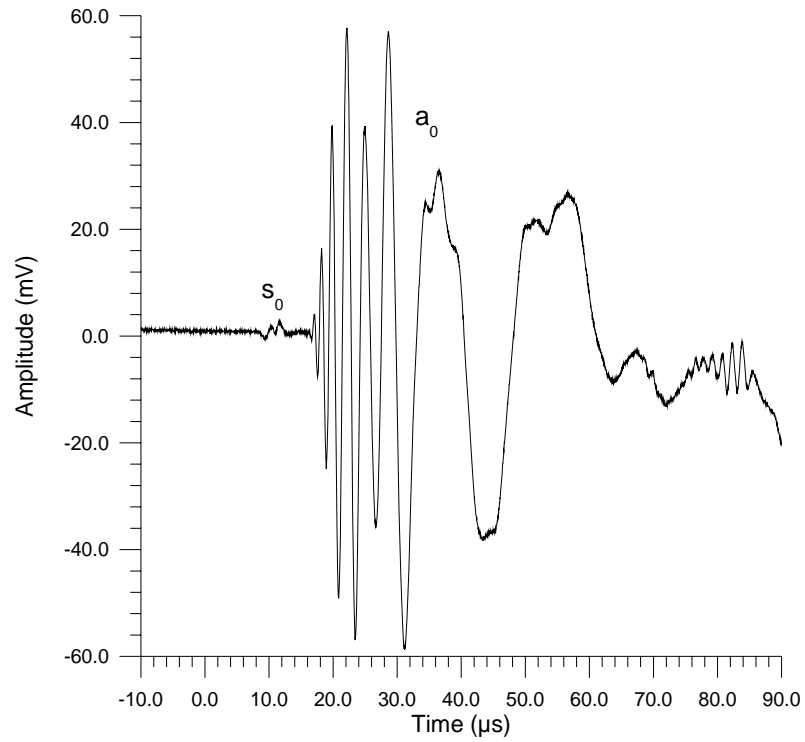


Figure 2.12(b): Lamb waves in a 0.69mm thick aluminium sheet, detected using the air-coupled capacitance transducer at an angle of 5°.

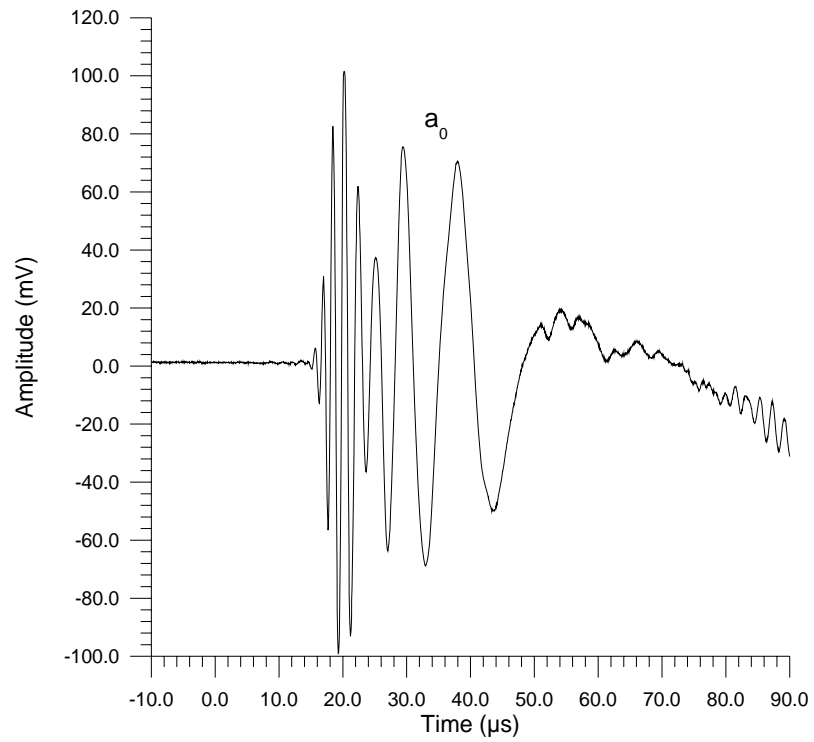


Figure 2.12(c): Lamb waves in a 0.69mm thick aluminium sheet, detected using the air-coupled capacitance transducer at an angle of 10°.

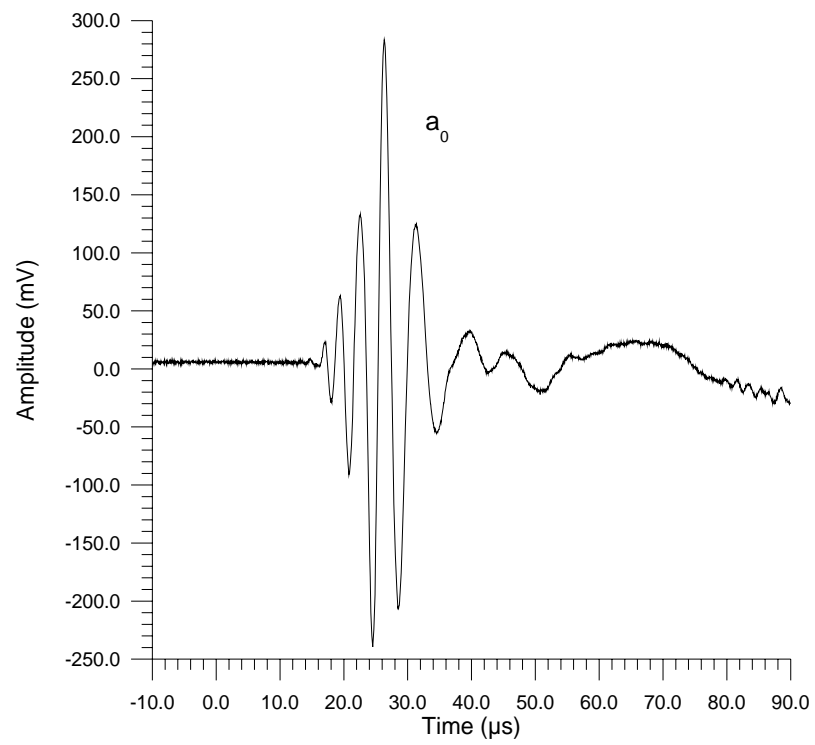


Figure 2.12(d): Lamb waves in a 0.69mm thick aluminium sheet, detected using the air-coupled capacitance transducer at an angle of 15°.

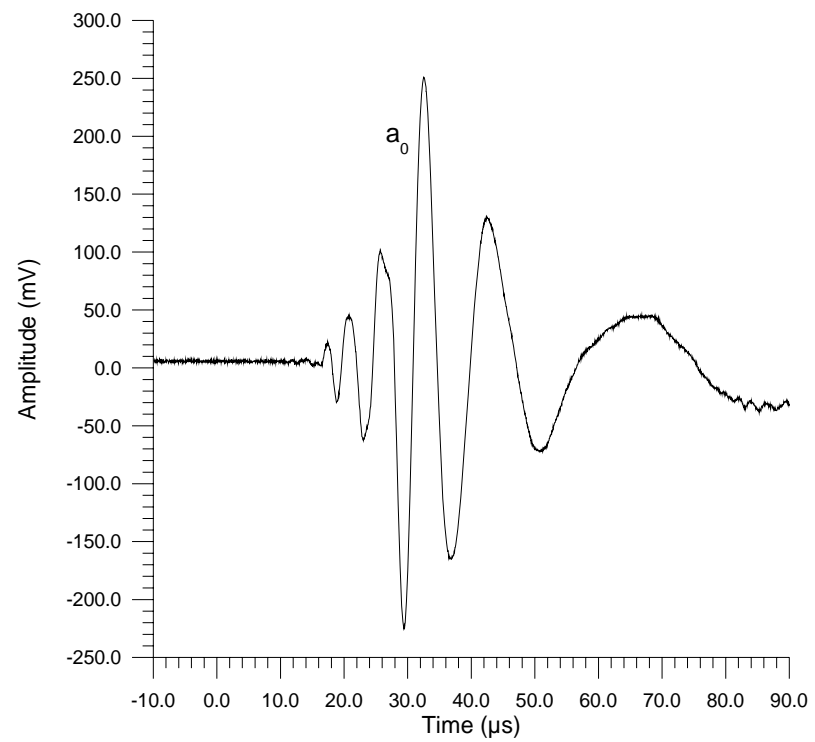


Figure 2.12(e): Lamb waves in a 0.69mm thick aluminium sheet, detected using the air-coupled capacitance transducer at an angle of 20°.

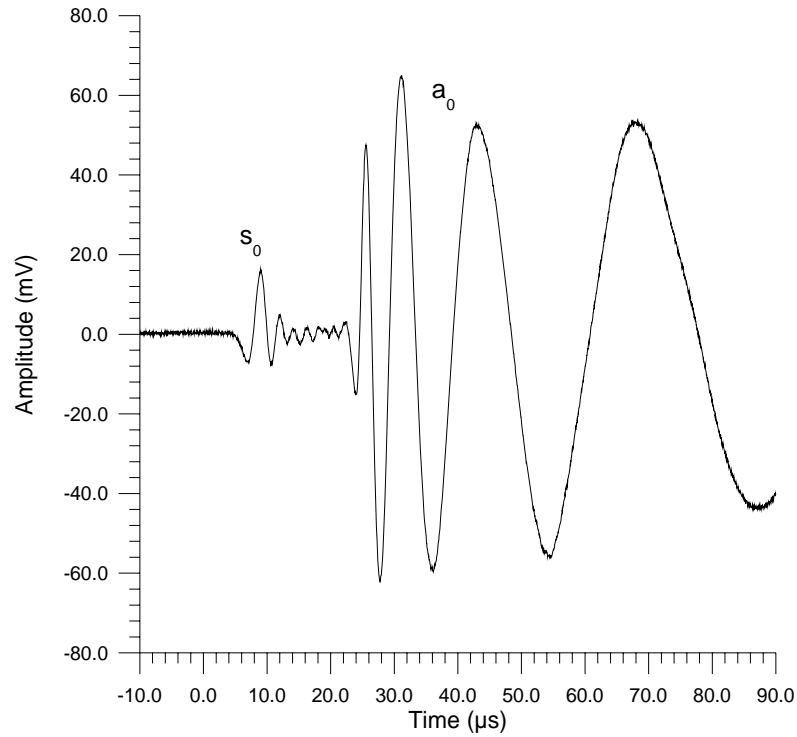


Figure 2.13: Lamb waves in a 1.5mm thick perspex sheet, detected using the air-coupled capacitance transducer at an angle of 12° .

signal is shown in Figure 2.13 at a transducer angle of $\theta=10^\circ$, where both the a_0 and s_0 modes are clearly visible.

2.4 Discussion

It is interesting to note that despite the very high frequencies present in the laser-generated bulk waves, the device seemed to have an upper frequency limit of approximately 2MHz, as shown in Figure 2.5(b). This feature has also been noted in other work on the same capacitance devices operating in air [10], when used as either transmitters or receivers of ultrasound to frequencies of up to 4MHz. This suggests

that there is some major limiting factor to the upper frequency limit of this device, and perhaps air-coupled ultrasound in general.

This is most probably the effects of absorption and attenuation in air, which has been extensively studied by many authors. Typical reviews of this subject are those by Bass *et al.* [18] and Hickling and Marin [19]. Hickling gives the governing equation as:

$$p(z) = p_o \cdot e^{-\alpha \cdot z} \quad \{2.1\}$$

where p_o is the r.m.s. pressure at some initial location, $p(z)$ is the pressure amplitude after travelling z metres, and α is the attenuation coefficient. Bass *et al.* further characterised this coefficient and state that α may be closely approximated by:

$$\alpha = \alpha_{cr} + \alpha_{vib,O} + \alpha_{vib,N} \quad \{2.2\}$$

where α_{cr} is a combination of classical absorption and rotational relaxation, and $\alpha_{vib,j}$ is the absorption due to the vibrational relaxation of both oxygen O and nitrogen N . α_{cr} is given by:

$$\alpha_{cr} = 1.83 \times 10^{-11} \left(\frac{T}{T_o} \right)^{\frac{1}{2}} \left(\frac{P}{P_o} \right)^{\frac{1}{2}} f^2 \quad \{2.3\}$$

where T and T_o are the actual and reference temperatures respectively, P and P_o are the actual and reference pressures respectively, and f is the frequency. $\alpha_{vib,j}$ is given by:

$$\alpha_{vib,j} = \frac{4 \cdot \pi \cdot X_j}{35 \cdot c} \frac{(\theta_j/T)^2 e^{-\theta_j/T}}{(1 - e^{-\theta_j/T})^2} \frac{f^2/f_{r,j}}{1 + (f/f_{r,j})^2} \quad \{2.4\}$$

where X_j is the molar fraction, θ_j is the vibrational temperature, and $f_{r,j}$ is the vibrational relaxation frequency for both oxygen and nitrogen. Equation {2.4} is also

affected by humidity, and becomes increasingly complex, and further investigation of this topic is outside the scope of this study. In most practical situations, where accurate knowledge of the attenuation caused by air is required, it may be simpler to experimentally measure values of α as shown in Section 1.3. Hickling gives typical theoretical values of 10^{-3}m^{-1} at 1kHz and 10m^{-1} at 1MHz in air at 30°C. Hickling also defines an extinction distance d_e , a distance in air over which the amplitude of a signal is reduced to $1/e$ of its original value. This may be approximated at a frequency f by:

$$d_e = \frac{5 \times 10^{13}}{f^2} \quad \{2.5\}$$

where d_e is in mm. For the sample-receiver distances (d_e) of 10mm used in the experiments described in this chapter, f is 2.24MHz, which was approximately the upper frequency of the devices. It was not practical to use smaller air gaps due to the construction of the capacitance transducers. Interestingly, for the 9.2MHz air-coupled device described earlier [10], d_e is approximately 0.6mm rather than the 5mm air gap used, probably for similar reasons. For practical air-coupled NDT, over distances of 10mm or more, devices operating at frequencies in excess of 2.5-3MHz are therefore at a distinct disadvantage.

2.5 Conclusions

The work described in this chapter has shown that air-coupled capacitance transducers, which have been micromachined from silicon, are well suited to the detection of a variety of laser-generated ultrasonic waveforms. The response of the transducer to bulk waves, surface waves in thick samples, and Lamb waves in thin plates was compared to the response of a wideband contact transducer. Bulk waves

were used to partly characterise the air-coupled device, which was found to operate as a sensor which gave a good representation of the displacement of the sample surface, but with a reduced bandwidth. Due to the present lack of a standard air-coupled transducer or high-frequency microphone operating in the MHz range, any sensitivity measurements of the silicon device would be uncalibrated and of little value, and so a more complete characterisation of the air-coupled capacitance device should form an important part of any work in the future.

2.6 References

- [1] M. Rafiq and C. Wykes, 'The performance of capacitive ultrasonic transducers using v-grooved backplates', *Meas. Sci. Technol.* **2**, 168-174 (1991)
- [2] W.S.H. Munro and C. Wykes, 'Arrays for airborne 100kHz ultrasound', *Ultrasonics* **32**, 57-64 (1994)
- [3] W.S.H. Munro, S. Pomeroy, M. Rafiq, H.R. Williams, M.D. Wybrow and C. Wykes, 'Ultrasonic vehicle guidance transducer', *Ultrasonics* **28**, 350-354 (1990)
- [4] H. Carr and C. Wykes, 'Diagnostic measurements in capacitive transducers', *Ultrasonics* **31**, 13-20 (1993)
- [5] K. Suzuki, K. Higuchi and H. Tanigawa, 'A silicon electrostatic ultrasonic transducer', *IEEE Trans. Ultrason. Ferroelec. Freq. Contr.* **UFFC-36**, 620-627 (1989)
- [6] D.W. Schindel, D.A. Hutchins, L. Zou and M. Sayer, 'Capacitance devices for the generation of air-borne ultrasonic fields', *Proc. 1992 IEEE Ultrason. Symp.* 843-846 (1992)

- [7] D.W. Schindel, D.A. Hutchins, L. Zou and M. Sayer, 'Capacitance transducers for generating ultrasonic fields in liquids and gases', *Proc. IEEE International Conference on Acoustic Sensing and Imaging ASI'93*, 7-12 (1993)
- [8] D.W. Schindel, D.A. Hutchins, L. Zou and M. Sayer, 'Micromachined capacitance transducers for air-borne ultrasonics', *Proc. Ultrasonics Int. Conf. 1993*, 675-678 (1993)
- [9] D.W. Schindel and D.A. Hutchins, 'Air-coupled ultrasonic transducer', U.S. Patent 5,287,331, February 1994
- [10] D.W. Schindel, D.A. Hutchins, L. Zou and M. Sayer, 'The design and characterization of micromachined air-coupled capacitance transducers', *IEEE Trans. Ultrason. Ferroelec. Freq. Contr.* **UFFC-42**, 42-50 (1995)
- [11] M.J. Anderson, J.A. Hill, C.M. Fortunko, N.S. Dogan and R.D. Moore, 'Broadband electrostatic transducers: Modeling and experiments', *J. Acoust. Soc. Am.* **97**, 262-272 (1995)
- [12] W. Kühnel and G. Hess, 'A silicon condenser microphone with structured back plate and silicon nitride membrane', *Sensors and Actuators A*, **30**, 251-258 (1992)
- [13] M.I. Haller and B.T. Khuri-Yakub, 'A surface micromachined electrostatic ultrasonic air transducer', *Proc. IEEE 1994 Ultrason. Symp.* Ch. 395, 1241-1244
- [14] B.T. Khuri-Yakub, I. Landabaum and D. Spoliansky, 'Micro machined ultrasonic air transducers', *Proc. 1995 Rev. Prog. Quant. Nondest. Eval. QNDE'95*, to be published
- [15] D.W. Schindel and D.A. Hutchins, 'Applications of micromachined capacitance transducers in air-coupled ultrasonics and nondestructive evaluation', *IEEE Trans. Ultrason. Ferroelec. Freq. Contr.* **UFFC-42**, 51-58 (1995)

- [16] W.M.D. Wright, D.W. Schindel and D.A. Hutchins, 'Studies of laser-generated ultrasound using a micromachined silicon electrostatic transducer in air', *J. Acoust. Soc. Am.* **95**, 2567-2575 (1994)
- [17] W. Sachse and N.N. Hsu, 'Ultrasonic transducers for materials testing and their characterisation', in *Physical Acoustics - Principles and Methods*, eds. W.P. Mason and R.N. Thurston, (Academic, New York, 1979), Vol. XIV, pp277-406
- [18] H.E. Bass, L.C. Sutherland, J. Piercy and L. Evans, 'Absorption of sound by the atmosphere', in *Physical Acoustics - Principles and Methods*, eds. W.P. Mason and R.N. Thurston, Vol. XVII, Chapter 3 pp145-232 (Academic Press, New York, 1984)
- [19] R. Hickling and S.P. Marin, 'The use of ultrasonics for gauging and proximity sensing in air', *J. Acoust. Soc. Am.* **79**, 1151-1160 (1986)

Chapter 3: Air-coupled 1-3 connectivity piezocomposite transducers

3.1 Introduction

The work to be presented in this chapter will look at devices made from 1-3 connectivity piezocomposites designed to act as air-coupled receivers. The first section will describe the devices that were available and some details of their manufacture, and then describe how the transducers were characterised using laser-generated ultrasound. The final part of this work will use a laser/piezoelectric air-transducer system for the non-destructive testing of composite materials, and the imaging of defects. Most of the work described in this chapter has again already been published [1-5].

The piezocomposite transducers used in this study were manufactured by Anthony Gachagan and Gordon Hayward at the Department of Electronic and Electrical Engineering at the University of Strathclyde, Glasgow. This was part of a joint research effort, financed by the EPSRC (Engineering and Physical Sciences Research Council), into the development of piezocomposite devices in conjunction with a laser generated source of ultrasound as a non-contact non-destructive testing system. The design criteria used in the construction of these devices will not be discussed here - the transducers have been extensively modelled at Strathclyde and their theoretical response has been well documented [6-7].

3.2 The manufacture of resonant (narrow bandwidth) devices

Three prototype resonant devices were made using the slice and fill technique mentioned earlier in Chapter 1, and are shown schematically in Figure 3.1. Elements were made from a 1-3 connectivity composite, consisting of square pillars of PZT-5A

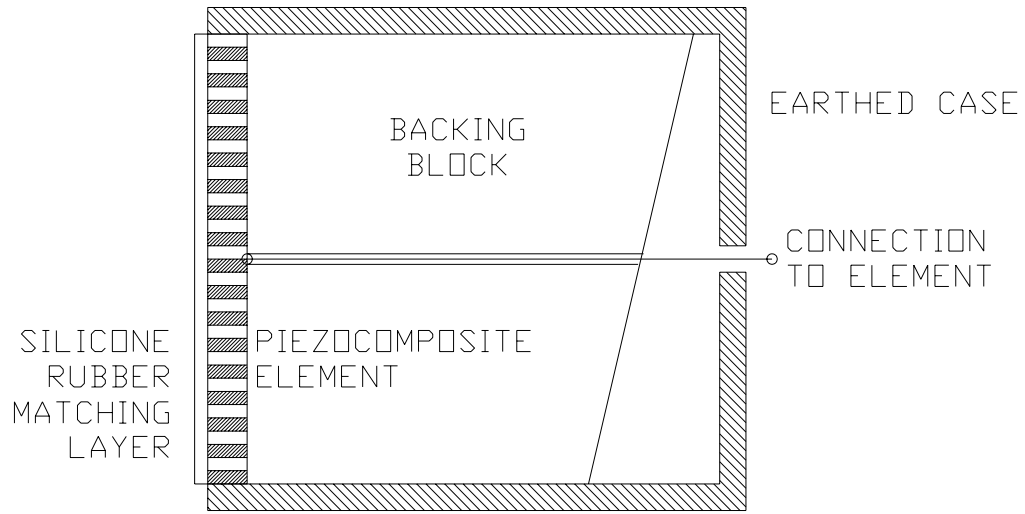


Figure 3.1: The 1-3 connectivity composite transducer.

piezoceramic in a matrix of CIBA-GEIGY CY1300/HY1301 hard setting epoxy resin. Each device was covered with a quarter wavelength matching layer of silicone RTV rubber, and the backing material, when used, was tungsten loaded hard setting epoxy. The transducers were 30mm in diameter, and further details are shown in Table 3.1, where f_e and f_m are the resonant frequencies of electrical impedance (minimum) and mechanical impedance (maximum) respectively. k_t is the fundamental thickness mode coupling coefficient, and Z_{ml} and Z_{bb} are the acoustic impedances of the matching layer and backing block respectively.

Two of the devices were designed to operate at frequencies between 500kHz and 700kHz, with the third being a high frequency device to work between 1.7MHz and 1.9MHz. One of the low frequency devices had a backing block attached to the element to produce a damped device, the other two transducers were undamped. All

	Transducer #1	Transducer #2	Transducer #3
volume fraction PZT/epoxy (%)	40	40	40
f_e (kHz)	525	541	1720
f_m (kHz)	643	656	1985
k_t	0.617	0.605	0.538
matching layer thickness (mm)	0.4	0.4	0.13
Z_{ml} (MRayl)	1.0	1.0	1.0
backing block length (mm)	40	-	-
Z_{bb} (MRayl)	8.0	-	-

Table 3.1: Properties of the prototype devices, courtesy of the University of Strathclyde [4].

three devices had impedance matching layers of the required thickness on the front face of the element.

3.2.1 Characterising the prototype resonant devices

The piezocomposite devices were evaluated in a similar way to the capacitance device in Chapter 2. The laser/air-coupled transducer system used in this study is shown schematically in Figure 3.2. Ultrasound was generated in the test samples using a pulsed Lumonics ‘Mini-Q’ Q-switched Nd:YAG laser, delivering 4ns pulses at a wavelength of 1064nm in the near infra red, with a maximum pulse energy of 120mJ.

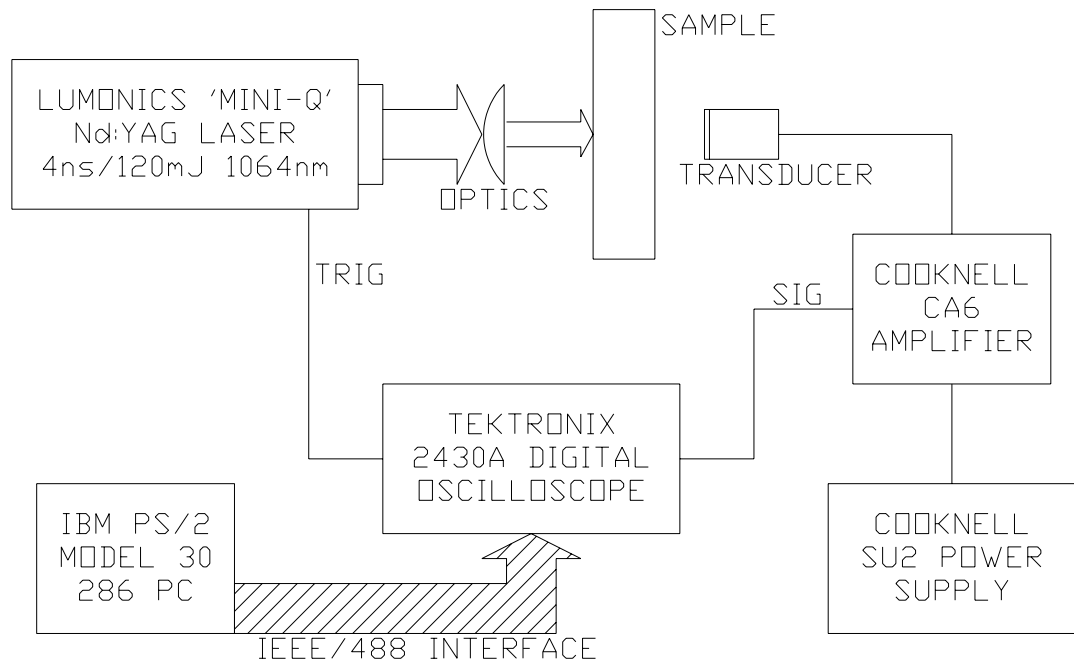


Figure 3.2: Schematic diagram of experimental apparatus.

Waveforms detected by the air-coupled devices were passed through a Cooknell CA6 charge amplifier and captured on a Tektronix 2430A digital oscilloscope. Digitised data was then transferred via an IEEE-488/GPIB interface to an IBM PS/2 Model 30 286 personal computer for storage and analysis. For more detailed equipment specifications, see Appendix A. To characterise the devices, a calibration block of aluminium 86.0mm thick was used as the sample, which was sufficiently thick to allow resonant transducers time to reach a steady state between successive echoes.

As described in Chapter 2 for the silicon device, a contact capacitance transducer which used the sample itself as one electrode was used to provide a waveform for comparison with the response of piezoelectric air-coupled devices. Figure 3.3(a) shows the waveform detected by this device in the calibration block, and

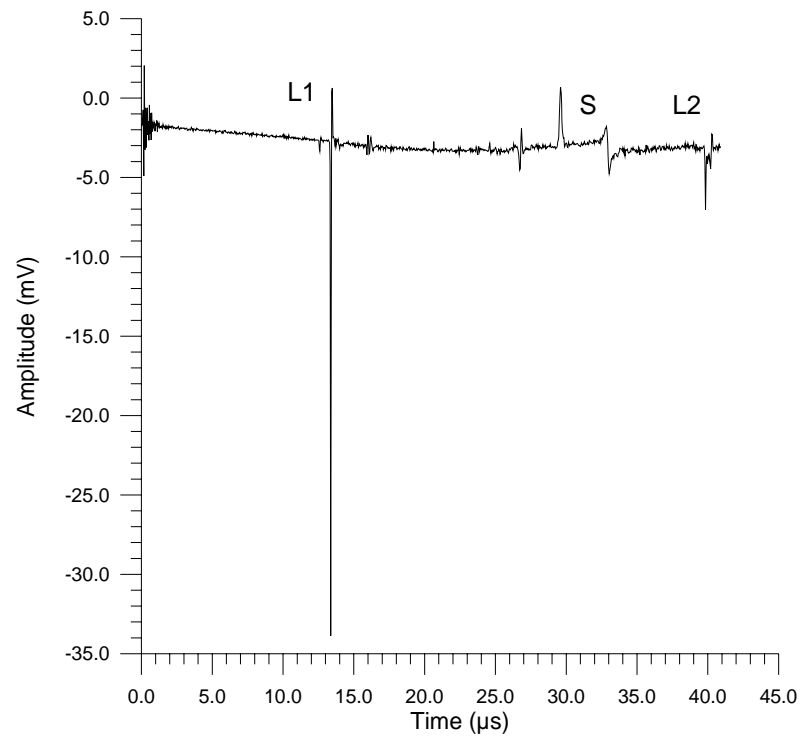


Figure 3.3(a): Waveform through 86mm of aluminium using the contact capacitance device, with longitudinal arrivals *L1* and *L2*, and shear arrival *S*.

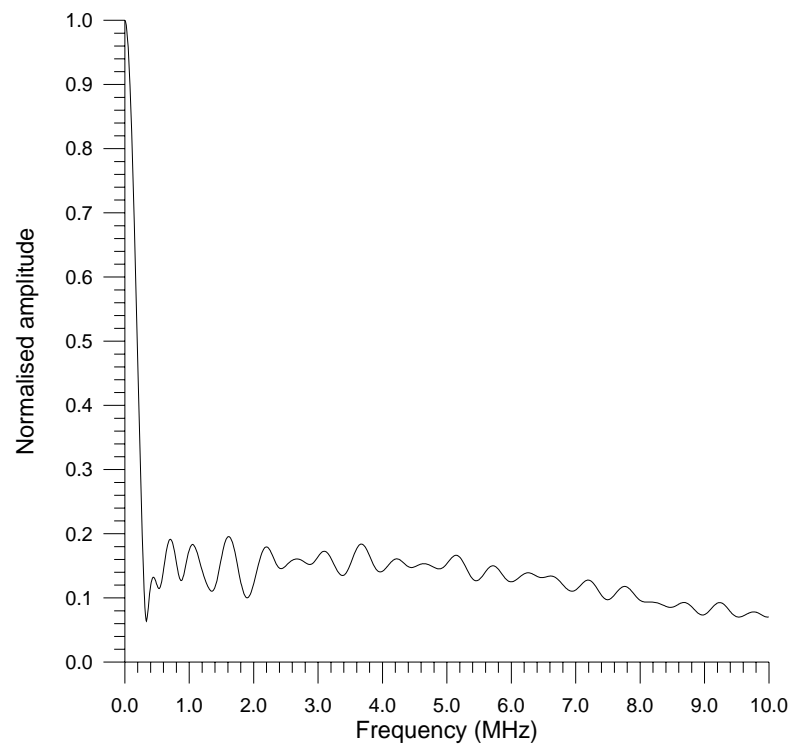


Figure 3.3(b): Frequency spectrum of the first longitudinal arrival in Figure 3.3(a).

longitudinal arrivals at $L1$ and $L2$, and the shear wave arrival at S , have been detected. The frequency content of the first longitudinal arrival at $L1$ is shown in Figure 3.3(b), which was broad band up to 10MHz which was the upper frequency limit of the amplifier.

3.2.2 Results using the resonant devices

Figures 3.4(a) to (c) show the response of the three resonant air-coupled devices for the same generation conditions, across an air gap of 10mm between sample and detector. The time delay caused by the air gap has been removed for presentation purposes. All three features seen in the contact capacitance transducer waveform were detected by (a) the damped transducer (b) the undamped transducer, and (c) the high frequency device. The frequency content of the first longitudinal arrival $L1$ for each of the signals are shown in Figures 3.5(a) to (c) respectively. The low frequency devices peaked in the range 600-700kHz and were narrowband, and the resonant response of the high frequency device had a twin peaked response at 1.215 and 1.599MHz.

A useful quantity for assessing the frequency characteristics of a transducer is Q , a measure of the bandwidth of the device relative to the resonant frequency, given by:

$$Q = \frac{f_r}{\Delta f_{3dB}} \quad \{3.1\}$$

where Δf_{3dB} is the 3dB bandwidth and f_r is the resonant frequency. The higher the value of Q , then the more resonant the device. For the damped low frequency resonant device, the resonant peak occurred at 494.4kHz with a 3dB bandwidth of 269.2kHz.

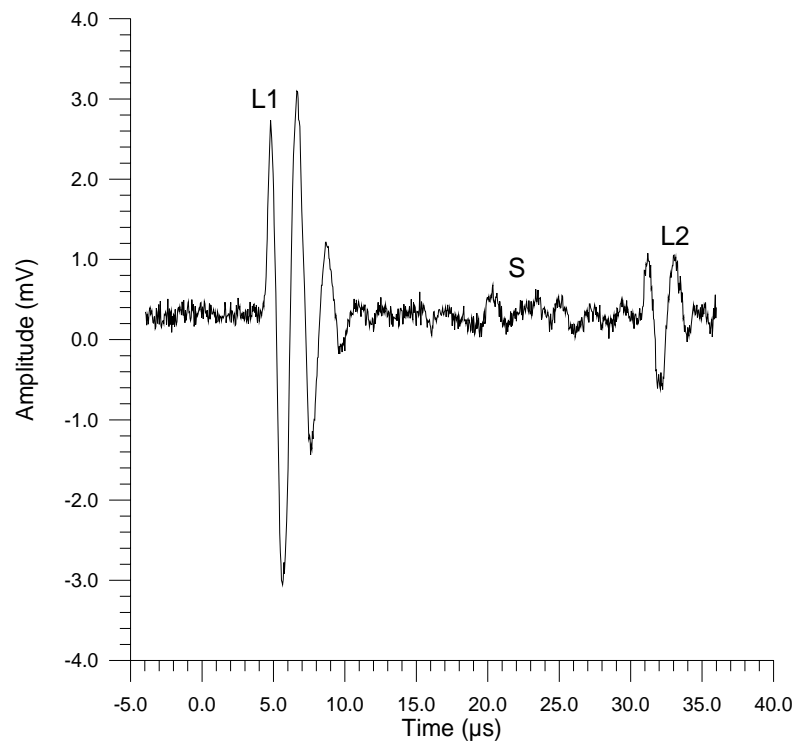


Figure 3.4(a): Waveform through 86mm of aluminium using the low frequency damped device, showing longitudinal (*L*) and shear (*S*) wave arrivals.

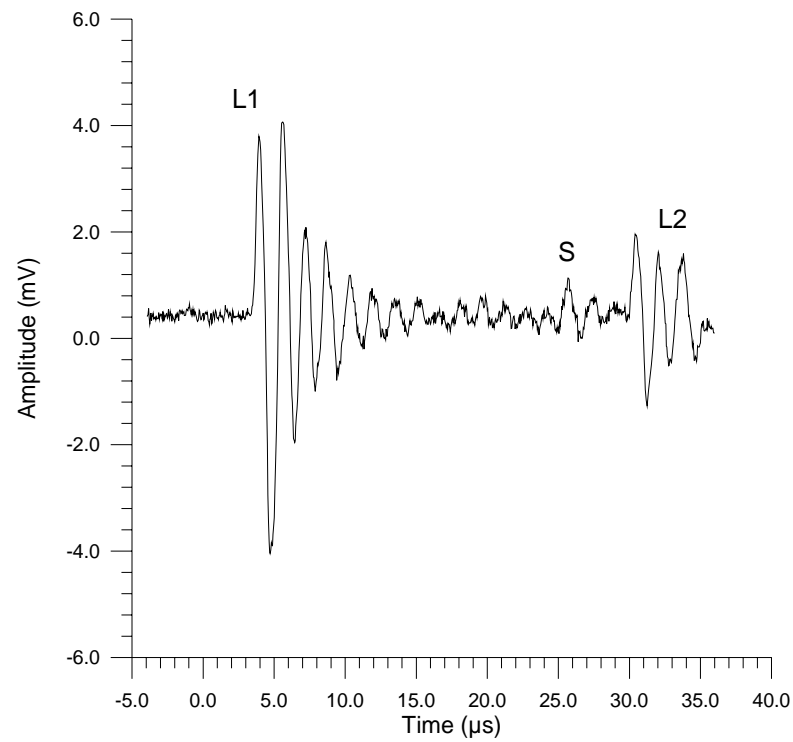


Figure 3.4(b): Waveform through 86mm of aluminium using the low frequency undamped device, showing longitudinal (*L*) and shear (*S*) wave arrivals.

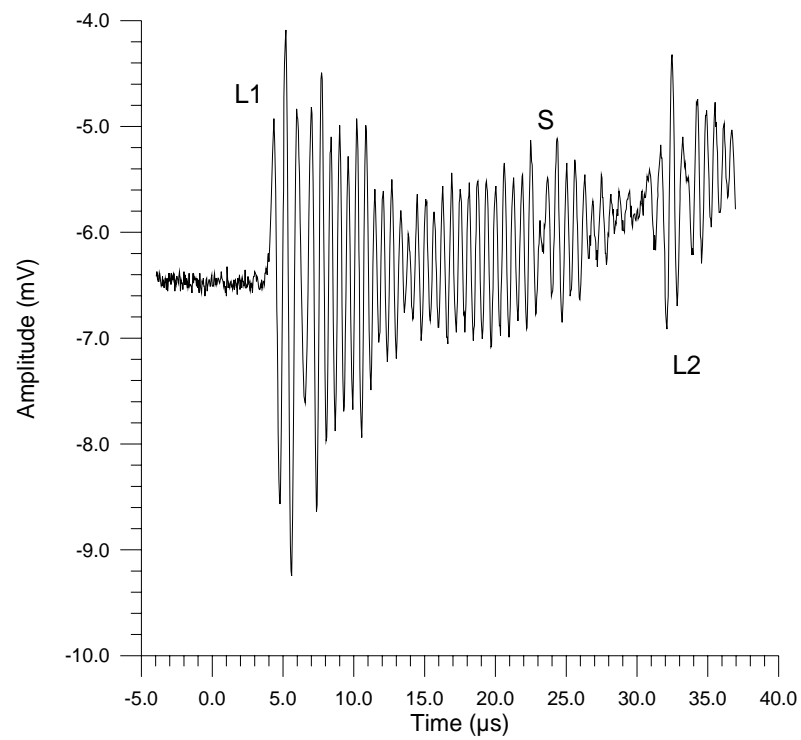


Figure 3.4(c): Waveform through 86mm of aluminium using the high frequency device, again showing longitudinal (L) and shear (S) wave arrivals.

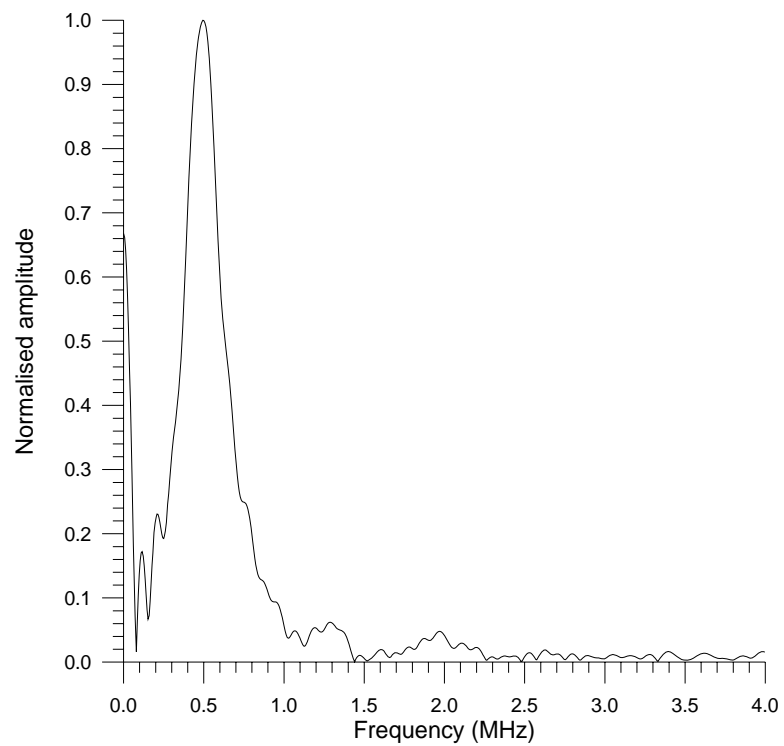


Figure 3.5(a): Frequency spectrum of the first longitudinal arrival in Figure 3.4(a).

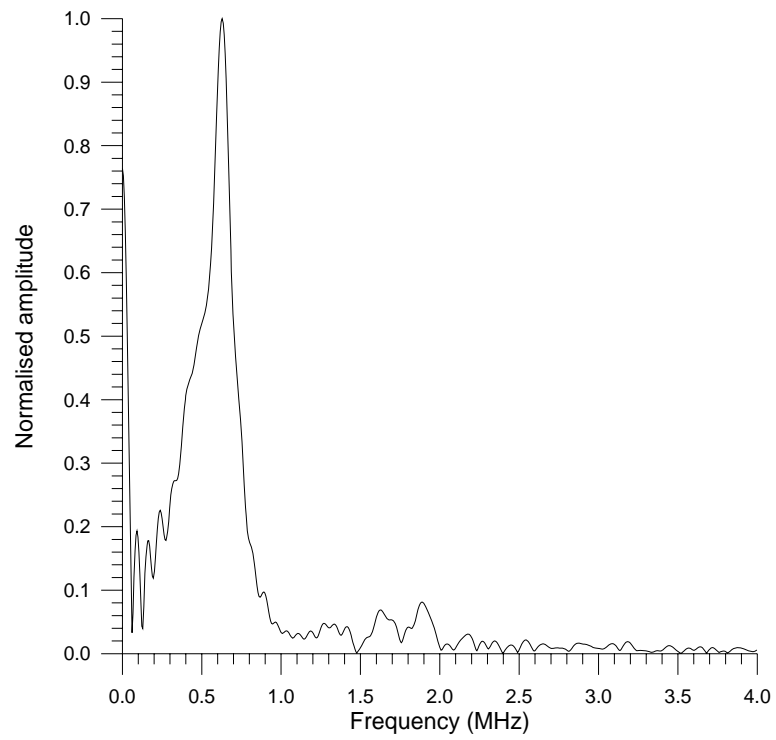


Figure 3.5(b): Frequency spectrum of the first longitudinal arrival in Figure 3.4(b).

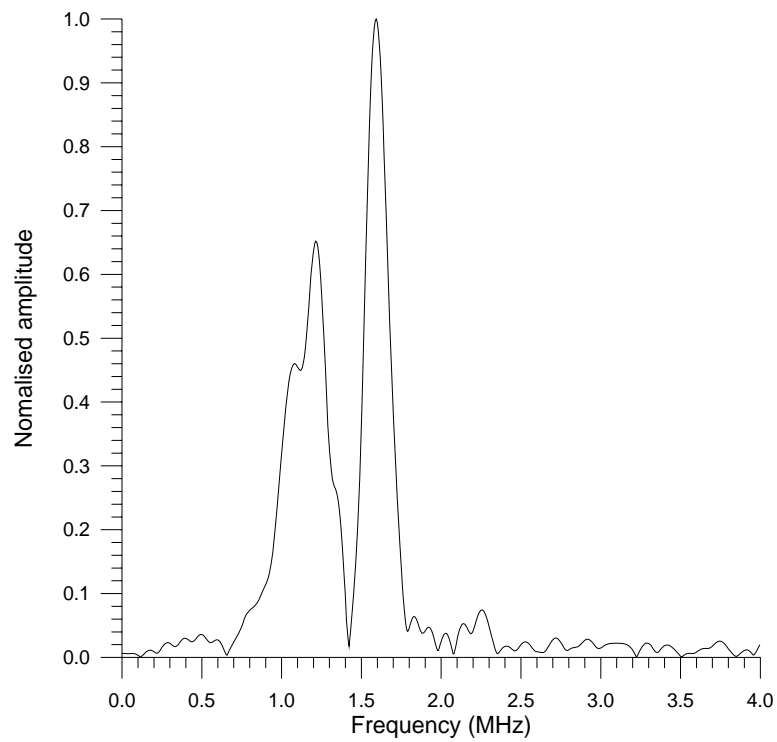


Figure 3.5(c): Frequency spectrum of the first longitudinal arrival in Figure 3.4(c).

For the undamped low frequency device, the resonant peak was at a frequency of 626.7kHz, with a 3dB bandwidth of 223.7kHz. The corresponding values of Q were therefore 1.84 and 2.80 respectively.

The system response to laser generated ultrasound in a thinner aluminium block 19.8mm thick is shown in Figure 3.6. The contact capacitance device response is shown in Figure 3.6(a), where longitudinal echoes $L1$, $L2$ and $L3$ have been detected, along with the shear wave arrivals $S1$ and $S3$. The longitudinal component of the mode conversion of the shear wave is also shown at $M1$ and again at $M3$. The responses of the air-coupled devices are shown in Figures 3.6(b) to (d) for the damped, undamped and high frequency devices respectively. However, due to the narrow bandwidth and low frequency of the air-coupled devices, it was difficult to resolve discrete longitudinal echoes for all but the high frequency device, even in the frequency domain. This may be achieved using deconvolution techniques, and results obtained by the University of Strathclyde using this data have been published [4].

3.3 Advancements in transducer design

After the success of this early work, a new approach to the design of the transducers was adopted, where the first inter-pillar resonance of the 1-3 piezocomposite was used to extend the bandwidth of the devices. Finite element techniques were used to predict a large gain in bandwidth for an aspect ratio (ratio of ceramic pillar width to height) of 0.24. A new transducer was manufactured by the University of Strathclyde, which consisted of another 1-3 connectivity composite element of PZT-5A piezoceramic and CY1300/HY1301 hard setting epoxy resin. This

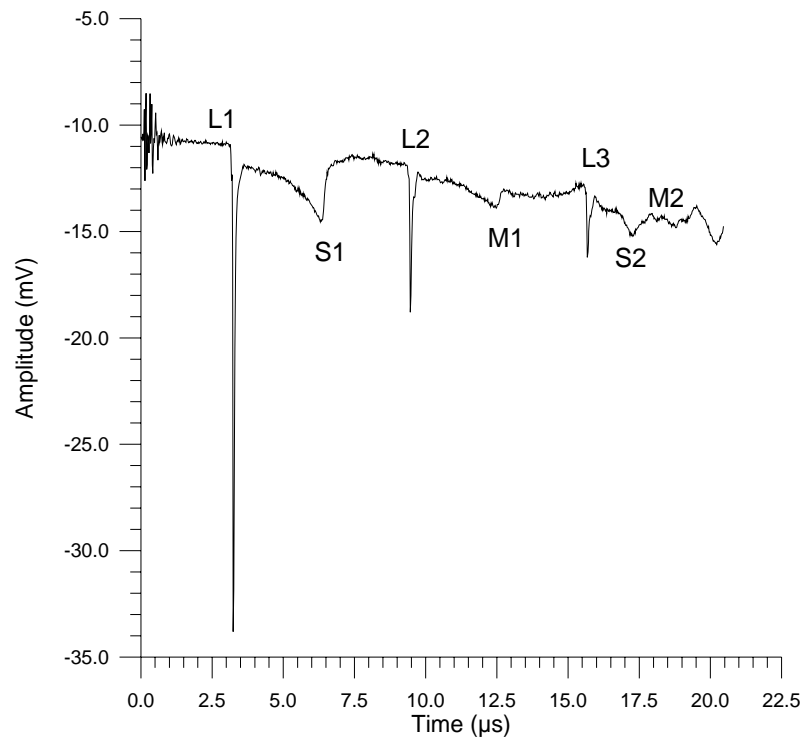


Figure 3.6(a): Response of the contact capacitance device to a waveform in 19.8mm of aluminium, with longitudinal (*L*), shear (*S*) and mode converted shear (*M*) arrivals.

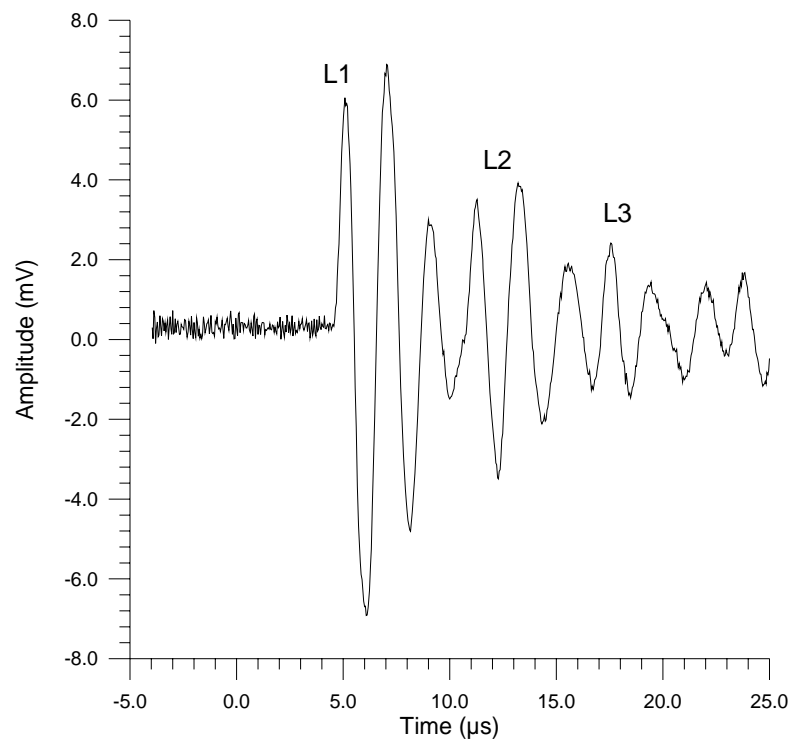


Figure 3.6(b): Response of the low frequency damped device to a waveform in 19.8mm of aluminium.

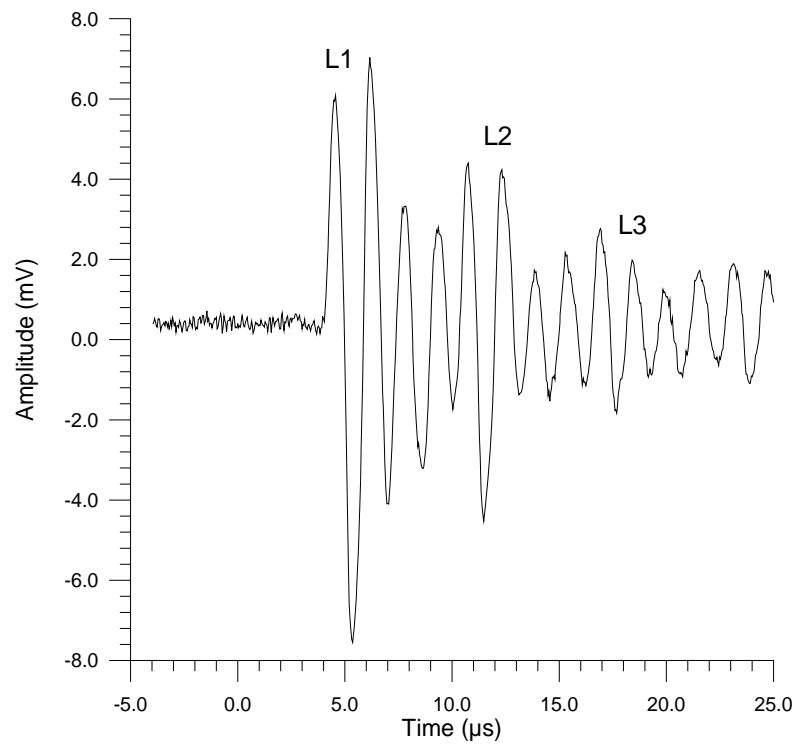


Figure 3.6(c): Response of the low frequency undamped device to a waveform in 19.8mm of aluminium.

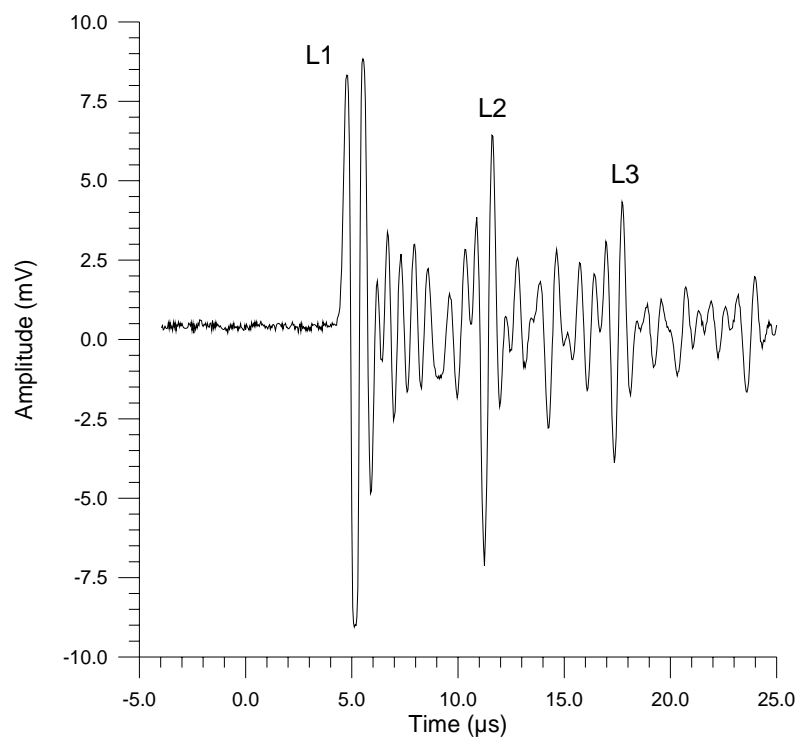


Figure 3.6(d): Response of the high frequency device to the waveform in 19.8mm of aluminium.

element had an aspect ratio of 0.24, and a diameter of 15mm. No impedance matching layer was used on the front face of the device.

3.3.1 Characterising the wideband piezocomposite device

The new device was then evaluated in an identical manner to the three prototype transducers. Figure 3.7(a) shows the waveform received through the 86mm thick aluminium calibration block used previously, and the corresponding frequency spectrum of the first longitudinal echo at $L1$ is displayed in Figure 3.7(b). The device was well damped with far less of the ringing seen in the earlier devices, and from the frequency spectrum it can be seen that the device had a centre frequency of 1.2MHz, with the bandwidth extending up to 2MHz. The waveform obtained through the 20mm thick plate of aluminium used earlier is shown in Figure 3.7(c), for comparison with the resonant devices. Not only are the individual longitudinal echoes $L1$, $L2$ and $L3$ easily resolved, but the shear arrival S and the subsequent mode conversion $M1$ may also be seen.

3.3.2 Comparison of the broadband piezoelectric and capacitance air transducers

The previous chapter examined the use of a silicon capacitance air-coupled receiver, which appeared to follow the surface displacement of the sample. The waveform shown in Figure 3.7(c) for the wide bandwidth piezocomposite device is also a similar approximation. To compare the two devices, a laser generated wave through the 86mm aluminium calibration block was detected using both transducers

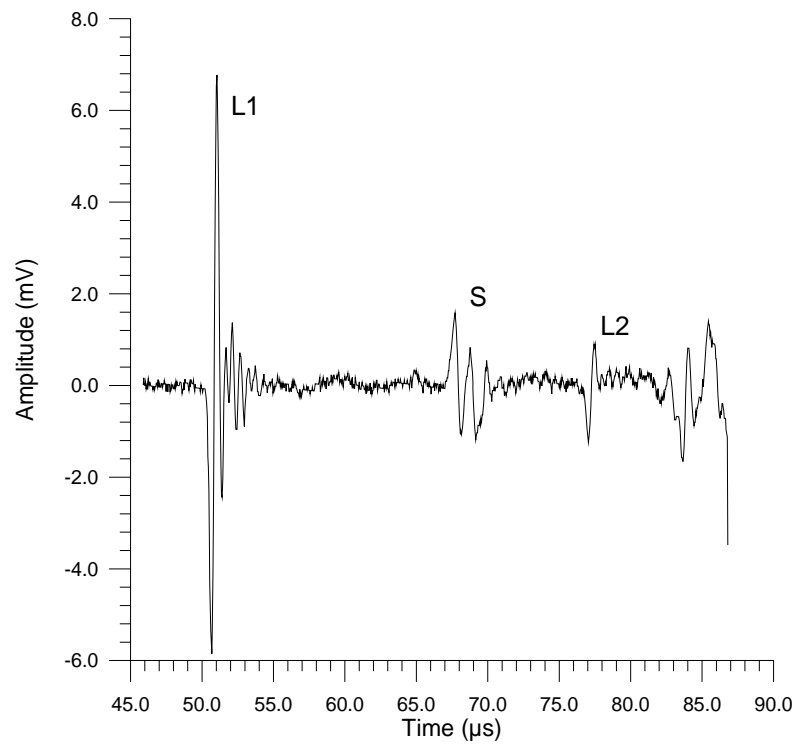


Figure 3.7(a): Waveform through 86mm of aluminium using the wide bandwidth device, showing longitudinal (*L*) and shear (*S*) wave arrivals.

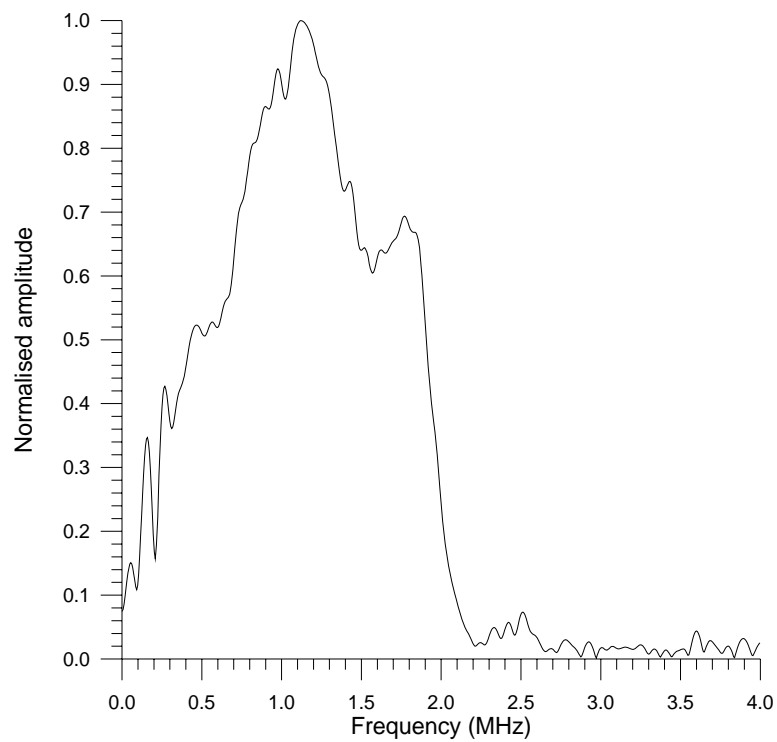


Figure 3.7(b): Frequency spectrum of first longitudinal arrival in Figure 3.7(a).

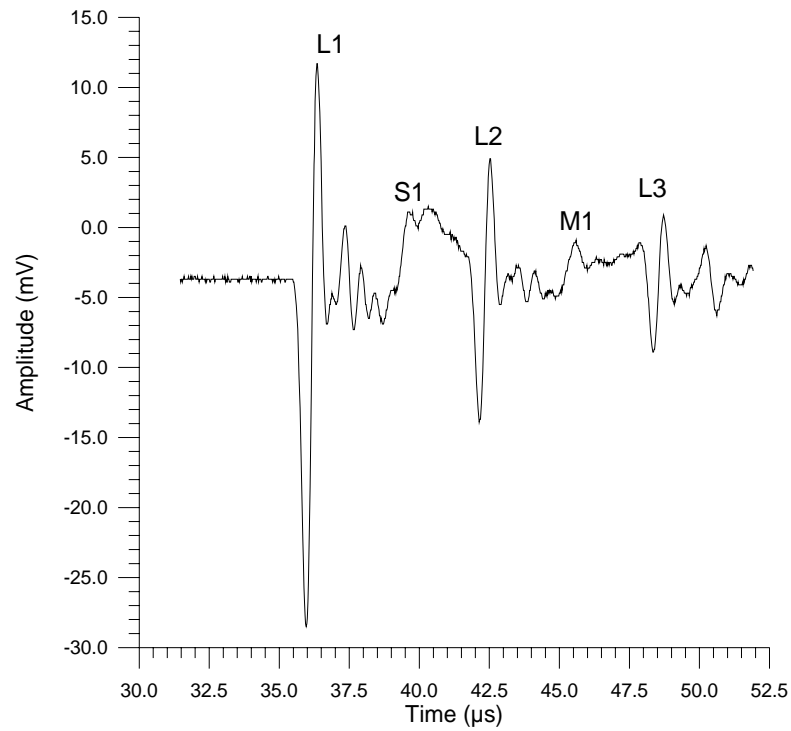


Figure 3.7(c): Response of the wide bandwidth device to the waveform in 19.8mm of aluminium.

for the same generation conditions. The resultant first longitudinal arrivals from both transducers are shown on the same axes in Figure 3.8(a) for comparison. The frequency spectra are likewise shown in Figure 3.8(b). From the time domain waveform for the piezoelectric device, the maximum peak to peak amplitude was 12.6mV, and from the frequency spectrum the 3dB bandwidth was 1.48MHz centred around 1.12MHz. These values gave a Q -value of 0.76. For the capacitance device, the peak to peak amplitude from the time domain waveform was 54.4mV, and the 3dB bandwidth was 882.5kHz centred about 564.6kHz in the frequency waveform. This gave a Q -value of 0.64. The Q value of a transducer is, however, more applicable to a narrow-band device, as it is difficult to determine the resonant frequency for devices

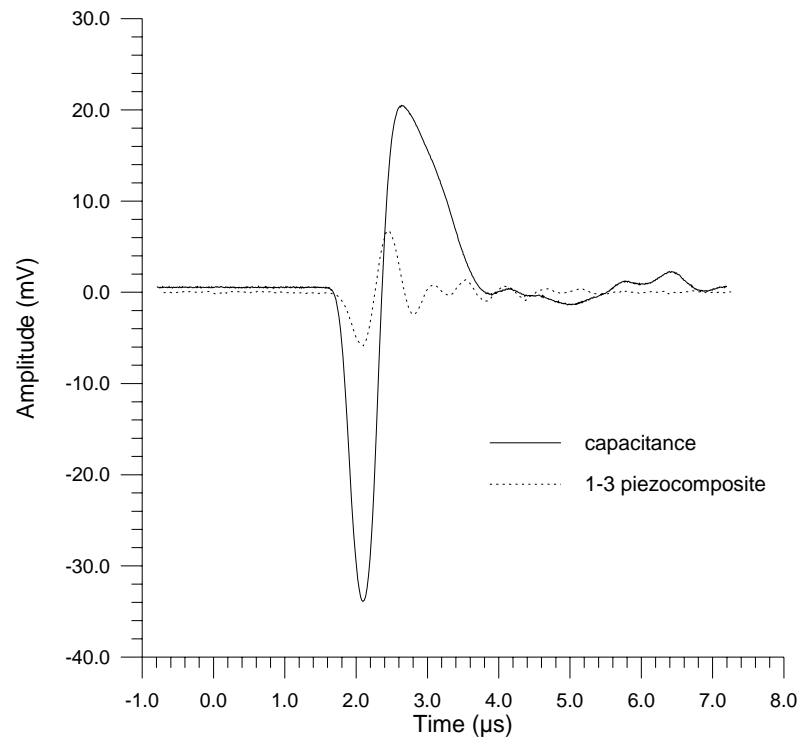


Figure 3.8(a): A comparison of the longitudinal arrivals in 86.0mm aluminium for the wideband capacitance and 1-3 connectivity piezocomposite air-coupled transducers.

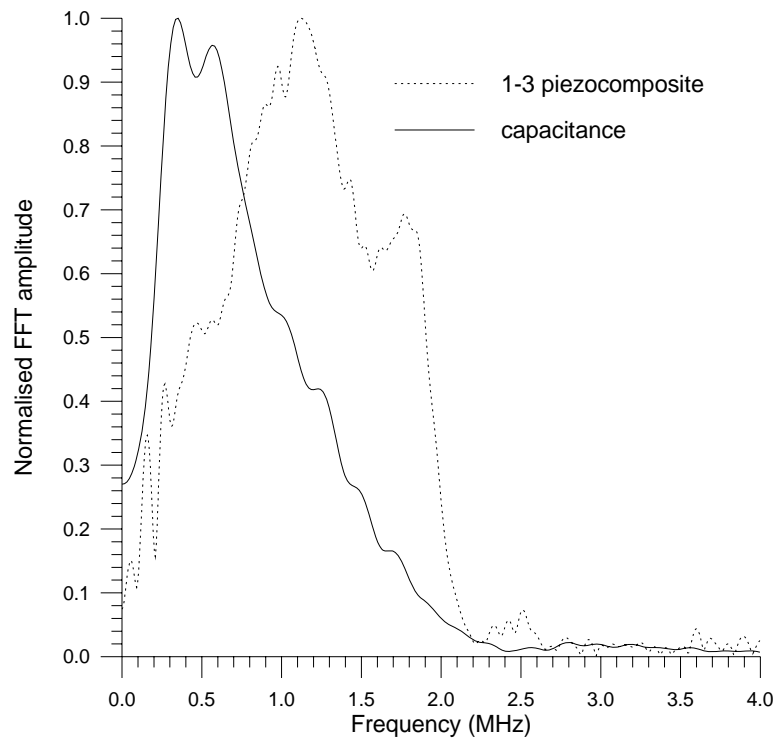


Figure 3.8(b): A comparison of the frequency spectra of the two waveforms shown in Figure 3.8(a).

with large bandwidths.

It can be seen from the plots that the capacitance device is more sensitive than the 1-3 piezocomposite transducer for the same generation conditions, although the piezoelectric device has a wider bandwidth. The shapes of the two frequency spectra were also interesting. It was stated in Section 3.3 that the available bandwidth of the piezocomposite device was extended by using the inter-pillar resonance, and this has produced a sharp cut-off at the upper frequency limit. The capacitance device, however, has a more gradual reduction in high frequency response, and in addition has a better low frequency response.

It should be noted, however, that this was not a fair test for either transducer. The piezocomposite device, while probably operating at its frequency limits, was not impedance matched to the amplifier used and greater signal levels could be obtained with the correct electronics. Similarly, the capacitance device used here was not optimised. The polymer film thickness used was $7.6\mu\text{m}$, and films as thin as $2.5\mu\text{m}$ may be used, which greatly increase the bandwidth and sensitivity. In addition the bias voltage applied to the device was only 100V, and it has been shown that bias voltages of up to 400V extend the bandwidth of these capacitance transducers to well over 2MHz, as mentioned in Chapter 2.

3.4 Through thickness waveforms in composite materials

The new broadband piezoelectric device was then used as a receiver of laser generated ultrasound in composite materials. The Nd:YAG laser used in the calibration experiments was replaced by a Lumonics 'Lasermark' Series Model 630 CO₂ TEA (Transversely Excited at Atmospheric pressure) laser, which delivered

100ns pulses at a wavelength of 10.6 μ m in the far infra red, giving a maximum pulse energy of 8J. This wavelength of radiation is more readily absorbed by polymers than that from the Nd:YAG laser used in the earlier characterisation experiments. The beam diameter and power density were selected using an adjustable iris, and by focusing with a Zn:Se lens.

3.4.1 The composite materials

There are many different non-destructive testing techniques which may be applied to composite materials, and the use of ultrasonics is well documented [8-10]. Traditional contact testing methods have been used to test for defects, but some forms of composite are absorbent to fluids. In other cases, rapid inspection of large structures such as aircraft wing panels [11] was required, and any form of contact would have increase the inspection times.

Two types of composite material were studied in this work. The first of these was a selection of pultruded composites [12] supplied by Fibreforce Composites Ltd., Runcorn, and are named after their method of manufacture. The reinforcement consisted of roving bundles of unidirectional 10 μ m diameter E-glass fibres (local volume fraction 62%) to provide the essential longitudinal properties, and continuous filament mats of E-glass fibres (local volume fraction 28%) to provide transverse strength and stiffness. These were then pulled through a bath of resin (the matrix) and passed through a series of rollers and curing equipment in a continuous process. The resulting material has a fairly random structure as limited control over the fibre orientation is available. Two standard structural EXTREN 525/625 (a registered trademark of MMFG Co., Bristol, Virginia USA) I-sections and flat sheeting, all of

10mm nominal thickness, were available for testing. The matrix material was either isophthalic polyester resin or vinylester resin, with 10-15% by volume of calcium carbonate filler. The weights of mat and roving used were approximately equal, but the exact amounts were unknown as the manufacturer considered this information proprietary.

There was also a section of pultruded U-channel of 4mm nominal thickness, made using Modar 855 resin (Modar is an ICI trademark), which is polyester based with methylmethacrylate additions and 20-25% by volume of alumina trihydrate as a fire retardant. E-glass continuous filament mats around a central core of unidirectional E-glass rovings were used as the reinforcement, with the same local volume fractions as before. Although not particularly anisotropic, in practice all these pultruded materials were extremely scattering and attenuating to ultrasound, and in most respects a 'worst case'.

The second group of materials was carbon fibre reinforced polymer (CFRP) composites [13-14], and these were manufactured [15] by arranging layers of carbon fibres (Enka Tenax HTA in 12K tows) pre-impregnated with epoxy resin (ICI 7716H) in any desired orientation, and then compression moulding them in a heated press at 120°C to cure the resin. This allowed the composite structure to be precisely controlled, and so the CFRP composites could be classified as unidirectional (all fibres running parallel to the principle fibre axis), cross-ply (fibre layers alternately at 0° and 90° to the principle fibre axis), and quasi-isotropic (fibre layers alternately at 0°, -45°, +45° and 90° to the principle fibre axis). The nominal fibre content was 60% by volume, which is typical of many CFRP materials. Ultrasonic properties (such as velocity) in two phase materials vary with the volume fraction of each phase, and so due to the lack of detailed material information, theoretical values were not calculated.

Many waveforms were taken in a variety of different samples, and so only a small fraction of the data will be presented here. Figure 3.9 shows three typical through thickness waveforms detected in (a) an 8-ply (1.1mm thick), (b) a 24-ply (3.3mm thick) and (c) a 40-ply (5.5mm thick) quasi-isotropic carbon fibre reinforced polymer composite plate. It can be seen that the wave sets up a resonant frequency, which is determined by the thickness of the plate, as shown in Figure 3.10 where the frequency spectra of the waveforms of Figure 3.9 are presented. The waveforms were differentiated prior to the frequency analysis, as this effectively removed any very low frequency components or linear slopes, as the change in signal between successive points is less at low frequencies than at high frequencies. In conjunction with the known thickness d of each sample, this resonant frequency f of the plate may be used to evaluate the longitudinal velocity c_L of the composite material, using:

$$c_L = 2.f.d \quad \{3.2\}$$

which is related to the elastic constants of the material as mentioned in Section 1.2 of Chapter 1.

The measured frequencies of the 8-ply, 24-ply and 40-ply composite plates were 1.28MHz, 433kHz and 262kHz (± 6.1 kHz) respectively, giving values for c_L of 2820ms⁻¹, 2860ms⁻¹ and 2887ms⁻¹ (± 13 ms⁻¹) respectively. The low value of c_L for the 8-ply plate could be caused by variations in material properties which would be more prominent in thinner samples. Similar waveforms were obtained in samples of unidirectional and cross-ply composite of the same thickness, as the bulk wave through thickness velocities are virtually unaffected by the fibre orientations.

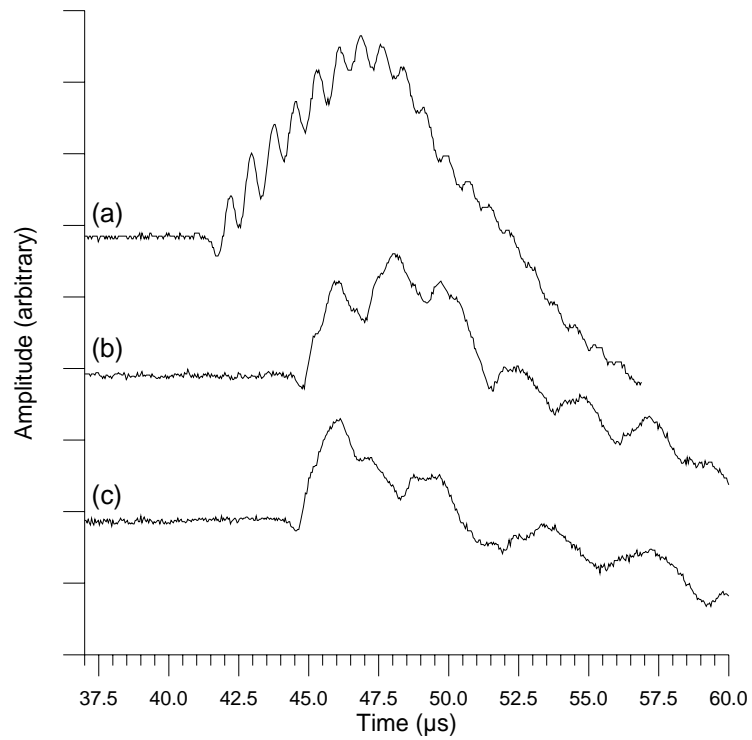


Figure 3.9: Waveforms in (a) 8-ply (1.1mm thick), (b) 24-ply (3.3mm thick) and (c) 40-ply (5.5mm thick) quasi-isotropic CFRP composite plates.

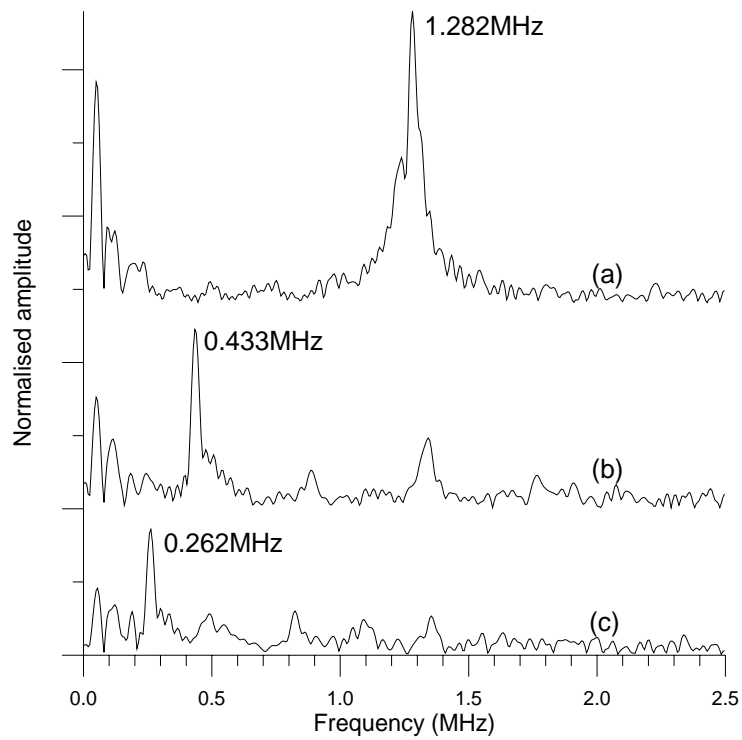


Figure 3.10: Frequency spectra of differentiated waveforms in Figure 3.9.

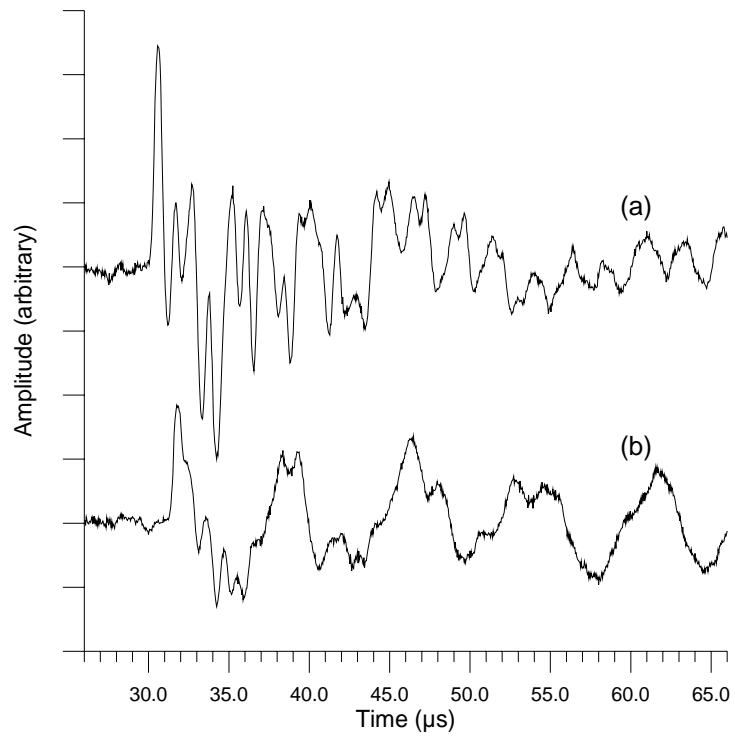


Figure 3.11: Waveforms through (a) 4.25mm thick pultruded U-channel and (b) 9.8mm thick pultruded I-beam composites.

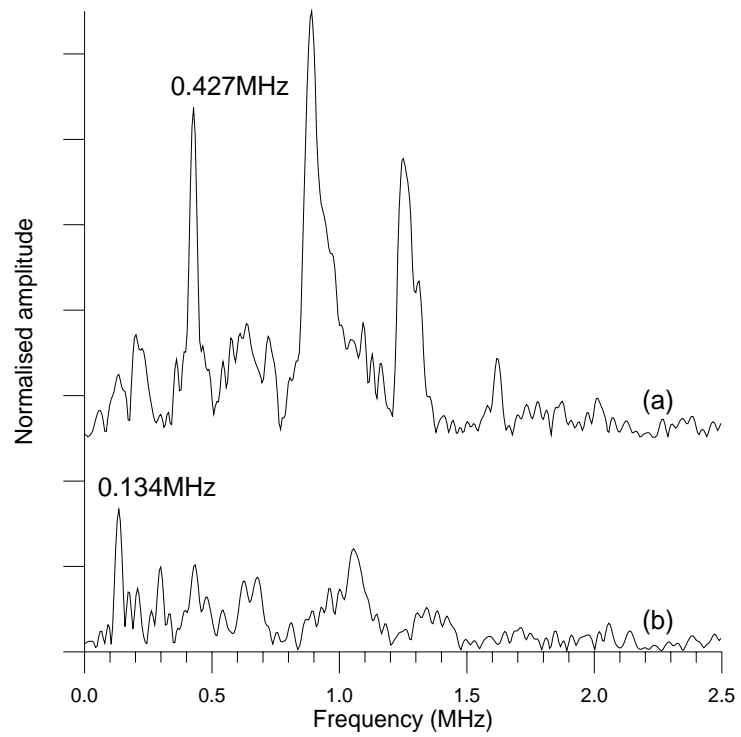


Figure 3.12: Frequency spectra of the differentiated waveforms in Figure 3.11.

Signals were also obtained in samples of pultruded glass fibre reinforced polymer (GFRP) composite, with different matrix polymers. Examples are presented in Figure 3.11 for (a) 4mm thick and (b) 9.8mm thick pultruded U-channel and I-beam samples respectively. The corresponding frequency spectra are shown in Figure 3.12, and the profiles are more complex than for the CFRP samples. A number of different resonant peaks are present in each plot, and the peaks relating to the thickness are at 427kHz and 134kHz ($\pm 6.1\text{kHz}$). These values correspond to velocities of 3418ms^{-1} and 2632ms^{-1} ($\pm 13\text{ms}^{-1}$) for the thinner U-channel and thicker I-section samples respectively. These velocities were also measured using conventional piezoelectric contact probes and found to be correct, and so the gross difference was attributed to the different matrix materials.

3.5 C-scanning of defects using bulk waves

A C-scan produces a plan view image of the sample under test, showing the shape, size and location of any defect, but no information about the depth of the flaw within the sample. Usually, a pulse-echo transducer is moved in a raster pattern over the sample, and an ultrasonic measurement is made at regular intervals. The change in some ultrasonic wave property at each point in the scan, such as signal amplitude or arrival time, is used to create the image.

By using the apparatus shown in Figure 3.13, it was possible to produce C-scan images of a variety of defects using the laser/air-coupled transducer system and through thickness waveforms. The sample to be tested was mounted on a pair of

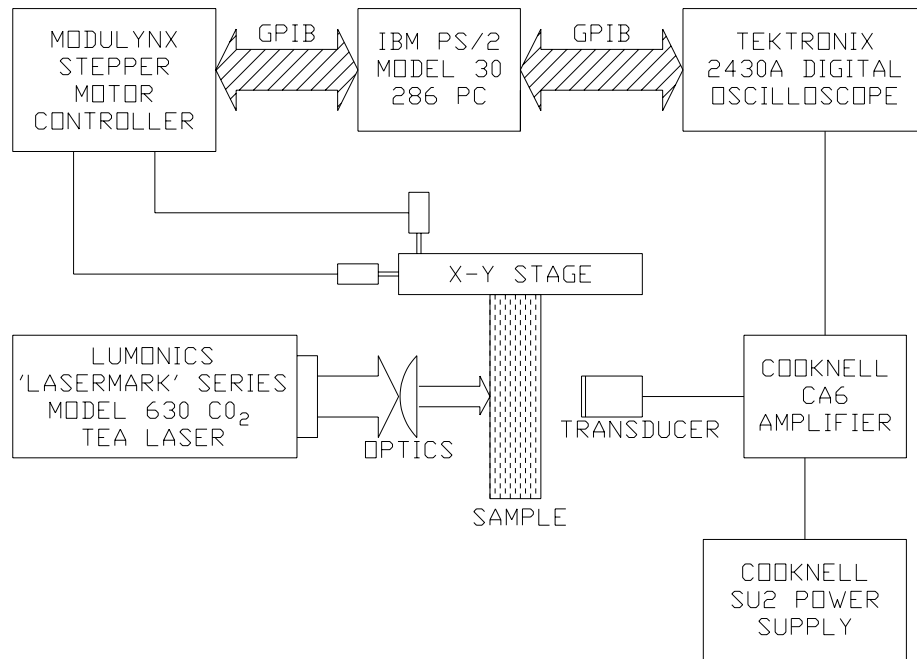


Figure 3.13: The C-scanning apparatus.

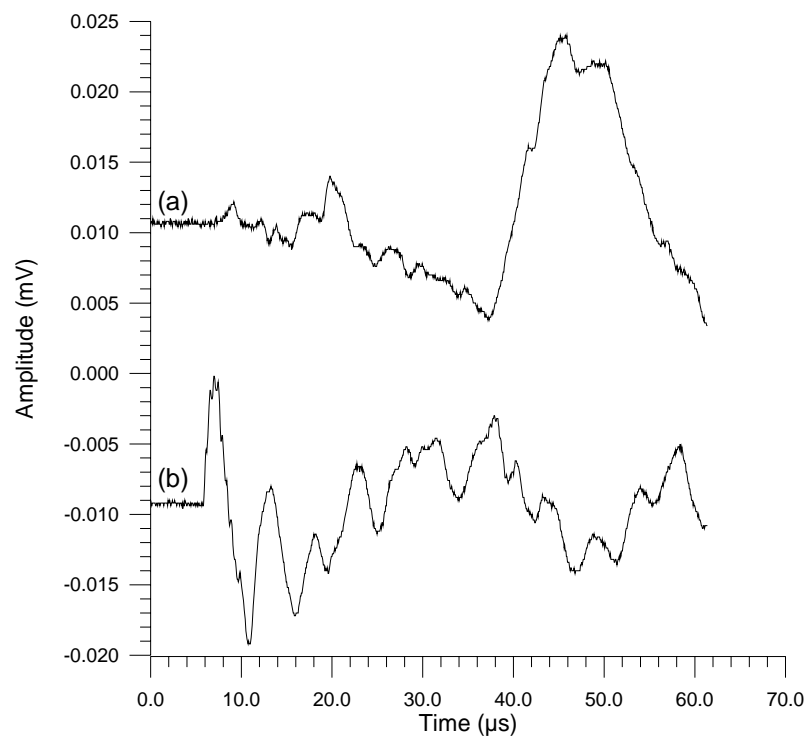


Figure 3.14: Waveforms from a typical scan, with (a) a delamination and (b) no delamination between source and receiver.

Daedal X-Y linear stages, driven by a computer controlled Modulynx stepper motor driver. For more detailed equipment specifications, see Appendix A. The laser source and air-coupled transducer were fixed on epicentre, with the remaining equipment identical to that described previously. The scanning software stored the digitised waveform at each point in the scan, and thus allowed a variety of processing techniques in both the time and frequency domain to be performed on a single set of data at a later date. Two typical waveforms from one of the scans are shown in Figure 3.14 for (a) one of the delaminations and (b) no delamination between source and receiver. The presence of the defect has effectively prevented the high frequency resonance of the plate from forming, and has reduced the received signal amplitude.

In each of the images to follow, the expected size, shape and location of the defect is shown by a broken white line. Figure 3.15 shows the images obtained for (a) a 25mm (1"), (b) a 12mm (0.5") and (c) a 6mm (0.25") square delamination in a 16-ply unidirectional CFRP composite plate 3.2mm thick. These defects were artificially produced by replacing the central 8 layers of carbon fibre with 8 layers of 120 μ m thick Teflon tape, to prevent adhesion during the manufacture of the plate. Each of these images was obtained by simply measuring the peak to peak amplitude of the ultrasonic signal at each point in the scan. Using this technique, the size, shape and position of each defect could be resolved, apart from the square shape of the smaller 6mm defect which was lost due to the size of the source and receiver, and diffraction effects. The image in Figure 3.15(b) for the 12mm defect also shows an area through which the signal amplitude was not reduced. This was caused by excessive heating of this region in a previous experiment, causing the carbon fibre layers to adhere despite the presence of the Teflon. Figure 3.16 shows the image obtained by scanning a 10mm

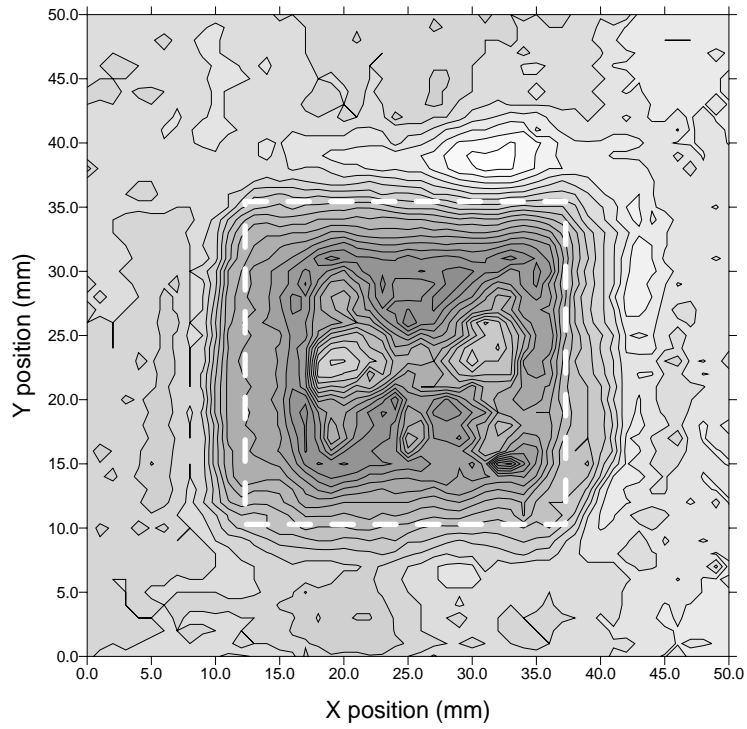


Figure 3.15(a): Image of a 25mm square delamination in 16-ply (3.2mm thick) CFRP, produced using signal amplitude. Grey scale is in mV.

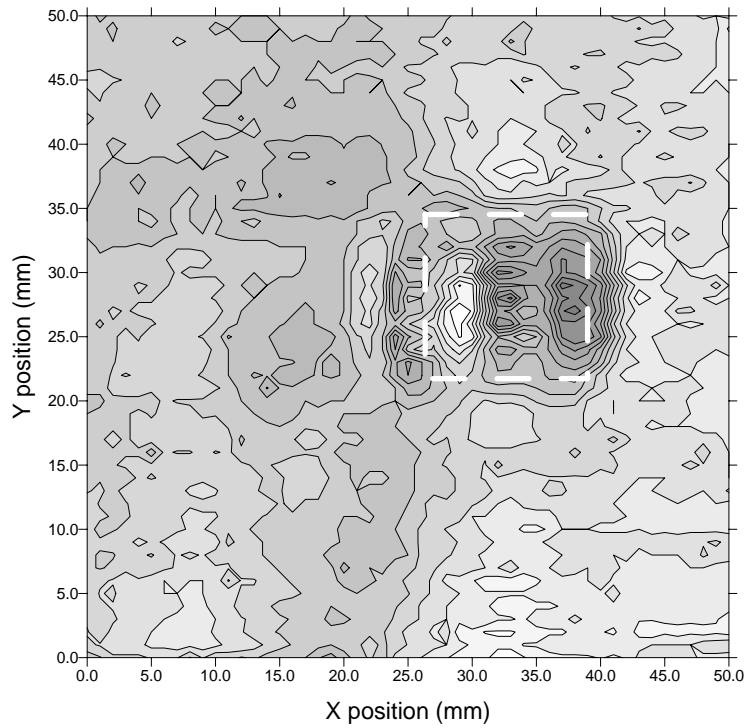


Figure 3.15(b): Image of a 12mm square delamination in 16-ply (3.2mm thick) CFRP, found using signal amplitude. Grey scale is in mV.

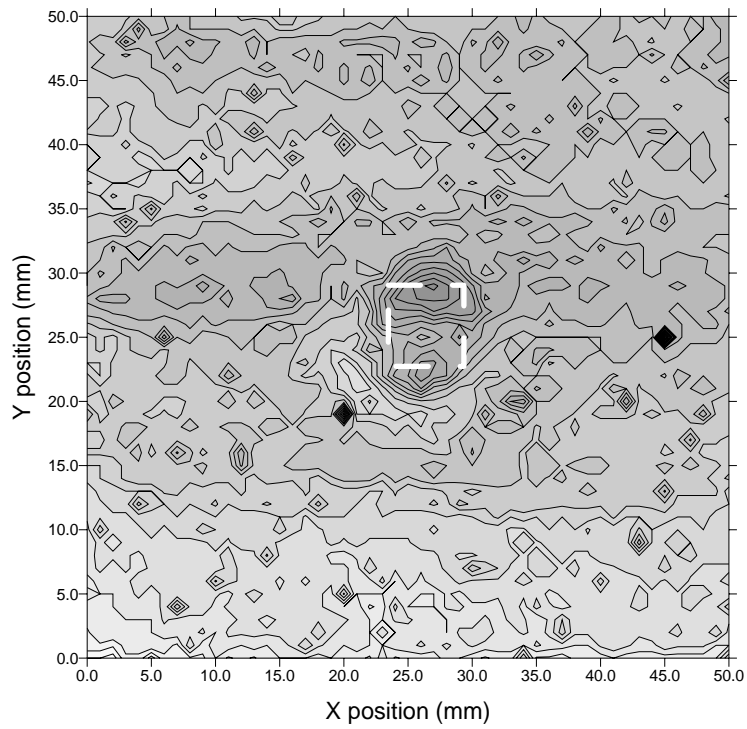


Figure 3.15(c): Image of a 6mm square delamination in 16-ply (3.2mm thick) CFRP, found using signal amplitude. Grey scale is in mV.

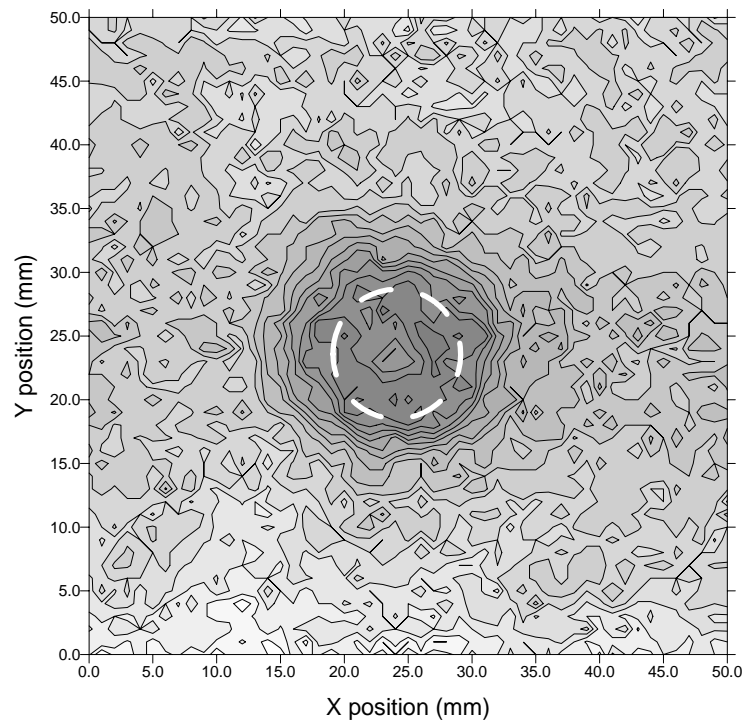


Figure 3.16: Image of a 10mm diameter flat recess machined to a depth of 3.2mm into a 32-ply (4.4mm thick) cross-ply CFRP plate. Grey scale is in mV.

diameter flat recess machined to a depth of 3.2mm in a 32-ply (4.4mm) cross-ply CFRP plate. Again, the size and shape of the defect could be determined, along with the position of the flaw.

Figure 3.17 shows images of another 10mm diameter defect, this time machined to a depth of 1mm into a 9.8mm thick sheet of pultruded GRP composite. Figure 3.17(a) was obtained using the signal amplitude as before, and as well as the defect another interesting feature was discovered. The pale horizontal stripe between 15mm and 20mm on the Y axis, just above the location of the hole, indicated a region of resin-rich composite which was not evident at the start of the experiment. The size and shape of the machined defect is more strongly indicated in Figure 3.17(b), which was produced using the shift in time of flight of the first arrival, caused by the reduction in thickness of composite material. The recess could also be imaged in the frequency domain, using the maximum amplitude in a selected frequency window as shown in Figure 3.17(c), and the shift in frequency of a resonant peak as shown in Figure 3.17(d). The advantages of using the frequency domain may be illustrated by examining Figures 3.18(a) and (b), obtained using amplitude of the time domain waveform and frequency spectrum respectively. The defect in this case was a 5mm diameter recess 1mm deep, which was not detected using either signal amplitude or time shift, but is discernible in the frequency image. The area of fibre rich composite was also more prominent in the frequency domain, as can be seen in Figure 3.18(b).

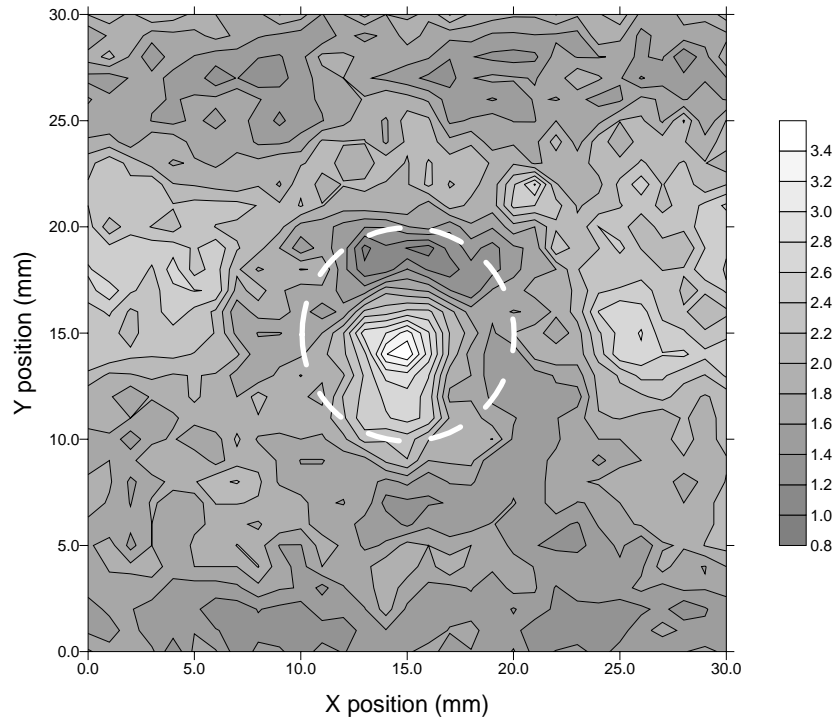


Figure 3.17(a): Image of a 10mm diameter flat recess machined 1mm into a 9.8mm thick pultruded GRP plate, found using signal amplitude. Grey scale is in mV.

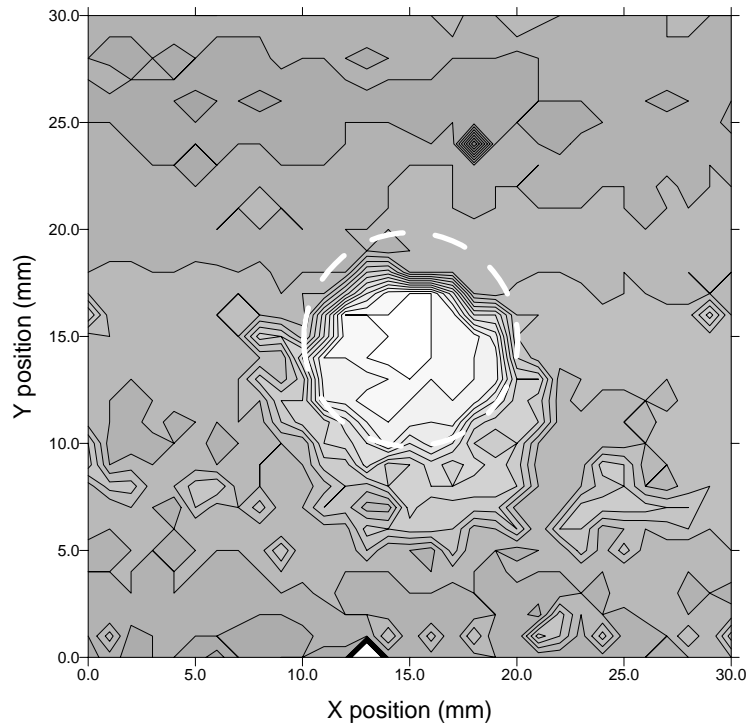


Figure 3.17(b): Image of a 10mm diameter flat recess machined 1mm into a 9.8mm thick pultruded GRP plate, found using time shift of first arrival. Grey scale is in μs .

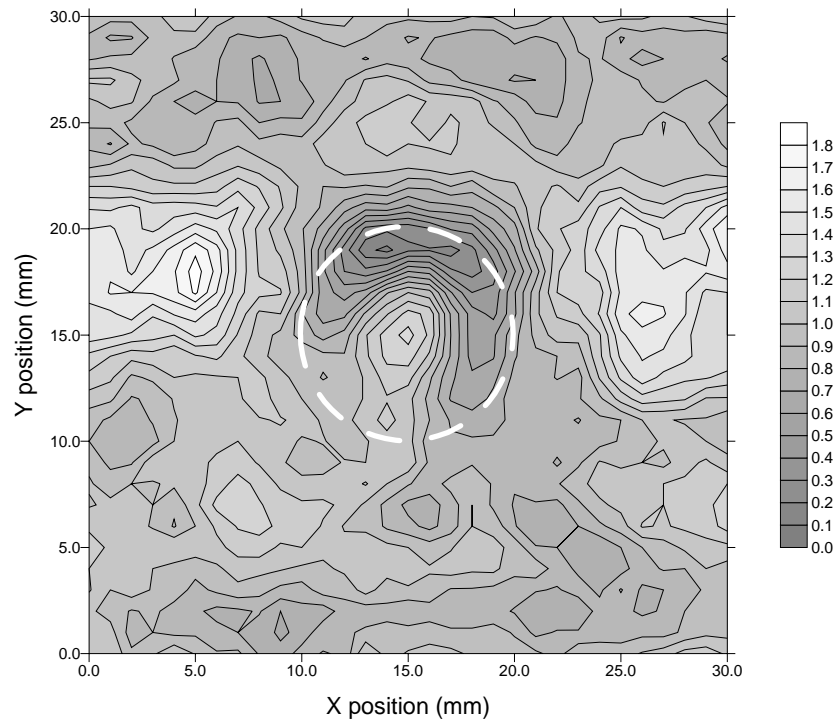


Figure 3.17(c): Image of a 10mm diameter flat recess machined 1mm into a 9.8mm thick pultruded GRP plate, found using FFT amplitude. Grey scale is arbitrary.

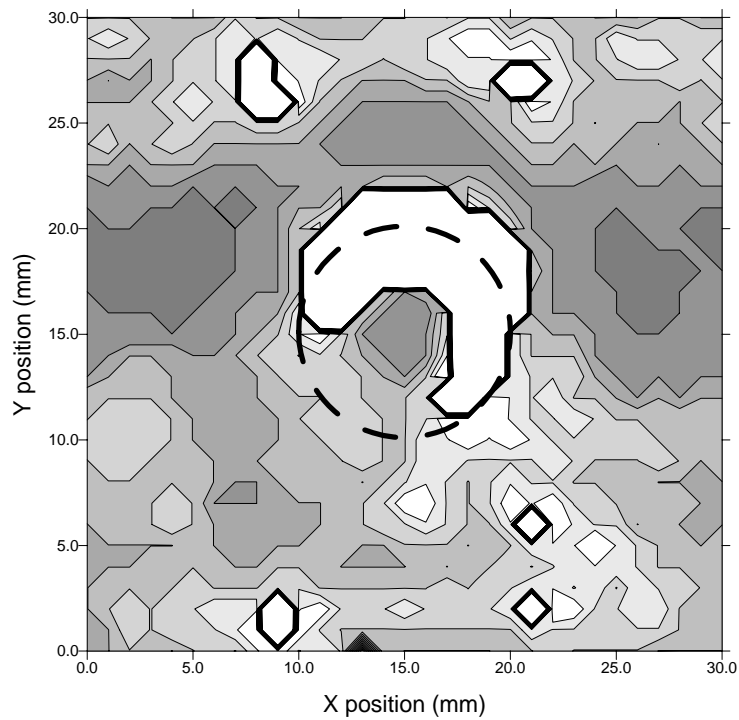


Figure 3.17(d): Image of a 10mm diameter flat recess machined 1mm into a 9.8mm thick pultruded GRP plate, found using frequency shift. Grey scale is in kHz.

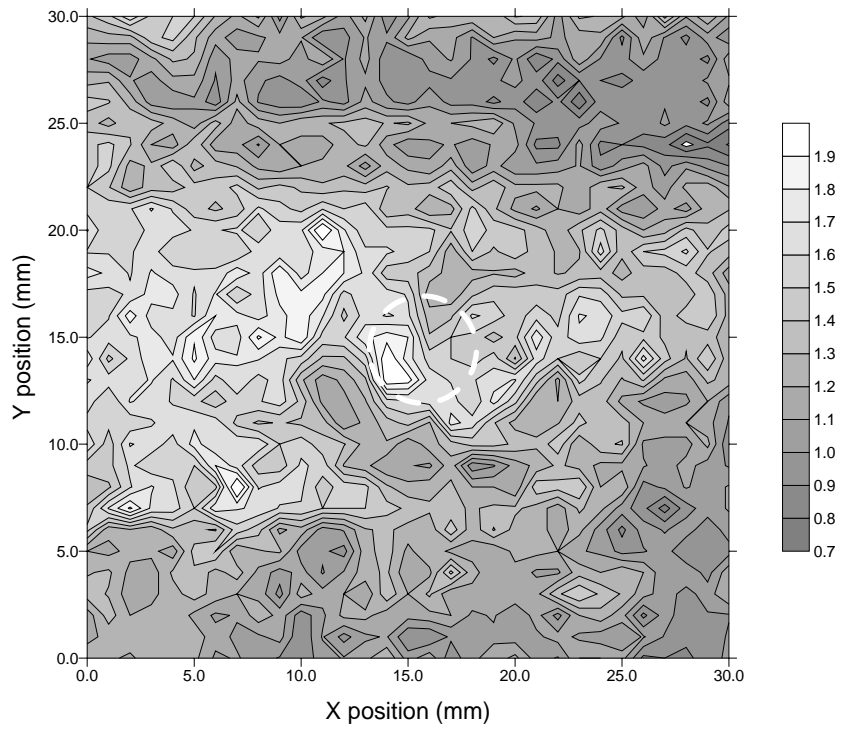


Figure 3.18(a): Image of a 5mm diameter recess 1mm deep in a 9.8mm thick pultruded GRP plate, found using signal amplitude. Grey scale is in mV.

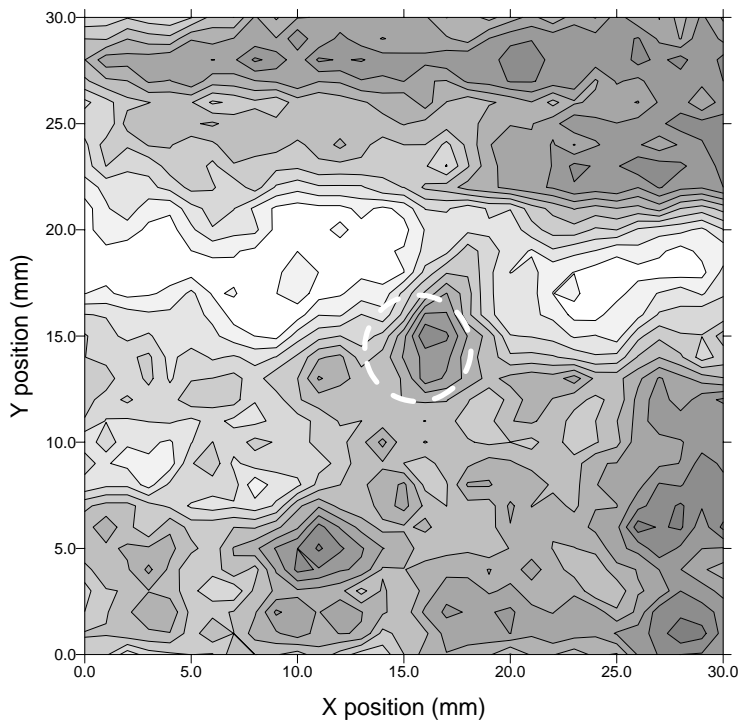


Figure 3.18(b): Image of a 5mm diameter recess 1mm deep in a 9.8mm thick pultruded GRP plate, found using FFT amplitude. Grey scale is arbitrary.

3.6 Discussion

From the results shown in this chapter, it would seem that the 1-3 connectivity piezocomposite transducers tested were well suited for the detection of laser-generated ultrasound, in both metals and polymer composite materials. The prototype devices had sufficient sensitivity, but due to the use of impedance matching layers, the bandwidth was fairly narrow between 100 and 200kHz. This limited the minimum thickness of material that could be reliably tested using through transmission, a problem associated with all transducers depending on their frequency of operation. The low operating frequencies ($\approx 600\text{kHz}$) of these devices meant that without sophisticated deconvolution algorithms, the number of practical applications for the laser/air-transducer system using these resonant prototypes would be few. The low frequency devices did not complement the wideband ultrasonic source available from the pulsed laser. The high frequency prototype was also not very practical, as the device was so resonant that any features present in the waveforms were heavily distorted. However, the broadband piezocomposite transducer with no matching layer was able to test a wider variety of samples due to the higher frequency of the device and its wideband response. There was no appreciable difference in sensitivity between the prototypes and the advanced device, as the new piezocomposite element was sufficiently impedance matched to air without the additional matching layer.

The non-contact system of laser and piezocomposite receiver proposed here is extremely versatile, and is well suited to testing a variety of materials of different thickness. However, the use of a pulsed laser poses safety problems, due to the nature of the infra-red light emitted which is damaging to the retina, particularly for the Nd:YAG laser. These items of equipment are also expensive and difficult to set up,

and so this system would probably only be useful in very specialised situations. Ideally, the pulsed laser would be replaced with another air-coupled piezocomposite transducer, or even one single transducer used in pulse-echo configuration. However, for maximum sensitivity and bandwidth, source and receiver require different volume fractions of ceramic and epoxy, so the use of only a single transducer is difficult. In addition, a pulse-echo device must be sufficiently well damped to reach a steady state quickly after pulsing before being used as a receiver, so that objects in close proximity may be tested.

3.7 Conclusions

A variety of 1-3 connectivity piezocomposite air-coupled transducers were evaluated using a pulsed laser to generate wideband high frequency ultrasound. Early prototype devices, using impedance matching layers and operating at 494kHz and 627kHz, were able to detect longitudinal waves in through transmission, Rayleigh and Lamb waves, in both aluminium and composite materials. A high frequency resonant prototype device, operating at 1.6MHz, was also similarly investigated. After these initial experiments, a broadband device without a matching layer was tested and found to operate at 1.2MHz, but with a 1.6MHz bandwidth, complementing the bandwidth of the laser source. The wideband piezocomposite device was compared to the air-coupled capacitance transducer evaluated in Chapter 2, and found to have a wider bandwidth but lower sensitivity. The piezocomposite transducer was then used to detect bulk waves in various samples of carbon fibre reinforced polymer (CFRP) and pultruded glass reinforced polymer (GRP) composites, and to calculate longitudinal velocities in these materials. In conjunction with a computer controlled stepper motor

X-Y scanning stage, the device was used with a laser source to produce C-scan images of various delaminations and machined defects in composite plates, in which the size, shape and location of each defect could be resolved.

3.8 References

- [1] G. Hayward, A. Gachagan, R. Hamilton, D.A. Hutchins and W.M.D. Wright, 'Ceramic-epoxy composite transducers for non-contact ultrasonic applications', *SPIE Symp. 1992*, Vol. 1733, 49-56 (1992)
- [2] W.M.D. Wright, D.A. Hutchins, A. Gachagan and G. Hayward, 'Evaluation of fiber-reinforced composites using a noncontact laser/air-transducer system', *Rev. Prog. Quant. Nondest. Eval.* **312 A&B**, 1333-1340 (1995)
- [3] A. Gachagan, G. Hayward, W.M.D. Wright and D.A. Hutchins, 'Air-coupled piezoelectric detection of laser-generated ultrasound', *Proc. IEEE 1993 Ultrason. Symp.* Ch259, 651-654 (1993)
- [4] D.A. Hutchins, W.M.D. Wright, G. Hayward and A. Gachagan, 'Air-coupled piezoelectric detection of laser-generated ultrasound', *IEEE Trans. Ultrason. Ferroelec. Freq. Contr.* **UFFC-41**, 796-805 (1994)
- [5] W.M.D. Wright, D.A. Hutchins, A. Gachagan and G. Hayward, 'Polymer composite material characterisation using a laser/air-transducer system', accepted for publication in *Ultrasonics*
- [6] G. Hayward and J.A. Hossack, 'Unidimensional modeling of 1-3 composite transducers', *J. Acoust. Soc. Am.* **88**, 599-608 (1990)

- [7] J.A. Hossack and G. Hayward, 'Finite-element analysis of 1-3 composite transducers', *IEEE Trans. Ultrason. Ferroelec. Freq. Contr.* **UFFC 38**, 618-629 (1991)
- [8] R.A. Blake, 'Ultrasonic non-destructive evaluation techniques for composite materials', in *Delaware Composites Design Encyclopedia Vol. VI - Test Methods*, (Technomic Publishing Company, Inc., Lancaster, Pennsylvania, 1990), pp57-109
- [9] R. Prakash, 'Non-destructive testing of composites', *Composites* **11**, 217-224 (1980)
- [10] K.V. Steiner, 'Defect classification in composites using ultrasonic non-destructive evaluation techniques', in *Damage detection in composite materials*, edited by J.E. Masters, (ASTM Philadelphia, Pennsylvania, 1992), ASTM-STP 1128, pp72-84
- [11] J.-P. Monchalin, J.-D. Aussel, P. Bouchard and R. Heon, 'Laser ultrasonics for industrial applications', in *Review of Progress in Quantitative NDE*, edited by D.O. Thompson and D.E. Chimenti, (Plenum Press, New York, 1988), Vol. 7B, pp1607-1614
- [12] R.W. Meyer, *Handbook of pultrusion technology*, (Chapman and Hall, New York, 1985)
- [13] D. Hull, *An Introduction to composite materials*, (Cambridge University Press, Cambridge, 1981)
- [14] P.K. Mallick and S. Newman (eds.), *Composite materials technology: Process and Properties*, (Hanser, Munich, 1992)

- [15] L.P. Scudder, 'Characterisation and testing of carbon fibre reinforced polymer composites using laser generated ultrasound', *Ph.D. Thesis* (University of Warwick, 1995)

Chapter 4: Air-coupled capacitance transducers with metal backplates

4.1 Introduction

The work to be described in this chapter will examine the manufacture and operation of air-coupled capacitance transducers with metallic backplates. The first section will give a brief review of capacitance transducers, followed by some of the theoretical models for the frequency response of the devices. In the first part of the experimental work, a series of ground and polished metal backplates with different surface properties are investigated, along with the effects of the polymer film thickness and the applied bias voltage. In a second study, metal backplates are chemically etched with a regular array of pits a few tens of microns across to produce different backplate profiles.

4.1.1 Air-coupled capacitance transducers

The capacitance or electrostatic transducer for operation in air is essentially a capacitor with one flexible electrode and one rigid electrode. The earliest form of this transducer was known as a condenser microphone, invented by Wente in 1917 [1], and consisted of a flexible metallic diaphragm separated from a back electrode by a 0.001” (25 μ m) air gap. This device had an undamped resonant frequency of about 17kHz, which was later improved by air damping the diaphragm by the addition of holes or grooves in the backplate [2-4]. Such microphones are still in use today, at frequencies up to about 160kHz [5-6]. The air gap between the two electrodes was soon complemented by using a solid dielectric [7], although these early devices had resonant frequencies of only a few kHz. Later work by Kuhl [8] set the precedent for modern capacitance transducers, using thin polymer films of approximately 10 μ m with

grooved, polished and sand blasted backplates to produce devices that operated well over 100kHz. A later study by Matsuzawa [9-10] extended this study using films from 6 μ m to 25 μ m thick with various backplate designs.

There has been much recent interest in the development of air-coupled capacitance transducers, investigating both grooved backplates [11-16] operating up to a few hundred kHz, and those with random surface profiles [17], working well into the MHz range. Many different backplate manufacturing processes have been investigated, such as roughening, chemical etching, machining, silk screening and shot peening [15], and photolithographic deposition [18]. In a further attempt to gain more control over the backplate surface properties, micromachining techniques have been used to produce devices made from silicon [19-21], which can work at MHz frequencies.

Previous work [17] examining capacitance devices with either grooved or random metallic backplates concentrated on their use as resonant sources, driving them with a 10ms sine wave at frequencies between 10kHz and 5MHz. Many aspects of non-destructive testing require the use of pulsed devices, and as capacitance air transducers are inherently wideband due to the small mass of the film electrode, it was thought that further study was merited in this area. The majority of capacitance devices with metallic backplates described in the literature have mechanically machined grooved electrodes, which have to date limited the frequency range to about 200kHz, although flat polished backplates have been used at frequencies up to 3MHz [17]. As the grooved devices were well characterised, it was decided to concentrate on backplates with both random surface profiles, and those into which features a few tens of microns in size were etched, to operate at frequencies over 200kHz.

4.1.2 Theoretical frequency response

There are several published theories describing the operation of capacitance transducers. The first assumes that the transducer operates like a frictionless piston, with the air trapped between the membrane and backplate acting as a spring. Thus the resonant frequency of the system is given by:

$$f = \frac{1}{2\pi} \left(\frac{\gamma \cdot P_a}{\rho \cdot t_a \cdot t_f} \right)^{\frac{1}{2}} \quad \{4.1\}$$

where γ is the adiabatic constant for air (the ratio of specific heats at constant volume and pressure c_p/c_v), P_a is atmospheric pressure, ρ is the film density, and t_f and t_a are the thickness of the film and air gap respectively. This theory has been used by various authors [9-11,17] with some success to predict the resonant frequency of a range of devices operating up to approximately 600kHz, using various surface roughness parameters and capacitance measurements to find an approximation to the air gap t_a . The capacitance of the device had to be measured experimentally for transducers with random backplates after assembly, although the capacitance for a v-grooved backplate may be calculated from theory [13].

Alternatively, the transducer may be modelled as a uniformly supported vibrating membrane [5-6,21-22], and so the resonant frequency of the device is determined using:

$$f = \frac{2.4048}{\pi \cdot D} \left(\frac{T}{\rho_f} \right)^{\frac{1}{2}} \quad \{4.2\}$$

where D is the film diameter, ρ_f is the film density and T is the tension of the membrane. Early work [8-9] with low frequency (up to 100kHz) devices showed that

the membrane tension T strongly affected the response of the device. However, work on transducers with random backplate profiles has found that the membrane tension has little or no effect on the frequency response of the device [17] but did alter the sensitivity. Later work of a similar nature on grooved backplate transducers found that the tension of the membrane was not important [12,23], and so a Helmholtz resonator theory was developed to predict the resonant frequency of the device using:

$$f = \frac{c}{\pi} \left(\frac{\rho_0}{2 \cdot \sigma \cdot h} \right)^{\frac{1}{2}} \quad \{4.3\}$$

where c is the sound velocity in air, ρ_0 the air density, σ the mass per unit area of the membrane, and h the height of the cavity. This is basically the same as equation {4.1}.

It is evident from these various and often conflicting theories and results that a sound understanding of the operation of the capacitance devices mentioned has not to date been achieved. Most of the models were based on experiments using grooved backplate transducers, as the dimensions of the backplate features are more readily known.

4.1.3 Construction of the transducers

The devices used in this work were constructed as shown schematically in Figure 4.1, where the backplate is epoxied into a Perspex insulator which fits inside an earthed front cover. The polymer film is then cut to size and placed between the backplate and the front cover which screws into the casing and fixes the whole

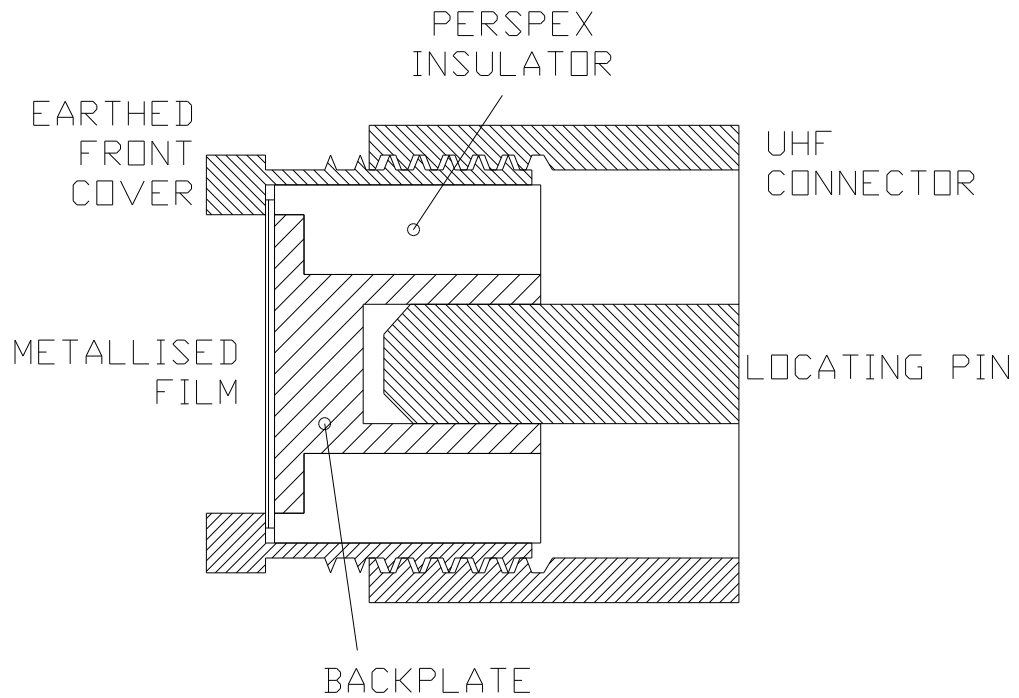


Figure 4.1: Construction of the air transducers.

assembly. A hole in the back of each backplate allows electrical connection via the pin of a UHF connector.

4.2 Manufacture of random metallic backplates by grinding and polishing

The backplate electrodes were manufactured from brass, to facilitate easy machining, although any conducting material would in principle be suitable. One of the problems associated with random surface backplates is the lack of reproducibility between devices. In an attempt to improve this as much as possible, a Struers ‘Planopol-3’ universal grinding, lapping and polishing machine was used to manufacture the backplates, in conjunction with a Struers ‘Pedemax-2’ sample moving

attachment. This partially automated the backplate surface preparation, and had the added advantage of ensuring that the sample was flat, as manual polishing techniques may produce a slightly convex surface, particularly at the sample edges. The recommended procedure [24] for grinding and polishing brass consisted of four grinding stages with SiC paste, and two final polishing stages, as shown in Table 4.1.

Six samples were prepared at the first grinding stage, with one sample being removed before progressing onto the next finer grade of SiC paper with three samples to keep the sample moving attachment in balance. After each grinding stage, the samples were thoroughly rinsed with water, and then placed in a Decon F51006 heated ultrasonic water bath for 3 minutes at 20°C to remove any loose particles. The final polish stage was also rinsed for 2 minutes with running water while still in the polishing machine. All the backplates were then cleaned with methanol to remove any remaining water, and dried with heated air to prevent tarnishing.

	Grinding				Polish
	Stage 1	Stage 2	Stage 3	Stage 4	Stage1
Abrasive	SiC	SiC	SiC	SiC	OP-U
Grit/Grain size	320#	800#	1200#	4000#	0.04μ
Disc/Cloth	Paper	Paper	Paper	Paper	OP-Chem
Lubricant	Water	Water	Water	Water	
Speed (rpm)	300	300	300	300	150
Pressure (N)	150	150	150	150	100
Time (sec)	30	30	30	30	120

Table 4.1: Grinding and polishing parameters for brass [24]

The surface properties of each backplate were then measured using a Taylor-Hobson Form Talysurf with a diamond stylus and He:Ne laser. The following surface properties for each of the backplates are shown in Table 4.2:

R_a	average roughness
R_{pm}	mean of maximum height points
R_{tm}	mean of maximum peak to valley heights
S	mean spacing of adjacent local peaks
S_m	mean spacing of profile peaks
λ_q	r.m.s. measure of the spatial wavelength

Backplate	R_a (μm)	R_{pm} (μm)	R_q (μm)	R_{tm} (μm)	S (μm)	S_m (μm)	λ_q (μm)
#320	0.577	2.258	0.757	4.760	17.689	31.209	32.628
#800	0.262	1.190	0.340	2.204	14.489	22.404	25.308
#1200	0.135	0.596	0.178	1.194	14.391	25.687	27.524
#4000	0.019	0.065	0.025	0.138	15.547	30.204	32.130
#0.04	0.049	0.127	0.063	0.380	17.397	30.775	31.086

Table 4.2: Selected surface properties for each backplate.

4.2.1 Experimental technique

The above backplates were tested in a transducer which could be fitted with several types of polymer membrane, and to which different bias voltages could be applied. A variety of films of different thickness and two materials were used. The polymers were Mylar (polyethylene terephthalate or PET), and Kapton (a polyimide). To investigate the effect of bias voltage, Kapton films of different thickness were used

to construct a series of transducers using the same backplate. When the devices were used as receivers, the Cooknell amplifier only allowed a maximum of 100V bias to be applied between membrane and backplate. However, by constructing a simple capacitive decoupling circuit shown schematically in Figure 4.2 to isolate the pulser unit from any bias voltage, the transducers could be used as sources of ultrasound with bias voltages of up to 1000V. A micromachined silicon capacitance transducer with a 2.5 μ m film and a bandwidth of up to 2MHz, as characterised previously in Chapter 2, was used as a broad band receiver for these experiments.

Preliminary experiments were performed using both a laser generated source as described previously, and a micromachined silicon device as a transmitter. It was found that there was no advantage in using the laser source, as the bandwidth of the metal backplate devices was well within the operating frequency range of the silicon device when used as a transmitter. In fact the micromachined device gave more consistent waveforms, and there was also more signal energy available as the silicon transmitter generated ultrasound directly into air, rather than in a solid material as with the laser.

It was therefore decided to conduct the experiments using a silicon micromachined transducer with a 7.6 μ m Kapton membrane to generate the ultrasound in air. The apparatus used is shown schematically in Figure 4.3, and is very similar to that used for the laser experiments in previous chapters, except that the source of ultrasound was an air-coupled transducer driven by a Panametrics 5055PR pulser/receiver unit. For more detailed equipment specifications, see Appendix A. The capacitive decoupling circuit allowed bias voltages of up to 350V to be applied to the silicon transducer, which was the maximum recommended by their manufacturer.

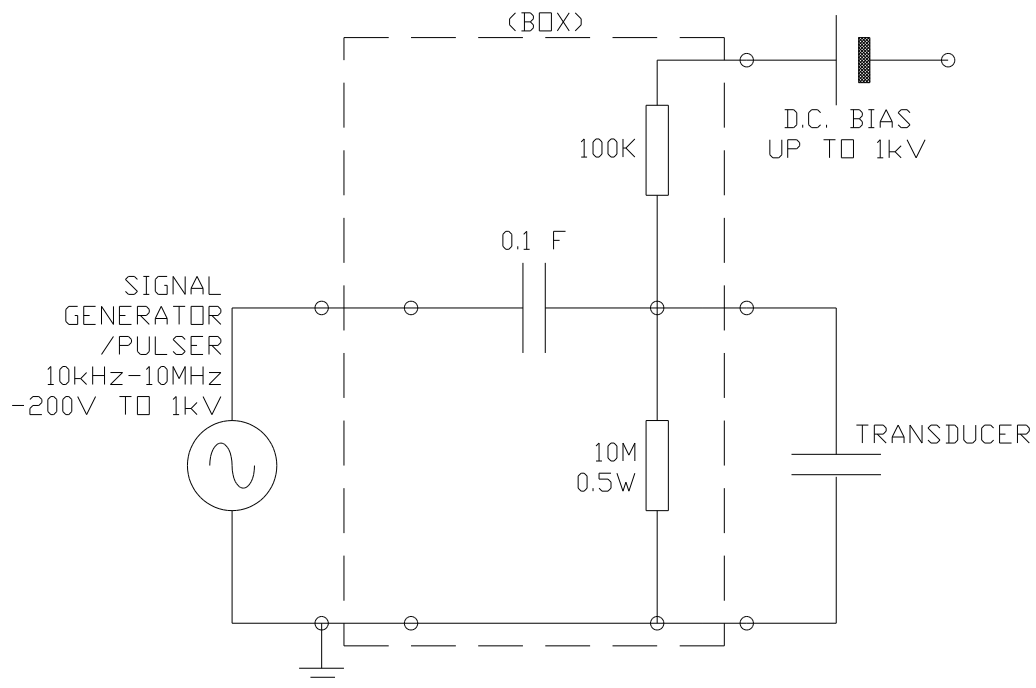


Figure 4.2: The capacitive decoupling circuit.

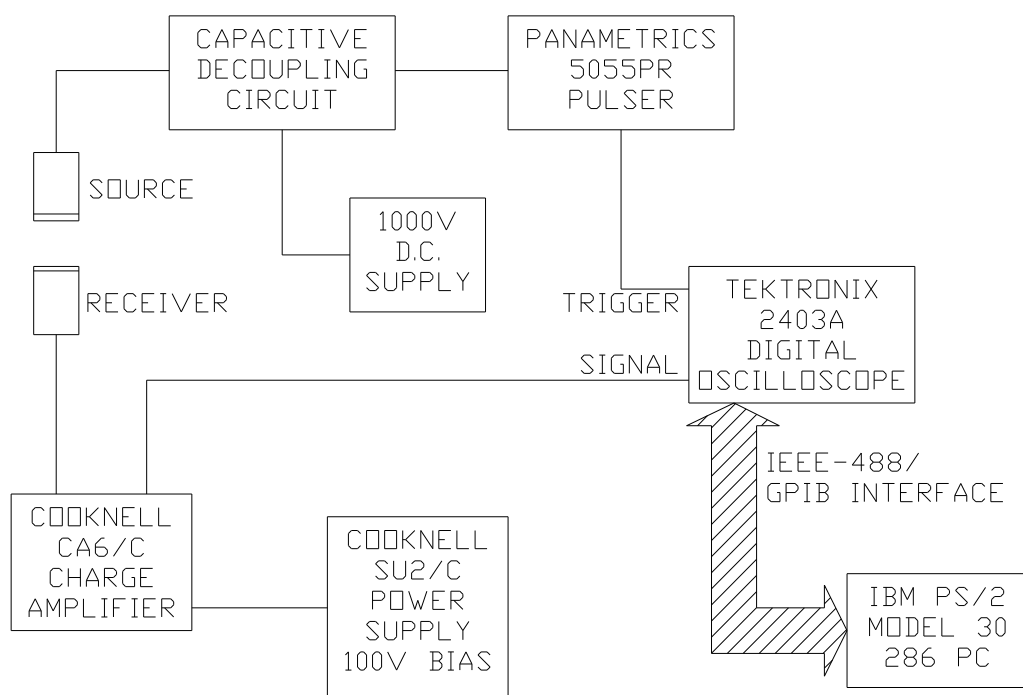


Figure 4.3: Schematic diagram of the experimental apparatus.

4.2.2 The effects of backplate surface properties

In this first series of experiments, receivers were assembled using each of the different backplates, and a 6 μ m Mylar film, which was the thinnest that could be consistently and reliably used without arcing on the Cooknell amplifier. Using the silicon transducer as a source, waveforms transmitted across a 20mm air gap were captured and analysed. The signal obtained for the #1200 transducer is shown in Figure 4.4(a), with the corresponding frequency spectrum shown in Figure 4.4(b). These plots are typical for all the different backplates, showing a well damped response with a wide bandwidth. The frequency spectra for all the backplates are shown on a single pair of axes for comparison, with Figure 4.5(a) showing arbitrary relative amplitude, and Figure 4.5(b) showing the plots normalised to the maximum amplitude in each FFT. From Figure 4.5(a) there is clearly a relationship between frequency and sensitivity. A plot of 3dB bandwidth against sensitivity, as shown in Figure 4.6, shows that the values are consistent with a linear relationship, with the sensitivity decreasing with increasing bandwidth, as might be expected. The straight line shown is a least squares best fit, with a coefficient of determination (R^2) of 0.9898.

The frequency response of each device was then plotted against each of the surface roughness properties shown earlier in Table 4.2. As many of these properties are very closely related, a large number of graphs were virtually identical and will therefore not be shown here. Figure 4.7 shows the relationship between $1/\sqrt{R_a}$ (which is representative of the other ‘amplitude’ surface properties R_q , R_{pm} , and R_{tm}) and (a) 3dB bandwidth, (b) sensitivity and (c) centre 3dB frequencies. There would appear to be a linear relationship between the inverse square root of the surface roughness and

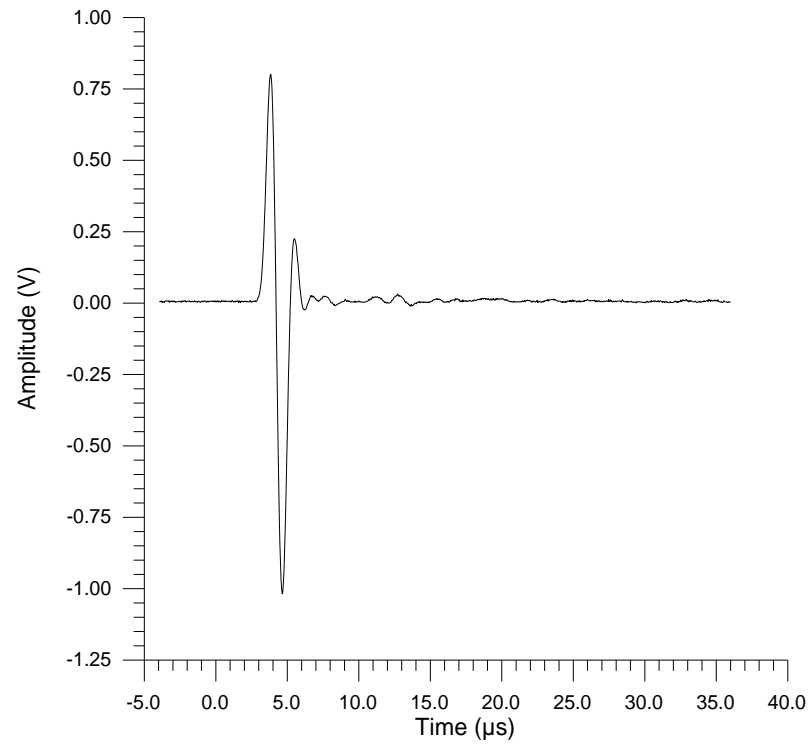


Figure 4.4(a): Typical air-coupled waveform using the silicon transducer source, received by the #1200 backplate filmed with 6µm Mylar.

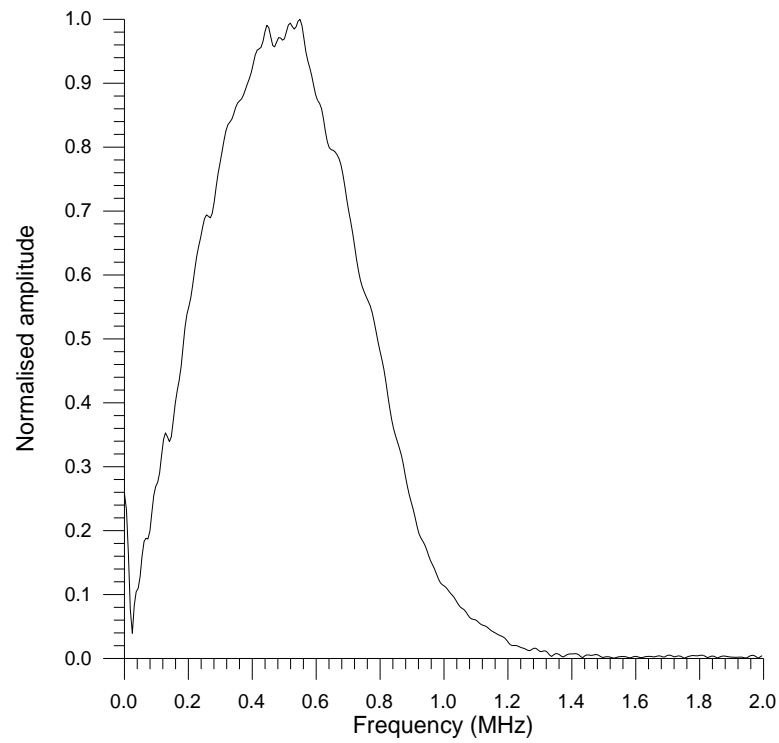


Figure 4.4(b): Frequency spectrum of Figure 4.4(a).

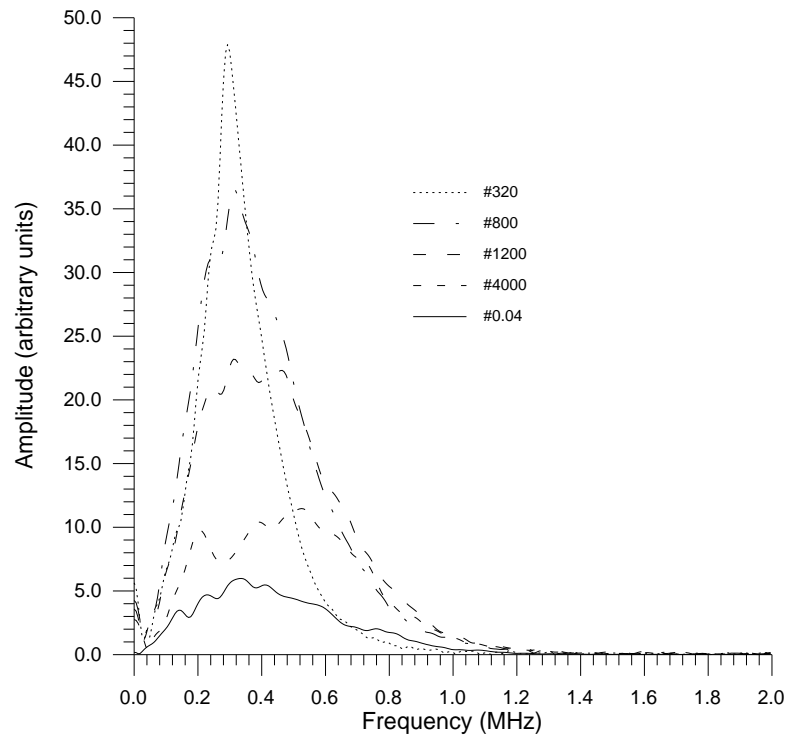


Figure 4.5(a): Comparison of frequency spectra for all brass backplates, showing their relative sensitivity.

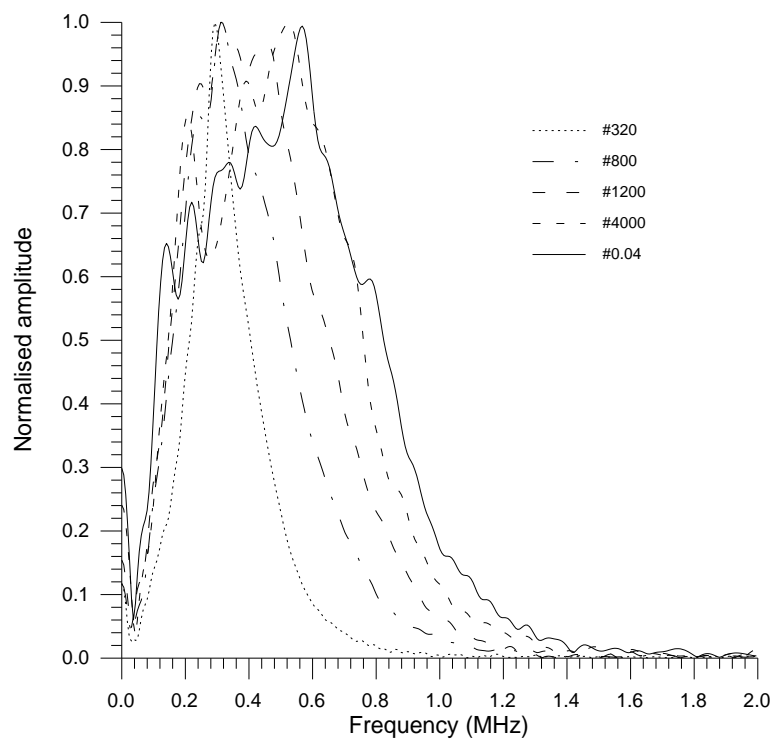


Figure 4.5(b): Comparison of normalised frequency spectra for all brass backplates, showing their relative bandwidth.

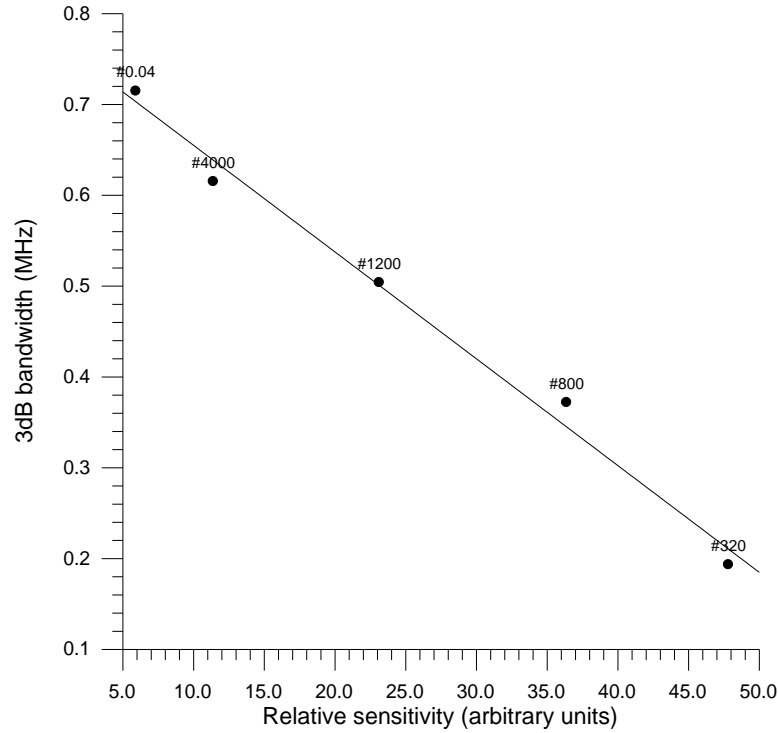


Figure 4.6: Plot of bandwidth against sensitivity for all brass backplates.

the frequency characteristics of the receiver, as stated earlier in equation {4.1} and shown in earlier work [17]. It is interesting to note that the frequency and sensitivity of the #4000 backplate were consistent with the trend of the other backplates, but that the surface properties were not - it is likely that this is due to an erroneous reading from the Talysurf. The least squares best fits have coefficients of determination (R^2) of 0.676, 0.602 and 0.716 for Figures 4.7(a), (b) and (c) respectively when all the data points are used, and 0.972, 0.960 and 0.976 when the #4000 data is omitted.

Figure 4.8 shows a plot of $1/\sqrt{S_m}$ (which is representative of the other 'spatial' surface properties S and λ_q) against sensitivity. The value of S_m ($31.2\mu\text{m}$) for the #320 backplate was not consistent with the trend observed for the rest of the backplates, and again was probably an erroneous Talysurf measurement. The least squares best fit gave values of coefficients of determination (R^2) of 0.0785 when all data points were used,

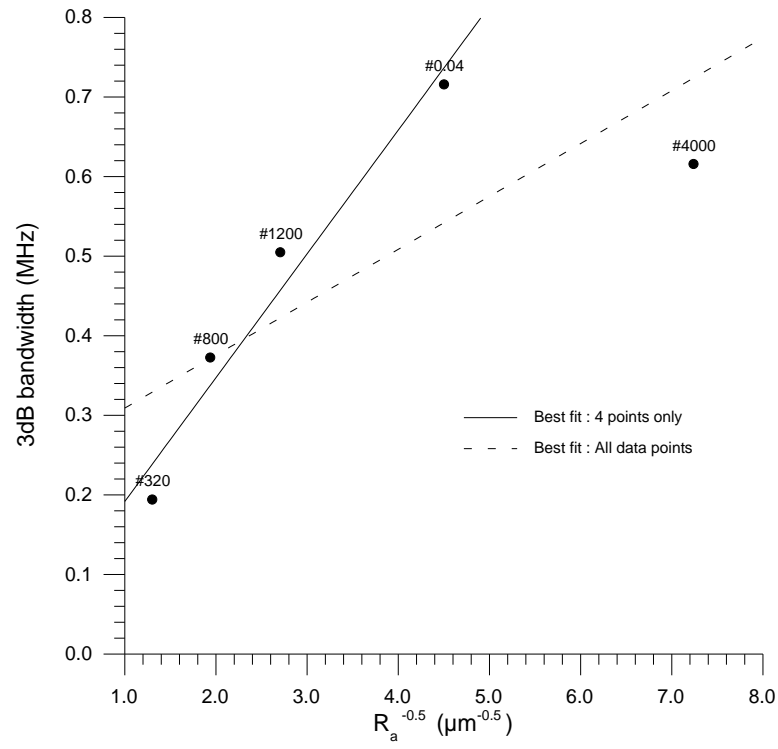


Figure 4.7(a): Plot of 3dB bandwidth against $1/\sqrt{R_a}$.

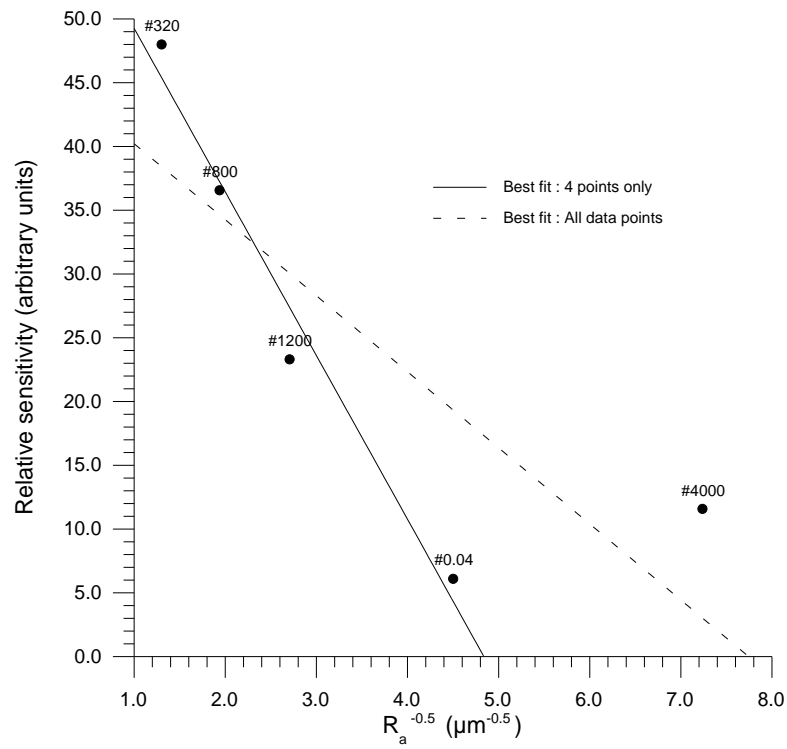


Figure 4.7(b): Plot of relative sensitivity against $1/\sqrt{R_a}$.

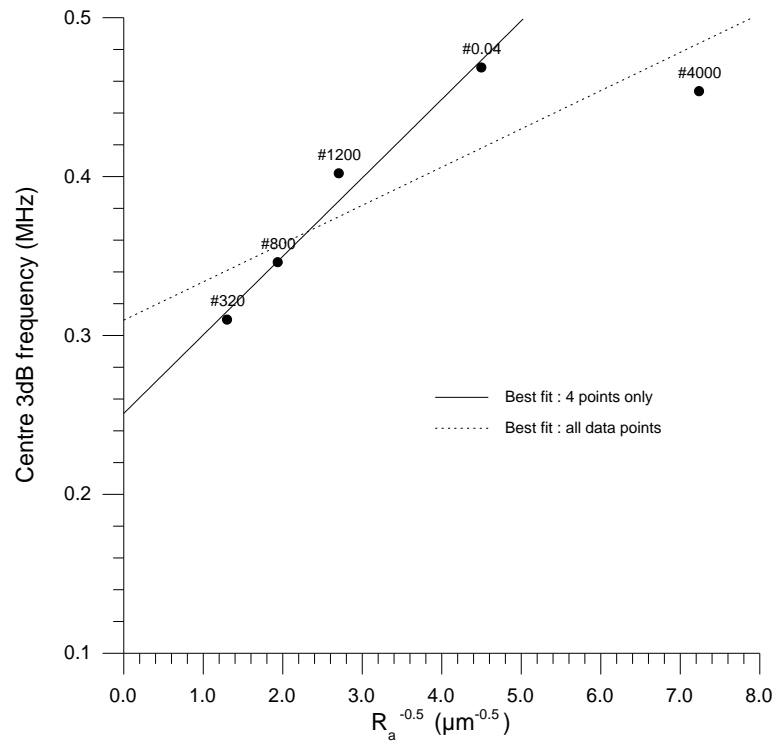


Figure 4.7(c): Plot of centre 3dB frequency against $1/\sqrt{R_a}$.

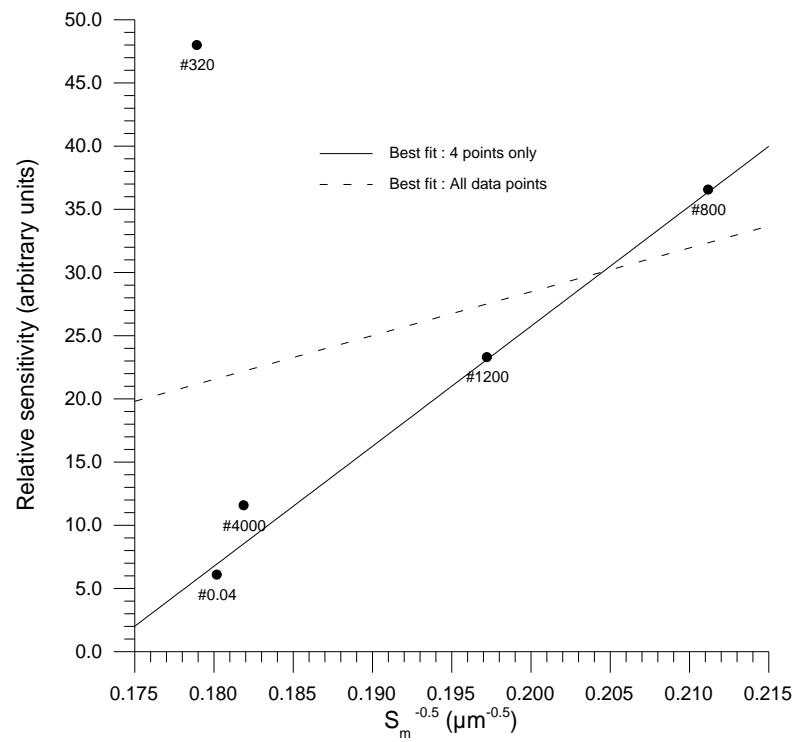


Figure 4.8: Plot of relative sensitivity against $1/\sqrt{S_m}$.

and 1.000 when the #320 data point was omitted. A similar plot of $1/S_m$ gave coefficients of 0.0665 and 0.955 respectively. These results are also consistent with previous work [17] on the same subject.

4.2.3 The effects of polymer film thickness

To investigate the effect of changing the polymer film thickness, a range of transducers was constructed using the #1200 backplate and various films, ranging from $5\mu\text{m}$ to $25\mu\text{m}$ of either Mylar or Kapton. Each transducer was then used as a receiver of ultrasound generated by the micromachined silicon device. Figure 4.9 shows the normalised frequency spectra for (a) the Kapton films and (b) the Mylar films that were available. There was also a $2.5\mu\text{m}$ Mylar film, but due to the design of the transducer casing it was not possible to construct a transducer without breaking the film. Figure 4.10 shows plots of the inverse square root of film thickness against (a) 3dB bandwidth and (b) the upper, lower and centre 3dB frequencies, and there appears to be a linear relationship, with the thinner films making wider bandwidth devices. The coefficient of determination (R^2) for the least squares best fit in Figure 4.10(a) was 0.972, and for Figure 4.10(b) the values were 0.972, 0.891 and 0.382 for the upper, centre and lower 3dB frequencies respectively. These results are consistent with earlier work [17]. Figure 4.10(c) shows a plot of relative sensitivity against film thickness, and the linear relationship seen previously [17] is not evident. One would expect that a transducer made with a thinner film would be the most sensitive, but this is not the case. It is possible that the sensitivity of a transducer may be optimised by matching the film

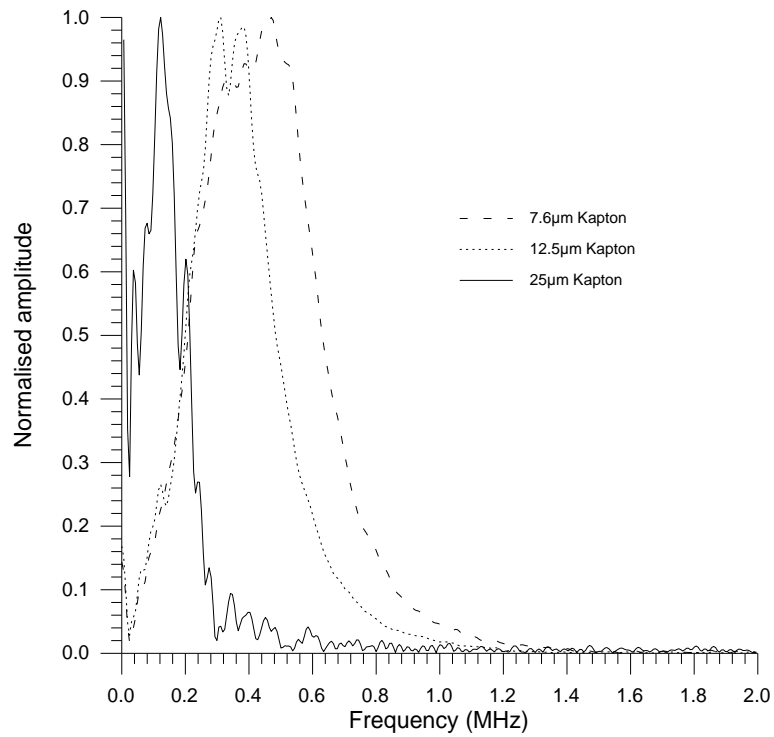


Figure 4.9(a): Frequency response using different Kapton polyimide films.

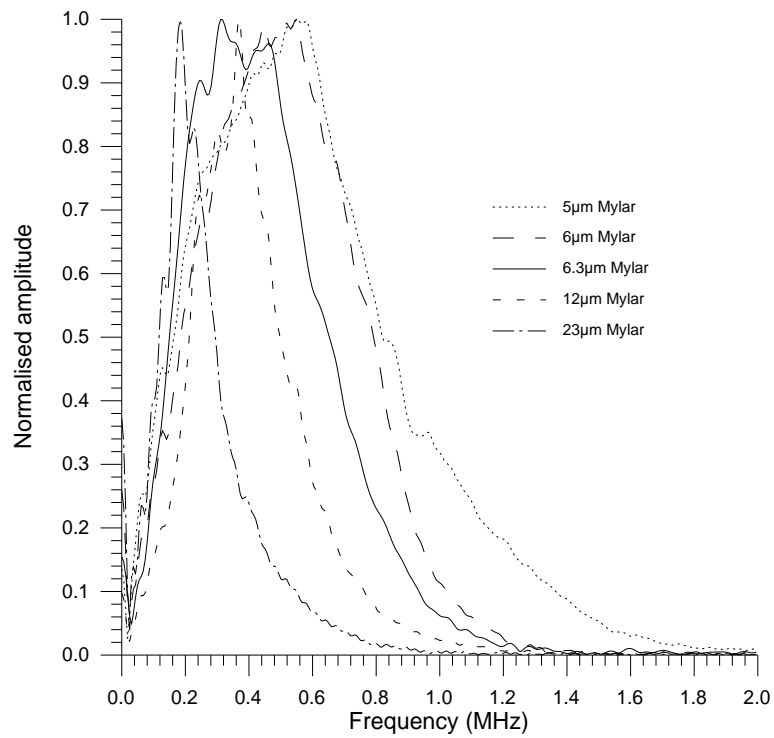


Figure 4.9(b): Frequency response using different Mylar polyethylene terephthalate (PET) films.

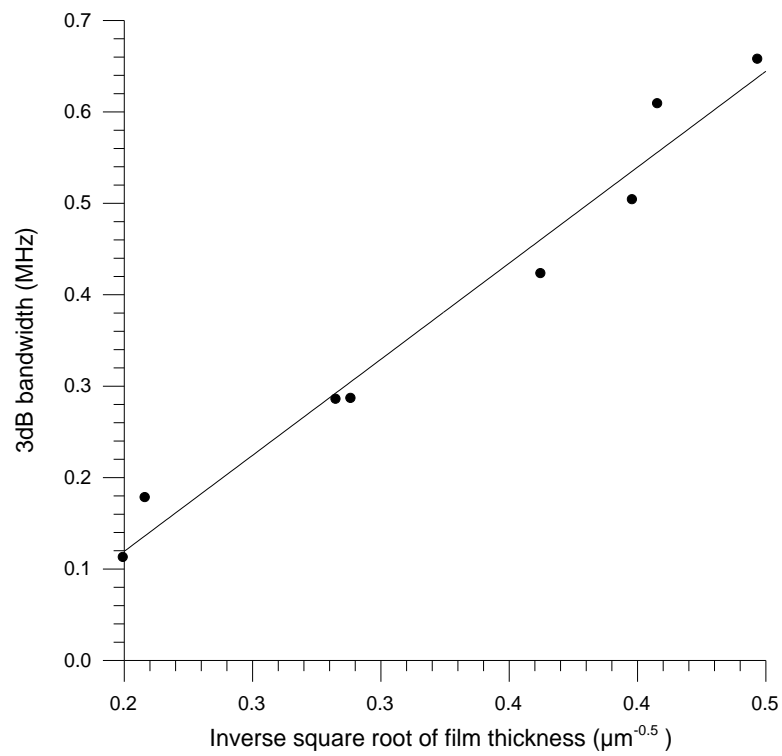


Figure 4.10(a): Plot of inverse square root of film thickness against 3dB bandwidth.

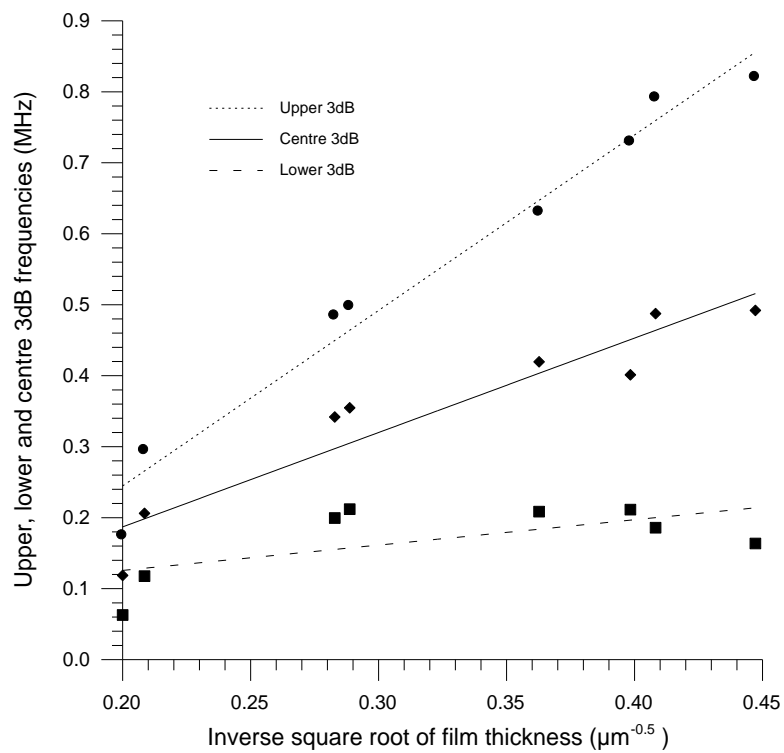


Figure 4.10(b): Plot of inverse square root of film thickness against upper, lower and centre 3dB frequencies.

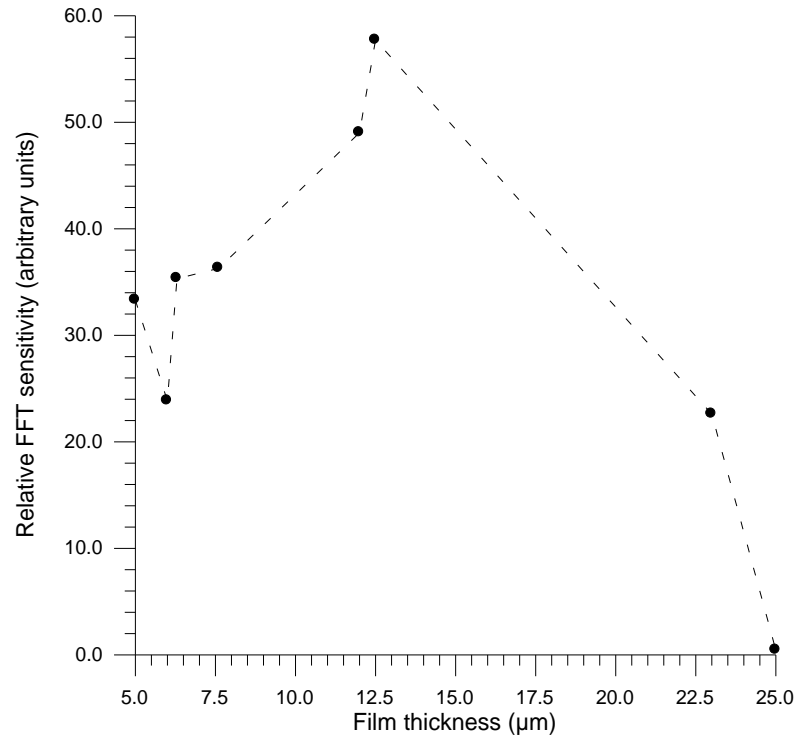


Figure 4.10(c): Plot of film thickness against sensitivity.

thickness to the roughness of the backplate. For the #1200 backplate used, using a film thinner than 7.6μm did not appear to increase the sensitivity.

4.2.4 The effects of applied bias voltage

To investigate the effects of bias voltage, a transducer was constructed with the #1200 backplate and 12.5μm Kapton film. Bias voltages of up to 1000V in steps of 50V were applied to the source, and waveforms were received by the silicon transducer with 100V bias and a 2.5μm thick film. Figure 4.11(a) shows the frequency spectra obtained when the bias voltage is increased (shown every 250V for clarity), and the curves may be explained as follows. At 0V bias, the film is lightly resting on the backplate and is undamped, so the frequency response is quite resonant and is

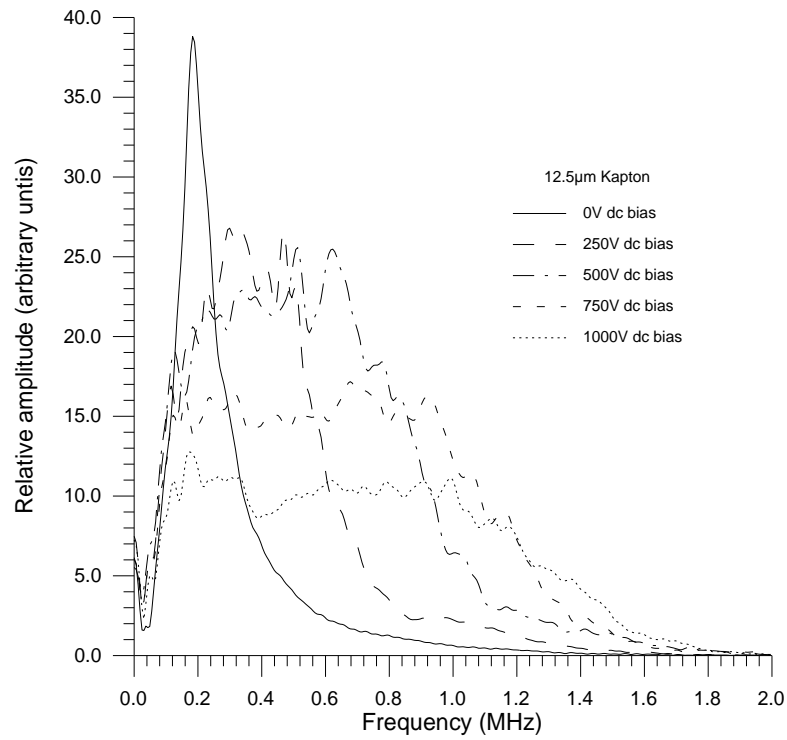


Figure 4.11(a): Change in frequency response of the #1200 backplate filmed with 12.5µm Kapton when the bias voltage is increased up to 1000V d.c.

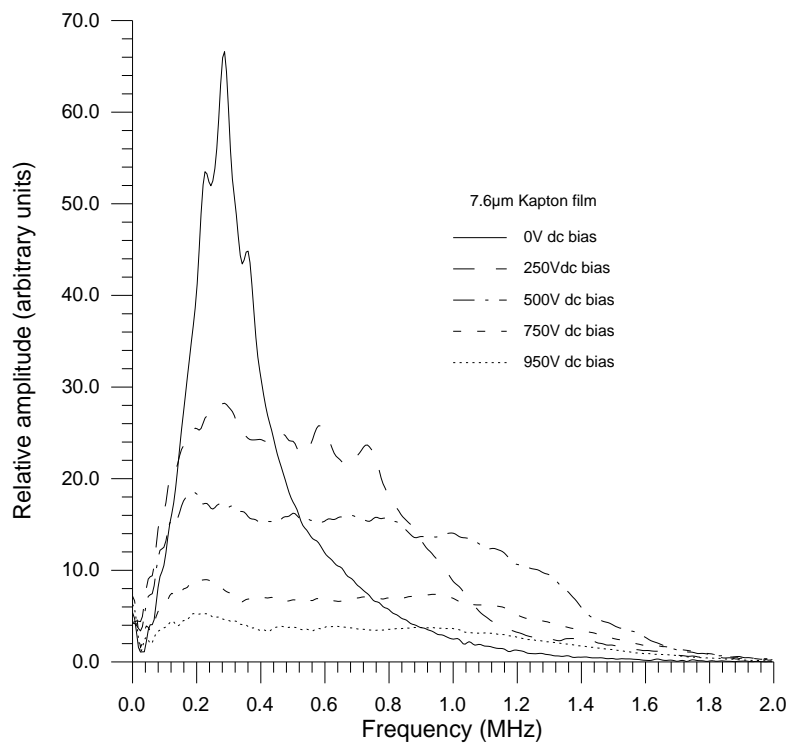


Figure 4.11(b): Change in frequency response of the #1200 backplate filmed with 7.6µm Kapton when the bias voltage is increased up to 1000V d.c.

affected little by the surface properties of the backplate. As the bias voltage is applied, the film is attracted to the backplate and becomes stiffer or tensioned. The amplitude decreases as the film cannot move as far due to the electrostatic attraction, and its motion becomes damped thus increasing the overall bandwidth of the device. At increasing values of dc bias, the characteristics of the backplate surface begin to take more of an effect, and at a bias of 1000V, it would appear that there are two separate peaks making up the frequency spectrum - the lower frequency peak is caused by the properties of the film (mass and thickness), while the flat portion of the spectrum at high frequencies is due to the surface of the backplate. These assumptions may be verified by the plot shown in Figure 4.11(b), which shows a similar situation for the same transducer made with a 7.6 μ m film. Again there is a resonant peak when 0V bias is applied, only it is at a higher frequency (\sim 300kHz as opposed to \sim 200kHz for the 12.5 μ m film) due to the reduced mass of the membrane. The high frequency response, however, has similar characteristics for either film.

Figures 4.12(a) shows a plot of the 3dB bandwidth against applied bias voltage, for both the 7.6 μ m and 12.5 μ m films. It would appear that there is an optimum bias voltage for the 7.6 μ m film, after which no increase in bandwidth is obtained. It is possible that there is a similar voltage for the 12.5 μ m film, but this appears to be in excess of the maximum d.c. available from the supply. Figure 4.12(b) shows a plot of sensitivity against bias voltage, and it can be seen that there is an optimum voltage for both films (350V and 250V for the 7.6 μ m and 12.5 μ m thick films respectively). The minimum at 100V for both films may have been caused by residual charge in the films, or perhaps the bias voltage was insufficient to force the cushion of air from between the film and backplate. Note that the devices had approximately the same sensitivity when a bias voltage was applied, even though the

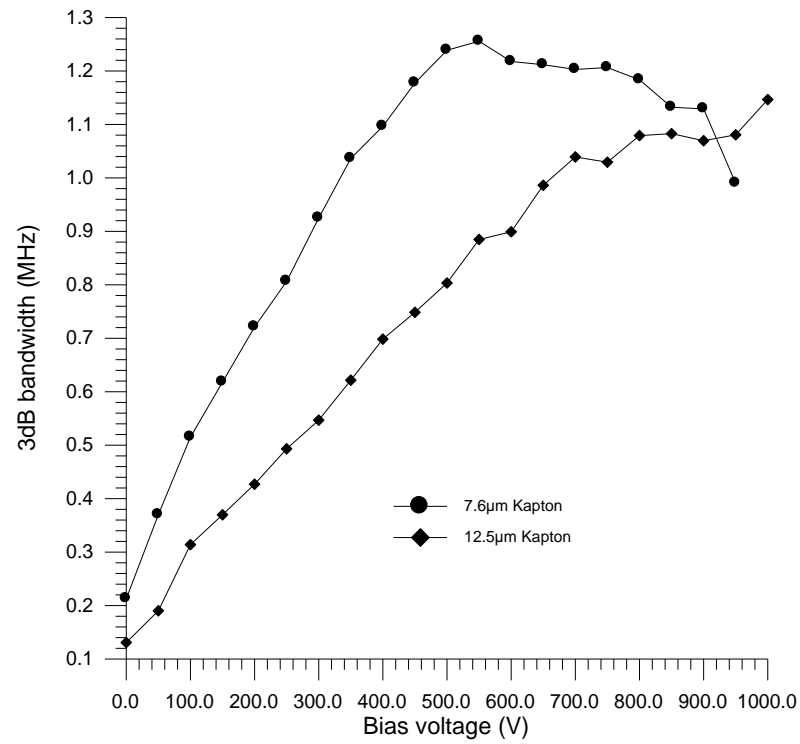


Figure 4.12(a): A plot of 3dB bandwidth against bias voltage for both the 7.6μm and 12.5μm Kapton films.

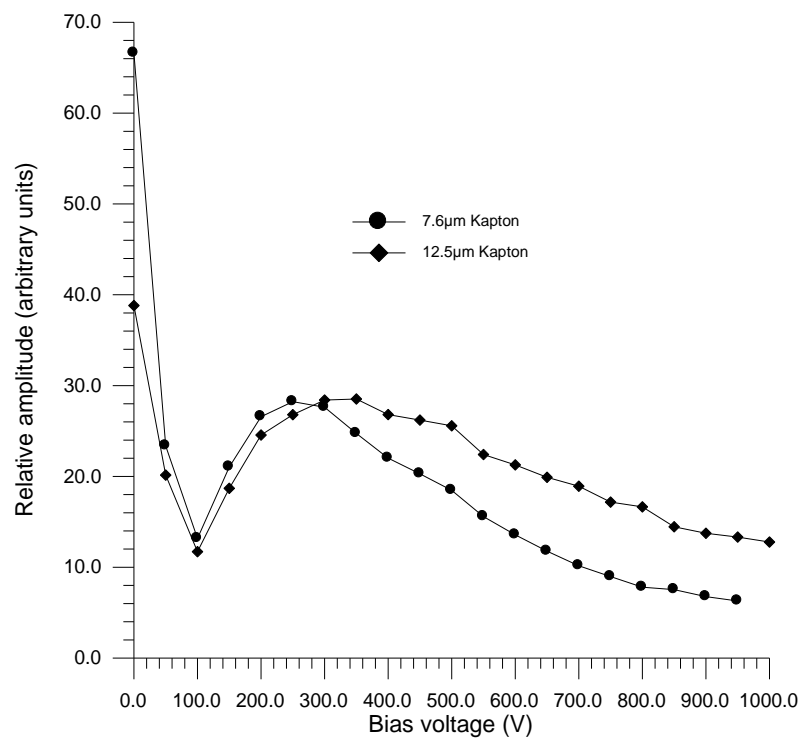


Figure 4.12(b): Plot of sensitivity against bias voltage for both the 7.6μm and 12.5μm Kapton films.

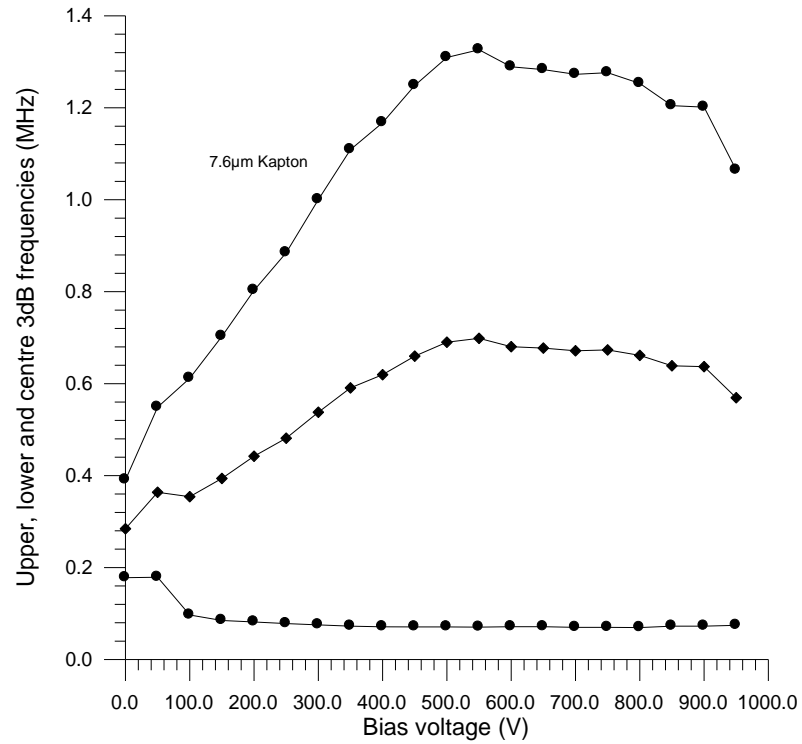


Figure 4.13(a): Plot of upper, lower and centre 3dB frequencies against bias voltage for the 7.6µm Kapton film.

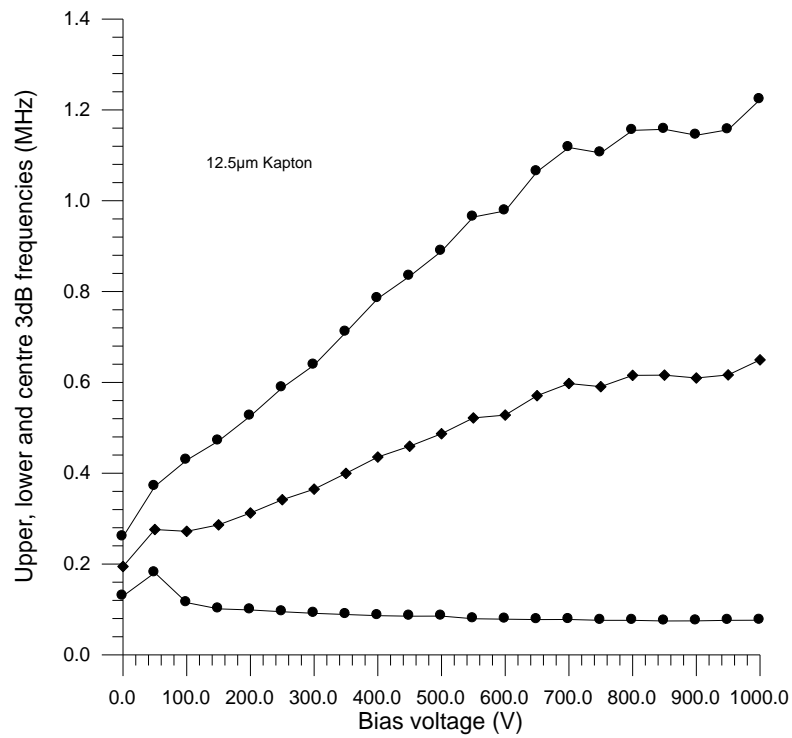


Figure 4.13(b): Plot of upper, lower and centre 3dB frequencies against bias voltage for the 12.5µm Kapton film.

polymer film thickness was different. Figure 4.13(a) and (b) show the upper, lower and centre 3dB frequencies for the two different films. The lower frequency limit seems to remain virtually constant when the bias voltage increases. Previous work [17] on the effect of bias voltage only showed results up to 250V and just over 100kHz, and one film thickness, and the frequency response was seen to flatten out after 180V.

4.2.5 Repeatability between ‘identical’ devices

One of the problems cited in the literature which may have prevented more widespread use of capacitance devices with mechanically manufactured backplates has been the lack of reproducible results between devices. This has been investigated previously [11,12] by measuring the characteristics of a single transducer over several hours of continuous operation. To see if different capacitance devices made using an identical process had similar characteristics, three identical transducers were manufactured using #4000 backplates and 12.5 μ m Kapton film. These devices were then used as sources with an applied bias voltage of 200V, and the silicon transducer was used as the receiver. Figure 4.14 shows (a) the received waveforms and (b) the frequency spectra of all three devices superimposed onto one set of axes for comparison. It would appear that there are small differences between the transducers.

Figures 4.15(a) to (c) show the beam plots for each of the three devices. Each plot was obtained by scanning the silicon capacitance receiver, fitted with a 1mm aperture, in the field of the source. There are some near field features which differ between transducers, but the far field region of each plot is virtually identical. It would appear that the automated grinding and polishing process has produced consistently flat backplates, but it is unrealistic to expect that the characteristics of the devices

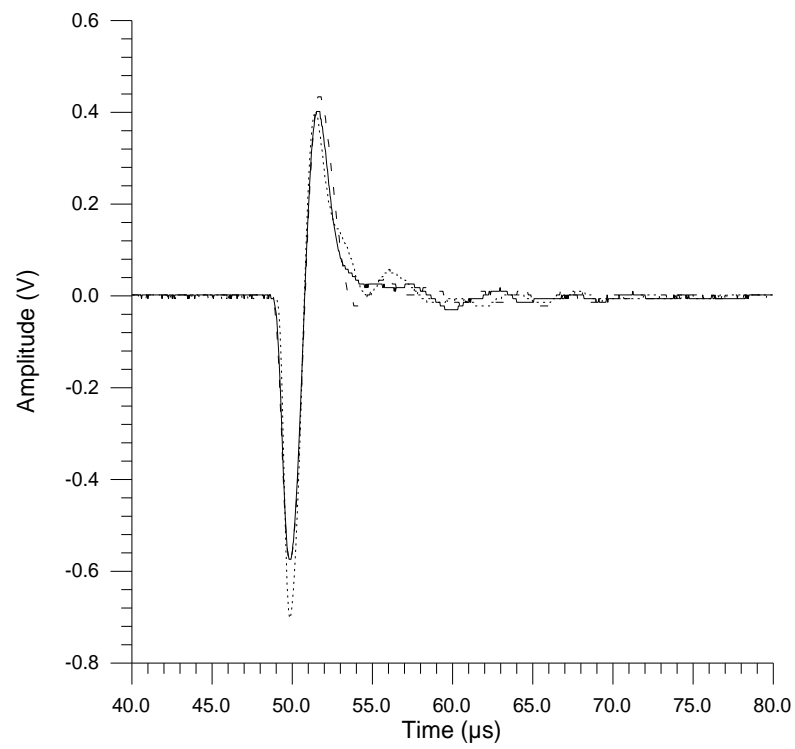


Figure 4.14(a): Received waveforms for three 'identical' devices.

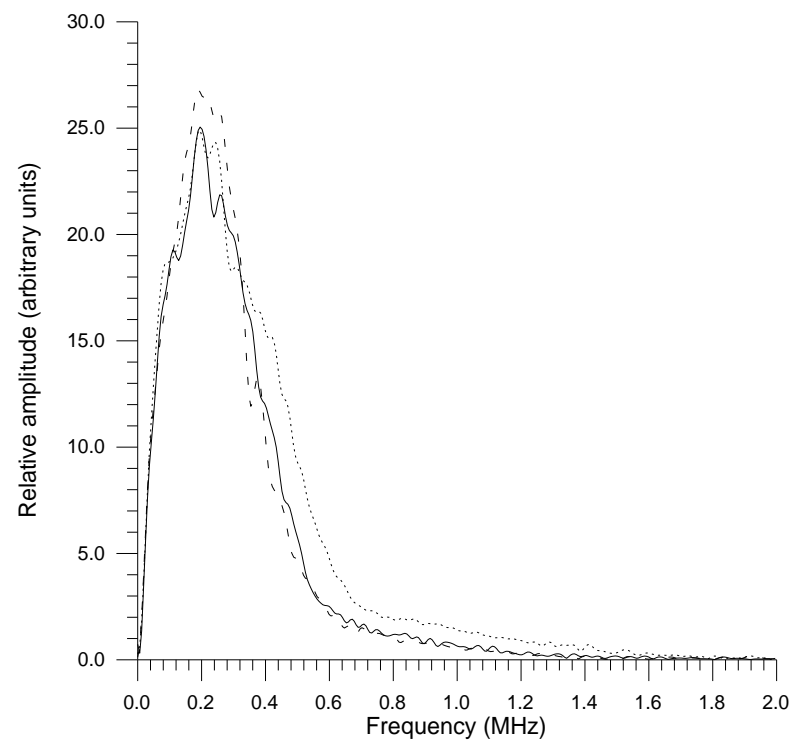


Figure 4.14(b): Frequency spectra for the three 'identical' devices.

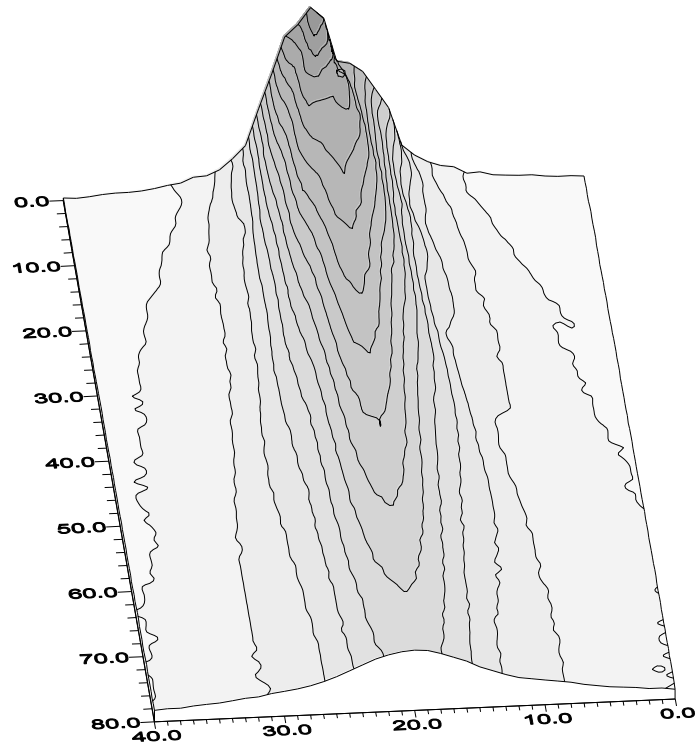


Figure 4.15(a): Beam plot for transducer 'a'.

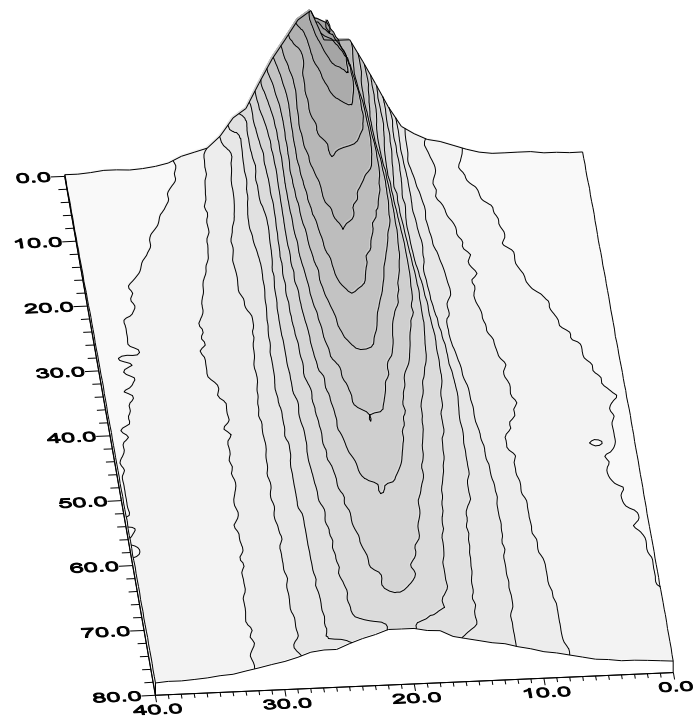


Figure 4.15(b): Beam plot for transducer 'b'.

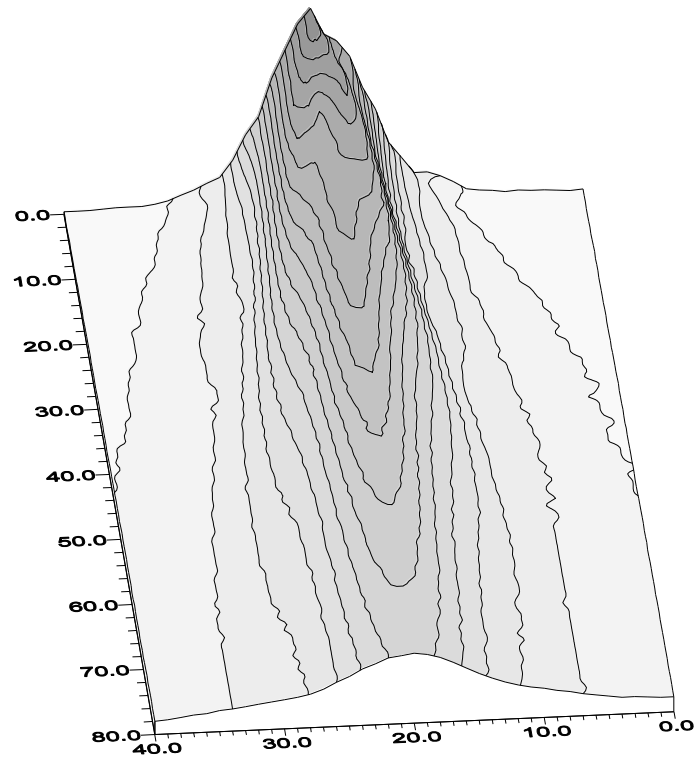


Figure 4.15(c): Beam plot for transducer 'c'.

would be identical. The design and construction of the transducers allows other unknown variables to take an effect. The backplate surface properties may change due to damage during assembly, or as particles of dust and dirt become trapped between membrane and backplate. There is also uneven clamping of the film between electrode and casing, resulting in the asymmetrical beam profiles as seen in Figure 4.15. It is also possible that the membrane may move slightly with time during operation if not uniformly clamped around the edges.

4.2.6 Comparison with the theoretical frequency response

Using the constant values shown in Table 4.3, the theoretical frequencies for the various ‘amplitude’ surface properties were calculated using equation {4.1} and are shown in Table 4.4. The theoretical frequencies for the same backplate (#1200) but different thickness of film are shown in Table 4.5, and compared to the measured 3dB bandwidth and centre frequency (midpoint of the 3dB limits).

It can be seen from the data in Tables 4.4 and 4.5 that the theoretical values for the resonant frequencies do not match the measured frequency responses of the devices. Previous work [17] found that using R_{pm} as the air gap approximation gave good agreement up to about 600kHz, but the devices were operating in a resonant rather than pulsed mode. Equation {4.1} is for resonant frequencies, yet the broadband frequency responses used here may be calculated in a number of ways, e.g.: using the 6dB limits instead of 3dB. It is possible that the mass and inherent rigidity of the polymer film used was masking the surface properties of the backplate, and that the film conforms more to the shape of the surface as the membrane becomes more flexible. The differences between the experimental and theoretical frequencies, as shown in Table 4.5, appear to reduce as the film thickness decreases.

γ for air	P_a (GPa)	ρ (kg.m ⁻³)	t_f (μm)
1.4	0.10135	1350	6.0

Table 4.3: Values of constants for theoretical frequency response.

Device	Frequency response (MHz)		Theoretical resonant frequency (MHz)			
	bandwidth	centre	R _a	R _{pm}	R _q	R _{tm}
320#	0.192	0.309	0.876	0.443	0.765	0.305
800#	0.371	0.345	1.276	0.610	1.141	0.449
1200#	0.503	0.401	1.811	0.862	1.577	0.610
4000#	0.614	0.453	4.827	2.610	4.209	1.793
0.04μ	0.714	0.468	3.006	1.867	2.651	1.081

Table 4.4: Theoretical resonant frequencies and measured frequency response for a 6.0μm film calculated using different surface properties.

Film (μm)	Frequency response (MHz)		Theoretical resonant frequency (MHz)			
	bandwidth	centre	R _a	R _{pm}	R _q	R _{tm}
5.0	0.657	0.492	1.984	0.944	1.728	0.668
6.0	0.608	0.487	1.811	0.862	1.577	0.610
6.3	0.503	0.401	1.767	0.841	1.539	0.595
7.6	0.422	0.419	1.609	0.766	1.401	0.542
12.0	0.286	0.355	1.282	0.610	1.116	0.431
12.5	0.285	0.342	1.255	0.597	1.093	0.422
23.0	0.177	0.206	0.925	0.440	0.806	0.311
25.0	0.112	0.119	0.887	0.422	0.773	0.299

Table 4.5: Predicted transducer frequencies and measured frequency response for a #1200 backplate and various films.

4.3 Manufacture of metallic backplates by chemical etching

The basic backplates were machined from 0.5” diameter copper bar. The backplates were then ground and polished using the same Struers ‘Pedemax-2’ and ‘Planopol-3’ machines and grinding parameters as for the brass backplates, but using the parameters shown in Table 4.6 for the polishing stages. The samples were rinsed and cleaned between each stage in the Decon F15006 ultrasonic bath as before. The highly polished backplates were then placed on the Taylor-Hobson Form Talysurf to determine their surface profile and properties, shown in Table 4.7.

The backplates were then prepared for etching using standard photolithography techniques. A 4µm layer of Shipley-Europe ‘Microposit’ photoresist TF-16 (containing acetate, ethyl glycol and xylene) was spun onto each of the polished copper backplates, using 2 drops of photoresist and spinning for 15 seconds. The layer of photoresist was then soft baked in a furnace at 90°C for 5 minutes in preparation for exposure to ultraviolet light. The photolithography mask was the same one used to manufacture the silicon devices mentioned in a previous chapter, and was manufactured by PPM Photomask Inc., Quebec, Canada. It consisted of a grid of 10mm by 10mm square sections, each containing a regularly spaced pattern of circular holes, square holes, or lines, all of various size and spacing. In the previous work by Schindel *et al.* [20], the authors were not able to clearly determine the relationship (if any) between the hole dimensions (diameter, depth and spacing) and the frequency response of the device. In an attempt to investigate this further, a selected range of masks with circular holes were used, as shown in Table 4.8. One of the backplates was not used so that a comparison could be made with a flat unetched backplate.

	Polish		
	Stage 1	Stage 2	Stage 3
Abrasive	Diamond	Diamond	OP-U
Grit/Grain size	3 μ m	1 μ m	0.04 μ
Disc/Cloth	DP-Mol	DP-Nap	OP-Nap
Lubricant	Red	Red	-
Speed (rpm)	150	150	150
Pressure (N)	120	90	90
Time (sec)	180	60	120

Table 4.6: Polishing parameters for copper [24].

R_a (μ m)	R_{pm} (μ m)	R_q (μ m)	R_{tm} (μ m)	S (μ m)	S_m (μ m)	λ_q (μ m)
0.010	0.046	0.013	0.087	13.697	26.380	29.256

Table 4.7: Surface properties for the copper backplates.

Hole diameter (μ m)	Hole spacing between centres (μ m)
10	20
20	40
30	60
40	60
40	80

Table 4.8: Hole dimensions on the photolithography masks.

The copper backplates were then etched in a solution of 50g ammonium persulphate in 350ml of water, maintained at 50°C in a heated water bath. In order to determine the etch rate of the copper bar used, a piece of the original bar was progressively immersed in the etchant for periods of 2 minutes, and then measured on the Taylor-Hobson Form Talysurf. From these measurements it was calculated that the etch rate was 4-5µm/minute. The range of backplate hole sizes was intended to show what effect the hole diameter and spacing would have on the frequency response of each device, as the depth would be kept constant. In order to investigate the effect of hole depth, two backplates with the same hole spacing but different hole diameters (30x60 and 40x60) were etched for different lengths of time until the holes were approximately the same diameter, but of different depths.

Photographs of the etched backplates are shown in Figures 4.16(a) to (f). Figure 4.16(a) shows the 30x60 mask after etching and is typical of all the backplates prepared. The photograph shows the pale area of polished copper beneath the layer of photoresist, and a regular array of circular features. Each feature consists of a dark central hole penetrating the layer of photoresist and on into the underlying copper substrate, surrounded by a pale annulus of undercut mask.

The mask was then removed by washing the backplates in acetone, and then rinsing firstly with water and finally with methanol before drying with hot air. With the mask layer removed, the surface of each backplate may now be seen in greater detail. Figure 4.16(b) shows the 30x60 backplate with the mask removed, with the other backplates being shown in Figures 16(c) to (f). All the holes are well defined, with the exception of Figure 4.16(f) for the 10x20 mask which moved during the etching process due to excessive undercutting, and Figure 4.16(b) for the 30x60 mask.

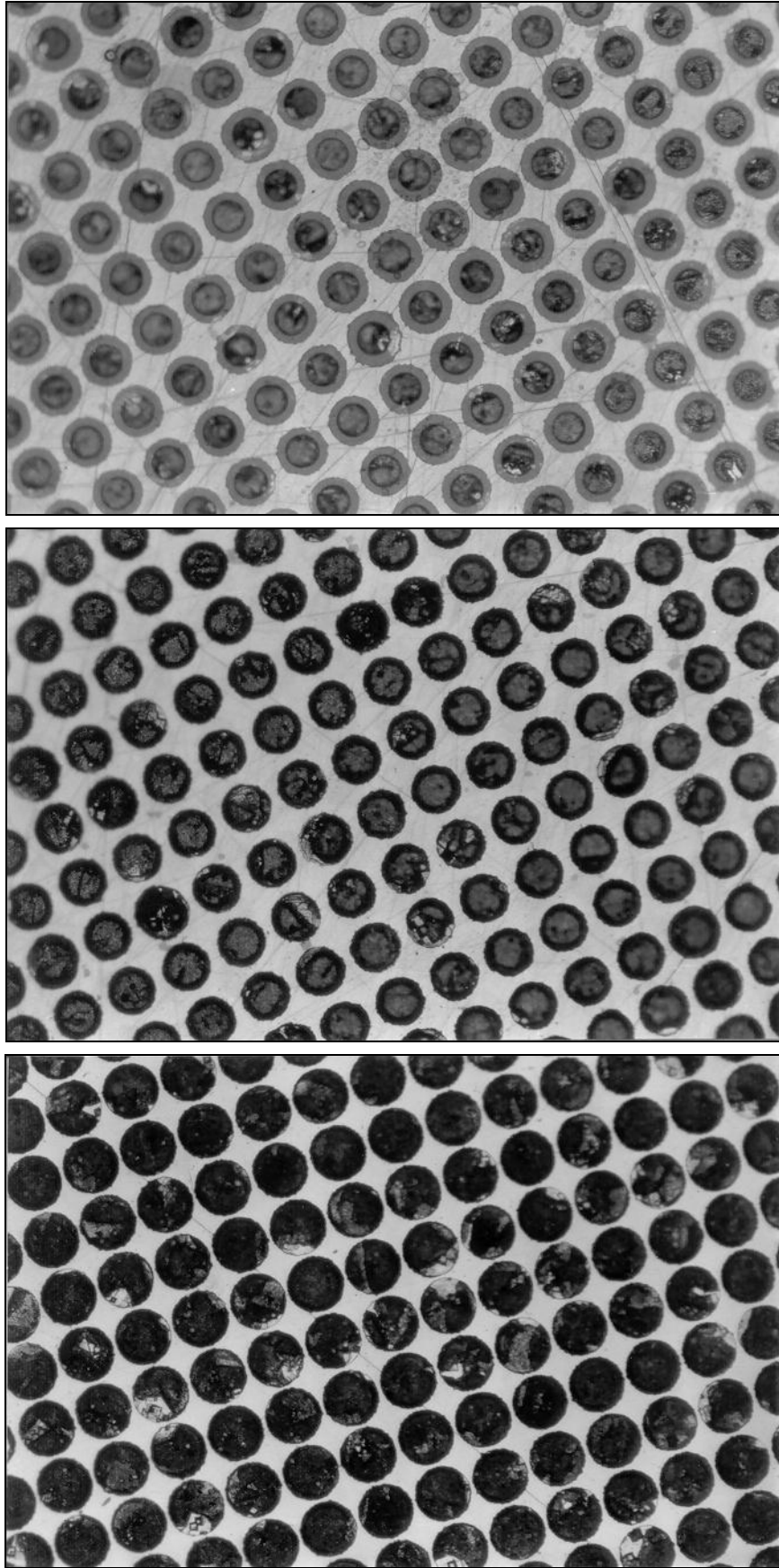


Figure 4.16: Etched backplates (a) with photoresist for the 30x60 mask, and without photoresist for (b) the 30x60 and (c) the 40x60 mask sizes. Scale 1mm:6.85 μ m

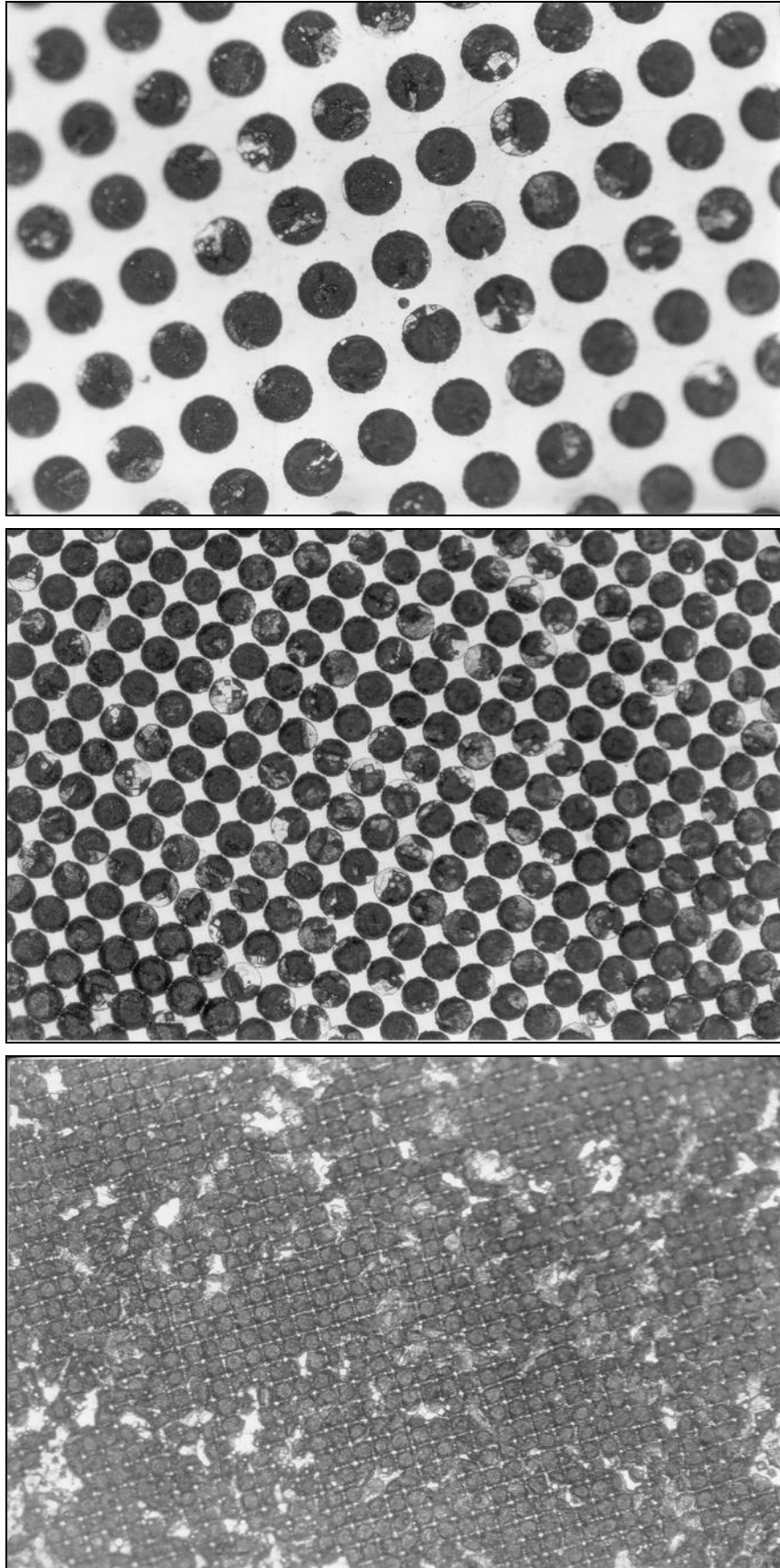


Figure 4.16: Etched backplates with the photoresist removed for (d) the 40x80, (e) the 20x40 and (f) the 10x20 mask sizes. Scale 1mm:6.85 μ m

Mask	Mask diameter (μm)	Mask spacing (μm)	Etched diameter (μm)	Etch rate ($\mu\text{m}/\text{min}$)
10x20	13.8	19.0	N/A	N/A
20x40	26.5	39.5	37.4	5.45
30x60	32.3	59.2	47.6	5.10
40x60	46.3	59.2	54.4	4.05
40x80	46.3	81.0	58.5	6.10

Table 4.9: Mask and hole dimensions for each of the copper backplates.

This backplate was etched for a longer time to try and obtain two backplates with holes of identical diameter and spacing, but different hole depths. The hole edges are therefore slightly rougher, as the etchant has had longer to remove copper along the crystal boundaries. The diameters of the holes were measured from the photographs in Figures 4.16 and are shown in Table 4.9 for the various masks.

It is evident from the dimensions shown in Table 4.9 that the hole diameters in the deposited layer of photoresist are different to those on the photolithography mask, whereas the hole spacing is virtually identical. This was due to the ultraviolet light diffusing around the edges of the photoresist layer and blurring the feature edges. In addition, the ultraviolet light source was not uniform in intensity, and the masks were probably slightly overexposed in some areas.

The depths of the holes were then measured using the Taylor-Hobson Talysurf. Figure 4.17 shows typical surface profiles obtained for (a) a 1mm section of the backplate and (b) an individual hole on the 40x80 backplate, and similar results were obtained for all backplates. No discernible regular structure could be determined for the 10x20 backplate and so this was not used in the experiments. Measuring the depth

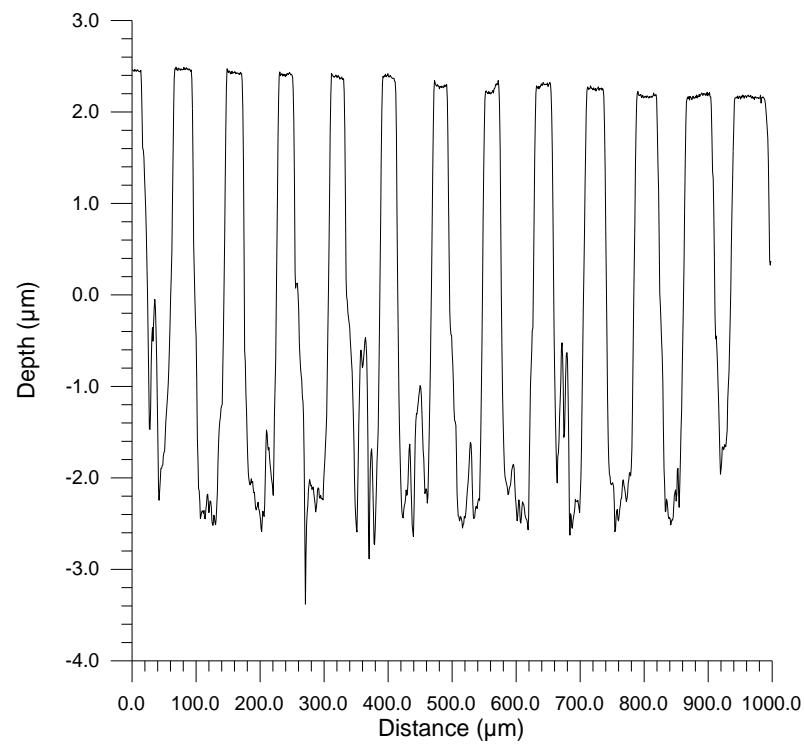


Figure 4.17(a): Talysurf profile for 1mm across the 40x80 backplate.

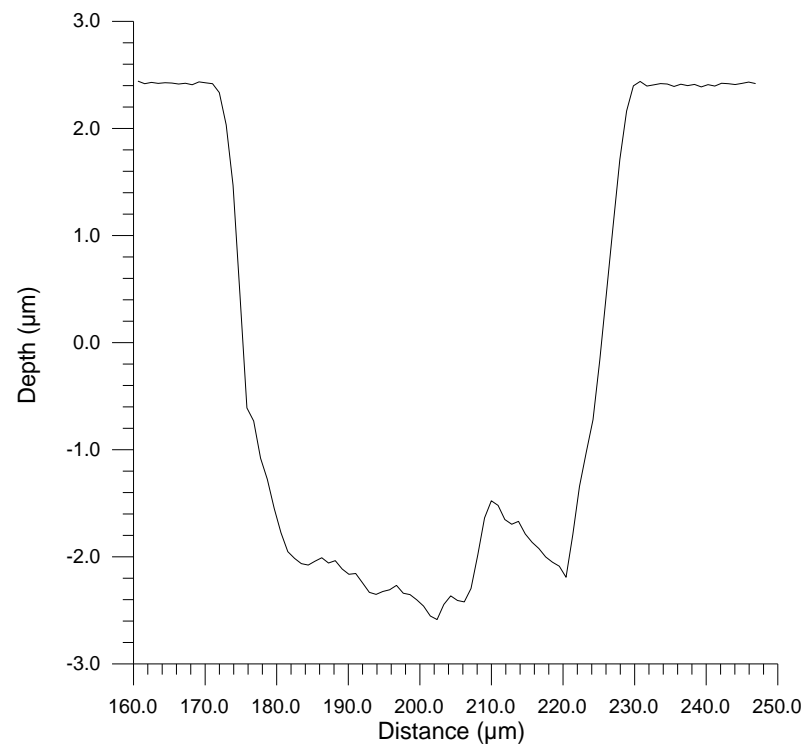


Figure 4.17(b): Talysurf profile for a single hole on the 40x80 backplate.

Device	20x40	30x60	40x60	40x80	Flat
hole diameter (μm)	37.4	47.6	54.4	58.5	-
hole area (μm^2)	1096.8	1779.5	2324.3	2687.8	-
hole spacing (μm)	39.5	59.2	59.2	81.0	-
hole depth (μm)	4.4	6.2	4.6	4.7	-
hole volume (μm^3)	4833.8	11032.9	10691.8	12632.7	-
minimum spacing (μm)	2.1	11.6	4.8	22.5	-
area ratio	0.70	0.51	0.66	0.41	-
spacing ratio	0.95	0.80	0.91	0.72	-
total flat area (mm^2)	52.68	37.99	49.62	30.65	74.82
total hole volume (mm^3)	0.09742	0.2283	0.1159	0.2076	0.0

Table 4.10: Backplate surface parameters.

of the holes in each backplate was not straightforward, as there was no guarantee that the stylus on the Talysurf was travelling down the centre line of a row of holes, and so the dimensions obtained must be treated with caution.

4.3.1 Experimental technique

A transducer was manufactured from each of the etched copper backplates and a $6\mu\text{m}$ Mylar film. Each transducer was then in turn used as a receiver of ultrasound generated by the silicon backplate device as described in the previous section on brass backplate transducers. 100V of d.c. bias was applied to each transducer via the Cooknell amplifier, and the air gap between source and receiver was 20mm.

In an attempt to find the connection (if any) between the frequency response and sensitivity of the devices, and the dimensions of the features of the backplates, the following properties were considered: hole diameter, hole depth, hole spacing, hole volume, minimum spacing, hole area, area ratio (hole area/hole spacing squared), spacing ratio (diameter/spacing), and the total flat area of the device. The values used are shown in Table 4.10.

4.3.2 The effects of the hole dimensions

The frequency spectra for each of the backplates are shown in Figure 4.18(a) showing their relative sensitivity and (b) normalised to the maximum amplitude in each FFT to show their relative bandwidth. The relationship between 3dB bandwidth and sensitivity is shown in Figure 4.19, and as before there is a trade off between the two. However, there were no conclusive trends visible between the various backplate parameters shown in Table 4.10, and absolute sensitivity and bandwidth for each transducer, although it is possible that there is a relationship between the hole volume and the response of the devices. A statistical analysis of a larger number of backplates is needed to verify this. There was, however, an increase in sensitivity for all the etched devices over the flat unetched backplate, so the holes are having some effect. More air has been introduced between the backplate and the polymer film by the holes, making the film less rigid. It was thought that there may have been a connection between hole spacing (or minimum distance between hole edges), hole diameter and hole depth, as these properties may be likened to the rail width, groove width and groove depth of grooved backplates. Such a connection has been seen in previous work by Suzuki *et al.* [21].

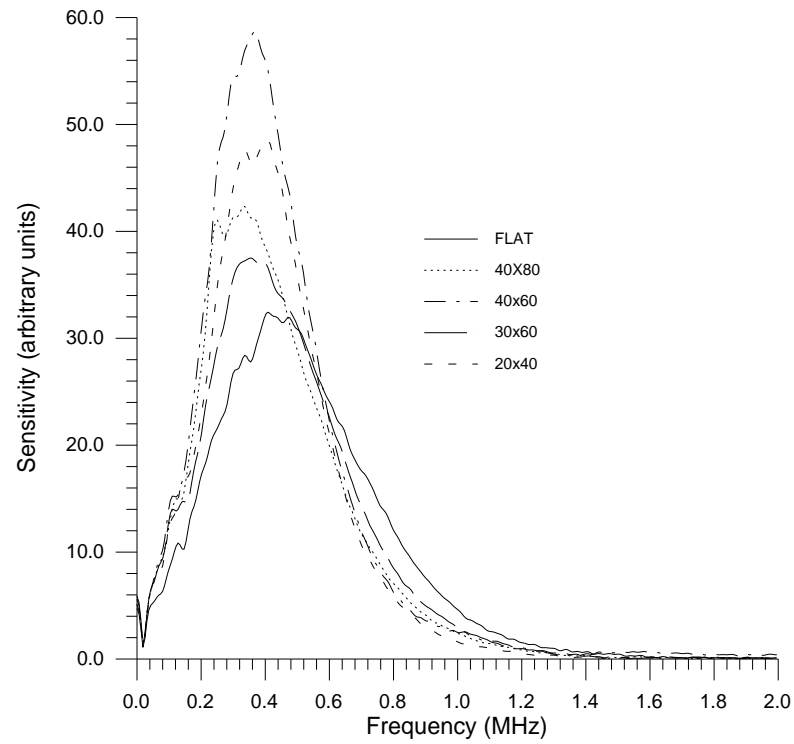


Figure 4.18(a): Frequency spectra for all the copper backplates, showing their relative sensitivity.

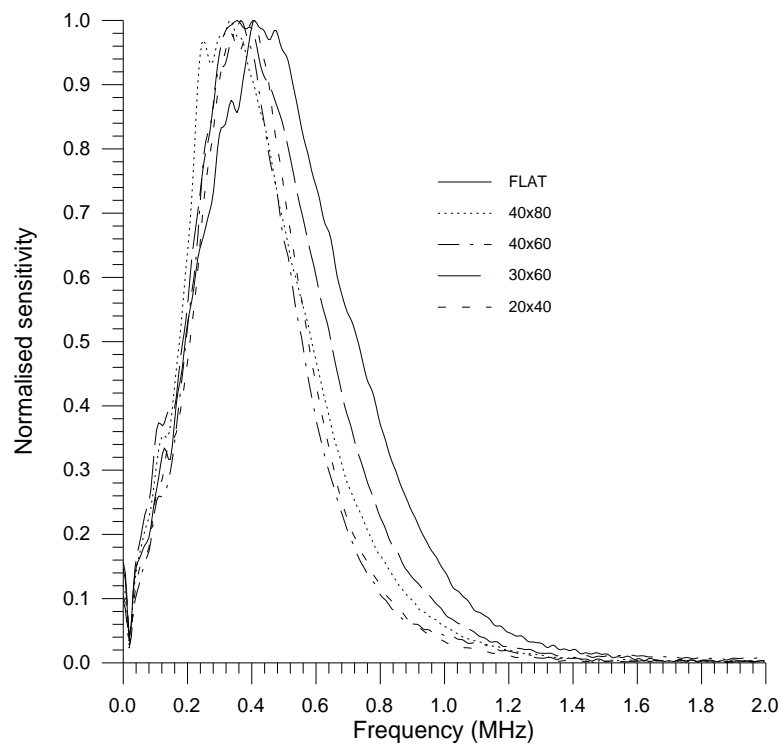


Figure 4.18(b): Normalised frequency spectra for all the copper backplates, showing their relative bandwidth.

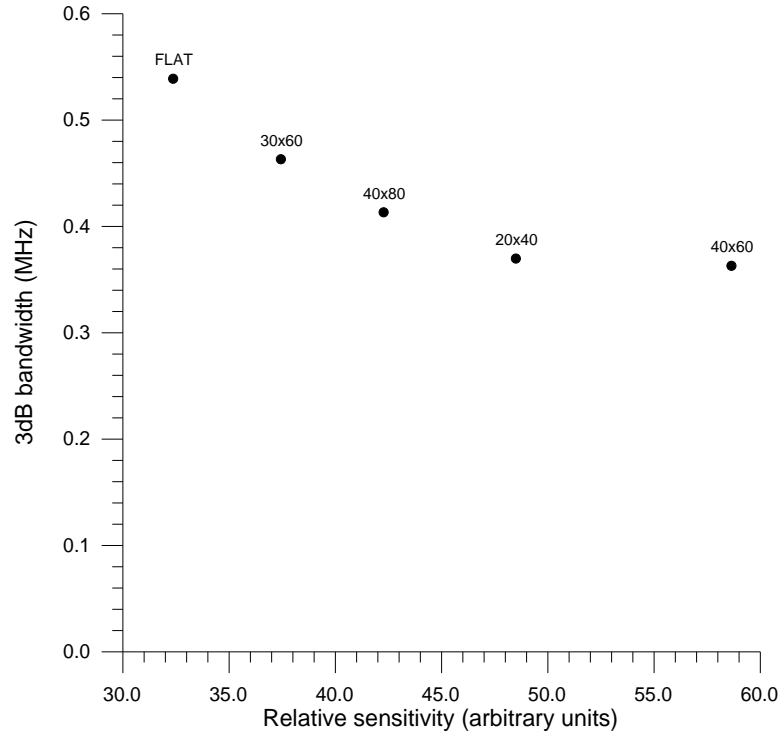


Figure 4.19: Plot of sensitivity against bandwidth for the copper backplates.

4.4 Discussion

The subject of capacitance air-coupled transducers is attracting much interest as there is yet to be found a definitive model for the devices. The work described here compliments previous work on random backplate transducers [17], and has shown that there appears to be an optimum bias voltage for the frequency response of the device, and the film thickness used.

However, there also appeared to be an optimum bias voltage to maximise the sensitivity of the device, which is different to that required for maximum bandwidth. As the film is pulled more firmly onto the backplate at higher bias voltages, the film becomes more heavily damped and so the bandwidth increases. The air behind the membrane is compressed or squeezed out completely, so that the film conforms more

precisely to the backplate surface profile. Where films of different thickness were used on the same backplate, and with the same bias voltage applied, there appeared to be an optimum thickness of film, below which there was no gain in sensitivity. It is possible that the film thickness also needs to be matched to the surface properties of the backplate, but due to the small number of backplates and films used in this study, further work is needed for confirmation of this.

It was noted that the shape of the frequency spectrum also changed with increasing bias voltage, and that the profile was made up from two distinct portions, the first possibly being determined by the film thickness, and the second by the backplate surface. It was not possible to calculate the theoretical frequencies for the membrane alone, as its stiffness was not known and could not easily be measured. It would be reasonable to assume that the stiffness of the film is related to the bias voltage applied, and that equation {4.2} could be adapted to account for this in future work.

From the data shown in Table 4.5, it would appear that there was little agreement between theory and experiment when using surface roughness parameters as an approximation to the air gap. However the linear relationship to the inverse square root seen in previous work [17] could be observed in Figures 4.7 and 4.10, and so it is possible that equation {4.1} needs to be modified to apply to broadband devices. It was also noted that results improved slightly when thinner films were used, possibly due to the film conforming more accurately to the surface profile of the backplate. The long term suitability of brass as the backplate material is probably not ideal, as the surface tarnishes with time, and so the surface properties of the backplates may change after the transducers have been assembled. Stainless steel may be more suitable.

The work on chemically etched backplates showed that in this study, there was no conclusive link between the hole dimensions and the response of the devices for the 6 μ m membrane thickness and 100V bias used, although a possible relationship with hole volume may have existed. Links between the hole dimensions and the frequency response of capacitance devices have, however, been observed by other authors [21] who worked with silicon. The use of chemical etching to consistently produce identical metallic backplates is difficult, as so many variables need to be removed. It was apparent that fresh chemicals were necessary for each backplate, or some other compensation for the loss in etchant strength between successive devices. The isotropic etch also caused problems, as it was difficult to produce holes of the same diameter but different depths. The anisotropic properties of silicon have been exploited by other authors [20-22] for this purpose, but silicon requires the use of hydrofluoric acid (HF) as an etchant which is far from ideal. Other processes such as ion beam machining or laser machining may produce more consistent results. However, a comprehensive study of this would probably fill several other Ph.D. theses, and so can only be speculated about here.

4.5 Conclusions

A series of capacitance air-coupled transducers with roughened and polished brass backplates were made, and the effects of changing the roughness of the surface were investigated. A linear relationship between sensitivity and bandwidth was observed, and the frequency response was inversely proportional to the square root of the surface roughness of the backplate, as seen in previous work on the same subject. Changing the thickness of the polymer film showed a similar relationship with the

frequency response, but the expected linear link between film thickness and sensitivity was not observed. There appeared to be an optimum film thickness for the backplate used in the experiments. The effects of bias voltages up to 1000V were also investigated, and again there appeared to be an optimum voltage for different film thicknesses, above which the sensitivity and frequency response of the device was reduced. Three devices manufactured in an identical fashion were compared, and found to have very similar responses.

A second series of devices were manufactured by chemically etching regular circular features a few tens of microns in diameter into polished copper backplates, and characterised in a similar way. No conclusive trends were observed between the hole dimensions and frequency response, but the addition of holes was seen to improve the sensitivity of the devices. A larger number of transducers is needed to provide a more conclusive statistical analysis for both the brass and copper backplates, and this would provide an excellent topic for further work, along with other more precise methods of backplate manufacture such as laser machining.

4.6 References

- [1] E.C. Wentz, 'A condenser transmitter as a uniformly sensitive instrument for the absolute measurement of sound intensity', *Phys. Rev.* **10**, 39-63 (1917)
- [2] I.B. Crandall, 'Air-damped vibrating system - theoretical calibration of the condenser transmitter', *Phys. Rev.* **11**, 449-460 (1918)
- [3] E.C. Wentz, 'The thermophone', *Phys. Rev.* **19**, 333-345 (1922)

- [4] E.C. Wente, 'Sensitivity and precision of the electrostatic transmitter for measuring sound intensities', *Phys. Rev.* **19**, 498-503 (1922)
- [5] Brüel and Kjær, *Master Catalogue - Electronic Instruments*, (K. Larsen & Sons, Denmark, 1989)
- [6] G.S.K. Wong and A.F.W. Embleton (eds.), *AIP Handbook of condenser microphones - Theory, calibration and measurements*, (AIP Press, New York, 1995)
- [7] N.W. McLachlan, *Loudspeakers*, (Clarendon Press, Oxford, 1934)
- [8] W. Kuhl, G.R. Schodder and F.-K. Schröder, 'Condenser transmitters and microphones with solid dielectric for airborne ultrasonics', *Acustica* **4**, 519-532 (1954)
- [9] K. Matsuzawa, 'Condenser microphones with plastic diaphragms for airborne ultrasonics I', *J. Phys. Soc. Japan* **13**, 1533-1543 (1958)
- [10] K. Matsuzawa, 'Condenser microphones with plastic diaphragms for airborne ultrasonics II', *J. Phys. Soc. Japan* **15**, 167-174 (1960)
- [11] M. Rafiq and C. Wykes, 'The performance of capacitive ultrasonic transducers using v-grooved backplates', *Meas. Sci. Technol.* **2**, 168-174 (1991)
- [12] J. Hietanen, P. Mattila, J. Stor-Pellinen, F. Tsuzuki, H. Väättäjä, K. Sasaki and M. Luukkala, 'Factors affecting the sensitivity of electrostatic ultrasonic transducers', *Meas. Sci. Technol.* **4**, 1138-1142 (1993)
- [13] J. Hietanen, J. Ignatius and J. Stor-Pellinen, 'Electrostatic solutions for a capacitive ultrasonic air transducer with a uniformly V-grooved backplate', *Sensors and Actuators A* **45**, 95-98 (1994)
- [14] P. Mattila and J. Hietanen, 'Bandwidth control of an electrostatic ultrasonic transducer', *Sensors and Actuators A* **45**, 203-208 (1994)

- [15] W.S.H. Munro and C. Wykes, 'Arrays for airborne 100kHz ultrasound', *Ultrasonics* **32**, 57-64 (1994)
- [16] W.S.H. Munro, S. Pomeroy, M. Rafiq, H.R. Williams, M.D. Wybrow and C. Wykes, 'Ultrasonic vehicle guidance transducer', *Ultrasonics* **28**, 350-354 (1990)
- [17] H. Carr and C. Wykes, 'Diagnostic measurements in capacitive transducers', *Ultrasonics* **31**, 13-20 (1993)
- [18] M.J. Anderson, J.A. Hill, C.M. Fortunko, N.S. Dogan and R.D. Moore, 'Broadband electrostatic transducers: Modeling and experiments', *J. Acoust. Soc. Am.* **97**, 262-272 (1995)
- [19] W. Kühnel and G. Hess, 'A silicon condenser microphone with structured backplate and silicon nitride membrane', *Sensors and Actuators A* **30**, 251-258 (1992)
- [20] D.W. Schindel, D.A. Hutchins, L. Zou and M. Sayer, 'The design and characterization of micromachined air-coupled capacitance transducers', *IEEE Trans. Ultrason. Ferroelec. Freq. Contr.* **UFFC-42**, 42-50 (1995)
- [21] K. Suzuki, K. Higuchi and H. Tanigawa, 'A silicon electrostatic ultrasonic transducer', *IEEE Trans. Ultrason. Ferroelec. Freq. Contr.* **UFFC 36**, 620-627 (1989)
- [22] M.I. Haller and B.K. Khuri-Yakub, 'A surface micromachined electrostatic ultrasonic air transducer', *IEEE Ultrason. Symp. 1994 (Cannes)*, 1241-1244
- [23] J. Hietanen, J. Stor-Pellinen, M. Luukkala, P. Mattila, F. Tsuzuki and K. Sasaki, 'A Helmholtz resonator model for an electrostatic ultrasonic air transducer with a V-grooved backplate', *Sensors and Actuators A* **39**, 129-132 (1993)

- [24] R. Høeg and E. Weidmann, *Metallographic sample preparation - How to select proper grinding and polishing procedures*, (Struers Personal Metalog, 1992)

Chapter 5: Thickness estimation using air-coupled Lamb waves

5.1 Introduction

This chapter describes how air-coupled plate waves (Lamb waves) may be used to estimate the thickness of thin plates of material. An overview of Lamb wave theory will be given, followed by a description of two methods by which the plate thickness may be found. A series of experiments is then described which use laser-generated Lamb waves and an air-coupled capacitance receiver to reconstruct the velocity dispersion curves. These are then compared to theoretical curves calculated using a FORTRAN program, and the thickness of the plate is estimated. The final part of the work will investigate the use of another air-coupled capacitance transducer to replace the laser source.

5.1.2 A brief history of Lamb waves

Plate waves or Lamb waves occur in a thin sample of material, where the two free boundaries of a plate parallel to the direction of wave motion are close enough to prevent the propagation of pure surface waves and bulk modes. The initial theory was devised by Lamb [1] in 1917, but the equations were not fully explained and only a limited number of solutions were presented. A more comprehensive set of solutions was not produced until 1950 by Mindlin [2], who showed the results for both real and imaginary wave numbers. Later works by Viktorov [3] and then Achenbach [4] cover the equations and general theory in greater detail. However, the results for even the simplest geometry in isotropic materials are still sufficiently complex to generate recent interest in the theory [5-7] or other approximations to the dispersion relations [8,9]. An overview of some of the more relevant parts of the theory will be given in the next section.

With the advent of more complicated engineering materials and techniques, interest in both the theory and practical applications of Lamb waves has increased, particularly in the examination of adhesive bonds [10-12] and anisotropic or composite materials [13-22]. Some of the experimental work has been carried out using standard direct coupling techniques [15,16], but most used some form of immersion tank [18-20], relying on the fact that Lamb waves ‘leak’ or re-radiate back into the surrounding medium, a phenomena which has been visualised using Schlieren optics [23,24]. Earlier work by Merkulov [25] showed that provided the density of the plate was much greater than that of the surrounding medium, damping effects were negligible. For some modern composite materials this is no longer the case.

By removing the coupling medium altogether, any possible damping effects are negated. This has been achieved to date by the use of entirely laser based non-contact techniques, using pulsed lasers for ultrasonic generation, and interferometers or some form of beam deflection device as the detector [26-32]. Some work has also been done using electromagnetic acoustic transducers (EMATs) [33]. However, these techniques have the usual associated drawbacks, namely the cost, fragility and surface requirements of most interferometers, and the restriction of only electrically conducting samples for EMATs.

An alternative method is to use air as the coupling medium, a method already used to study the mechanical properties of paper [34,35]. With the recent advances in air-coupled capacitance transducer technology [36,37], giving improved sensitivity and bandwidth, a further investigation into this technique was undertaken. The work to be presented in this chapter will describe how air-coupled Lamb waves were successfully used to evaluate a variety of materials.

5.2 An overview of Lamb wave theory

As mentioned in previous chapters, Lamb waves [3,4] or plate waves occur in thin samples of material, where the two boundaries of the plate parallel to the direction of wave motion are close enough to prevent propagation of pure surface waves and bulk modes. Lamb waves are dispersive, i.e. waves with different frequencies travel at different velocities in the same material, and so the well known relation:

$$f = \frac{c}{\lambda} \quad \{5.1\}$$

still applies, but here c is no longer a constant, rather a function of the wavelength. Lamb waves may be classified into two groups depending on their mode of vibration. Asymmetric or ‘a’ modes occur when the motion of the plate surfaces is asymmetrical about a line through the centre of the sample in the direction of propagation, as shown schematically in Figure 5.1(a). Symmetric or ‘s’ modes occur when the motion of the plate surfaces is symmetric about this line, as shown schematically in Figure 5.1(b).

The fundamental characteristic of a Lamb wave is its phase velocity c_p , which is a function of the frequency of the wave and the thickness of the plate. This differs from the velocity of energy propagation, or group velocity c_g , although this is also frequency dependent. Referring to Figure 5.2, the interference of two or more carrier waves of slightly different frequencies f_1 and f_2 , travelling at their respective phase velocities c_{p1} and c_{p2} , form a modulation or group of waves of frequency f_g travelling with a group velocity of c_g . The group velocity may be determined using:

$$c_g = \frac{d\omega}{dk} \quad \{5.2\}$$

where k is the wave number.

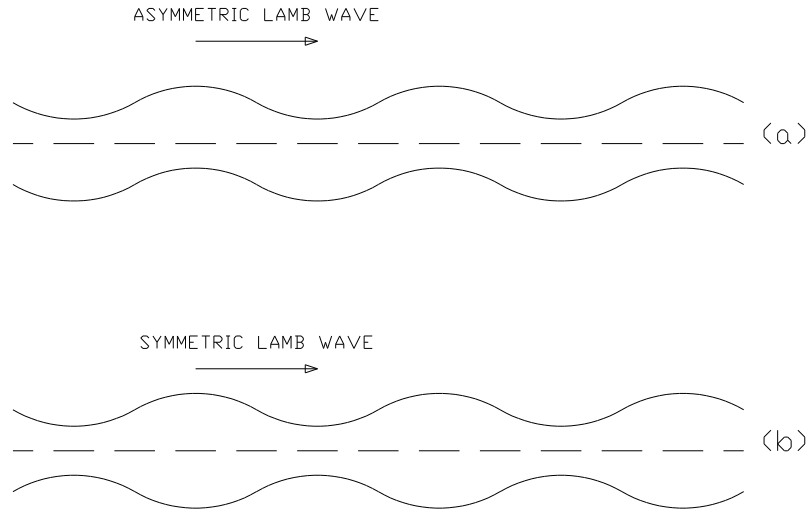


Figure 5.1: Plate surface motion for (a) asymmetric and (b) symmetric Lamb waves.

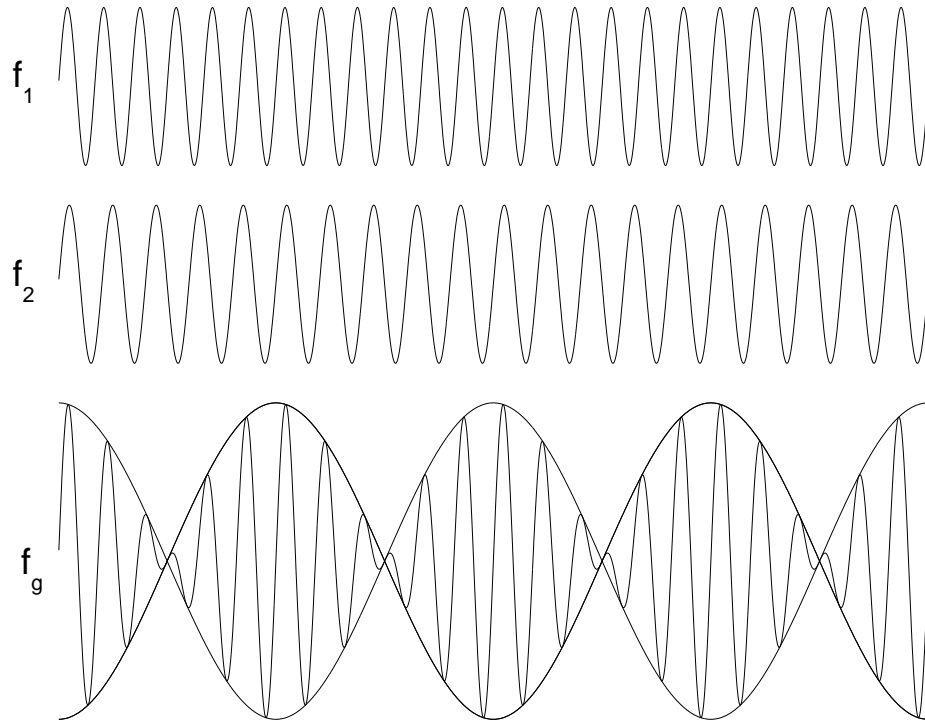


Figure 5.2: The interference of two waves of slightly different frequencies f_1 and f_2 , travelling at phase velocities c_{p1} and c_{p2} , to produce a modulation of frequency f_g travelling at a group velocity c_g .

The phase velocity may be found using the Rayleigh-Lamb frequency relations.

For the symmetric 's' modes:

$$\frac{\tan(\sqrt{1 - a^2} \cdot d)}{\tan(\sqrt{b^2 - a^2} \cdot d)} = - \frac{4a^2 (\sqrt{1 - a^2}) (\sqrt{b^2 - a^2})}{(2a^2 - 1)^2} \quad \{5.3\}$$

and for the asymmetric 'a' modes:

$$\frac{\tan(\sqrt{1 - a^2} \cdot d)}{\tan(\sqrt{b^2 - a^2} \cdot d)} = - \frac{(2a^2 - 1)^2}{4a^2 (\sqrt{1 - a^2}) (\sqrt{b^2 - a^2})} \quad \{5.4\}$$

where:

$$a = \frac{c_t}{c_p} \quad b = \frac{c_t}{c_L} \quad d = \frac{\pi \cdot f \cdot t}{c_t} \quad \{5.5\}$$

with c_t and c_L being the transverse and longitudinal bulk wave velocities in the material, c_p the phase velocity at frequency f , and t the thickness of the plate.

These Rayleigh-Lamb frequency relations have a finite number of real roots, but an infinite number of imaginary roots and so cannot be solved directly, but rather by numerical methods. The first root is known as the zero order mode, the next as the first order, and so on. Figure 5.3 shows a plot of normalised phase velocity (c_p/c_t) against frequency-thickness product ($f \cdot t$) for the first four asymmetric and symmetric modes in aluminium, with Figure 5.4 showing a similar plot for normalised group velocity (c_g/c_t) against frequency-thickness product ($f \cdot t$). in the same material. It can be seen that apart from the zero order (a_0 and s_0) modes, the plots do not extend down to the origin at 0Hz, and have a cut-off or critical frequency. This is determined by the thickness t of the plate, and both the longitudinal and transverse wavelengths in the material. For symmetric modes, critical frequencies occur when:

$$t = \frac{\lambda_L}{2}, \frac{3\lambda_L}{2}, \frac{5\lambda_L}{2}, \text{etc.} \quad \{5.6\}$$

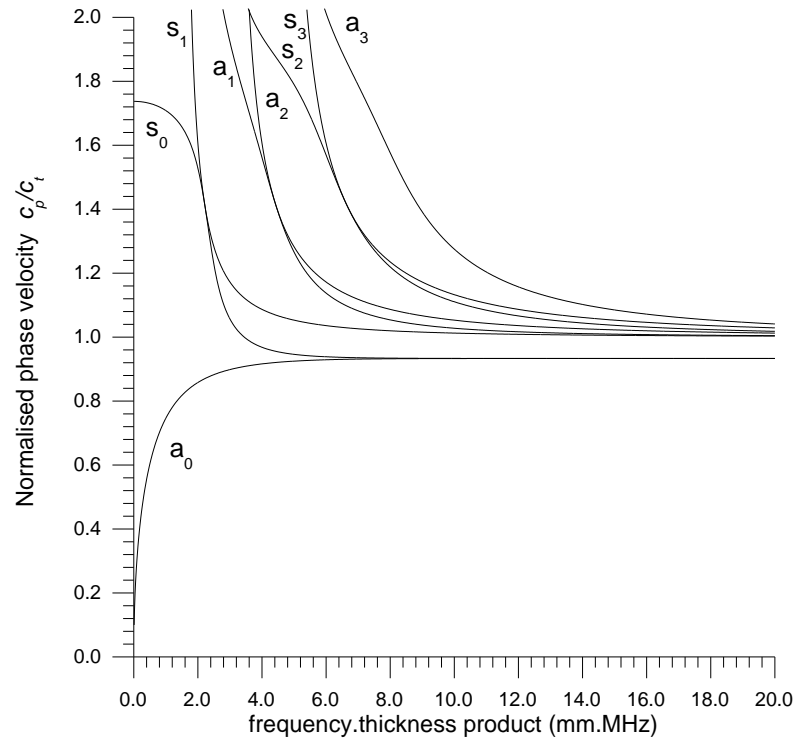


Figure 5.3: Phase velocity dispersion curves for the first four asymmetric and symmetric Lamb wave modes in aluminium.

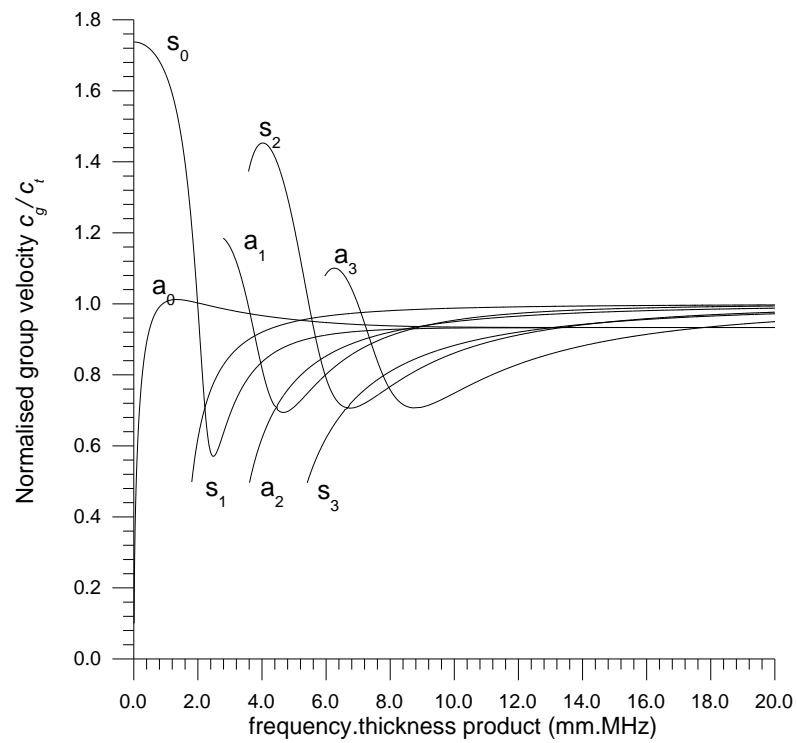


Figure 5.4: Group velocity dispersion curves for the first four asymmetric and symmetric Lamb wave modes in aluminium.

and:

$$t = \lambda_t, 2\lambda_t, 3\lambda_t, \text{etc.} \quad \{5.7\}$$

Similarly for asymmetric modes:

$$t = \frac{\lambda_t}{2}, \frac{3\lambda_t}{2}, \frac{5\lambda_t}{2}, \text{etc.} \quad \{5.8\}$$

and:

$$t = \lambda_L, 2\lambda_L, 3\lambda_L, \text{etc.} \quad \{5.9\}$$

The total number of modes N in a plate of thickness t at a given frequency f is given by:

$$N = 1 + \left[\frac{t}{\lambda_t} \right] + \left[\frac{t}{\lambda_L} + \frac{1}{2} \right] \quad \{5.10\}$$

for the symmetric modes, and by:

$$N = 1 + \left[\frac{t}{\lambda_L} \right] + \left[\frac{t}{\lambda_t} + \frac{1}{2} \right] \quad \{5.11\}$$

for the asymmetric modes. In both cases, the expressions in square parentheses are rounded to the nearest integer.

The cut-off frequencies for symmetric and asymmetric modes higher than zero order have a physical explanation. The zero order modes are formed by the interaction of two surface waves, as shown schematically in Figure 5.5(a), and thus exist at all frequencies in any thickness of plate. As the plate thickness increases (at a given frequency) or the wavelength decreases (for a given plate thickness), the two surface waves interact less and less until they become pure surface waves and travel at the Rayleigh wave velocity, as can be seen from the dispersion curves at high frequency-thickness products.

The higher order modes are formed by the interaction of bulk waves reverberating in the plate thickness, to form a standing wave or resonance as shown in

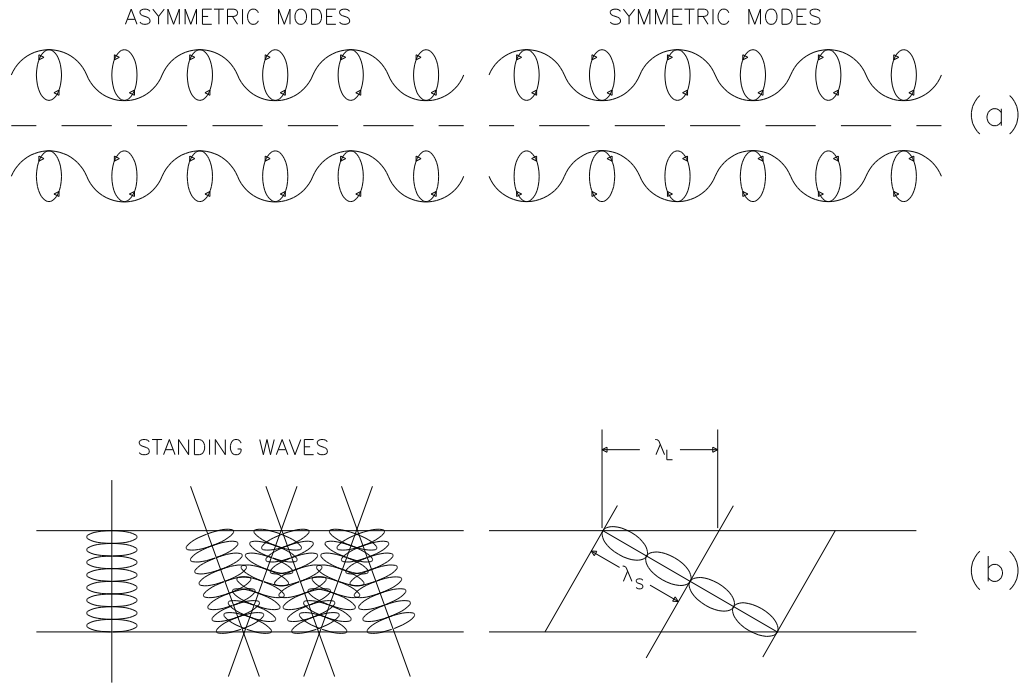


Figure 5.5: Formation of (a) zero order modes from surface waves, and (b) higher order modes from standing waves.

Figure 5.5(b). A new mode exists when there is an integral number of half wavelengths within the plate thickness, for either longitudinal or transverse waves. At lower non-critical values for a given mode, waves cannot propagate as they are purely imaginary. At higher non-critical values, the standing wave is no longer travelling perpendicularly to the surfaces of the plate, and so will propagate with a characteristic phase velocity. The standing wave is non-dispersive and so has a fixed wavelength λ_s , whereas the Lamb wave mode will have a varying wavelength λ_L depending on the angle it makes with the plate surface, and so will exhibit the characteristic dispersion. The actual situation is far more complex than described here, and a more comprehensive explanation may be found in the works by Viktorov [3] and Achenbach [4].

5.3 Extracting the dispersion relations from Lamb wave data

As can be seen from the Rayleigh-Lamb equations, the velocity (phase or group) of a Lamb wave is heavily dependent on frequency, plate thickness and bulk wave velocities. As stated in Chapter 1, the bulk wave velocities are directly related to the elastic properties (Young's modulus and Poisson's ratio) of the material. There are many methods for extracting the dispersion relations from Lamb wave data, so only the two used in this work will be described here. The method used by Dewhurst *et al.* [26] measured the group velocity using the mean arrival time of a 'group' of frequencies, found by inverting the time between successive maxima in the dispersive a_0 mode. A variant of this method, known as the 'zero-crossing' technique, was used in this work and may be explained as follows. As Lamb waves disperse, waves of different frequencies arrive at different times due to their varying velocities. For the a_0 mode, higher frequencies arrive first, and lower frequencies later, as both the phase and group velocities increase with frequency, as can be seen from the dispersion curves in Figures 5.3 and 5.4. For the s_0 mode, the low frequency components arrive first. The zero crossing technique involves measuring the times at which the waveform crosses the zero amplitude origin, after subtracting any d.c. offset. Due to the dispersion, a portion of the waveform between successive crossings at, say, t_1 and t_2 will contain a range of different frequencies, and so may be thought of as a group with a central frequency f , which corresponds to the inverse of the time difference between the two crossing times. Provided that the propagation distance x is known, the group velocity c_g at the frequency f may be found using:

$$c_g(f) = \frac{x}{t_1 - t_2} \quad \{5.12\}$$

The second method used by Hutchins *et al.* [29] is an extension of the earlier work by Sachse and Pao [38] for bulk waves, in which the dispersion relation is obtained using the phase information contained in the fast Fourier transform (FFT) of a Lamb wave signal, given by:

$$\phi(n) = \tan^{-1} \left[\frac{F(i)}{F(r)} \right] \quad -\frac{\pi}{2} < \phi(n) < \frac{\pi}{2} \quad 5.13\}$$

where n is the number of points in the FFT, and $F(i)$ and $F(r)$ are the real and imaginary parts of the FFT respectively. If the change in phase between successive points of the FFT is greater than π , then discontinuities will occur in the phase spectrum. These may be corrected by adding π to all subsequent points when $\phi(i+1) < \phi(i)$. The total number of wavelengths n_λ at a certain frequency f between the source and receiver is given by:

$$n_\lambda(f) = \frac{\phi(f)}{2\pi} \quad \{5.14\}$$

If the propagation distance x between source and receiver is known, then the wavelength at the specific frequency f may be found from:

$$\lambda_f = \frac{x}{n_\lambda(f)} \quad \{5.15\}$$

Then the phase velocity c_p will be:

$$c_p = \frac{\omega}{k} = f \cdot \lambda \quad \{5.16\}$$

5.4 Calculation of theoretical curves

The real roots of the Rayleigh-Lamb equations must be found by numerical methods, the most common being to select a constant frequency f , and then substitute an increasing value of c_p until the equations change sign. The lowest value of c_p at which a

root occurs will be the zero order mode, the next the first order mode, and so on. A computer program (see Appendix B) was written in FORTRAN to calculate the dispersion curves for Lamb waves in isotropic materials. Both phase velocity and group velocity curves were generated, as the group velocity is simply the differentiation of the phase velocity curve with respect to frequency, i.e.:

$$c_g = \frac{d\omega}{dk} = \frac{\Delta\omega}{\Delta k} \quad \{5.17\}$$

$$c_g = \frac{[2.\pi.f_2 - 2.\pi.f_1]}{\left[\frac{2.\pi.f_2}{c_2} - \frac{2.\pi.f_1}{c_1} \right]} \quad \{5.18\}$$

$$c_g = \frac{[f_2 - f_1]}{\left[\frac{f_2}{c_2} - \frac{f_1}{c_1} \right]} \quad \{5.19\}$$

where 1 and 2 denote adjacent points in the frequency spectrum.

Dispersion curves are usually presented as plots of normalised velocity versus frequency-thickness product (see Figures 5.3 and 5.4), which enable a large number of plates of different thickness to be represented on one plot. However, a FFT contains frequency information at discrete intervals, which will be fixed for time domain waveforms of the same length. Frequency-thickness products for samples of the same material but different thickness will therefore be difficult to compare with one single dispersion curve without interpolation. The FORTRAN program used here calculated the dispersion curves for one specific plate thickness, for any given frequency range at any frequency interval. This allowed the theoretical curves to be directly compared with experimentally obtained curves, which would be of velocity versus frequency.

5.5 Trial experiments using a contact detector

Experiments were first performed to test the methods of extracting the dispersion relations from Lamb wave signals. To ensure that sufficient bandwidth was available for the experiments, a pulsed laser was used to generate signals in thin ($<1.0\text{mm}$) sheets of various materials, and an electrostatic air-coupled transducer was used as a detector. The apparatus is shown schematically in Figure 5.6. The laser used was a Lumonics 'Mini-Q' q-switched Nd:YAG, operating at a wavelength of 1064nm in the near infra-red, with a pulse duration of 4ns and maximum pulse energy of 120mJ . The beam was directed onto the sample using a suitable 45° mirror, and a lens to reduce the 3mm beam diameter to a point. The air transducer used as a receiver was held in a rotating mount which enabled the angle θ between the plate and transducer face to be varied. This altered the range of frequencies of leaky Lamb waves seen by the detector. The rotary mount was fixed to a micrometer stage, the motion of which was parallel to the surface of the sample. This permitted precise changes in the propagation length of the Lamb wave through the sample. Signals were amplified using a Cooknell CA6/C charge sensitive amplifier, in conjunction with a SU2/C power supply which enabled a d.c. bias of up to 100V to be applied between the film and backplate electrodes of the receiver. Waveforms were captured and digitised on a Tektronix 540 TDS digital oscilloscope, and then transferred via an IEEE-488/GPIB interface to an IBM PS/2 Model 30 286 computer for storage and later analysis. To ensure detection of the correct waveform, a contact capacitance device which used the sample as one electrode as described in previous chapters, was used as a calibrated receiver. This used the sample as one electrode of a capacitor, and a steel sphere as the other, with a thin

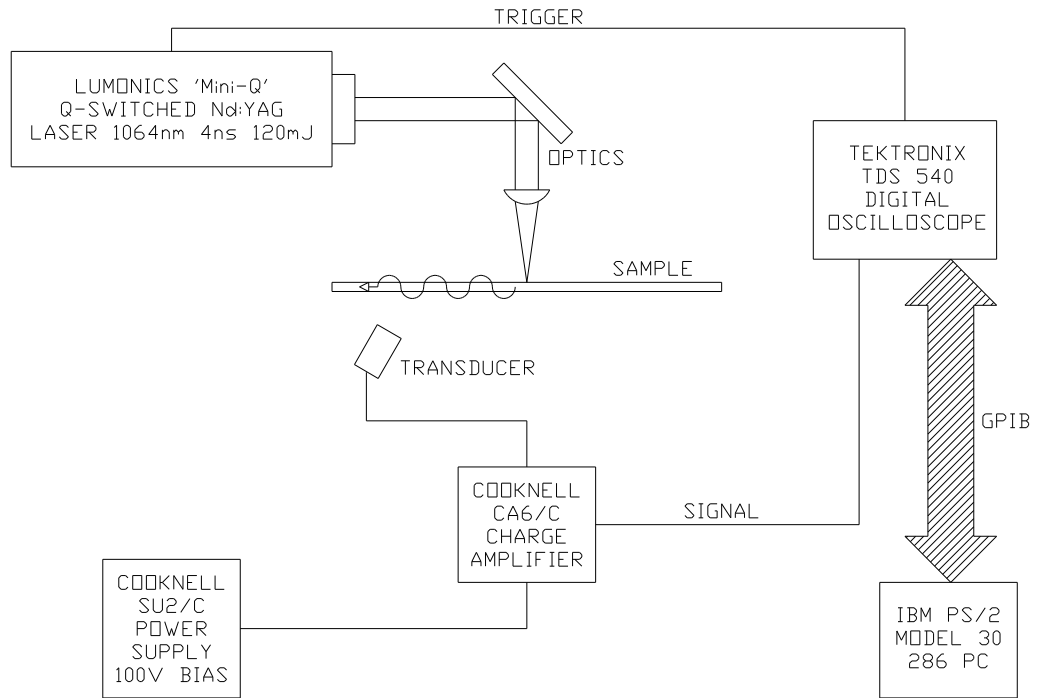


Figure 5.6: Schematic diagram of experimental equipment.

polymer dielectric film between them. For more detailed equipment specifications, see Appendix A.

The first sample to be tested was a 1.2mm thick aluminium sheet. From the relevant portion of the phase velocity dispersion curves, it can be seen that at frequencies up to approximately 2MHz in this thickness of plate, the frequency thickness product is sufficiently low to allow only the two zero order (a_0 and s_0) modes to exist. A typical Lamb wave which had propagated through 55mm of the plate is shown in Figure 5.7(a). Both the s_0 and a_0 modes are clearly visible, and show the characteristic dispersion. The contact capacitance transducer is wideband, and has a flat response up to the 10MHz limit of the charge amplifier. This high bandwidth has allowed some of the higher order modes to be

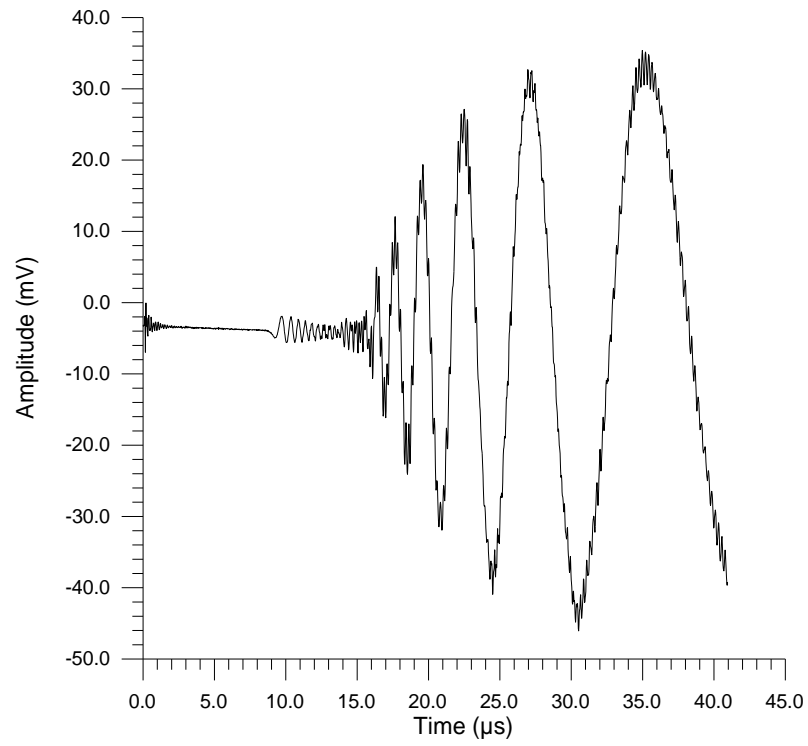


Figure 5.7(a): Multimode Lamb waves in a 1.2mm aluminium plate, detected using the contact capacitance device.

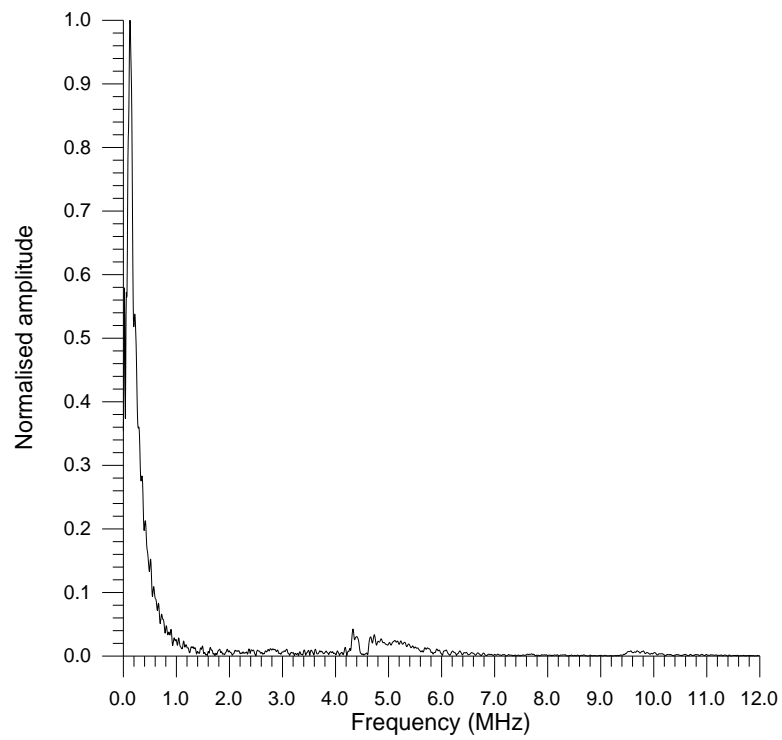


Figure 5.7(b): Frequency spectrum of Figure 5.7(a).

	Theoretical cut off frequency (MHz)				
	1st order	2nd order	3rd order	4th order	5th order
asymmetric 'a' modes	1.30	3.91	5.27	6.52	9.13
symmetric 's' modes	2.61	2.63	5.22	7.83	7.90

Table 5.1: Theoretical cut off frequencies in a 1.2mm thick plate of aluminium.

detected, as at least four other symmetric and four other asymmetric modes will exist at these values of frequency and thickness. They appear as the high frequency oscillations on the lower frequency a_0 mode, and the non-dispersive vibrations between the s_0 and a_0 portions of the waveform. A selection of theoretical cut off frequencies up to 10MHz for asymmetric 'a' modes and symmetric 's' modes in a 1.2mm thick plate of aluminium is shown in Table 5.1, calculated using equations {5.6} to {5.9}, and values of $c_t=3130\text{ms}^{-1}$ and $c_L=6320\text{ms}^{-1}$. The FFT of the Lamb wave signal is shown in Figure 5.7(b), where it can be seen that at least three higher order modes were detected, corresponding to the peaks beginning at 4.2MHz (possibly the a_2 mode), 4.6MHz (a_3 or s_3 modes) and 9.6MHz (possibly the a_5 mode). The experimental frequencies will not exactly match the theoretical predictions shown in Table 5.1, as the values of c_L and c_t used in the calculations will differ from those in the actual plate.

Using the contact capacitance transducer as a receiver and the laser as a source, the propagation path of 55mm through the sample was known fairly accurately. The group velocity of the a_0 mode in the 1.2mm aluminium plate is shown in Figure 5.8, where it is compared with the theoretical curve as calculated by the FORTRAN program using values

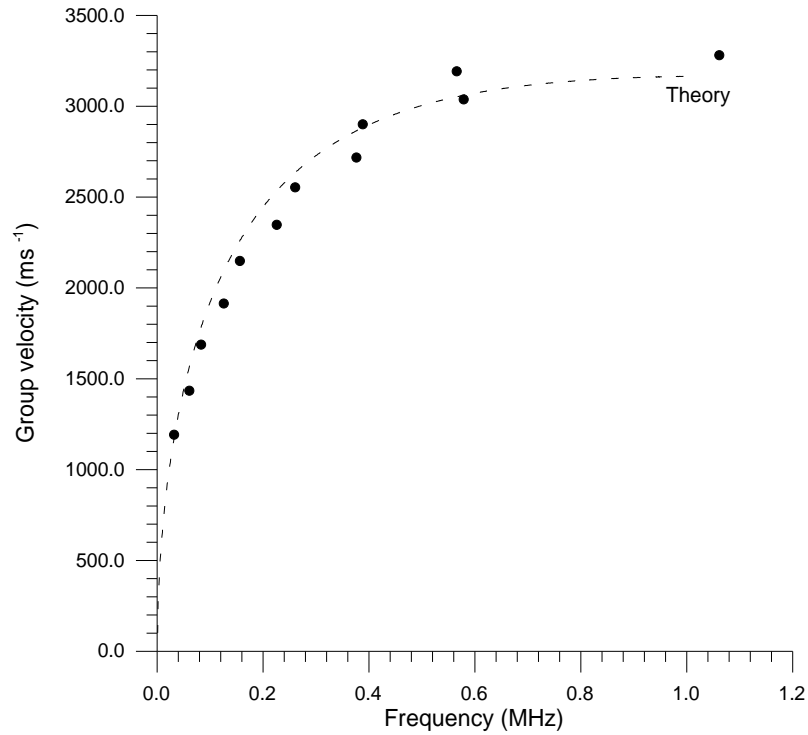


Figure 5.8: a_0 group velocity in a 1.2mm aluminium plate, found using zero crossing technique and a contact capacitance transducer - theory vs. experiment.

of 3130ms^{-1} and 6320ms^{-1} for the shear and longitudinal velocities respectively. There was close agreement between the theoretical and experimental results, but there were some discrepancies. There are several possible sources of error when using this technique, the most likely being that the method of determining both the frequency of a ‘group’ (inverting the crossing interval) and the arrival times is inaccurate, the source to receiver distance may have been inaccurately measured, or that the velocities used to calculate the theoretical curve were different to the actual velocities in the sample.

Figure 5.9(a) shows the phase information obtained from the FFT of the contact capacitance transducer waveform. This is the uncorrected phase, and has numerous discontinuities of π which must be removed as described at the end of Section 5.2. The

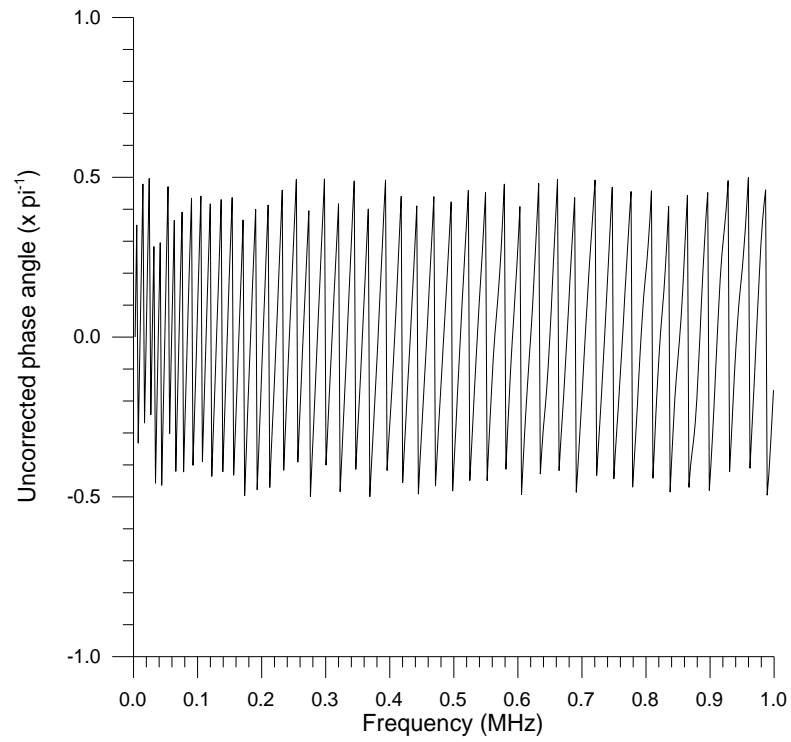


Figure 5.9(a): Uncorrected phase information from the contact capacitance transducer waveform in a 1.2mm aluminium sheet.

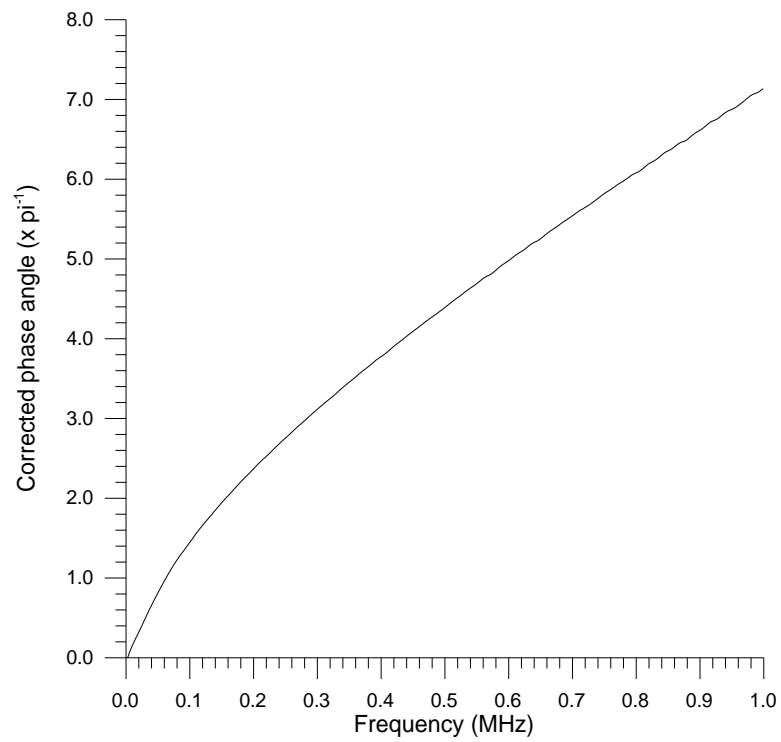


Figure 5.9(b): Corrected phase information from the contact capacitance transducer waveform in a 1.2mm aluminium sheet.

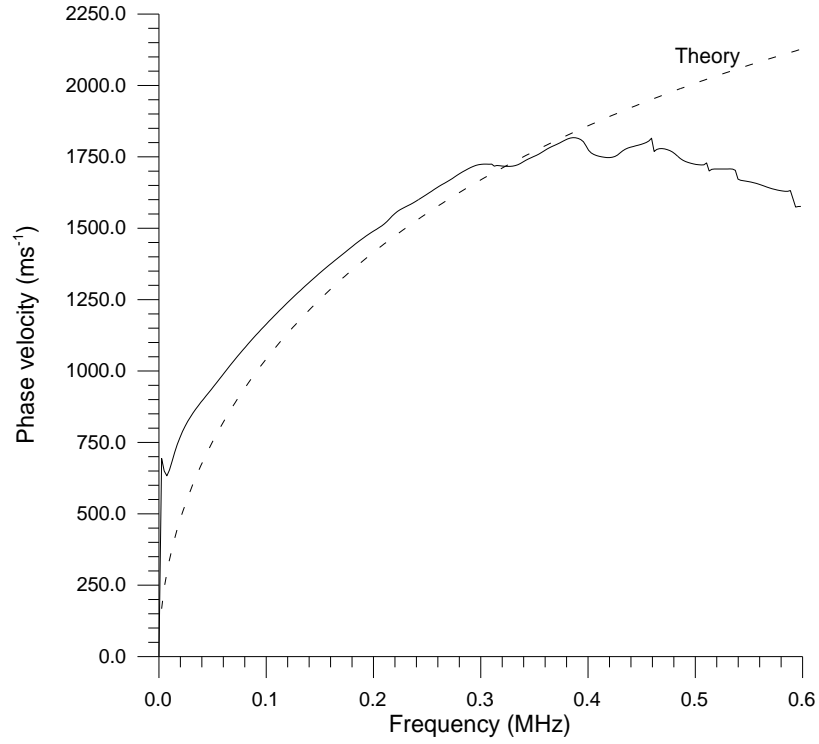


Figure 5.10: a_0 phase velocity in a 1.2mm aluminium plate, found using the FFT phase reconstruction technique and a contact capacitance transducer - theory vs. experiment.

resulting corrected phase information is shown in Figure 5.9(b). Using the known propagation path length of 55mm, the reconstructed phase velocity dispersion curve is shown in Figure 5.10, for the aluminium plate and the contact capacitance transducer. The experimental data follows the shape of theoretical prediction, but does not agree at high frequencies. The data is also suspect at very low frequencies because (a) the bandwidth of the Cooknell amplifier is only well characterised at frequencies in excess of 10kHz, and (b) the low frequency information contained in the FFT is limited by the length ΔT of the time domain waveform, i.e.:

$$f_{\min} = \frac{1}{2\Delta T} \quad \{5.20\}$$

Similarly, at higher frequencies the information is limited to the upper resolution limit given by:

$$f_{\max} = \frac{1}{2\Delta t} \quad \{5.21\}$$

Due to the 10MHZ bandwidth of the amplifier, higher order modes were present, superimposed over the dispersive a_0 signal. Interference between these modes may have occurred, particularly at the higher a_0 frequencies, but the upper frequency limit of the air-coupled transducer is low enough so that only the zero order modes will be detected. By using a larger number of points in the time domain waveform so that the accuracy of this technique improves, the methods described seemed suitable for use with air-coupled ultrasound for frequencies up to a few hundred kHz .

5.6 Experiments using the air-coupled detector

By replacing the contact capacitance detector with an air-coupled transducer, similar waveforms were detected in air. Note that the contact device directly measured the surface displacement caused by the passage of the Lamb wave through the plate, whereas the air-coupled transducer measures the leaky modes of the Lamb wave. Waves of different velocity will radiate into air at different angles as dictated by Snell's law, and so reception of the symmetric and asymmetric modes will be optimised at different angles. Figure 5.11 shows a selection of Lamb waves taken at different transducer orientations to the plate. As expected, the s_0 mode (travelling at approximately the longitudinal velocity c_L) was optimised at $\theta=2.5^\circ$, and the a_0 mode (travelling at velocities less than the transverse velocity c_t) was optimised at angles of $\theta=7^\circ$ and above. As the s_0 mode did not disperse significantly over this frequency range, it was optimised over only a narrow range of angles.

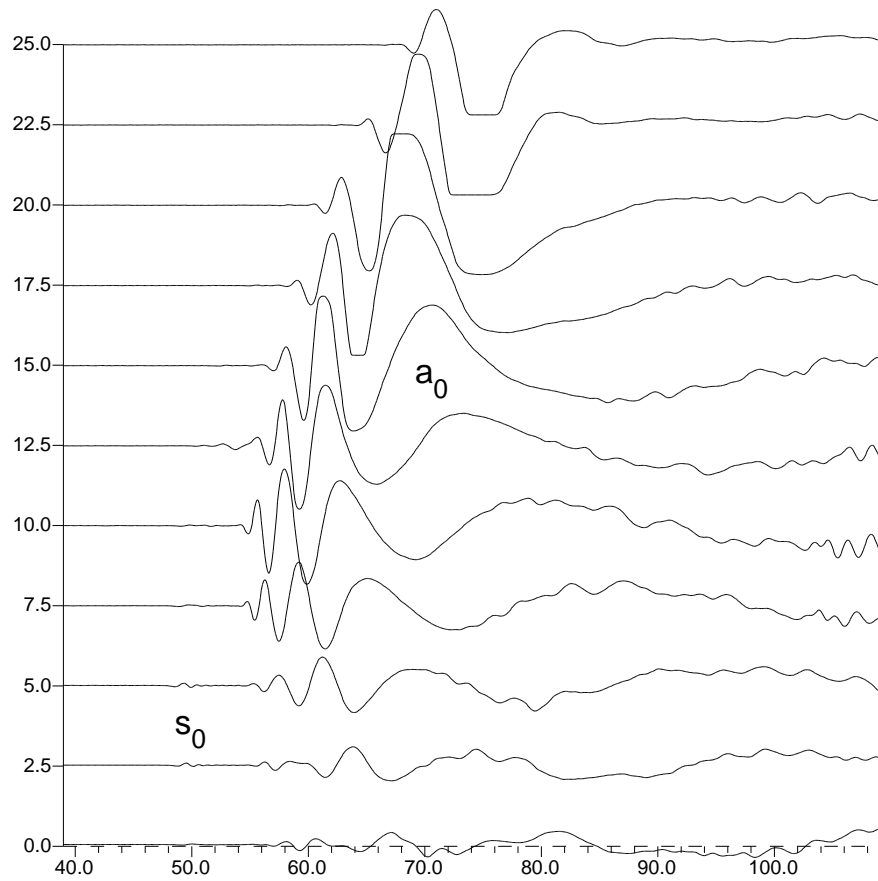


Figure 5.11: A selection of air-coupled Lamb waves in 1.2mm aluminium at transducer/plate angles of 0° to 25°.

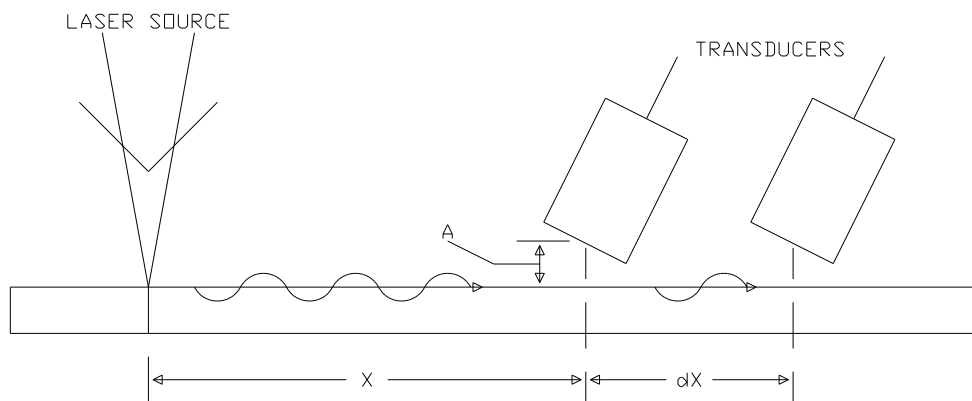


Figure 5.12: Using a difference technique, where X is the known propagation length in the sample, A is the unknown propagation length in the air gap, and dX is the change in the sample propagation path.

Conversely, the highly dispersed a_0 mode was optimised over a wide range of angles (and hence velocities). As the bandwidth of the air transducer was approximately 1.5MHz, only the two zero order modes (a_0 and s_0) were present in these waveforms. The amplitude of the a_0 mode was much greater than those for the s_0 mode, due to the larger normal motion of the plate caused by propagation of the Lamb wave. As the a_0 mode was present at all angles and gave a larger signal to noise ratio, it was decided to use this mode for the remainder of the analysis.

The phase and group velocity dispersion curves cannot be determined accurately from the waveforms shown in Figure 5.11, as the propagation path is not precisely known due to the air gap. In addition, the air gap will change as the transducer is rotated, and as the receiver aperture is large (10mm), then this air gap cannot be accurately determined. There is also an unknown phase delay at the laser source. In order to overcome these unknowns, a difference technique was employed which is shown schematically in Figure 5.12. The air-coupled receiver was situated some distance X from the laser source, with a suitable air gap A , and a waveform recorded. The receiver was then moved parallel to the surface of the plate a known distance dX , so that the perpendicular air gap A was unchanged, and another waveform recorded. By subtracting the phase and group information of these two waveforms, the unknown air gap and any phase offset at the source was eliminated. Thus, any changes were due to the known change in propagation path in the sample, and the velocities could be calculated with greater accuracy.

5.6.1 Group velocity dispersion curves

The group velocity dispersion curve for the 1.2mm thick aluminium plate as measured using the difference technique is shown in Figure 5.13, averaged over a range of

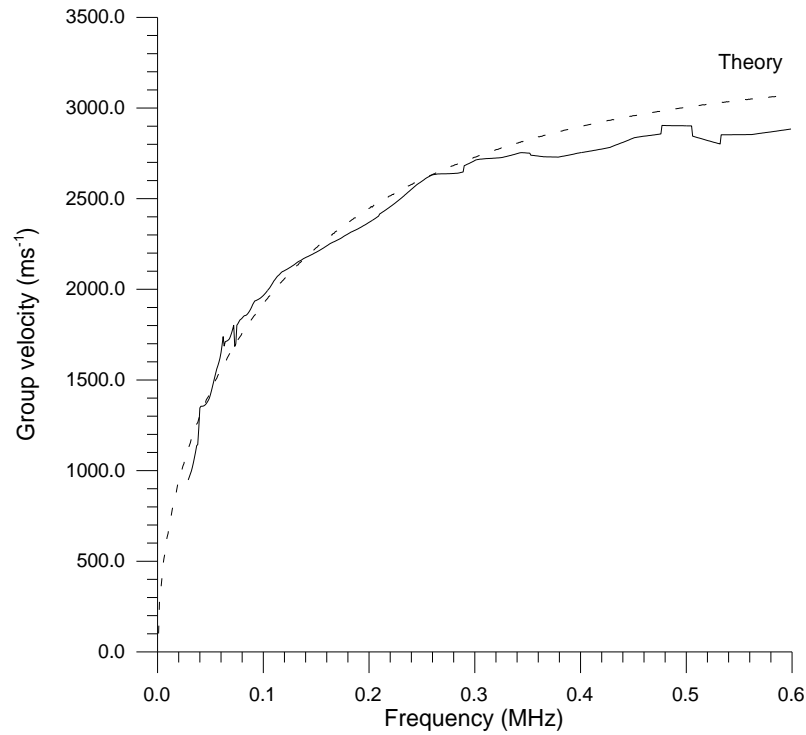


Figure 5.13: Group velocity dispersion curve for a 1.2mm aluminium plate, found using the zero crossing technique.

transducer angles. It can be seen that the experimental data follows the theoretical curve much more closely than the previous results for the same plate using the contact capacitance transducer, shown earlier in Figure 5.8. The zero crossing method loses accuracy at higher frequencies, as the digitisation interval of the time domain waveform begins to limit the precision with which (a) the arrival time and (b) the frequency of each ‘group’ can be determined. Similar results were obtained in a thinner (0.69mm thick) aluminium plate, where the discrepancies at higher frequencies were larger than for the thicker sample. At the lower frequency end of the spectrum, the dispersion between successive zero crossings was greater, and so the assumption used to determine the frequency of a ‘group’ may not have been valid.

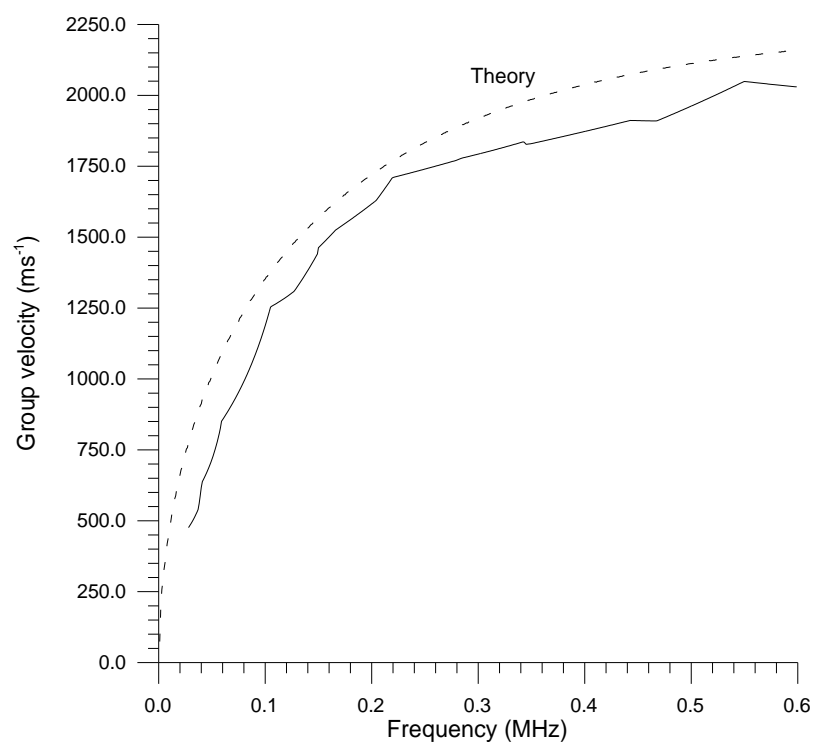


Figure 5.14: Group velocity dispersion curve for a 0.85mm brass plate, found using the zero crossing technique.

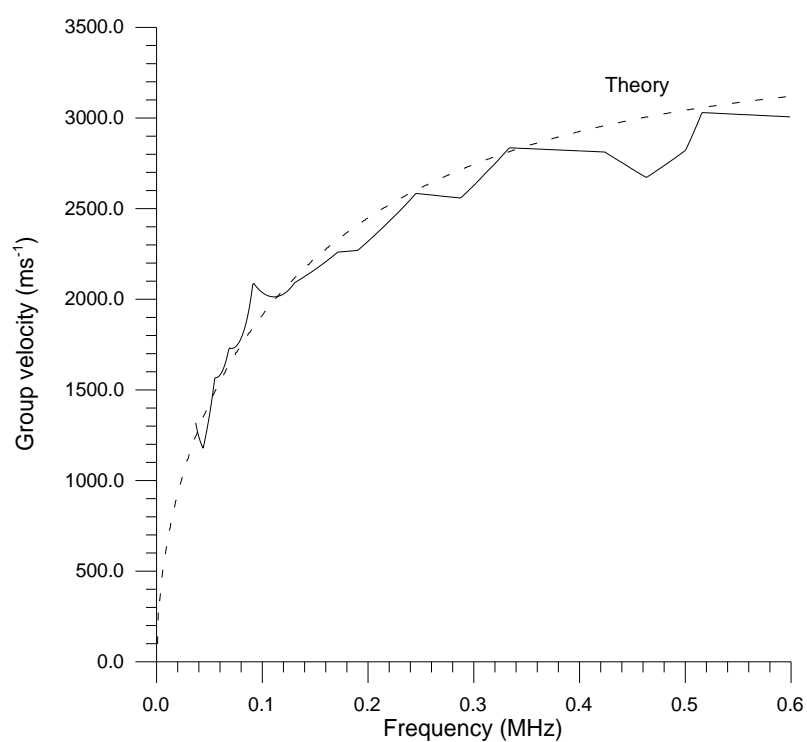


Figure 5.15: Group velocity dispersion curve for a 1.18mm steel plate, found using the zero crossing technique.

The technique was applied to plates of other materials, with curves for 0.85mm thick brass and 1.18mm thick mild steel being shown in Figures 5.14 and 5.15 respectively. The discrepancies between theory and experiment for brass are attributed to the values of longitudinal and shear velocity used in the calculations, which are known to vary widely between different brasses of the same composition, due to the extremely crystalline structure of the material. By replacing the Nd:YAG laser with a Lumonics ‘Lasemark’ Model 630 CO₂ TEA laser, which produced 8J pulses of 100ns duration at 10.6μm in the far infra-red spectrum, a 1.5mm thick sheet of polymethylmethacrylate (PMMA or perspex) was also be tested with similar results.

5.6.2 Extracting the sheet thickness from the group velocity dispersion curves

The method used by Dewhurst *et al.* [26] assumed that the plate was thin enough so that there was little or no dispersion of the zero order symmetric mode. The group velocity of this s_0 mode would then tend towards a single value known as the sheet velocity, c_s . This is in turn related to the square of the group velocity c_g of the zero order asymmetric a_0 mode by the expression:

$$c_g^2 = \frac{4 \cdot \pi \cdot f \cdot t}{\sqrt{3}} \cdot c_s \quad \{5.22\}$$

where t is the plate thickness and $f = \omega/2\pi$. As the s_0 mode was not present in the data obtained, the values of the sheet velocity had to be calculated from the material properties using the following relation:

$$c_s = \left[4 \left(\frac{\lambda + \mu}{\lambda + 2\mu} \right) \frac{\mu}{\rho} \right]^{\frac{1}{2}} \quad \{5.23\}$$

where ρ is the density of the material, and λ and μ are the Lamé constants, given by:

$$\mu = \frac{E}{2(1 + \nu)} \quad \{5.24\}$$

$$\lambda = \frac{E}{3(1 - 2\nu)} - \frac{2}{3\mu} \quad \{5.25\}$$

where E is the Young's modulus and ν is the Poisson's ratio of the material. The physical constants used to calculate the sheet velocities in aluminium, brass and steel are shown in Table 5.2, with the theoretical sheet velocities c_s . By rearranging equation {5.22} to isolate the thickness, the following expression is obtained:

$$t = \frac{\sqrt{3}}{4 \cdot \pi \cdot c_s} \cdot \frac{c_g^2}{f} \quad \{5.26\}$$

where the term containing c_s is the gradient of a graph of c_g^2 against f that passes through the origin. Dewhurst *et al.* [26] used the slope of a best fit line passing through the first four data points and the origin. For this study, the first linear portion of each plot of c_g^2 was used, as shown in Figures 5.16(a) to 5.16(c) for the aluminium, brass and steel sheets respectively. The estimated sheet thickness of each material, along with the measured thickness and percentage difference, is shown in Table 5.3.

Material	ρ (kg.m ⁻³)	ν	E (x10 ⁹ Pa)	μ (x10 ⁹ Pa)	λ (x10 ⁹ Pa)	c_s (ms ⁻¹)
Aluminium	2800	0.34	73.0	27.24	57.88	5429
Brass	8500	0.35	100.0	37.04	86.42	3662
Steel	7860	0.29	210.0	81.40	16.67	5646

Table 5.2: Physical constants and the calculated sheet velocities c_s .

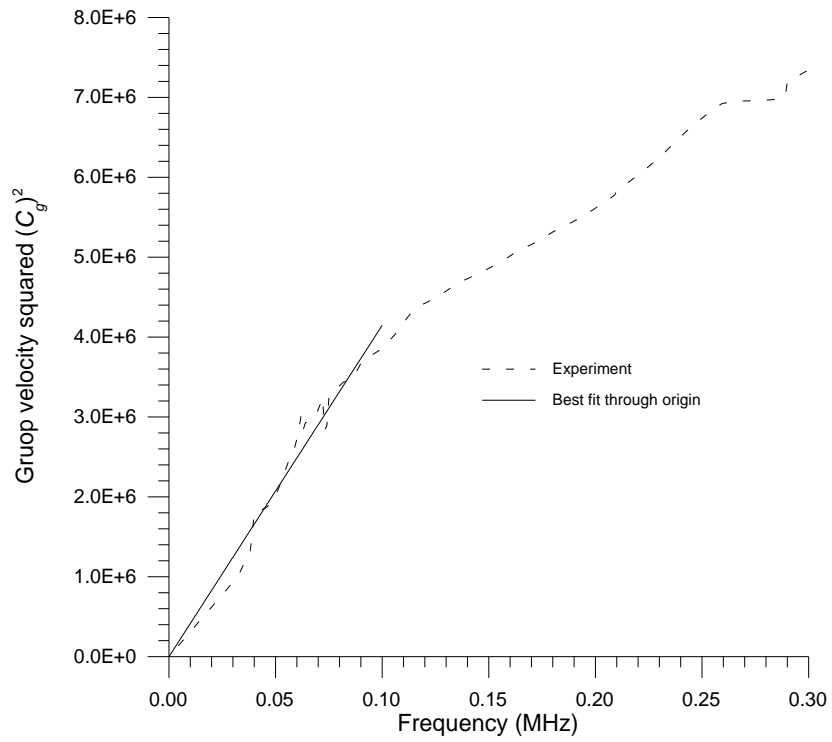


Figure 5.16(a): Best fit line through origin and first part of curve for the square of the group velocity in a 1.2mm aluminium plate. Gradient of best fit is $41.39\text{m}^2\text{s}^{-3}$

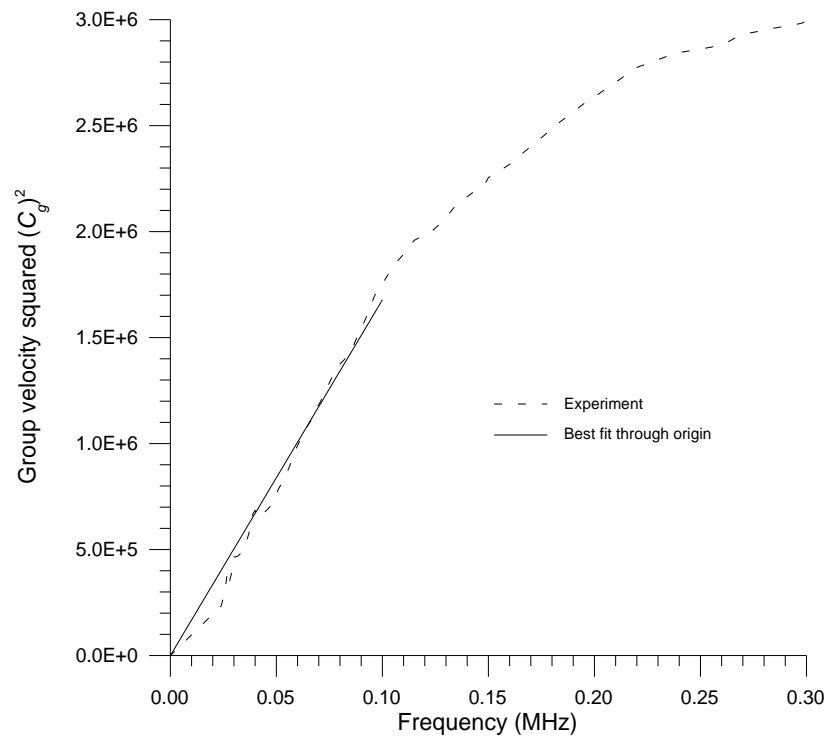


Figure 5.16(b): Best fit line through origin and first part of curve for the square of the group velocity in a 0.85mm brass plate. Gradient of best fit is $16.8\text{m}^2\text{s}^{-3}$

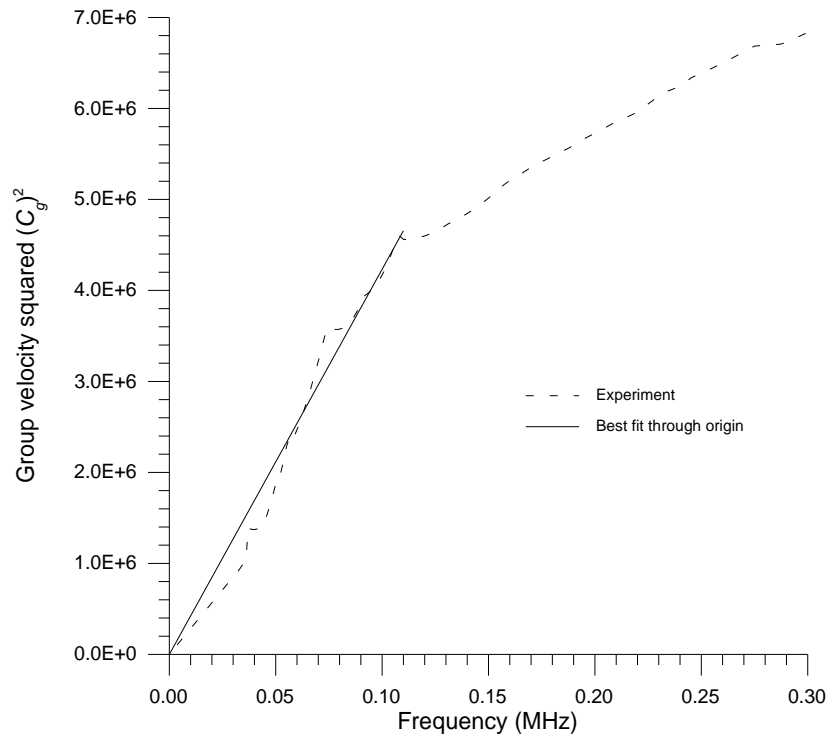


Figure 5.16(c): Best fit line through origin and first part of curve for the square of the group velocity in a 1.2mm mild steel plate. Gradient of best fit is $42.33\text{m}^2\text{s}^{-3}$

	Estimated thickness (mm)	Measured thickness (mm)	Difference (%)
Aluminium	1.07	1.20	11%
Brass	0.67	0.85	21%
Steel	1.11	1.18	6%

Table 5.3: Comparison of measured and estimated thickness.

The high difference between estimated and measured thickness for brass (21%) was most probably due to the use of inaccurate material constants, and hence an incorrect value for the sheet velocity, c_s .

5.6.3 Phase velocity dispersion curves

The phase velocity dispersion curve calculated using the FFT reconstruction technique for a 0.69mm thick aluminium plate is shown in Figure 5.17, and there is excellent agreement between the experimental and theoretical curves. The low frequency portion of the experimental curve is suspect, as this phase information when obtained from the FFT is not real measured data, as the waveforms were padded from 2048 points to 4096 points prior to the FFT. This was to decrease the digitisation interval in the frequency domain, as the lowest measurable frequency is determined by the total length of the time domain waveform, as mentioned previously in equation {5.20}. By padding the waveform with zeros to increase ΔT before the FFT to increase the frequency resolution, additional errors are introduced, as the true signal over this period should contain low frequency flexural modes which are difficult to compensate for.

Similar results were obtained in steel plates, as shown in Figure 5.18 for a 0.254mm (0.010") thick shim, although the higher frequency portion of the curve is more distorted than that for the aluminium. Dispersion curves were also obtained for shims 0.381mm (0.015"), 0.127mm (0.005"), and 0.0762mm (0.003") thick, with the agreement between theory and experiment tending to reduce with decreasing thickness. This was due in part to greater distortion of the shims themselves, and the practical difficulties encountered when clamping the thinner specimens during the experiments. Note that more higher frequency information was available in the steel specimens than for the aluminium plate. Anisotropy may be one other explanation for the increasing errors between theory and experiment for the thinner steel shims, as they will also become more anisotropic with reduced thickness due to the rolling processes in their manufacture.

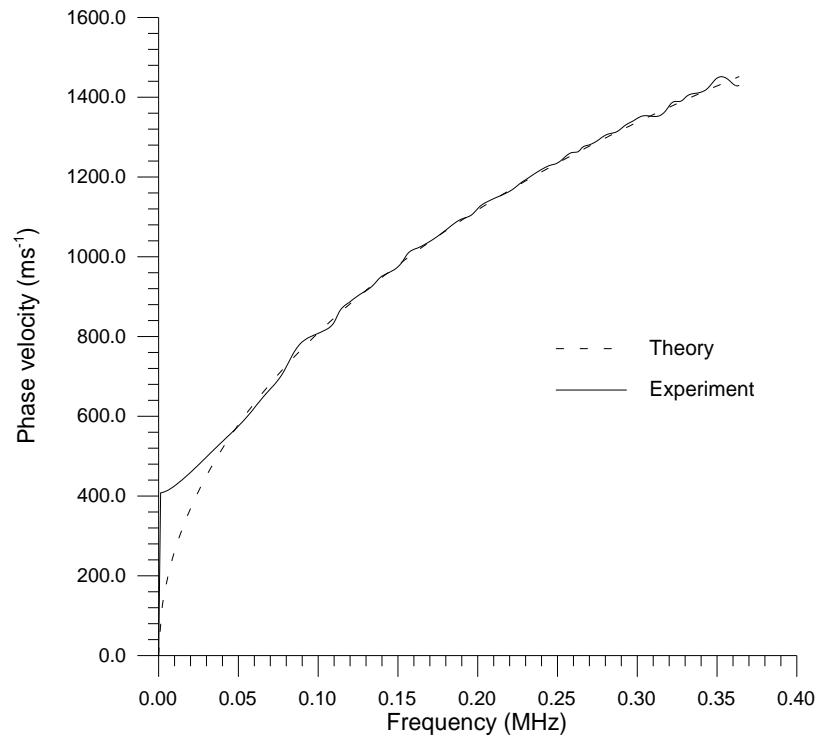


Figure 5.17: Phase velocity dispersion curve for a 0.69mm aluminium plate, found using the FFT reconstruction technique.

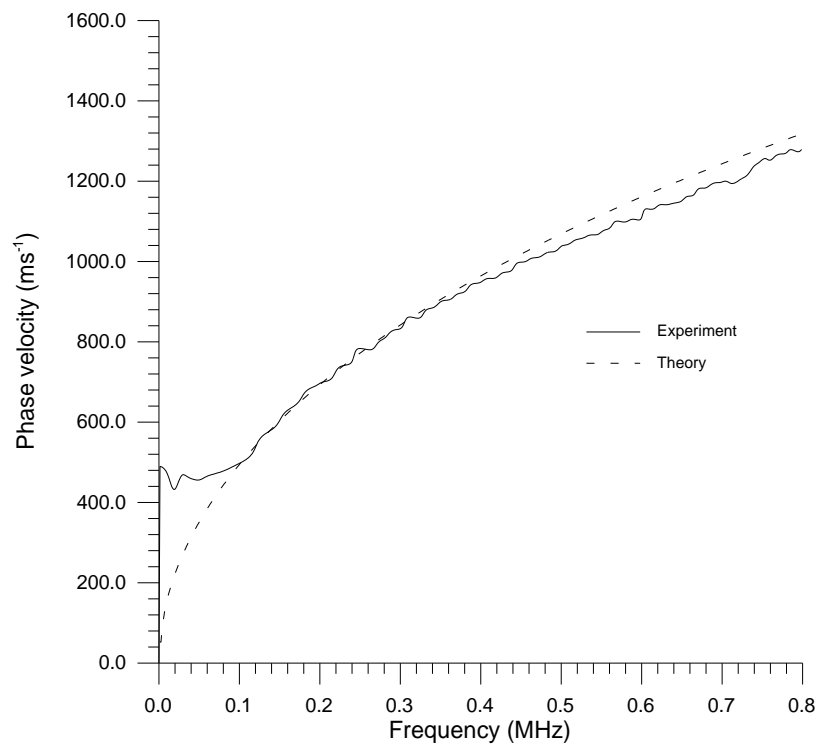


Figure 5.18: Phase velocity dispersion curve for a 0.254mm (0.010”) steel shim, found using the FFT reconstruction technique.

Nominal thickness (mm)	Estimated thickness (mm)	Percentage difference
0.381	0.38	0.3%
0.254	0.25	1.6%
0.127	0.13	2.4%
0.0762	0.08	5.0%

Table 5.4: Nominal thickness, estimated thickness and percentage difference.

5.6.4 Extracting the sheet thickness from the phase velocity dispersion curves

The earlier work by Hutchins *et al.* [29] and Oksanen *et al.* [35] used an approximation to the dispersion relation to try and obtain the material properties. In this work to determine the plate thickness, the experimentally obtained phase velocity dispersion curves were compared directly to the theoretical curves using the well known χ^2 (chi-squared) numerical fitting between two curves, given by:

$$\chi^2 = |D(i) - F(i)|^2 \quad \{5.27\}$$

where $D(i)$ is the i^{th} data point, and $F(i)$ is the i^{th} point of the fitting function. A best fit is achieved when χ^2 is a minimum. The results for the various steel shims between 0.381mm (0.015”) and 0.0762mm (0.003”) thick are shown in Table 5.4, with the nominal thickness, estimated thickness and percentage difference. The discrepancies are less than 5% of the nominal thickness, and the difference increases with decreasing shim thickness.

Figure 5.19(a) shows a typical air-coupled Lamb wave obtained in a 0.254mm (0.010”) thick brass plate, and is typical of Lamb waves in various thickness of this

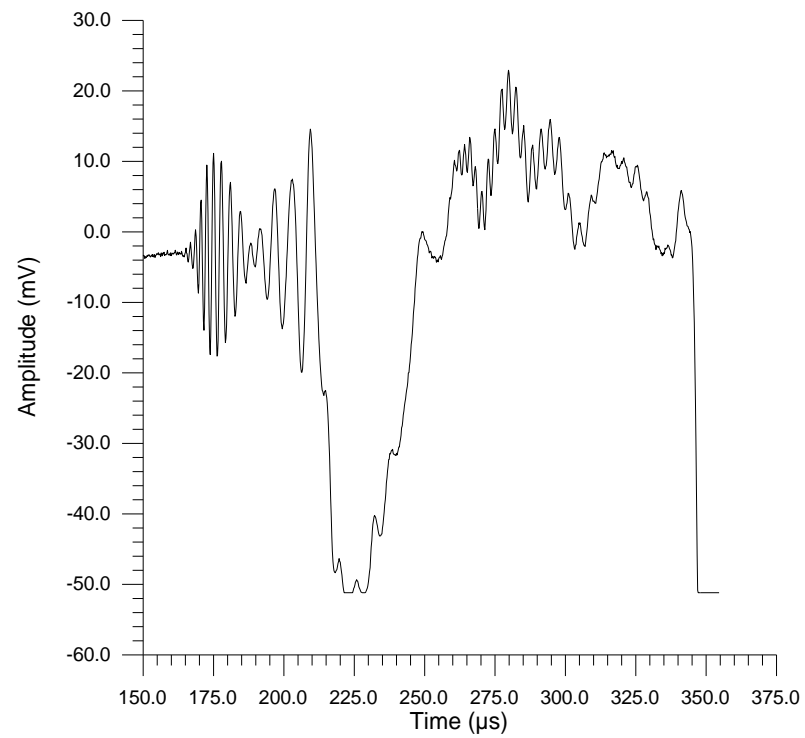


Figure 5.19(a): A typical Lamb wave in 0.254mm brass shim.

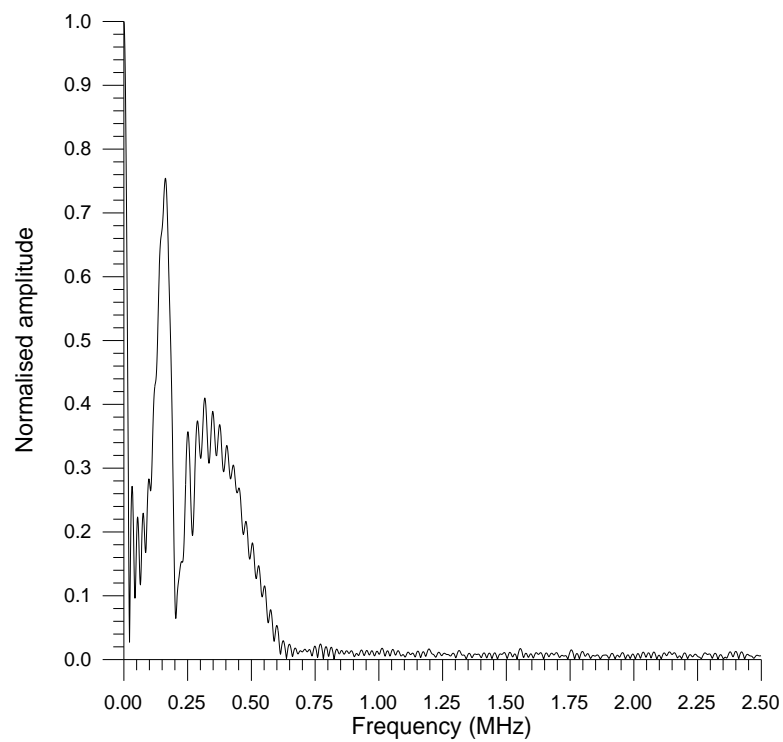


Figure 5.19(b): The fast Fourier Transform (FFT) of Figure 5.19(a).

material. There appears to be some form of modulation in the first part of the signal, caused by the interference of two waves with similar frequencies. This is further demonstrated by the FFT of the Lamb wave, shown in Figure 5.19(b), where there are two spectral peaks. It is possible that the brass was so isotropic that quasi-shear modes were producing two similar asymmetric modes which were interfering. The theory outlined in this chapter is restricted to isotropic materials, and so without accurate knowledge of the physical significance of this phenomenon, further experiments in brass shim were not performed.

5.7 Entirely air-coupled experiments

A second set of experiments was performed, using the apparatus shown schematically in Figure 5.20, where the pulsed laser source had been replaced by a second air transducer, so that the entire system was air-coupled. The source was driven using a Panametrics pulser/receiver model 5055PR, which generated transient voltages of approximately -200V. Both the source and receiver were orientated at the same angle to the plate, and offset to allow the Lamb waves to propagate in the sample before being detected. The difference technique employed with the laser source was again used here.

The phase velocity dispersion curve for a 0.69mm aluminium plate is shown in Figure 5.21, and there is reasonable agreement between 0.1 and 0.25MHz. Similar results were obtained in 0.381mm (0.015") and 0.254mm (0.010") thick steel shims. Discrepancies between the theoretical curves and the experimental data are more prominent than for the laser source, because of practical problems aligning both the source and receiver transducers with the plate, and the reduced bandwidth and energy of the source, as all three curves appear to agree best with the theoretical predictions over the same frequency range.

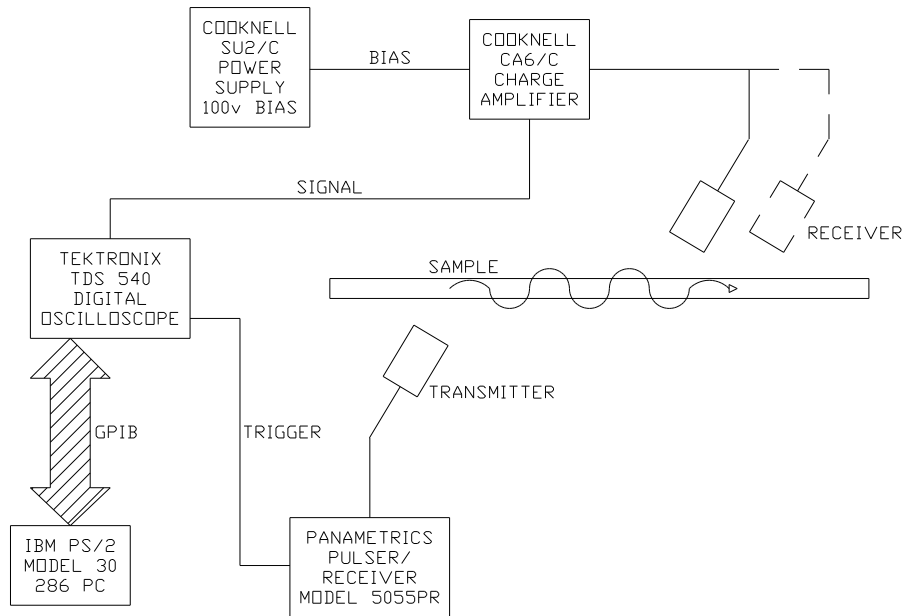


Figure 5.20: Schematic diagram of apparatus for entirely air-coupled testing using Lamb waves.

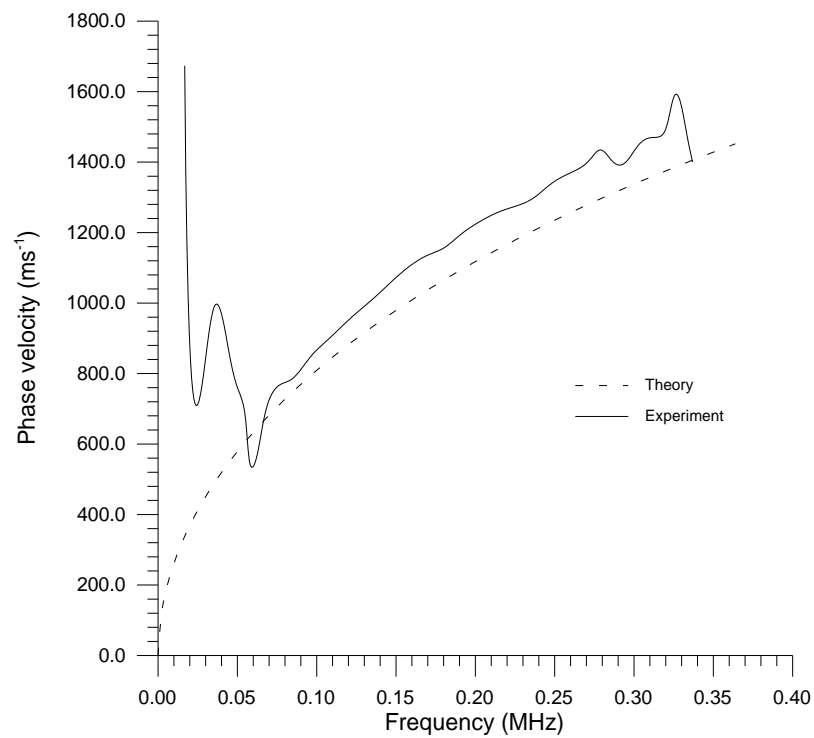


Figure 5.21: Phase velocity dispersion curve for a 0.69mm aluminium plate, obtained using air-coupled source and receiver.

5.8 Discussion

The two methods of Lamb wave analysis used in this chapter have different requirements when collecting the experimental data. The zero crossing technique requires as small a time sampling interval as possible, so that each crossing point may be precisely determined. For the FFT phase reconstruction technique, a long total time is needed to ensure both accurate low frequency sampling, and that the change in phase between successive points in the FFT is less than π radians. This means that either a large number of data points or a long sampling interval is needed. In practice, a compromise between the two had to be used, due to the physical limitations of the oscilloscope and the memory available on the PC used for analysis.

It would seem from the limited success of the air transducer as a source that there was insufficient bandwidth and signal energy to investigate metal shims using an entirely air-coupled system. Both transducers need to be inclined at the correct angle for maximum energy transfer, and the range of frequencies which leak into air at that angle will also be limited. Using a laser source increased the bandwidth of the Lamb wave generated in the shims, and hence the accuracy of the results. The pulsed laser may not be practical for use on thin polymer films, though, as localised melting of the sample would probably occur, and so the entirely air-coupled technique may have more success with polymer and composite materials, particularly as the impedance mismatch between the sample and air would be reduced. This would be an ideal subject for further investigation.

The zero crossing technique, while simple and quick to implement, has several possible sources of error. The sheet velocity in the material must be known to determine the plate thickness, and to avoid using material constants obtained from the literature, this must be measured experimentally using the s_0 mode. However, the s_0 mode only

approaches the sheet velocity when the sample is extremely thin, or when the wavelength is very small (i.e.: at high frequencies). The angles at which the s_0 and a_0 modes leak into the surrounding air are different, and so the air transducer may only be optimised for one of them at a time.

The FFT phase reconstruction technique would appear to be more accurate, although computationally laborious as the comparison of the theoretical and experimental curves using the χ^2 technique requires the calculation of multiple curves for samples of different thickness and frequency ranges. A single curve of frequency-thickness product could be used, but the theoretical and experimental points would not necessarily coincide, and so some form of interpolation would be required and thus introduce further errors. As with the zero crossing technique, the bulk wave velocities must be known in the material to determine the plate thickness, and the values in thin rolled shims may differ widely from the theoretical values, or those obtained from thicker samples. The FFT phase reconstruction technique has the advantage that it may be used for any Lamb mode in any thickness of plate, provided that the individual modes can be isolated. In addition, the technique may be used to evaluate both phase and group velocity dispersion, as the group velocity curve may be found by a simple differentiation of the phase dispersion curve.

5.9 Conclusions

Two techniques have been used to estimate the thickness of thin metal plates using non-contact leaky Lamb waves. Using a pulsed laser source and a micromachined air-coupled capacitance transducer as a receiver, a difference technique was employed to overcome the unknown delays of the air gap between plate and receiver. The thickness was estimated by comparing the zero order mode velocity dispersion curves to theoretical

predictions calculated by a FORTRAN program. The first experimental technique determined the group velocity dispersion curves using a zero crossing method, and the thickness of aluminium and steel plates 1.2mm thick was estimated to within 11%, and a brass plate to within 21%. The second technique reconstructed the phase velocity dispersion curves from the FFT of a Lamb wave, and the thickness of steel shims between 0.07mm and 0.4mm thick were estimated to within 5%.

Limited success was achieved using an air-transducer as the ultrasonic source due to the reduced bandwidth, although this technique shows promise for future work with broadband transducers. The techniques shown here may be used to test any isotropic sample, and could also be applied to anisotropic materials such as fibre reinforced composites if the theoretical dispersion curves can be calculated.

5.10 References

- [1] H. Lamb, 'On waves in an elastic plate', *Proc. Royal Society London, Series A*, **93**, 114-128 (1917)
- [2] R.D. Mindlin, 'Waves and vibrations in isotropic elastic plates', in *Structural Mechanics*, J.N. Goodier and N.J. Hoff (eds.), (Pergamon, New York, 1950)
- [3] I.A. Viktorov, 'Rayleigh and Lamb waves - Physical Theory and Applications', Plenum Press, New York (1967)
- [4] J.D. Achenbach, 'Wave Propagation in Elastic Solids', Elsevier Science Publishers, Netherlands (1990)
- [5] J. Wolf, T.D.K. Ngoc, R. Kille and W.G. Mayer, 'Investigation of Lamb waves having a negative group velocity', *J. Acoust. Soc. Am.* **83**, 122-126 (1988)

- [6] Q. Zhu and W.G. Mayer, 'On the crossing points of Lamb wave velocity dispersion curves', *J. Acoust. Soc. Am.* **93**, 1893-1895 (1993)
- [7] D.S. Chandrasekharaiah, 'Rayleigh-Lamb waves in an elastic plate with voids', *J. Appl. Mech.* **54**, 509-512 (1987)
- [8] W. Maysenhölder, 'Analytical determination of the group velocity of an arbitrary Lamb wave from its phase velocity', *Acustica* **77**, 208 (1992)
- [9] J. Kaplunov, J. Nolde and N. Veksler, 'Determination of parameters of elastic layer by measured dispersion curves of zero-order Lamb-type waves', *Proc. Estonian Acad. Sci. Phys. Math.* **41**, 39-48 (1992)
- [10] A.K. Mal, P.-C. Xu and Y. Bar-Cohen, 'Analysis of leaky Lamb waves in bonded plates', *Int. J. Eng. Sci.* **27**, 779-791 (1989)
- [11] M.R. Karim and A.K. Mal, 'Inversion of leaky Lamb wave data by simplex algorithm', *J. Acoust. Soc. Am.* **88**, 482-491 (1990)
- [12] R.Y. Vasudeva and P.G. Rao, 'Influence of voids in interface zones on Lamb wave propagation in composite plates', *J. Acoust. Soc. Am.* **89**, 516-522 (1991)
- [13] D.E. Chimenti and A.H. Nayfeh, 'Leaky Lamb waves in fibrous composite laminates', *J. Appl. Phys.* **58**, 4531-4538 (1985)
- [14] A.N. Podlipenets and N.A. Shulga, 'Numerical study of the propagation of Rayleigh and Lamb waves in orthotropic periodic structures', *Soviet Applied Mechanics* **23**, 1013-1017 (1987)
- [15] B. Tang and E.G. Henneke II, 'Lamb-wave monitoring of axial stiffness reduction of laminated composite plates', *Mat. Eval.* **47**, 928-934 (1988)
- [16] D. Noiret and J. Roget, 'Calculation of wave propagation in composite materials using the Lamb wave concept', *Journal of Composite Materials* **23**, 195-206 (1989)

- [17] G.R. Liu, J. Tani, K. Watanabe and T. Ohyoshi, 'Lamb wave propagation in anisotropic laminates', *J. Appl. Mech.* **57**, 923-929 (1990)
- [18] V. Dayal and V.K. Kinra, 'Leaky Lamb waves in an anisotropic plate. I: An exact solution and experiments', *J. Acoust. Soc. Am.* **85**, 2268-2276 (1989)
- [19] D.E. Chimenti and R.W. Martin, 'Nondestructive evaluation of composite laminates by leaky Lamb waves', *Ultrasonics* **29**, 13-21 (1991)
- [20] V. Dayal and V.K. Kinra, 'Leaky Lamb waves in an anisotropic plate. II: Nondestructive evaluation of matrix cracks in fiber-reinforced composites', *J. Acoust. Soc. Am.* **89**, 1590-1598 (1991)
- [21] W. Lin and L.M. Keer, 'A study of Lamb waves in anisotropic plates', *J. Acoust. Soc. Am.* **92**, 888-894 (1992)
- [22] T. Kundu and B. Maxfield, 'A new technique for measuring Rayleigh and Lamb wave speeds', *J. Acoust. Soc. Am.* **93**, 3066-3073 (1993)
- [23] L.R. Dragonette, 'Schlieren visualization of radiation caused by illumination of plates with short acoustical pulses', *J. Acoust. Soc. Am.* **51**, 920 (1972)
- [24] J.-F. Piet, G. Quentin, M. de Billy, Q.-G. Zhu and W.G. Mayer, 'Phase of Lamb wave radiation from a plate immersed in a liquid', *Ultrasonics* **30**, 297-300 (1992)
- [25] L.G. Merkulov, 'Damping of normal modes of a plate immersed in a liquid', *Sov. Phys. Acoust.* **10**, (1964)
- [26] R.J. Dewhurst, C. Edwards, A.D.W. McKie and S.B. Palmer, 'Estimation of the thickness of thin metal sheet using laser generated ultrasound', *Appl. Phys. Lett.* **51**, 1066-1068 (1987)
- [27] D.A. Hutchins, K. Lundgren and S.B. Palmer, 'A laser study of transient Lamb waves in thin materials', *J. Acoust. Soc. Am.* **85**, 1441-1448 (1989)

- [28] H. Nakano and S. Nagai, 'Laser generation of antisymmetric Lamb waves in thin plates', *Ultrasonics* **29**, 230-234 (1991)
- [29] S.E. Bobbin, J.W. Wagner and R.C. Cammerata, 'Determination of the flexural modulus of thin films from measurement of the first arrival of the symmetric Lamb wave', *Appl. Phys. Lett.* **59**, 1544-1546 (1991)
- [30] S.E. Bobbin, J.W. Wagner and R.C. Cammerata, 'Interpretation of laser-generated low-order Lamb waves for elastic modulus measurements in thin films', *Ultrasonics* **30**, 87-90 (1992)
- [31] N.A. Schumacher, C.P. Burger and P.H. Gien, 'A laser-based investigation of higher-order modes in transient Lamb waves', *J. Acoust. Soc. Am.* **93**, 2981-2984 (1993)
- [32] H.I. Ringermacher, F.A. Reed and J.R. Strife, 'Laser ultrasonics for coating thickness evaluation at 1200°C', in *Review of Progress in Quantitative Nondestructive Evaluation*, Vol. 12, Plenum Press (1993)
- [33] H.J. Salzburger, 'Defect characterisation by multimode testing of steel strips and plates with E.M.A. excited Lamb waves', *Proc. Ultrasonics International 1979 Conf.*, (IPC Press, London, 1979), p404
- [34] M. Luukkala, P. Heikkila and J. Surakka, 'Plate wave resonance - a contactless test method', *Ultrasonics*, **11 (October)**, 201-208 (1971)
- [35] M. Oksanen, J. Stor-Pellinen and M. Luukkala, 'Determining mechanical properties of cardboard from photoacoustic Lamb wave transmission data', *Proc. 21st Annual Review of Quantitative NonDestructive Evaluation 1994*, **Vol 15**, (1995)
- [36] H. Carr and C. Wykes, 'Diagnostic measurements in capacitive transducers', *Ultrason.* **31**, 13-20 (1993)

- [37] D.W. Schindel, D.A. Hutchins, L. Zou and M. Sayer, 'The design and characterization of micromachined air-coupled transducers', *IEEE Trans. Ultrason. Ferroelec. Freq. Contr.* **UFFC-42**, 42-50 (1995)
- [38] W. Sachse and Y.-H. Pao, 'On the determination of phase and group velocities of dispersive waves in solids', *J. Appl. Phys.* **49**, 4320-4327 (1978)

Chapter 6: Materials testing using an air-coupled source and receiver

6.1 Introduction

The work to be described in this chapter will examine an entirely air-coupled ultrasonic inspection system which used a pair of broadband capacitance air-coupled transducers with micromachined silicon backplates, as described earlier in Chapter 2. After a brief discussion of the associated problems, the first part of the work will look at the through transmission of bulk modes in a variety of materials including composites, polymers and metals. Later sections will investigate a range of defects in these materials by C-scanning, and the generation and detection of Lamb waves in a range of thin samples, all using an entirely air-coupled system. Most of the work in this chapter has been published by the author [1].

6.1.1 Entirely air-coupled ultrasonics

As stated in Chapter 1, there are several non-contact ultrasonic techniques cited in the literature, but few are suitable for or readily applicable to a wide range of different materials. The use of electromagnetic acoustic transducers (EMATs) [2] and capacitive devices which use the sample itself as one electrode [3] is restricted to electrically conducting materials, and stand-off distances of up to a few millimetres at best. Entirely laser based systems [4] encounter practical problems, in that composite materials tend to have rough surfaces and therefore poor optical reflectivity. Hence, most interferometers and other laser based detectors are either unsuitable, or very expensive and delicate. As sources of ultrasound, pulsed lasers [5-7] are well documented and have been successfully used in many situations, and so the main problem seems to be the lack of a suitable non-contact detector. Air-coupled

transducers have shown great promise in this role, with either piezoelectric [8,9] or capacitance designs [10] being equally successful. However, the laser source is itself not without problems. Some common materials are transparent to certain wavelengths of laser light, and very often the laser generated source is not truly non-destructive, as surface damage or marking may occur due to material ablation.

An ideal system therefore would use air-coupled devices as both source and receiver of ultrasound. As mentioned in earlier chapters, the mismatch of acoustic impedances between air and most solids causes the incident energy to be reduced by a factor of up to 10^8 , due to the presence of two air/solid interfaces. However, this assumption is based on the fact that both interfaces are acting independently, i.e.: that the sample under test is fairly thick when compared to the shortest wavelength. For thinner samples, this is often not the case, and the situation becomes slightly less simplistic. Consider the situation shown in Figure 6.1, where a ‘thin’ sample of solid material with an acoustic impedance Z_2 is surrounded by a medium with an acoustic impedance Z_1 . The transmission coefficient is then given by [11]:

$$T = \frac{1}{\sqrt{1 + \frac{1}{4} \left(\frac{Z_1}{Z_2} - \frac{Z_2}{Z_1} \right)^2 \sin^2 \left(\frac{2\pi d}{\lambda_2} \right)}} \quad \{6.1\}$$

where d is the thickness of the sample and λ_2 is the wavelength in the solid. From the \sin^2 term in equation {6.1} it can be seen that T will be a maximum when:

$$d = \frac{n \cdot \lambda_2}{2} \quad \{6.2\}$$

i.e. when the sample is an integer number of half wavelengths thick. Similarly, T is a minimum when d is an odd number of quarter wavelengths thick. For air ($Z_1 = 420 \text{ kg.m}^{-2}.\text{s}^{-1}$) and a typical polymer ($Z_2 = 3.2 \times 10^7 \text{ kg.m}^{-2}.\text{s}^{-1}$), the transmission

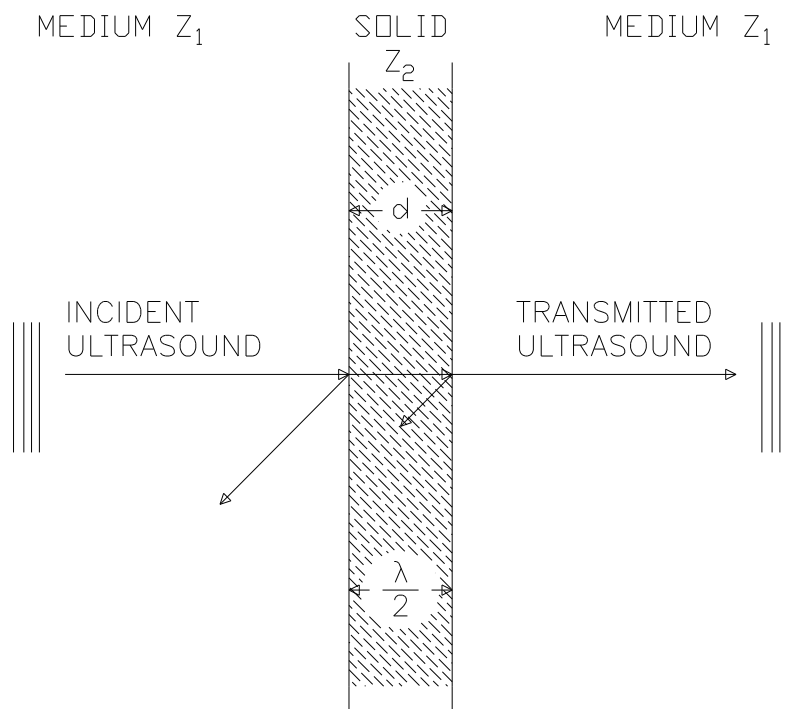


Figure 6.1: Transmission through a thin layer half a wavelength thick.

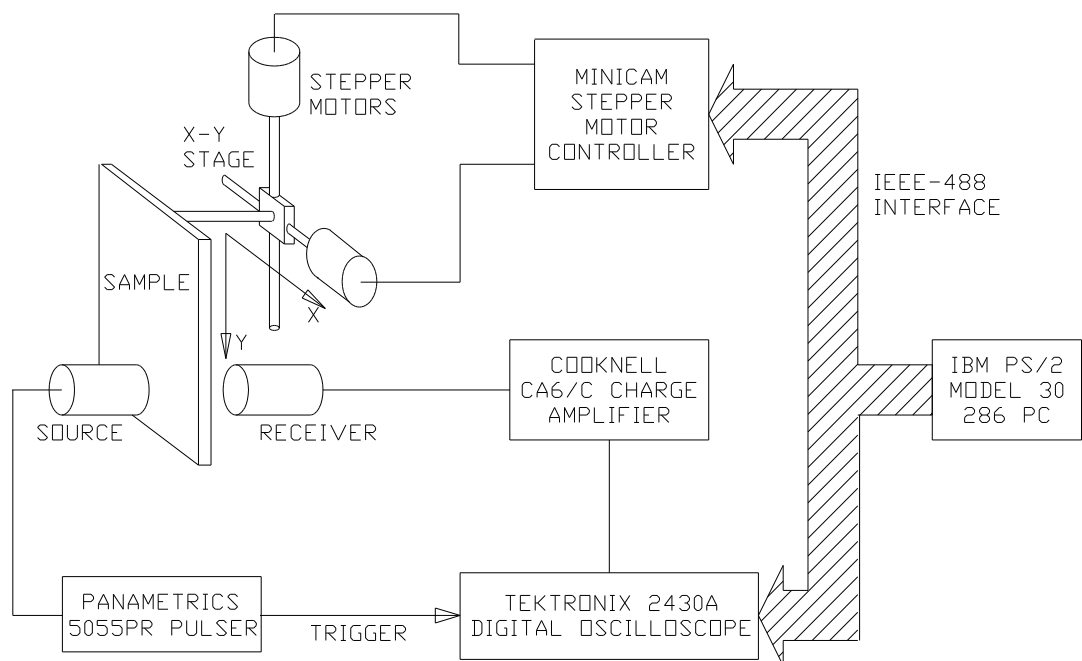


Figure 6.2: Apparatus for through thickness experiments and C-scanning.

coefficient through two separate interfaces gives $T = 2.8 \times 10^{-9}$, but through a sample half a wavelength thick the coefficient is $T = 7.2 \times 10^{-3}$, making entirely air-coupled inspection more feasible, in theory at least. In order to test as wide a range of samples as possible with one air transducer system, air-coupled devices with broad bandwidths and high sensitivities are required, as samples of different thickness and material will have a wide range of wavelengths and frequencies.

6.2 Through thickness experiments

The equipment used for the through thickness experiments is shown schematically in Figure 6.2. A micromachined silicon capacitance transducer, described and characterised in earlier chapters, was driven by a -200V spike with a rise time of $\leq 4\text{ns}$ from a Panametrics 5055PR pulser receiver to generate ultrasound in air. After passing through the sample, the waveform was received by another silicon device, attached to a Cooknell CA6/C charge sensitive amplifier with a 100V d.c. bias applied between the polymer film and backplate electrodes of the transducer. The signal was captured on a Tektronix 2430A digital oscilloscope, and then transferred via an IEEE-488/GPIB interface to an IBM PS/2 Model 30 286 PC for storage and analysis. The PC was also used to control an X-Y translational stage via a Minicam stepper motor controller, to move the sample when acquiring C-scan data. For more detailed equipment specifications, see Appendix A. The air gap between the two transducers was 30mm unless stated otherwise, and either 128 or 256 signal averages were used to improve the signal to noise ratio. Figure 6.3(a) shows a typical waveform transmitted from source to receiver through the air, with no sample between the two transducers.

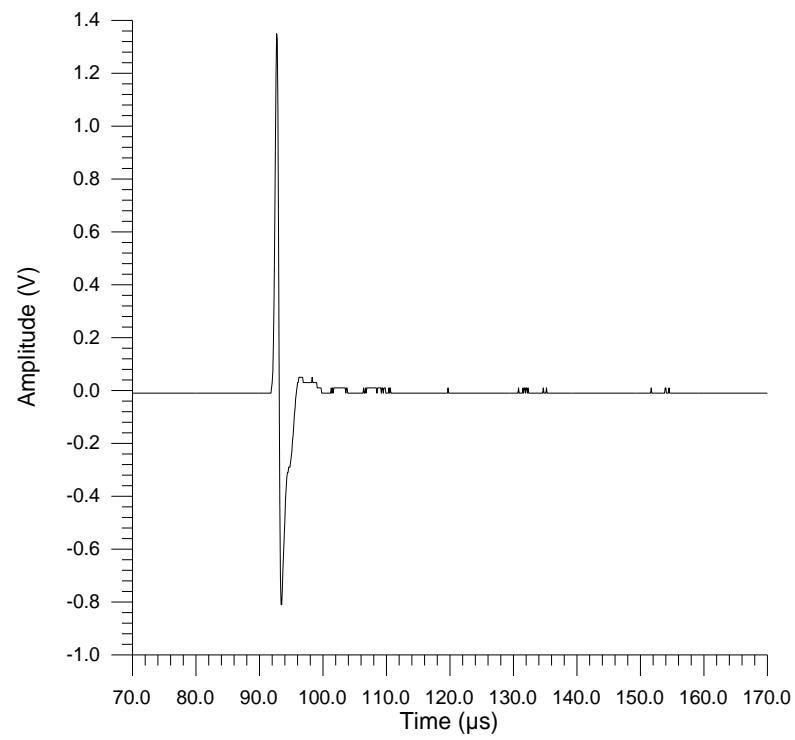


Figure 6.3(a): Waveform through a 30mm air gap.

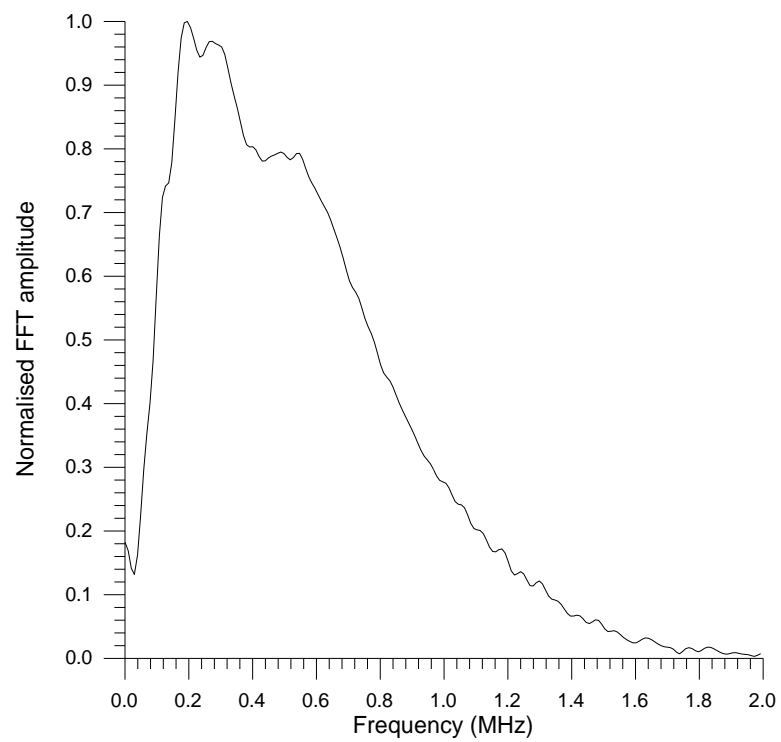


Figure 6.3(b): Frequency spectrum of Figure 6.3(a).

The corresponding frequency spectrum is shown in Figure 6.3(b). The signal is a well damped wide bandwidth response, with useful energy extending well over 1MHz.

6.2.1 Results in CFRP composite materials

A range of CFRP samples, described previously in Chapter 3, were tested by measuring the longitudinal velocity, which is linked to the elastic constants of the material as mentioned in Chapter 1. Figure 6.4(a) shows the waveform obtained through a 16-ply (2.2mm thick) cross-ply plate, with a sustained resonance lasting for approximately 40 μ s. The corresponding frequency spectrum is shown in Figure 6.4(b), with a clearly defined peak at 625kHz, (± 9.8 kHz). Using the known thickness of the plate, this gave a velocity of 2750ms⁻¹ (± 43 ms⁻¹). A similar waveform was obtained in a 16-ply quasi-isotropic plate of the same thickness. However, Figure 6.5(a) shows the signal transmitted through another 16-ply (2.1mm thick) plate, this time with a unidirectional lay-up. The resonance is more heavily damped, and lasts for only approximately 15 μ s. This is confirmed in the frequency spectrum shown in Figure 6.5(b), where the peak is considerably wider than that in Figure 6.4(b). The resonant frequency is still at 625kHz (± 9.8 kHz), giving a similar velocity of 2625ms⁻¹ (± 43 ms⁻¹). This was expected, as the configuration of the layers should not have any marked effect on the through thickness velocities, and any differences are due to variation in the thickness of the plies used to make up the plate. The additional damping may be attributed to the very anisotropic nature of the unidirectional composite, as more energy will be directed along the fibres away from the point of excitation and will not contribute to the formation of the resonance.

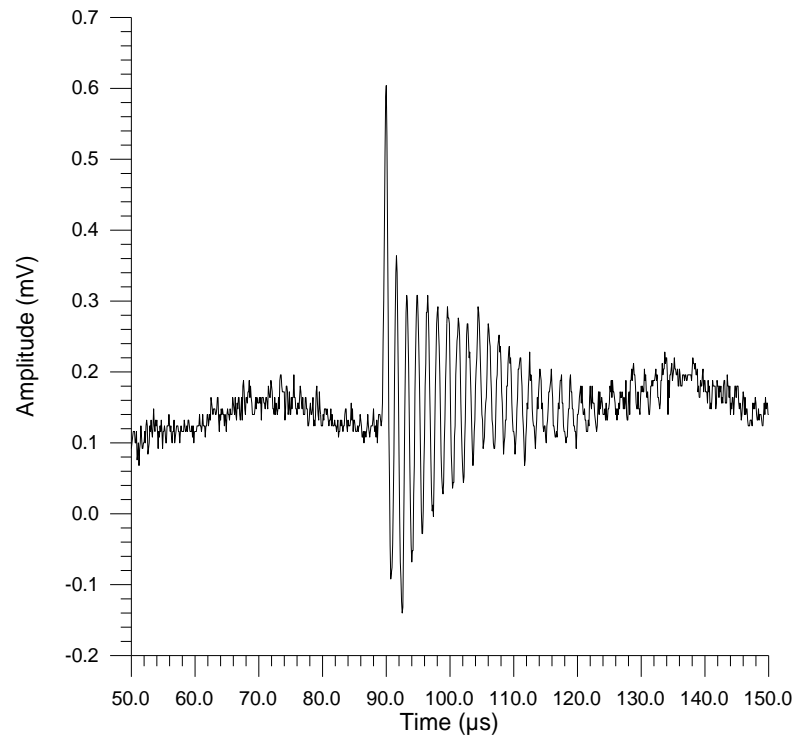


Figure 6.4(a): Waveform obtained through a 16-ply (2.2mm thick) cross-ply CFRP composite plate.

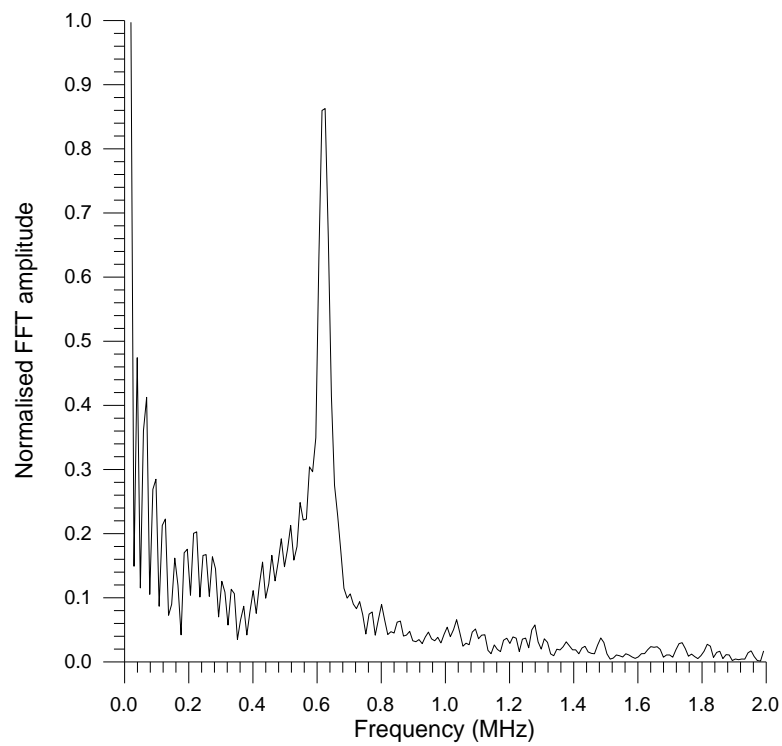


Figure 6.4(b): Frequency spectrum of Figure 6.4(a)

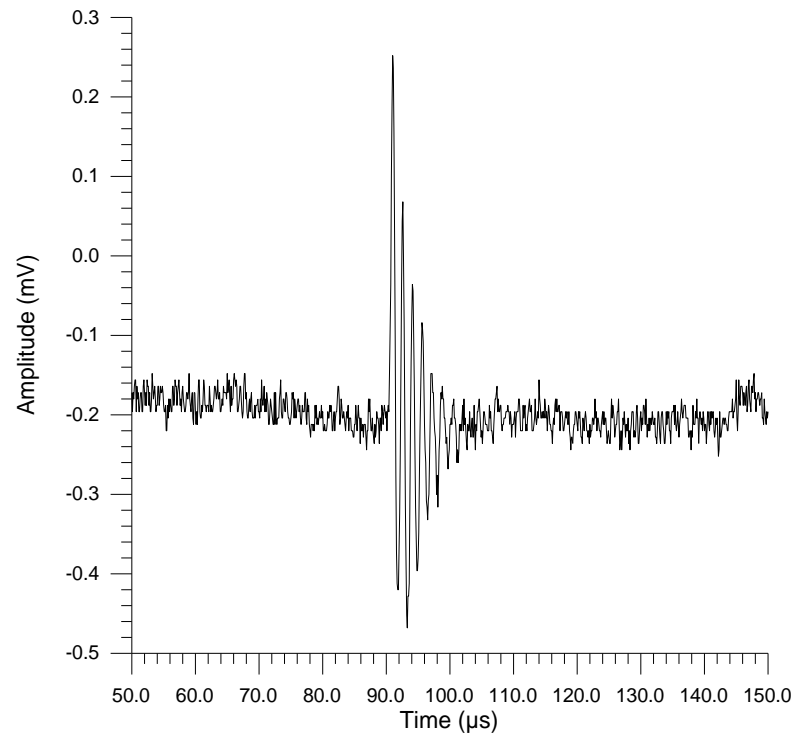


Figure 6.5(a): Waveform obtained through a 16-ply (2.2mm thick) unidirectional CFRP composite plate.

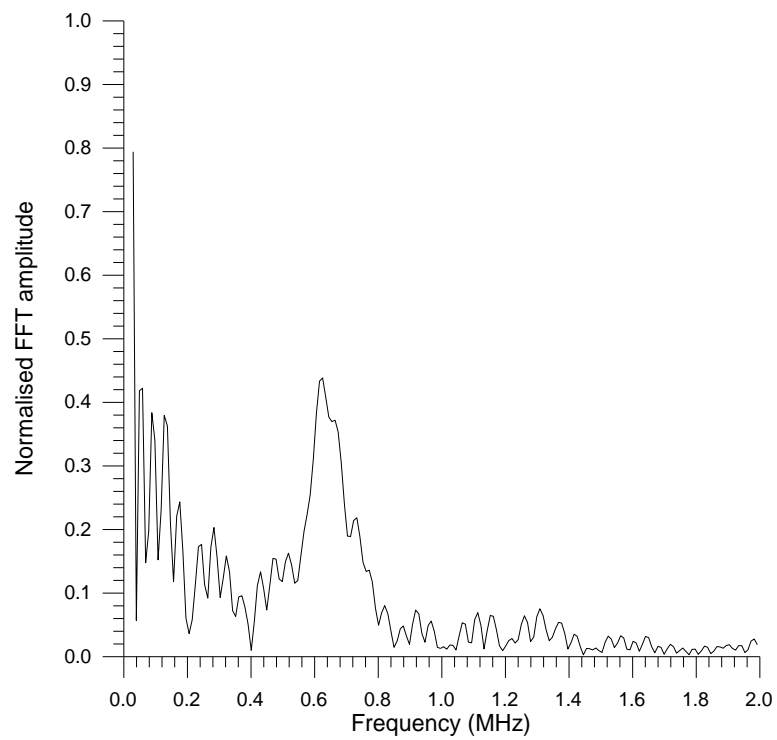


Figure 6.5(b): Frequency spectrum of Figure 6.5(a).

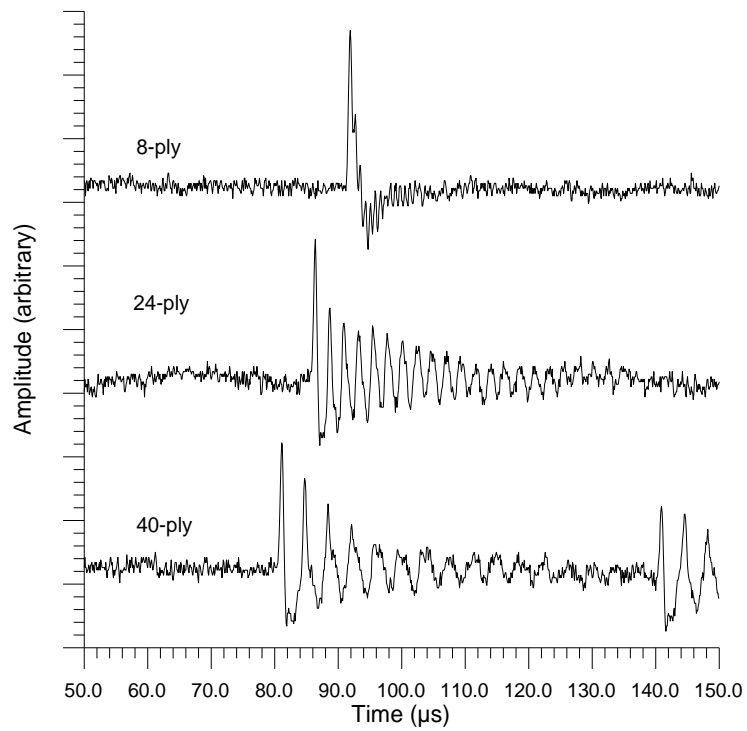


Figure 6.6(a): Waveforms in 8-ply, 24-ply and 40-ply quasi-isotropic CFRP plates.

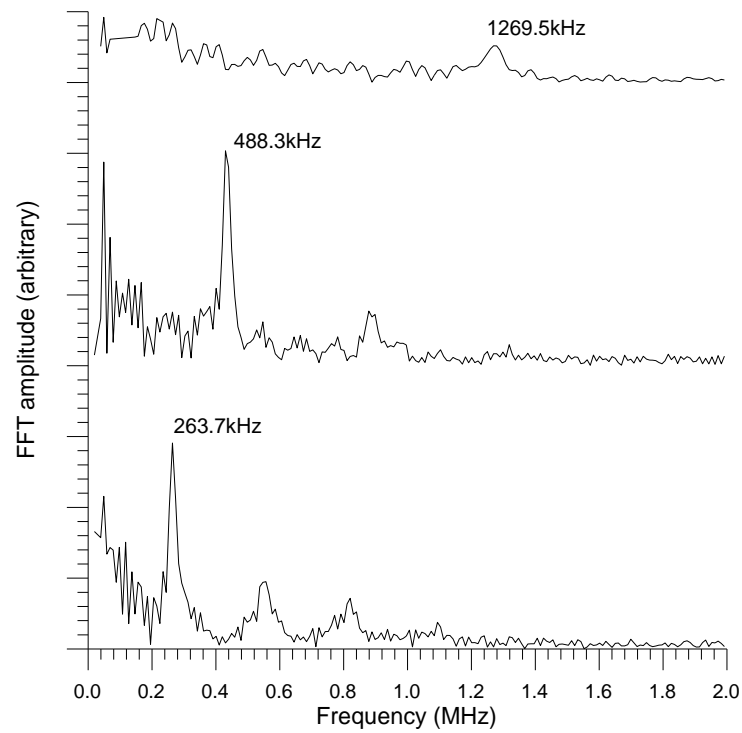


Figure 6.6(b): Frequency spectra of waveforms in Figure 6.6(a).

A range of composite plates 8-ply, 24-ply and 40-ply thick were then tested. Figure 6.6(a) shows the waveforms for three quasi-isotropic plates, with the corresponding frequency spectra in Figure 6.6(b). The sustained resonances produced are very similar to those obtained in the cross-ply plate shown earlier, which is to be expected as these samples are virtually isotropic. For the 40-ply (5.3mm thick) and 24-ply (3.1mm thick) samples, with resonant peaks at 263.7kHz and 488.3kHz (± 9.8 kHz), harmonics of the initial half wave resonances are clearly visible in the frequency spectra in Figure 6.6(b). These occur at frequencies which are an integral number of half wavelengths as stated in equation {6.2}. For the 8-ply (1.0mm thick) plate, the resonant peak of 1.27MHz was close to the upper frequency limit of the device, and the half wave resonance was only just detected. It is interesting to note that the arrival time of each waveform in Figure 6.6(a) decreased as the plate thickness increased, which was expected as a larger proportion of the air gap between the source and receiver was being replaced by a material with a higher velocity. Similar results were also obtained for unidirectional plates. The resonant peaks were wider and not as prominent as those for the quasi-isotropic plates, as the vibrations were more heavily damped due to the anisotropy as mentioned earlier. The resonances for the 40-ply (5.3mm thick) and 24-ply (3.2mm thick) samples were 253.9kHz and 410.2kHz respectively (± 9.8 kHz), and again harmonics were visible at higher frequencies. The peak for the 8-ply (1.0mm thick) composite was at 1.34MHz, although the peak was not very prominent and difficult to clearly distinguish from the background level of the frequency spectrum. This was also evident from the time domain waveform for the 8-ply plate, as there was little apparent resonance in the signal. It was also possible to obtain through thickness waveforms in very thick composite samples, with a signal in a 120-ply (17.5mm thick) unidirectional plate

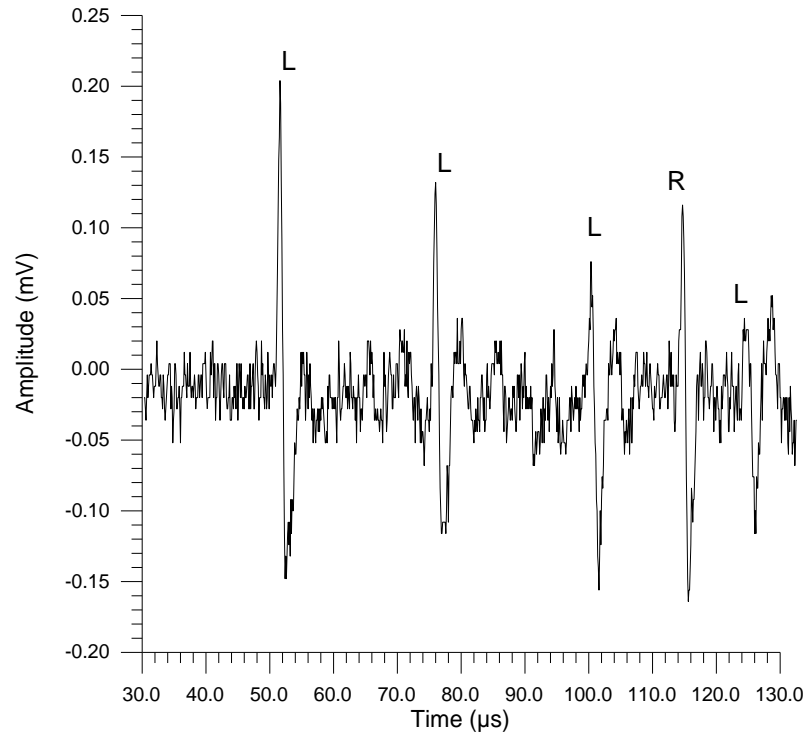


Figure 6.7: Waveform through a 120-ply (17.5mm thick) unidirectional CFRP plate.

shown in Figure 6.7, where discrete reflections L can be observed. The feature at R is the first reflection of the waveform in the air gap between the sample and the face of the receiver.

6.2.2 Results in other materials

Other materials were also successfully tested using the pair of air-coupled transducers. Figure 6.8(a) shows waveforms obtained through 4.0mm and 9.8mm thick samples of pultruded glass fibre reinforced polymer composites, and the associated frequency spectra are given in Figure 6.8(b). The resonant peaks are at 419.9kHz and 127.0kHz respectively (± 9.8 kHz), giving velocities of 3359ms^{-1} and 2489ms^{-1} ($\pm 43\text{ms}^{-1}$), and as for the CFRP samples, harmonics are visible, particularly for the thicker composite. Different matrix resins were used in the manufacture of

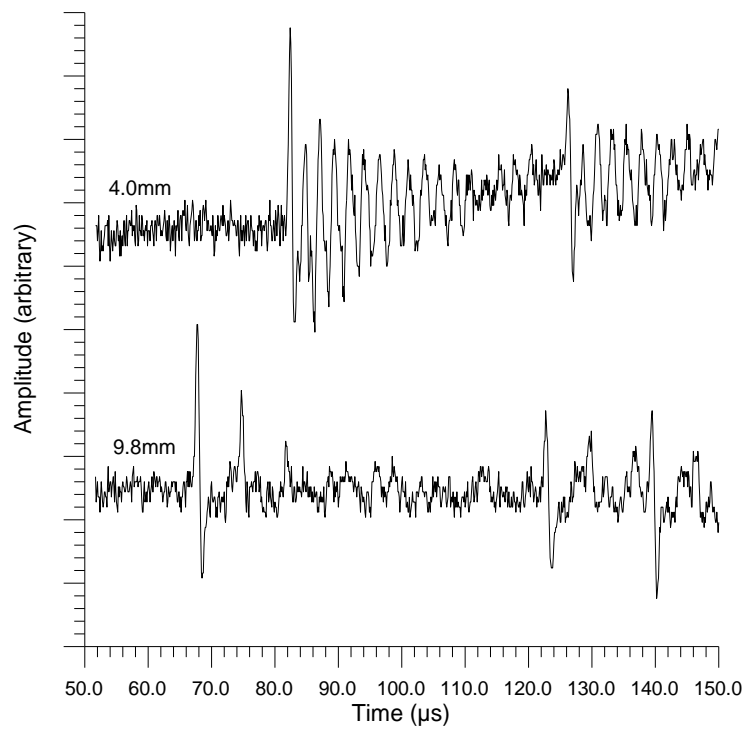


Figure 6.8(a): Waveforms through 4.0mm and 9.8mm thick pultruded glass fibre reinforced polymer composite.

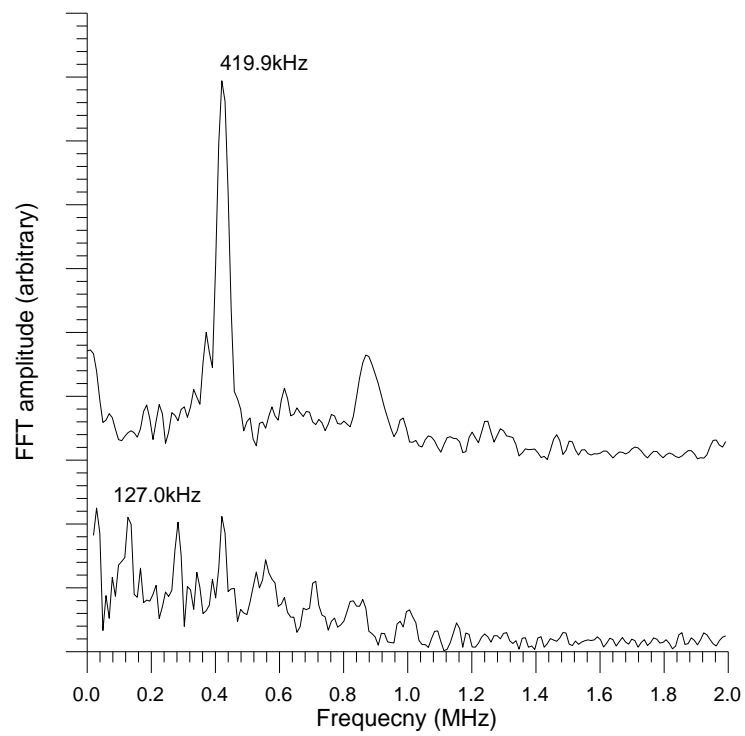


Figure 6.8(b): Frequency spectra of the waveforms in Figure 6.8(a)

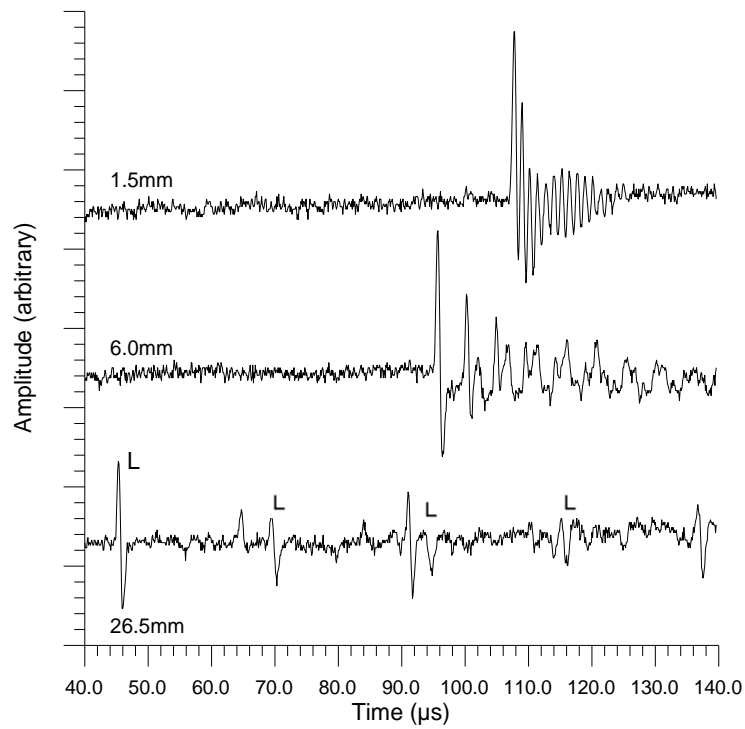


Figure 6.9(a): Waveforms through 1.5mm, 6.0mm and 26.5mm thick perspex (polymethylmethacrylate).

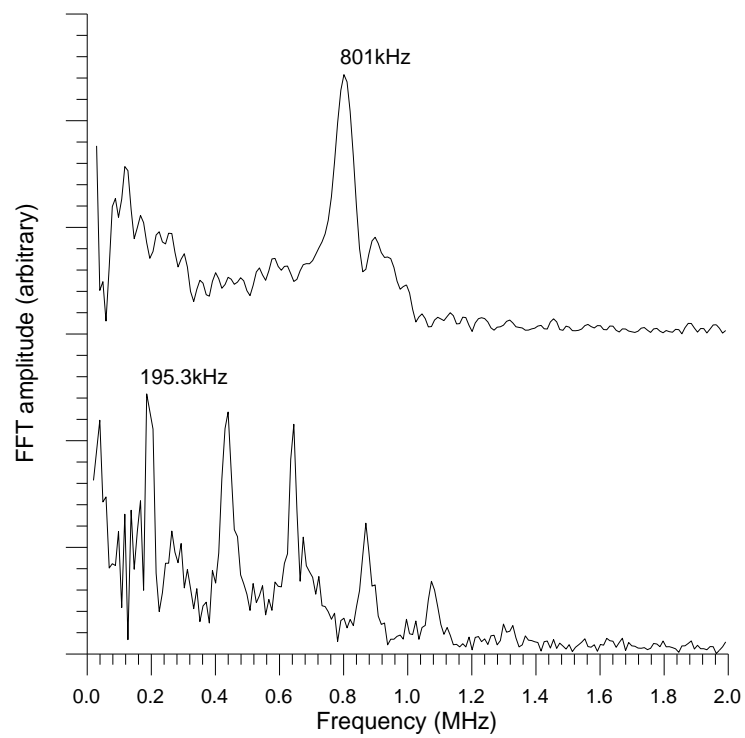


Figure 6.9(b): Frequency spectra of waveforms in 1.5mm and 6.0mm thick perspex.

these two pultruded samples, which accounts for the large difference in velocity. Figure 6.9(a) shows signals obtained in 1.5mm, 6.0mm and 26.5mm thick samples of perspex. Individual longitudinal echoes (L) in the 26.5mm sample can be resolved, so the frequency spectra of the two thinner samples only are given in Figure 6.9(b), where the resonant peaks are at 801kHz and 195.3kHz (± 9.8 kHz) respectively. The corresponding velocities are 2403ms^{-1} , 2344ms^{-1} ($\pm 43\text{ms}^{-1}$) and 2199ms^{-1} (for the 26.5mm sample, using a transit time of $24.1\mu\text{s} \pm 0.1\mu\text{s}$), showing that the velocity appears to decrease with thickness.

One interesting class of materials, for which entirely air-coupled transduction is well suited, is expanded open cell polyurethane foams. In fact, it is difficult to test these foams using any other ultrasonic technique, as (a) any kind of fluid couplant will be absorbed, (b) direct pressure coupling (such as rubber faced transducers) will deform the sample, and (c) any laser based systems will scatter off the surface of the foam. Waveforms are shown in Figure 6.10 for (a) 25mm thick and (b) 12mm thick samples. Due to the highly attenuating nature of these foams, multiple reflections were not detected, and so the direct wave between the source and receiver through air only is given for comparison. It can be seen that the wave through the foam arrives after the wave through the air gap because the velocity of bulk waves in this material is lower than in air, and the propagation of sound in porous foams is actually quite complex [12, 13]. The frequency content of the received wave is also much reduced. Velocities were calculated using the following formula:

$$v_{foam} = \frac{d_{foam}}{t_{gap+foam} - \left(\frac{d_{gap} - d_{foam}}{v_{air}} \right)} \quad \{6.3\}$$

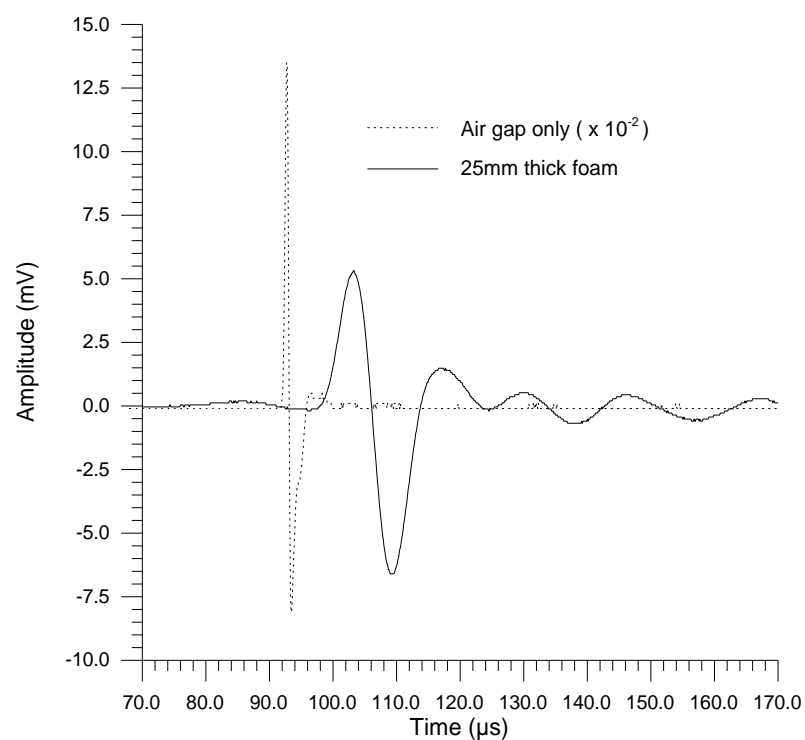


Figure 6.10(a): Waveform through 25mm of expanded polyurethane foam (solid line), and signal through air gap only (dashed line, scaled by 10^{-2} for presentation purposes).

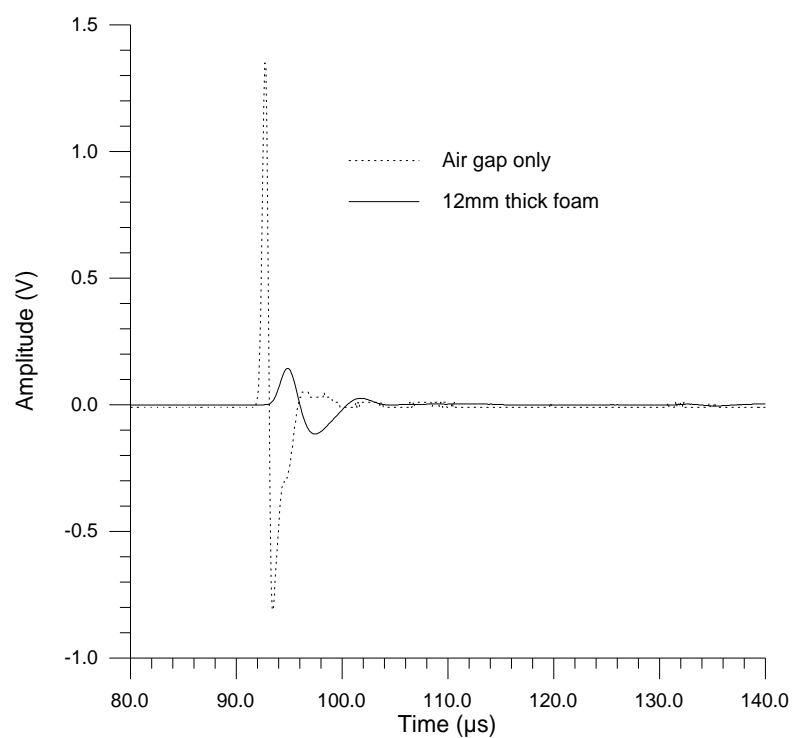


Figure 6.10(b): Waveform through 12mm of expanded polyurethane foam (solid line), and through the air gap only (dashed line to same scale).

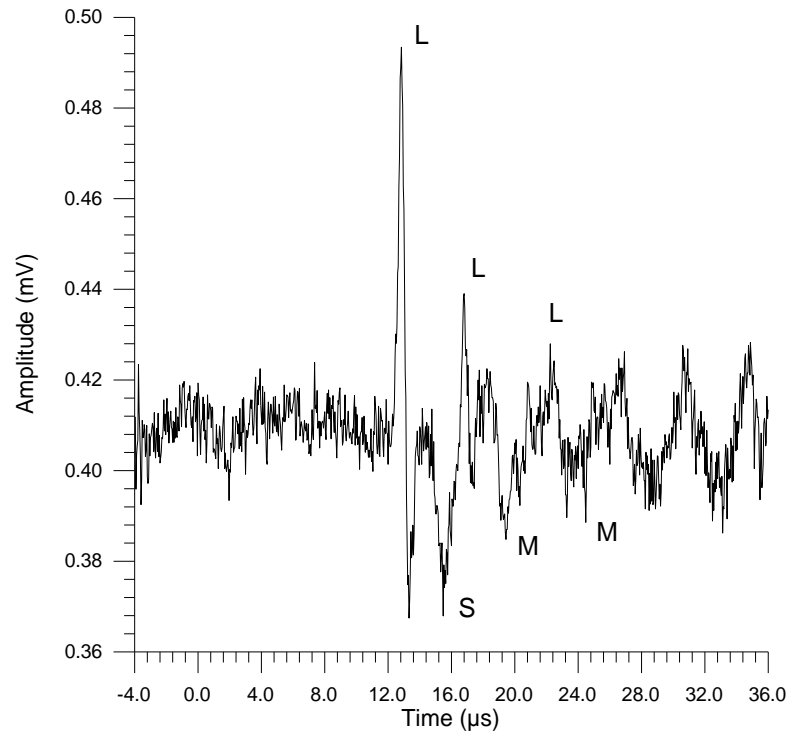


Figure 6.11(a): Waveform through 12.9mm thick aluminium, showing longitudinal arrivals *L*, shear wave arrival *S* and its mode conversions *M*.

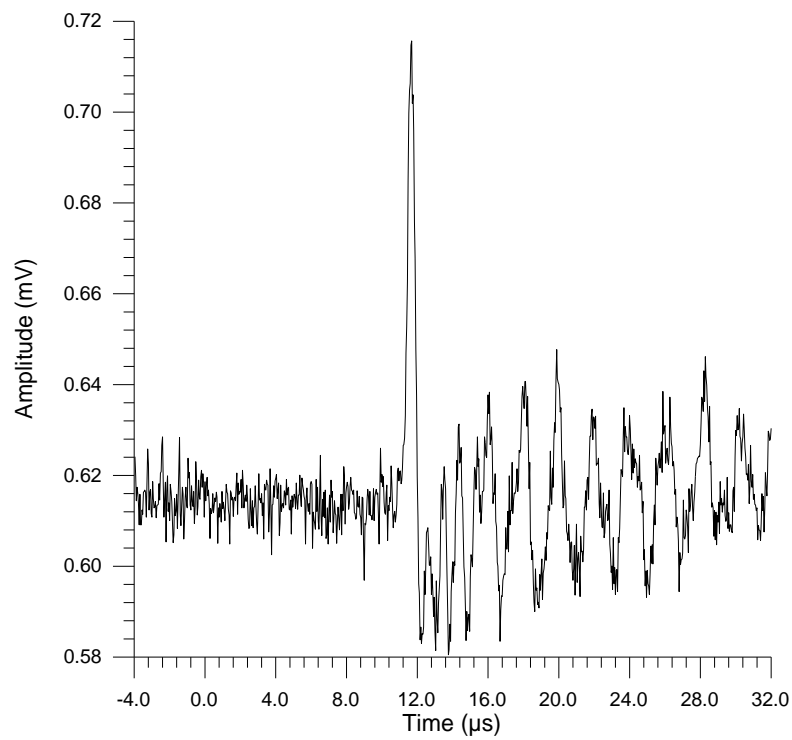


Figure 6.11(b): Waveform through 6.0mm thick aluminium.

where v , d and t are velocity, distance and time respectively. The velocity in the air gap was calculated to be 324ms^{-1} , and the velocities in the foams were found to be 315ms^{-1} and 252ms^{-1} for the thin and thick foams respectively. However, this technique is highly dependent on the accuracy of the measurement of the source-receiver distance and the thickness of the foam samples.

Waveforms were also obtained in samples of aluminium. Figure 6.11(a) shows the through-thickness waveform in a 12.8mm thick sample, and the individual longitudinal echoes (L) may be clearly resolved. The shear wave arrival (S) has also been detected, along with subsequent mode conversions (M). The velocity in aluminium was calculated to be 6505ms^{-1} . This waveform is very similar to those obtained for laser generated signals detected by other air-coupled devices, as shown previously in Chapters 2 and 3. Figure 6.11(b) shows the waveform through a 6mm thick sample, where the separate echoes are difficult to resolve and the resonant frequency analysis used previously is required. Thinner samples of aluminium encountered similar problems to the very thin 8-ply CFRP laminates - the half wave resonant frequencies of the samples were beyond the frequency range of these devices. The signal levels shown here are much lower than for the composite materials due to the greater impedance mismatch between the sample and air, and so the signals shown here were heavily averaged, over 10^4 times.

6.3 C-scanning of defects

As mentioned earlier, the pair of air-coupled transducers was used in a C-scanning system to obtain images of defects in composite materials. Using the apparatus shown previously in Figure 6.2, a range of defects were scanned with a

spatial resolution of 1mm. A digitised waveform which was the result of 128 averages was recorded at each point in the scan, and saved to a PC for storage and later analysis. Software could then be used to perform a variety of different data processing techniques on a single set of waveforms.

Some typical waveforms obtained in a scan are shown in Figure 6.12 for (a) an area of a 16-ply (2.2mm thick) unidirectional CFRP plate without a defect, and (b) a delaminated area of the same plate, with the amplitude axes the same scale for comparison. The delaminations were introduced into the plates by replacing the centre 8 plies with layers of Teflon tape during the lay up of the composite. It can be seen from Figure 6.12 that the resonance, present in the undamaged plate, is completely removed by the presence of the delamination.

A selection of different delaminations were scanned, and the resultant images are displayed in Figure 6.13 for (a) a 1" (25mm) square, (b) a 0.5" (12.5mm) square and (c) a 0.25" (6.25mm) square defect. The images were produced by simply plotting the amplitude of the signal in a specified time window, and the white dashed lines show the expected size, shape and location of each defect. The square shape of the 25mm defect is clearly visible, although diffraction effects due to the size of the source and receiver distort the shape of the 12.5mm and 6.25mm delaminations. The size of each defect is also clearly resolved in each image. Figure 6.13(d) is an image of a delamination in a 6.35mm thick cross-ply CFRP composite, caused by an impact 5mm in diameter, shown by the white dashed circle. It can be seen that the area of delamination is considerably larger than the impact area. Figure 6.14 shows two images obtained in a sample of 9.8mm thick pultruded GRP composite for (a) a 10mm diameter flat recess machined 1mm deep, and (b) a 5mm diameter recess machined

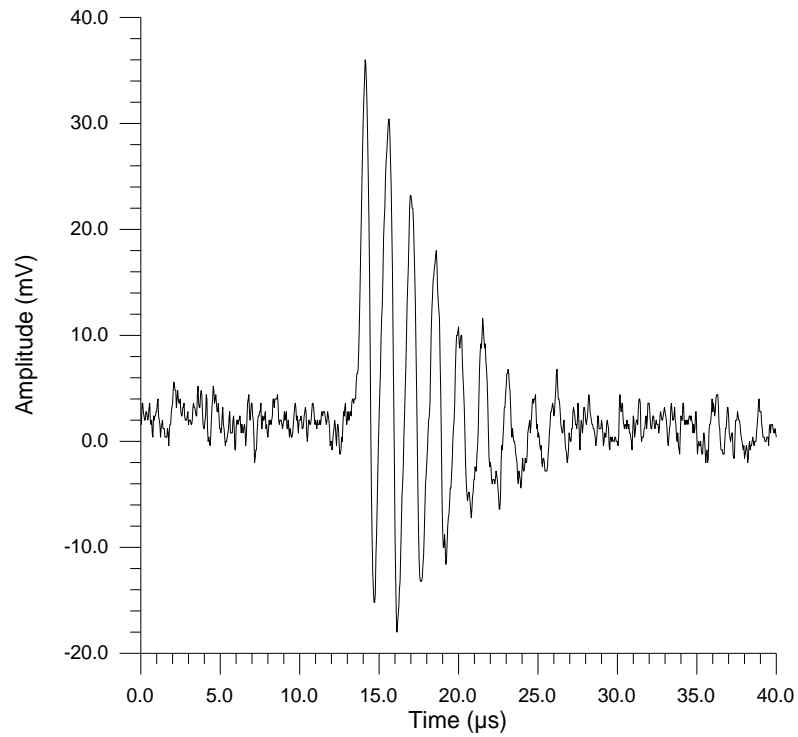


Figure 6.12(a): Waveform through a defect free area of a 16-ply unidirectional CFRP composite plate.

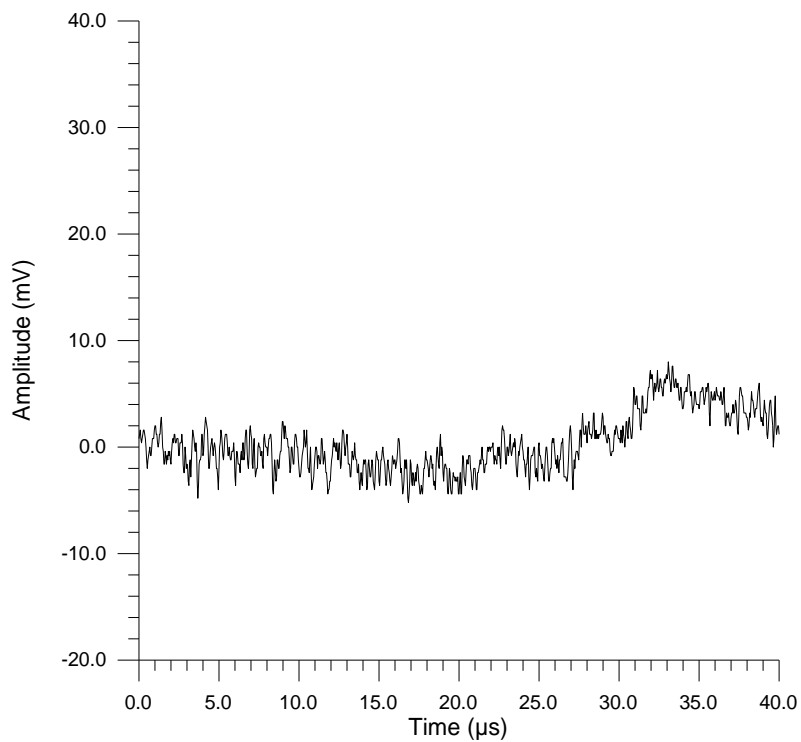


Figure 6.12(b): Waveform through a delaminated area of a 16-ply unidirectional CFRP composite plate.

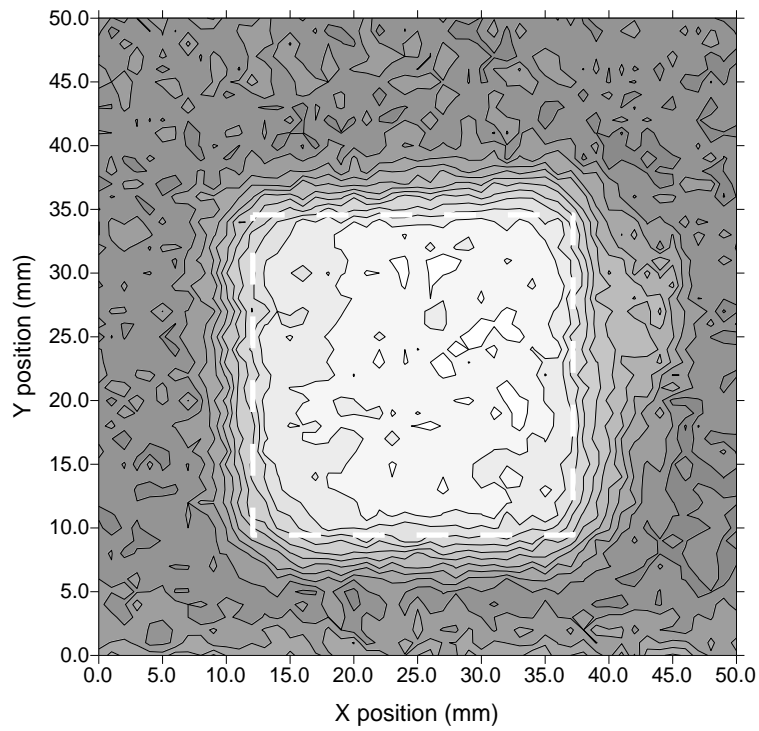


Figure 6.13(a): Image of a 25mm square Teflon delamination in a 16-ply (2.2mm thick) CFRP composite plate. Grey scale is in mV.

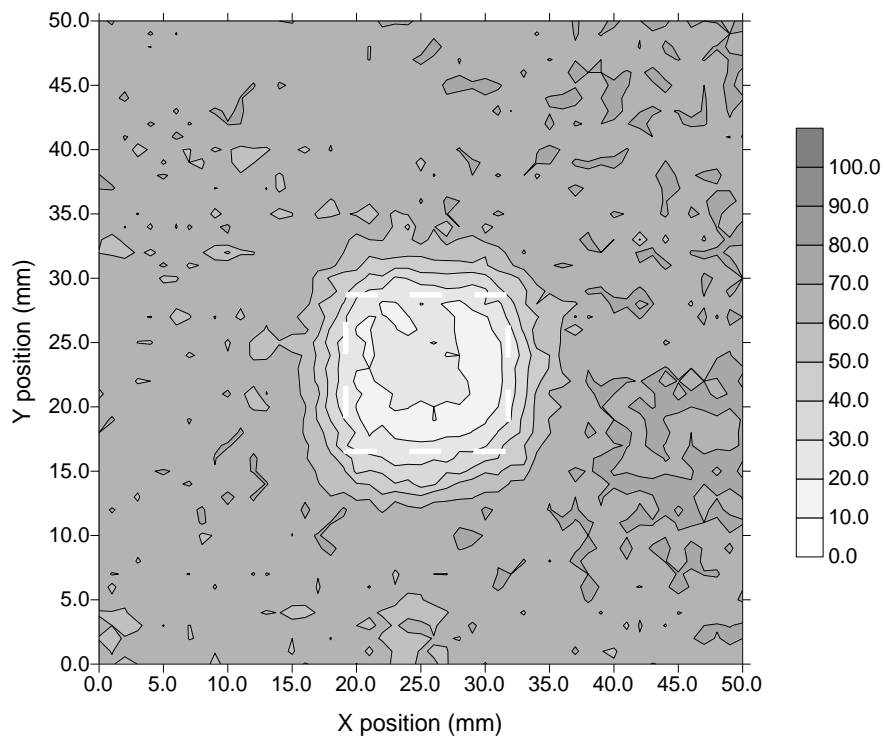


Figure 6.13(b): Image of a 12.5mm square Teflon delamination in a 16-ply (2.2mm thick) CFRP composite plate. Grey scale is in mV.

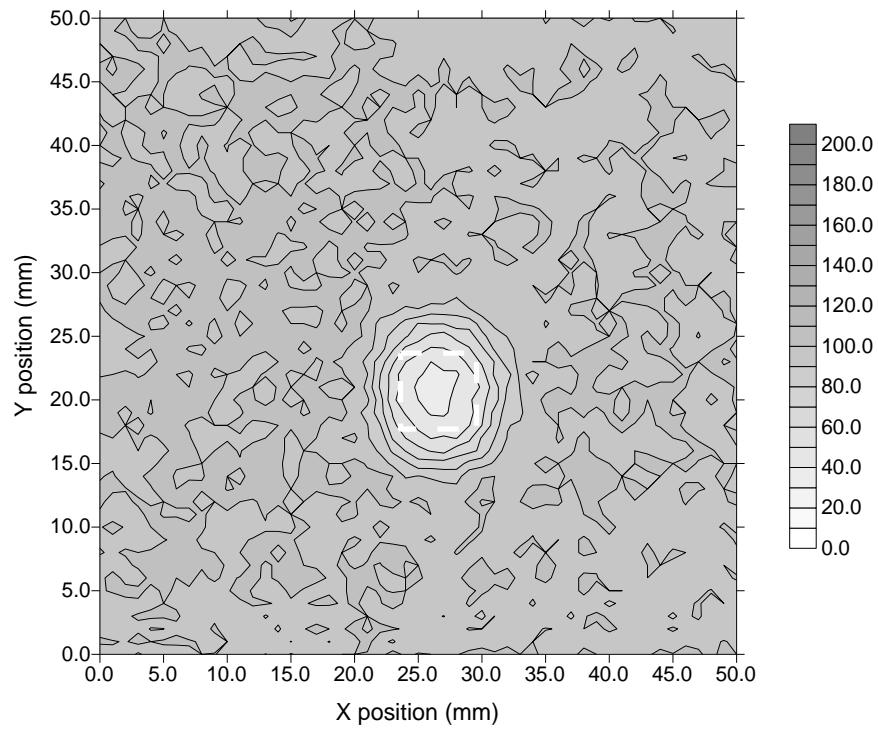


Figure 6.13(c): Image of a 6.25mm square Teflon delamination in a 16-ply (2.2mm thick) CFRP composite plate. Grey scale is in mV.

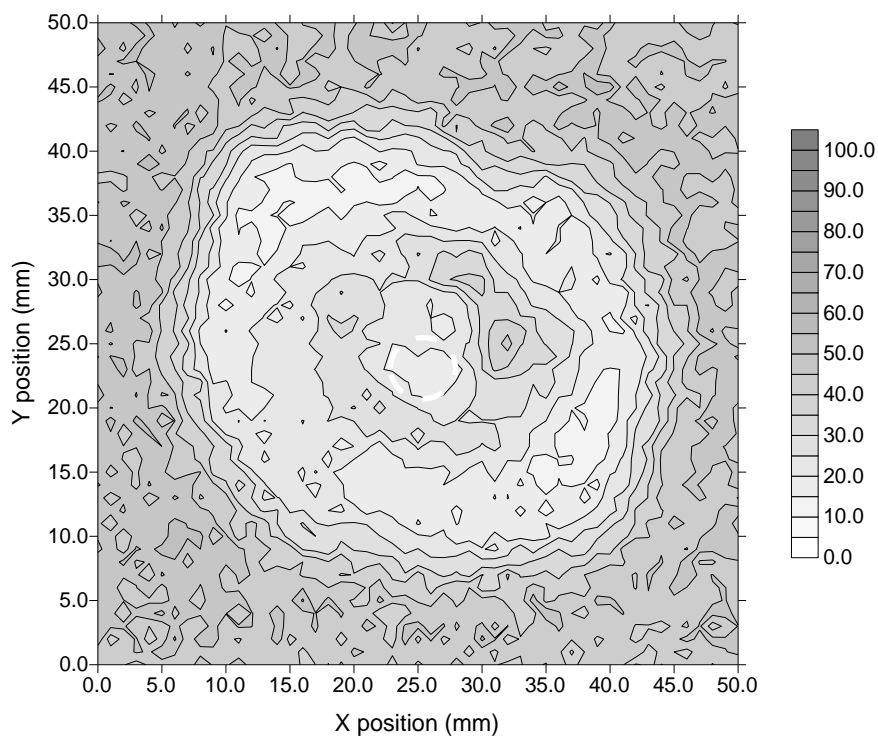


Figure 6.13(d): Image of a delamination caused by a 5mm diameter impact in a 6.35mm thick CFRP cross-ply composite plate. Grey scale is in mV.

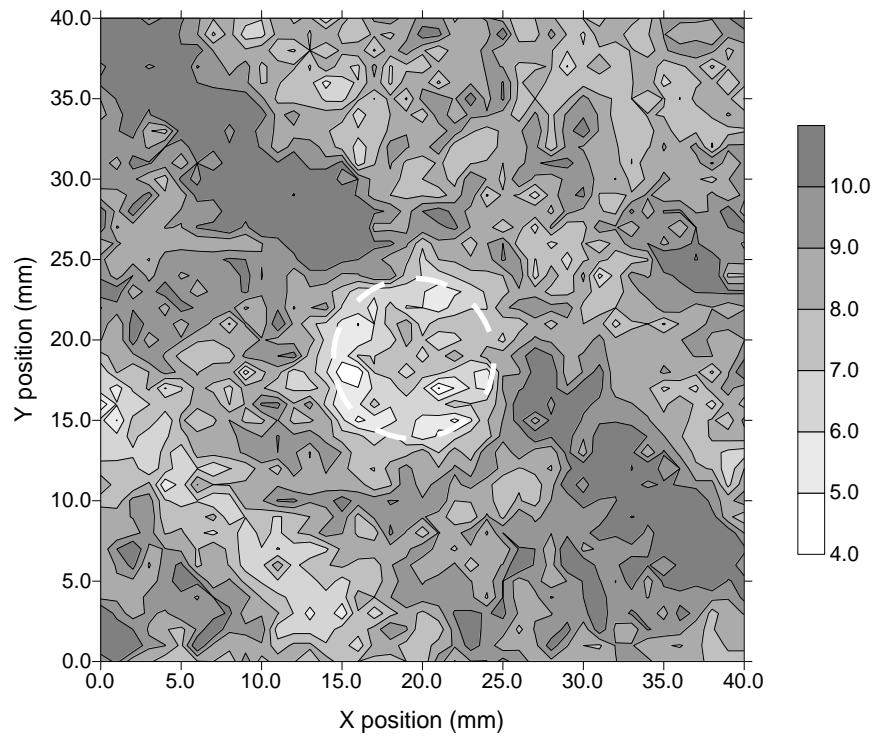


Figure 6.14(a): Image of a defect 10mm diameter by 1mm deep machined into a 9.8mm thick pultruded composite plate. Grey scale is in mV.

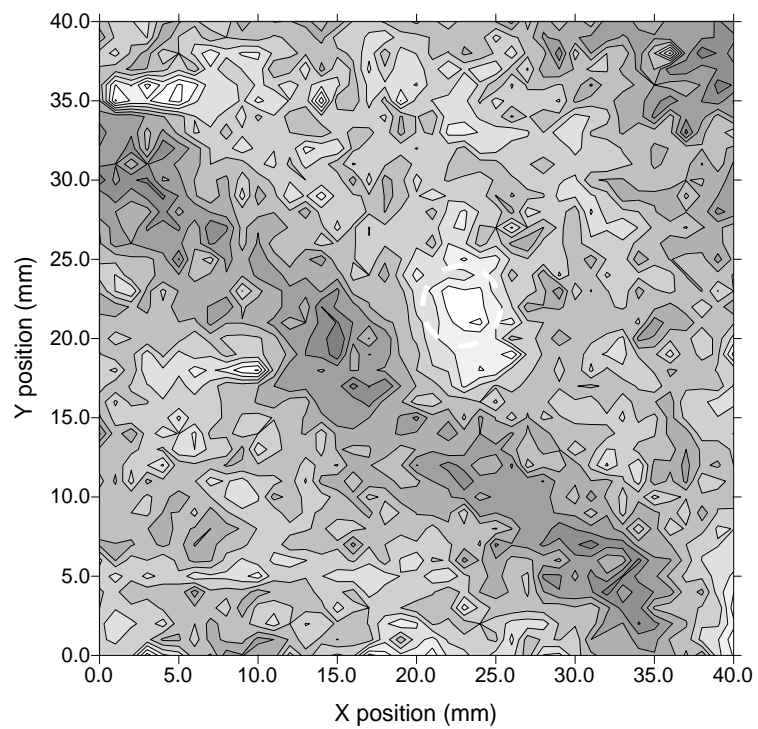


Figure 6.14(b): Image of a defect 5mm diameter by 2mm deep machined into a 9.8mm thick pultruded composite plate. Grey scale is in mV.

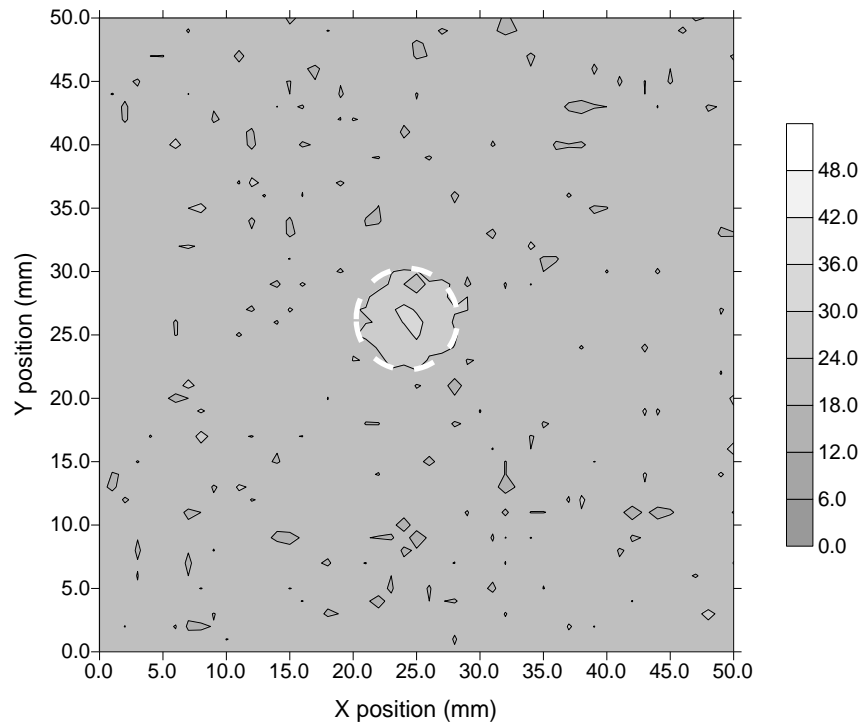


Figure 6.15(a): Signal amplitude image of an 8mm diameter recess machined halfway into a 0.7mm thick aluminium plate. Grey scale is in mV.

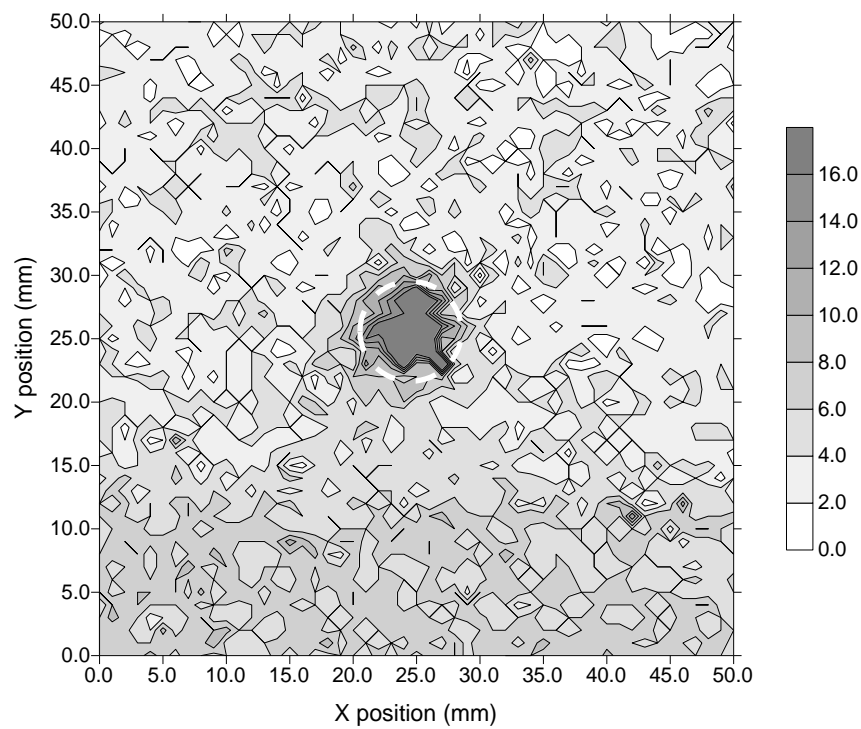


Figure 6.15(b): Change in time of arrival image of an 8mm diameter recess machined halfway into a 0.7mm thick aluminium plate. Grey scale is in μs .

2mm deep. The size of each defect is clearly resolved, and the scan has also highlighted areas both rich and deficient in the resin matrix material, which appear as dark and light diagonal stripes respectively.

Despite the low signal levels seen earlier for air-coupled through-thickness waveforms in aluminium, it was still possible to obtain images using the scanning apparatus using only 256 averages. Figure 6.15 shows images of an 8mm diameter recess machined into a 0.7mm thick aluminium plate to half the plate thickness. Figure 6.15(a) was obtained by plotting the signal amplitude, and (b) was obtained by plotting the arrival time of the first wavefront. Although the half wave resonance of the aluminium plate was too high to be detected by the receiver, the overall signal amplitude transmitted through the recess increased due to the reduction in material thickness. The arrival time also varied due to the increase in the length of the path through air, and the reduction of the path length in the aluminium.

6.4 Lamb waves in composite and polymer plates

The pair of air-coupled transducers were also used to generate and detect Lamb waves in thin plates of composites and polymers, by displacing the two devices off epicentre by 50mm, and inclining them at an angle of 15° to the plate. This angle was the optimum, calculated using Snell's law, for the frequency range of the devices and the velocities in the materials tested. Figure 6.16(a) shows a typical Lamb wave obtained after propagating 50mm in a 1.5mm thick sheet of perspex, and displays the a_0 mode with characteristic dispersion. Figure 6.16(b) shows a Lamb wave in an 8-ply8-ply unidirectional CFRP plate, propagating parallel to and perpendicularly to the fibres respectively. The two waveforms are radically different in shape, which is to

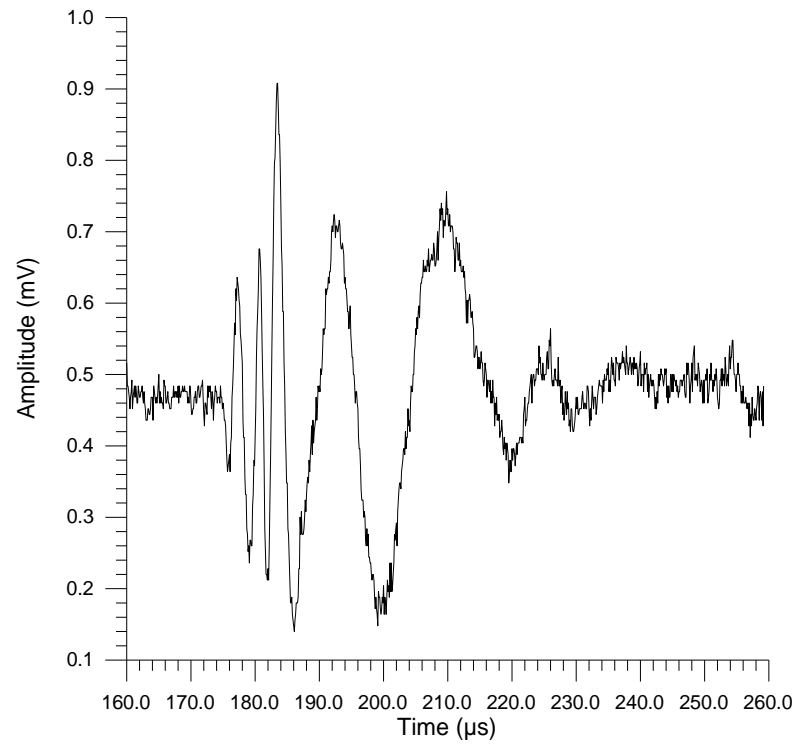


Figure 6.16(a): Lamb wave in a 1mm thick perspex sheet, propagating over a distance of 50mm through the plate.

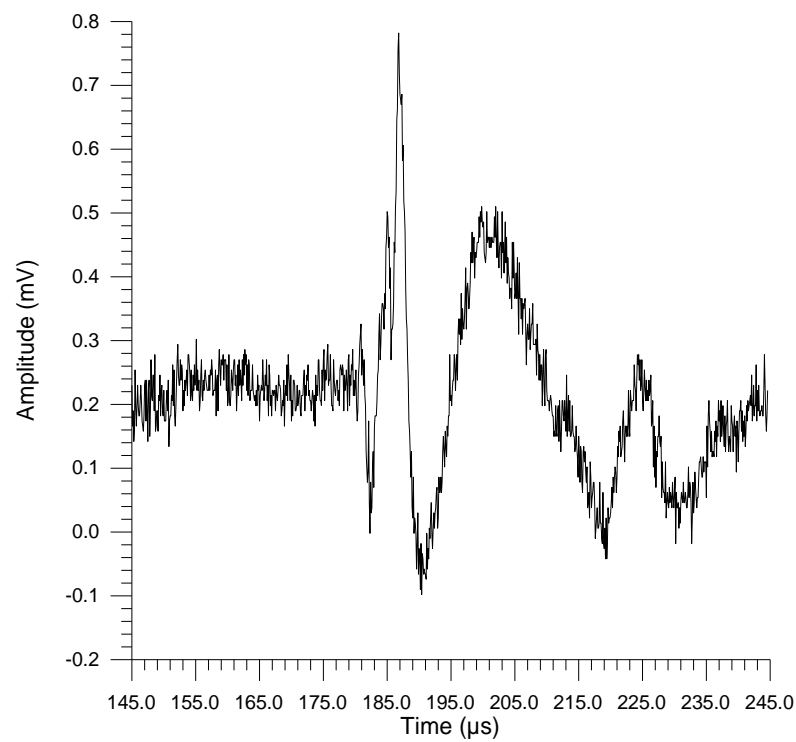


Figure 6.16(b): Lamb wave in a 8-ply (1.1mm thick) quasi-isotropic CFRP composite.

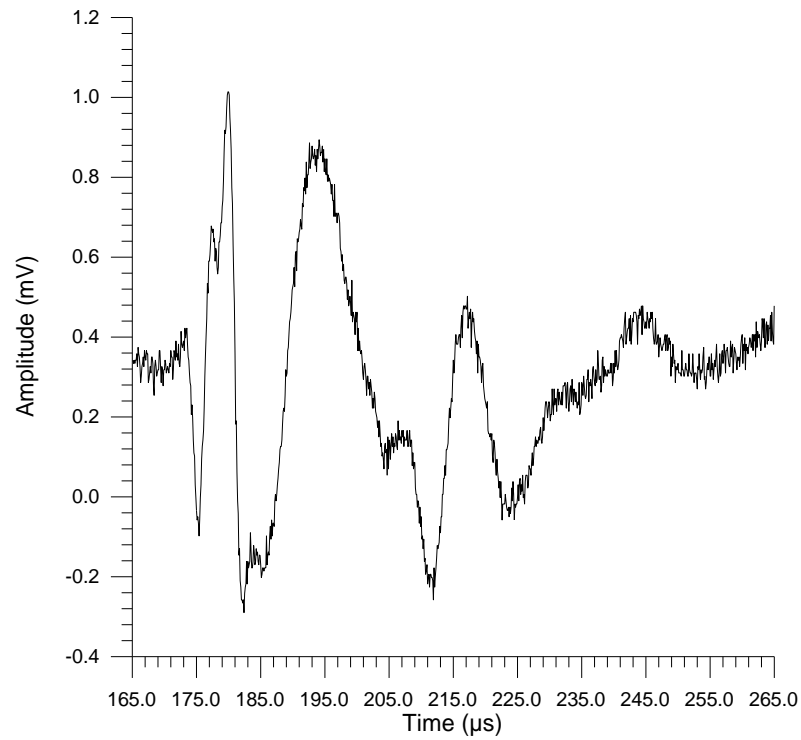


Figure 6.17(a): Lamb wave in 8-ply (1.1mm thick) unidirectional CFRP composite, travelling 50mm parallel to the principle fibre axis.

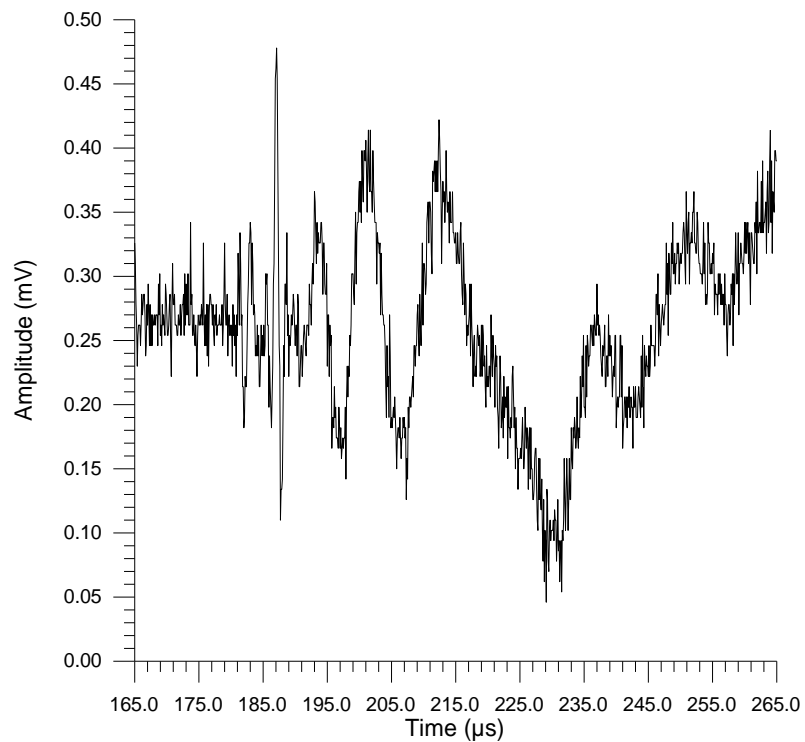


Figure 6.17(b): Lamb wave in 8-ply (1.1mm thick) unidirectional CFRP composite, travelling 50mm perpendicularly to the principle fibre axis.

be expected as the composite is highly anisotropic. The wave travelling along the fibres is greater in amplitude (1.3mV compared to 0.35mV), as most of the incident energy will travel preferentially along the fibres, and has a greater velocity in this direction. A lesser degree of anisotropy was also observed in cross-ply plates. The outer layers of the cross-ply composite still had fibres running in only one direction, and so the flexing of these anisotropic layers will tend to dominate the a_0 mode. It was also possible to generate and detect Lamb waves in thin plates of aluminium and other metals, as was seen in the previous chapter.

6.5 Conclusions

A pair of capacitance air-coupled transducers, with backplates micromachined from silicon, have been used to generate and detect through thickness waveforms in a variety of materials. Despite the high impedance mismatch between solids and air, signals were obtained through various plates of CFRP composite with different lay-up configurations. The samples ranged from 1.0mm to 17.5mm thick, and bulk wave longitudinal velocity values were calculated in each sample. Where individual echoes were difficult to resolve, the half wavelength through-thickness resonant frequency was used to calculate the velocity. Signals were also detected in pultruded GRP composites, expanded polyurethane foams, perspex and even aluminium up to 12.9mm thick. Through thickness waveforms were also used to create images of delamination defects in CFRP, and machined defects in pultruded GRP and aluminium plates. Lamb waves in thin plates were also generated and detected by repositioning the air-coupled devices. It has thus been demonstrated that an entirely

air-coupled system using micromachined capacitance devices can lead to an extremely versatile NDE technique. When suitable transducers with sufficient bandwidth and sensitivity are developed, the techniques shown here could be applied to a much wider range of applications, such as non-contact NDT of aerospace composite panels, or pipe wall thickness estimation.

6.6 References

- [1] D.A. Hutchins, W.M.D. Wright and D.W. Schindel, 'Ultrasonic measurements in polymeric materials using air-coupled capacitance transducers', *J. Acoust. Soc. Am.* **96**, 1634-1642 (1994)
- [2] H.M. Frost, 'Electromagnetic ultrasonic transducers: Principles, Practice and Applications', in *Physical Acoustics*, edited by W.P. Mason and R.N. Thurston, (Academic, New York, 1979), Vol. XIV, pp179-276
- [3] W. Sachse and N.N. Hsu, 'Ultrasonic transducers for materials testing and their characterisation', in *Physical Acoustics*, edited by W.P. Mason and R.N. Thurston, (Academic, New York, 1979), Vol. XIV, pp277-406
- [4] C.A. Calder and W.W. Wilder, 'Non-contact material testing using laser energy deposition and interferometry', *Mat. Eval.* **38**, 86-91 (1980)
- [5] R.M. White, 'Generation of elastic waves by transient surface heating', *J. Appl. Phys.* **34**, 3559-3567 (1963)
- [6] D.A. Hutchins, 'Ultrasonic generation by pulsed lasers', in *Physical Acoustics*, edited by W.P. Mason and R.N. Thurston, (Academic, New York, 1988), Vol. XVIII, pp21-123

- [7] C.B. Scruby and L.E. Drain, 'Laser ultrasonics - Techniques and Applications', (Adam Hilger, Bristol, 1990)
- [8] W. Kuhl, G.R. Schodder and F.-K. Schröder, 'Condenser transmitters and microphones with solid dielectric for airborne ultrasonics', *Acustica* **4**, 519-532 (1954)
- [9] D.A. Hutchins, W.M.D. Wright, G. Hayward and A. Gachagan, 'Air-coupled piezoelectric detection of laser-generated ultrasound', *IEEE Trans. Ultrason. Ferroelec. Freq. Contr.* **UFFC-41**, 796-805 (1994)
- [10] W.M.D. Wright, D.W. Schindel and D.A. Hutchins, 'Studies of laser-generated ultrasound using a micromachined silicon electrostatic transducer in air', *J. Acoust. Soc. Am.* **95**, 2567-2575 (1994)
- [11] J. Krautkrämer and H. Krautkrämer, *Ultrasonic testing of Materials*, 4th edition, (Springer-Verlag, Berlin, 1990)
- [12] J.F. Allard, B. Castagnede, M. Henry and W. Lauriks, 'Evaluation of tortuosity in acoustic porous materials saturated by air', *Rev. Sci. Instrum.* **65**, 754-755 (1994)
- [13] W. Lauriks, B. Castagnede, J. Thoen, W. Wright, D. Hutchins and D. Schindel, 'Determination of the tortuosity of porous materials using new air-coupled ultrasonic transducers', *Proc. 11th Int. FASE Symp.* **Nov 1994**, 11-14 (1995)

Chapter 7: Air-coupled Lamb wave tomography

7.1 Introduction

This chapter will describe how a filtered back projection algorithm used ultrasonic Lamb waves to reconstruct tomographic images of defects in thin sheets of a variety of materials. The following sections will include a brief review of tomographic methods, before describing in detail the theory for the reconstruction algorithm. In a first series of experiments, a pulsed laser will be used as an ultrasonic source, and an air-coupled capacitance transducer as a receiver. In the second part of the work, a pair of air-coupled capacitance transducers will be used in an entirely air-coupled system.

7.1.1 Different tomographic reconstruction techniques

Tomographic reconstruction [1] is a method of imaging by illuminating the object in many different directions in the plane of interest, typically using X-rays or ultrasound. An image is formed from changes in a physical variable occurring in the planar cross section. Changes in amplitude may be used to produce an attenuation image, or changes in propagation delay or arrival time are used to reconstruct an image of the velocity variations via slowness, which is the inverse of velocity.

The initial theory for tomographic reconstruction was attributed to Radon [2] in 1917, who showed that a function could be reconstructed from line integral data. Despite being initially developed for use with X-rays, the various techniques were soon applied to ultrasonics, with perhaps the earliest medical experiments being those of Greenleaf *et al.* [3,4] who imaged soft tissue. The current major uses of ultrasonic tomography are still medical [5], with most techniques using high frequency

ultrasound to image soft tissues such as the breast. Other areas where acoustic tomography is used are oceanography and seismology [6], with applications such as measuring water temperature [7] and investigating layers of sediment [8]. Due to the extensive number of articles in the literature, a comprehensive review of these topics is not practical for the limited scope of this work. Many of these medical and geophysical techniques are applicable to non-destructive testing, although industrial and NDT applications appear to be quite rare. Early examples are the testing of SiO_2 ingots [9], solid propellant rocket motors [10] and wooden poles [11].

Perhaps one of the most restricting factors for ultrasonic tomography is the volume of data which must be taken. Recent work has automated this process using scanned transducers [12] and transducer arrays [13,14]. With improved non-contact transduction techniques and new composite materials, there has been a resurgence in ultrasonic tomography for non-destructive testing [15-18].

There are two main groups of tomographic image reconstruction algorithms. The first of these is known as series expansion methods [19], which use iteration to reconstruct the desired image. These methods are fairly flexible, as they can correct for anisotropy [20], ray bending, and non standard sampling geometry, but they are computationally inefficient. Two well known series expansion methods are the Algebraic Reconstruction Technique (ART) [21] and the Simultaneous Iterative Reconstruction Technique (SIRT) [22]. The second group of reconstruction techniques is known as transform methods [23], and they use Fourier analysis to reconstruct the image. These algorithms are fast and efficient, but require precise sampling geometry and are thus perhaps not as popular as iterative techniques. Two well known transform methods are Fourier inversion [24], and Filtered back

projection [25-26]. Other techniques use time-of-flight diffraction tomography (TOFDT) [27-28], filtered back propagation [29] and scattering area functions [30].

7.2 Tomographic reconstruction using Fourier analysis

The filtered back projection algorithm and reconstruction software used in this chapter was developed for geophysics, and was written by Dion Jansen at Queen's University, Canada [31]. The technique may be explained by considering the sampling geometry shown schematically in Figure 7.1(a), where an ultrasonic source and receiver a fixed distance apart are scanned in one direction over the object to be imaged, and a waveform is taken at regularly spaced intervals. The time of arrival is extracted from each waveform or 'ray', and this forms one point on a 'silhouette' or projection through the object.

Assuming the ray path is linear, the time of arrival for each waveform is in fact the integral of all the variations in slowness (which is the inverse of velocity) in a direct line between the source and receiver. By rotating the object or transducer pair through a small angle, and repeating the scanning process again and again until a full 180° has been turned, a series of projections of the slowness function at different angles through the object is built up. These are then used by the filtered back projection algorithm to reconstruct a 2-dimensional cross-sectional image of all the slowness variations everywhere within the scan area. Although described in terms of times of arrival and slowness function, the technique is the same for any acoustic variable such as attenuation or frequency shift.

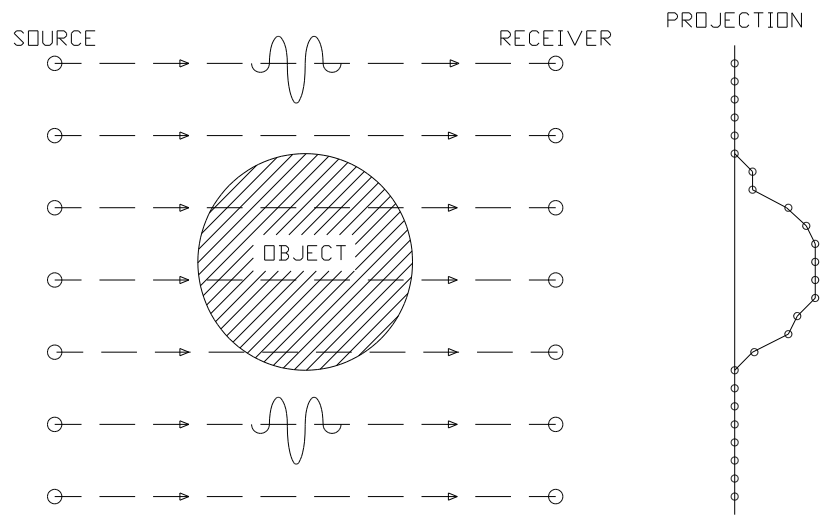


Figure 7.1(a): Schematic diagram of the sampling geometry.

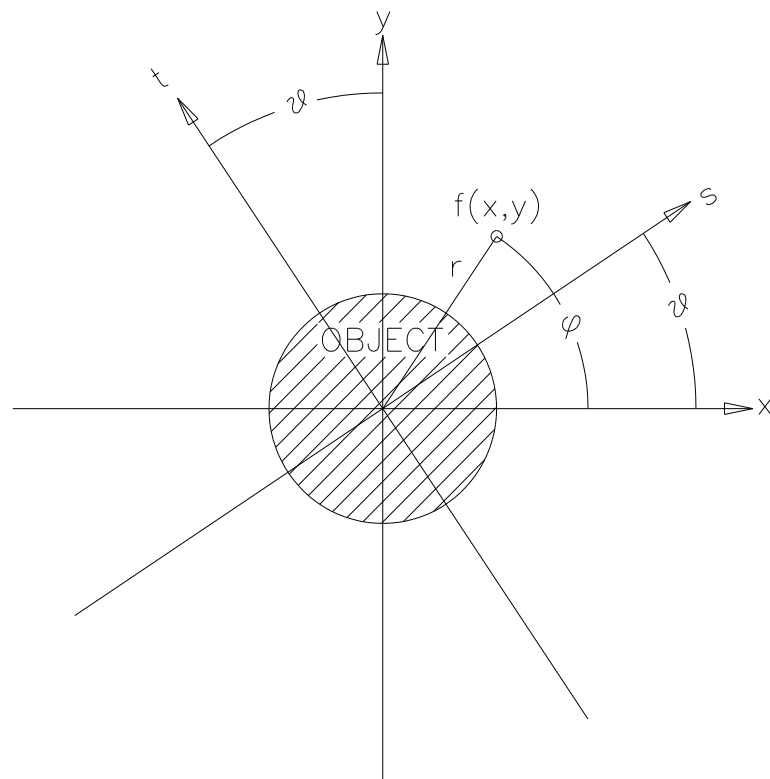


Figure 7.1(b): The rotated co-ordinate system.

7.2.1 The Projection Theorem

The projection p at an angle θ of the slowness function f at the same angle is the line integral:

$$p_{\theta}(s) = \int_{-\infty}^{\infty} f_{\theta}(s, t) \cdot dt \quad \{7.1\}$$

where (s, t) is the (x, y) plane rotated through an angle θ , as shown schematically in Figure 7.1(b), so that:

$$f(s, t) = f([x \cos \theta + y \sin \theta], [-x \sin \theta + y \cos \theta]) \quad \{7.2\}$$

The Fourier transform P of the projection p is:

$$P_{\theta}(S) = \int_{-\infty}^{\infty} p_{\theta}(s) \cdot e^{-j2\pi s S} ds \quad \{7.3\}$$

Substituting equation {7.1} for the projection p_{θ} gives:

$$P_{\theta}(S) = \int_{-\infty}^{\infty} \int_{-\infty}^{\infty} f_{\theta}(s, t) \cdot e^{-j2\pi s S} ds \cdot dt \quad \{7.4\}$$

The two dimensional transform of the slowness function is:

$$F_{\theta}(S, T) = \int_{-\infty}^{\infty} \int_{-\infty}^{\infty} f_{\theta}(s, t) \cdot e^{-j2\pi(sS + tT)} ds \cdot dt \quad \{7.5\}$$

When evaluated at $T=0$, i.e.: through the centre of the object in the Fourier domain, this becomes:

$$F_{\theta}(S, 0) = \int_{-\infty}^{\infty} \int_{-\infty}^{\infty} f_{\theta}(s, t) \cdot e^{-j2\pi(sS)} ds \cdot dt \quad \{7.6\}$$

which is simply the transform of the projection, as shown in equation {7.4}. When using the (x,y) co-ordinate system, this becomes:

$$P_{\theta}(S) = F_{\theta}(S,0) = F(S \cos \theta, S \sin \theta) \quad \{7.7\}$$

Thus, the projection theorem states that the Fourier transform of a projection of the slowness function at an angle θ is equal to the two dimensional Fourier transform of the actual slowness function through the centre of the object at the same angle θ .

7.2.2 Filtered back projection

The slowness function f may be obtained at any point (x,y) in the scan area by the inverse Fourier transform:

$$f(x, y) = \int_{-\infty}^{\infty} \int_{-\infty}^{\infty} F(X, Y) \cdot e^{j2\pi(xX + yY)} dX \cdot dY \quad \{7.8\}$$

The series of projections p_{θ} may be thought of as being arranged through the centre of the object like the spokes of a wheel, and so the data in the Fourier domain is held in a form of polar grid as shown in Figure 7.2(a). However, the inverse Fourier transform requires the data to be in Cartesian form, as shown in Figure 7.2(b). To avoid interpolation in the Fourier domain, which can lead to large inaccuracies, particularly at the edge of the scan area where data is sparse, the following polar co-ordinates were

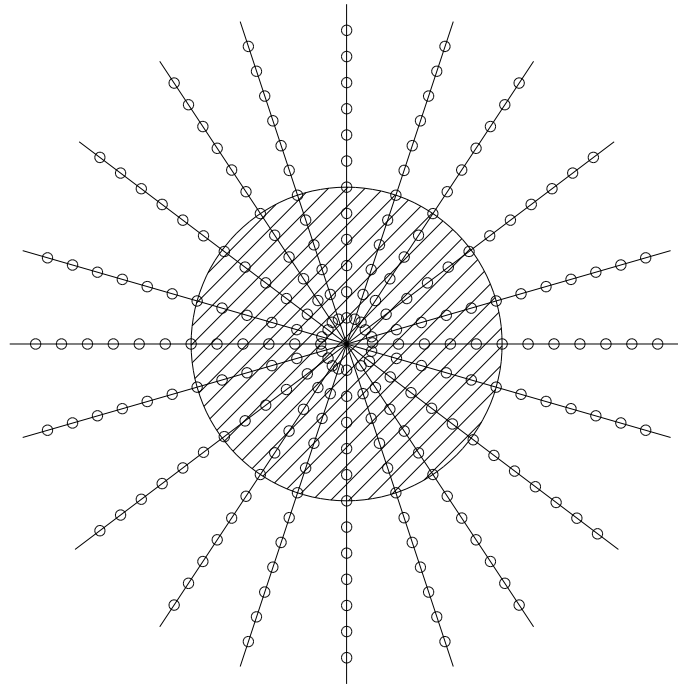


Figure 7.2(a): The data points in a polar grid.

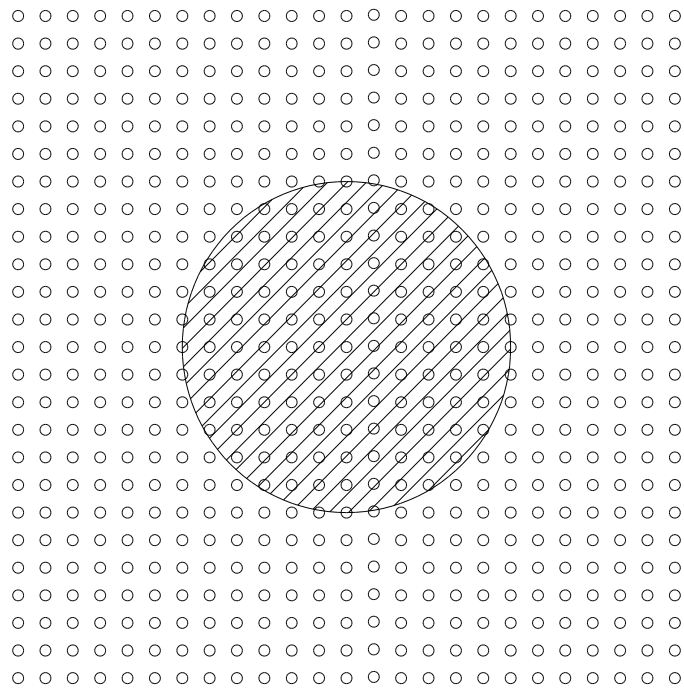


Figure 7.2(b): The data points in a Cartesian grid.

used in the spatial domain:

$$x = r \cos \phi \quad 0 \leq r < \infty$$

$$y = r \sin \phi \quad 0 \leq \phi < 2\pi$$

and similarly in the Fourier domain:

$$X = R \cos \theta \quad -\infty < R < \infty$$

$$Y = R \sin \theta \quad 0 \leq \theta < \pi$$

Equation 7.8 thus becomes:

$$f(x, y) = \int_0^\pi \int_{-\infty}^\infty F(R \cos \theta, R \sin \theta) \cdot e^{j2\pi(r \cos \phi \cdot R \cos \theta + r \sin \phi \cdot R \sin \theta)} \cdot |R| \cdot dR d\theta \quad \{7.9\}$$

where:

$$|R| \cdot dR d\theta = dX dY \quad \{7.10\}$$

This may be further reduced using $\cos(\theta - \phi) = \cos \theta \cdot \cos \phi + \sin \theta \cdot \sin \phi$ to:

$$f(x, y) = \int_0^\pi d\theta \int_{-\infty}^\infty dR \cdot |R| \cdot F(R \cos \theta, R \sin \theta) \cdot e^{j2\pi R \cos(\theta - \phi)} \quad \{7.11\}$$

By substituting in the transform of a projection $P(R)$ and introducing a new variable

$r' = r \cos(\theta - \phi)$, equation {7.11} becomes:

$$f(x = r \cos \phi, y = r \sin \phi) = \int_0^\pi d\theta \int_{-\infty}^\infty dR \cdot |R| \cdot P(R) \cdot e^{j2\pi R r'} \quad \{7.12\}$$

The inner integral of equation {7.12} is simply a convolution in the Fourier domain of the projection $p_\theta(r)$ with a ‘kernel’ function $k(r)$ whose Fourier transform is $|R|$. By defining a new function $g_\theta(r)$ which is the result of this convolution, given by:

$$g_\theta(r) = p_\theta(r) * k(r) \quad \{7.13\}$$

and:

$$G_{\theta}(R) = P_{\theta}(R) \cdot |R| \quad \{7.14\}$$

The outer integral of equation {7.12} finally reduces to:

$$f(x = r \cos \phi, y = r \sin \phi) = \int_0^{\pi} g_{\theta}(r').d\theta \quad \{7.15\}$$

$$f(x = r \cos \phi, y = r \sin \phi) = \int_0^{\pi} g_{\theta}(r \cos[\theta - \phi]).d\theta \quad \{7.16\}$$

Equation {7.16} is just a simple back projection of all the convolved projections $g_{\theta}(r')$ associated with all the rays passing through the point $(x=r \cos \phi, y=r \sin \phi)$. Therefore, the slowness function may be obtained using the inverse two dimensional Fourier transform, and by the substitution and manipulation shown, this simplifies to a back projection of all the projections, convolved with a kernel function $|R|$ in the Fourier domain, which is a simple filtering operation.

The integrals in the above theory are for continuous functions, and as the data is in discrete form, Riemann approximations were used for the integrals, as the waveforms were taken at n evenly spaced intervals over m equally spaced angular projections through 180° . As the points in the back projection did not exactly match the positions of the data points in each convolved projection, linear interpolation was used to accurately obtain the slowness function at any desired point in the scan area. Due to the discrete sampling of data, the frequency content of the convolutions in the Fourier domain were bandwidth limited by the Nyquist sampling theorem, given by:

$$B = \frac{1}{2\Delta s} \quad \{7.17\}$$

where B is the bandwidth, and Δs is the linear spacing of each ray. For the spacing used in this work of 1mm, which was also partly governed by the accuracy of the linear stages, the corresponding bandwidth was 500kHz. There is also the possibility of aliasing, again governed by the ray spacing. The highest spatial frequency S_0 is given by

$$S_0 \geq \frac{1}{2\Delta s} \quad \{7.18\}$$

The kernel function $|R|$ used in the convolution will exaggerate the signal at higher frequencies, where there is little real information, and thus increase the levels of noise present in each image. In addition, the kernel function must be set to zero above the cut-off frequency defined by equation {7.18}, and this may well add high frequencies which are a further source of noise in the images. To reduce these effects, a low pass filter or window function is included in the convolution stage, with the frequency limit set at the bandwidth B . For the experiments in this work, the filter function was a simple Hamming window, which offered the best compromise between inclusion of the higher frequencies, and suppression of noise.

7.3 Equipment and experimental technique

The first set of experiments was performed using the apparatus shown schematically in Figure 7.3(a). In this part of the work, ultrasonic waves were generated in the sample using a Lumonics ‘Lasermark’ series Model 630 CO₂ TEA laser, which delivered 100ns pulses at a wavelength of 10.6μm and a maximum energy of 8J. Waveforms were received by a micromachined silicon capacitance device, described previously in Chapter 3, connected to a Cooknell CA6/C charge

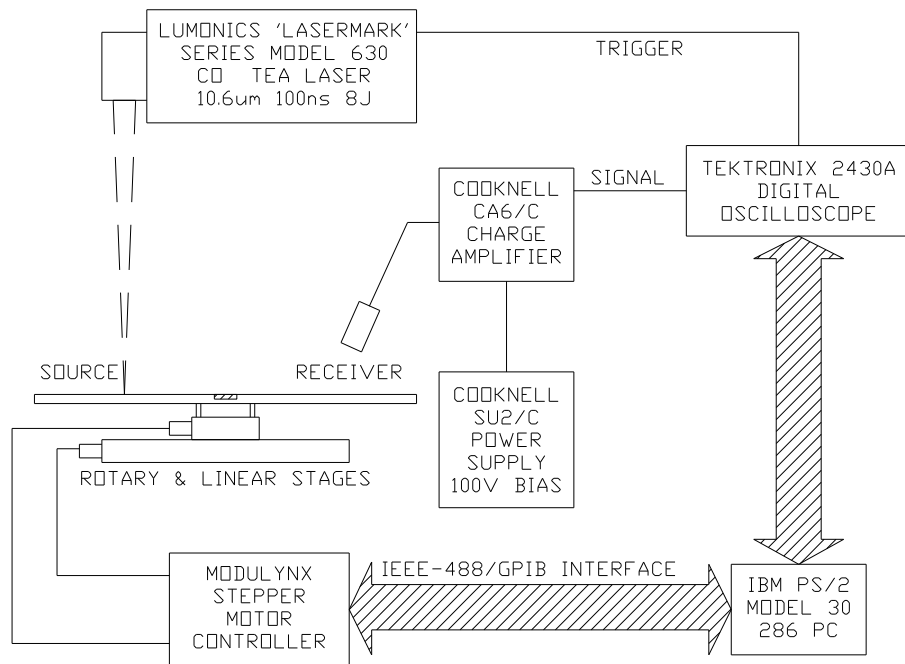


Figure 7.3(a): Schematic diagram of the experimental apparatus with the pulsed laser source and air-coupled receiver.

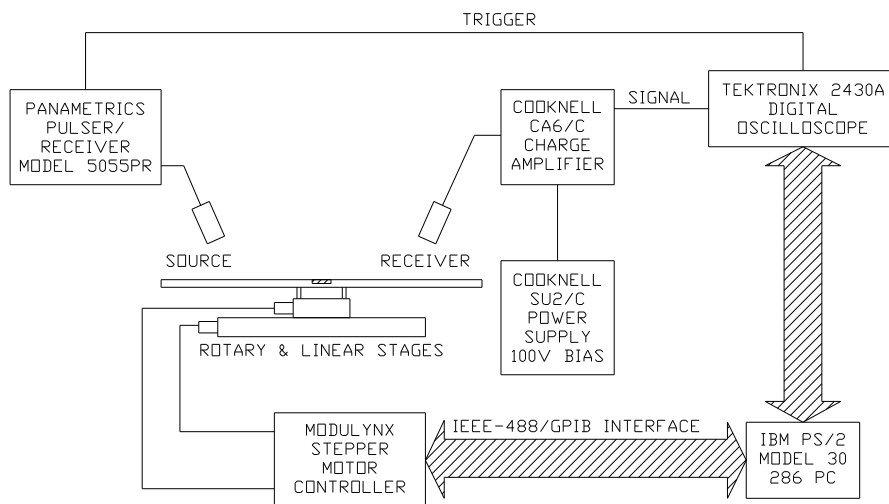


Figure 7.3(b): Schematic diagram of experimental apparatus using a pair of capacitance transducers for an entirely air-coupled system.

sensitive amplifier with a power supply providing a 100V d.c. bias between the two electrodes. Signals were captured using a Tektronix 2430A digital oscilloscope, and transferred via an IEEE-488/GPIB interface to an IBM PS/2 model 30 286 PC, which was also used to control the linear and rotary Daedal stages using a Modulynx stepper motor controller. In the second part of the work, the pulsed laser was replaced by another capacitance transducer driven by a Panametrics pulser-receiver model 5055PR, thus giving an entirely air-coupled system, as shown schematically in Figure 7.3(b). For more detailed equipment specifications, see Appendix A.

Conventional tomographic imaging usually requires absolute measurements of arrival time or amplitude along known ray paths. However, using the air-coupled transducers the exact point of generation or reception was not known, and there were additional delays and attenuation caused by the air gap. To overcome these unknowns, a form of difference tomography was employed, in which all measurements were made with respect to the first ray path in each projection. The reconstructed image would then be of the change in a parameter caused by the presence of a defect. In addition to arrival time and signal amplitude, another useful parameter in determining the presence of a defect was the shift in the centroid frequency f_C of a fast Fourier transform (FFT) of a waveform or ray, given by:

$$f_C = \frac{\sum_{i=1}^n f_i \cdot a(f_i)}{\sum_{i=1}^n a(f_i)} \quad \{7.15\}$$

where n is the number of points in the FFT, f_i is the frequency at point i and $a(f_i)$ is the amplitude at frequency f_i . As stated in the earlier chapters, Lamb waves ‘leak’ or re-radiate energy into the surrounding medium as they propagate through the plate. As

Lamb waves are dispersive, waves of different frequency travel at different velocities in the same material, and hence will leak into air at an angle determined by Snell's law. This means that any air transducer will have to be aligned at different angles to the plate surface to be optimised for each mode. The s_0 mode could not be reliably obtained in each of the samples, so the a_0 mode was used for the majority of the analysis. Unless stated otherwise, the dimensions of each scan were 50mm in steps of 1mm, giving 51 rays per projection, and 180° in steps of 5° , giving 37 projections.

7.4 Results using the laser source and the capacitance receiver

A typical Lamb wave obtained using the pulsed laser as a source is shown in Figure 7.4(a) for a 0.69mm thick aluminium sheet, with the corresponding frequency spectrum being shown in Figure 7.4(b). Each waveform was the sum of 8 averages to reduce high frequency noise, and the characteristic dispersion of the a_0 mode is clearly visible, along with the direct blast wave through the air. Figure 7.5 shows the images of a 5mm diameter hole through a 0.69mm thick sheet of aluminium, in the centre of the scan area, obtained using (a) signal amplitude ($\text{dB}\cdot\text{mm}^{-1}$), and (b) shift in centroid frequency (Hz). Despite an annular appearance due to diffraction effects, the defect can be clearly resolved. Note that there is no information in the four corners of the image as they are outside the scan area. It was not possible to reconstruct a slowness image from this set of data, possibly due to the highly dispersive nature of the Lamb wave which affects the cross-correlation method used to obtain the time of flight. The technique works well in other materials, with Figure 7.6(a) showing a typical waveform in a 1mm thick sheet of perspex ('Plexiglas'), and the corresponding frequency spectrum in Figure 7.6(b). Note that the frequency content is much lower

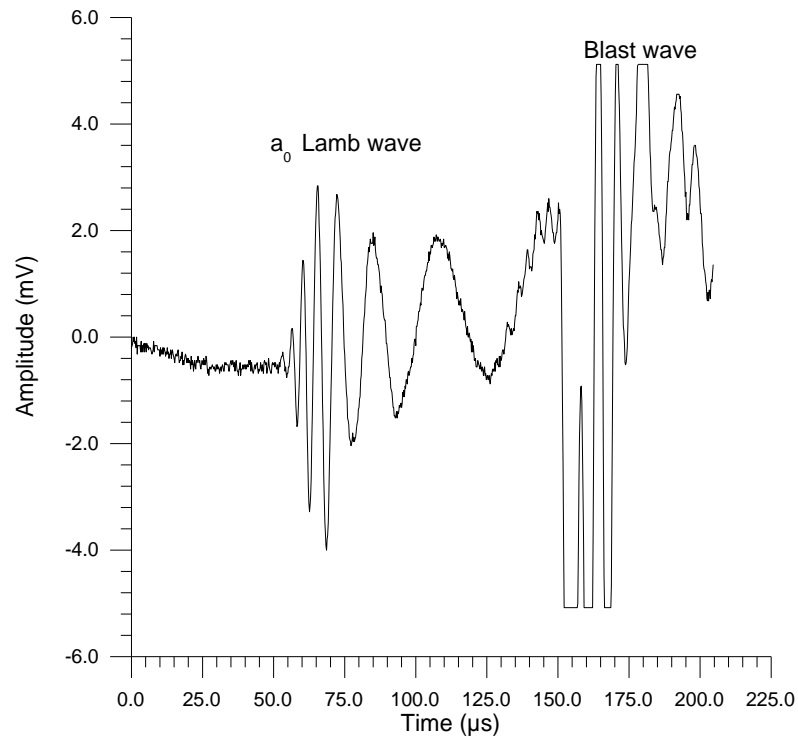


Figure 7.4(a): Typical Lamb wave in 0.69mm thick aluminium sheet using the laser source.

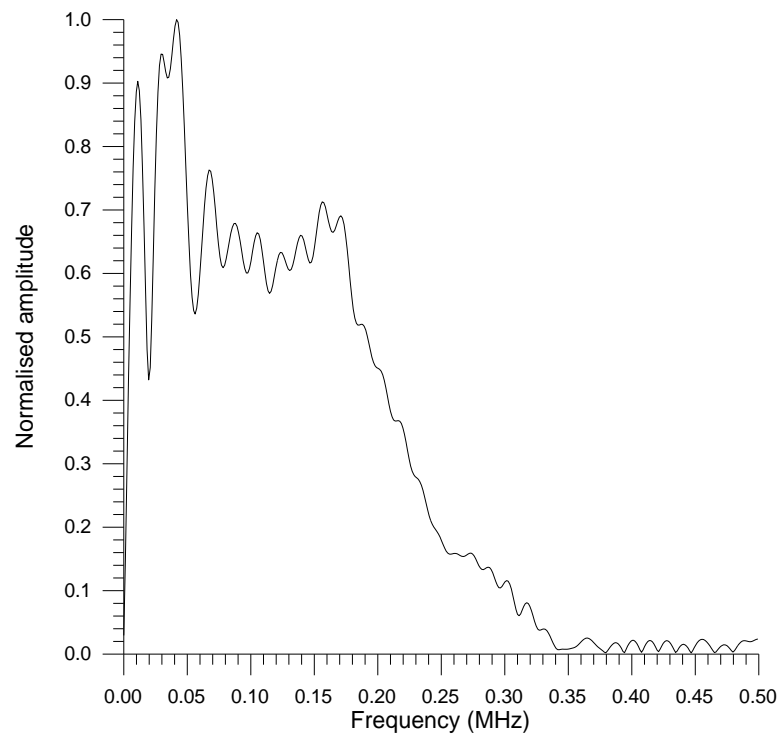


Figure 7.4(b): Frequency spectrum of Figure 7.4(a).

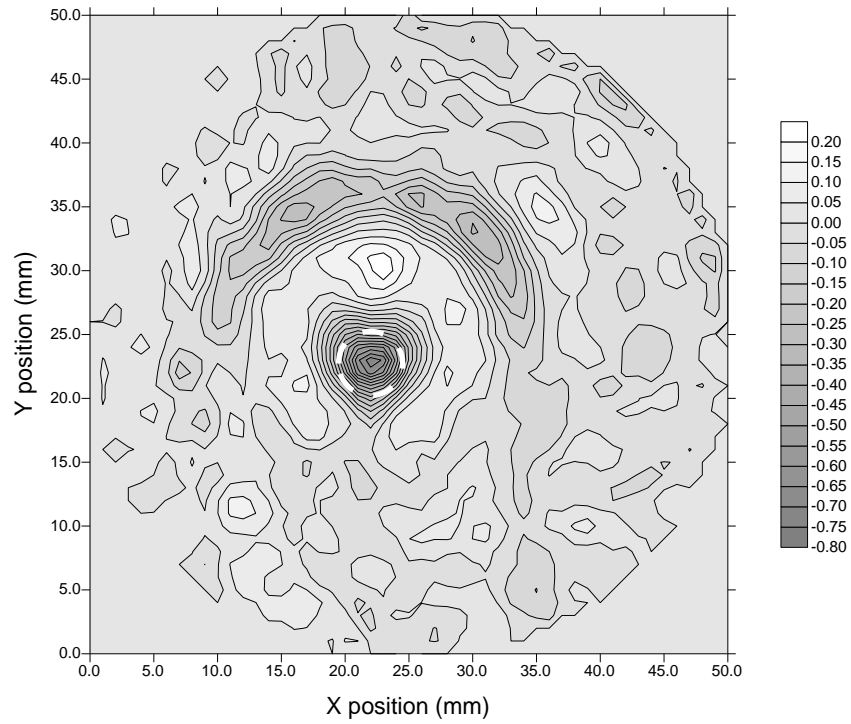


Figure 7.5(a): Attenuation image in $\text{dB}\cdot\text{mm}^{-1}$ for a 5mm hole through a 0.69mm thick aluminium sheet, obtained using signal amplitude.

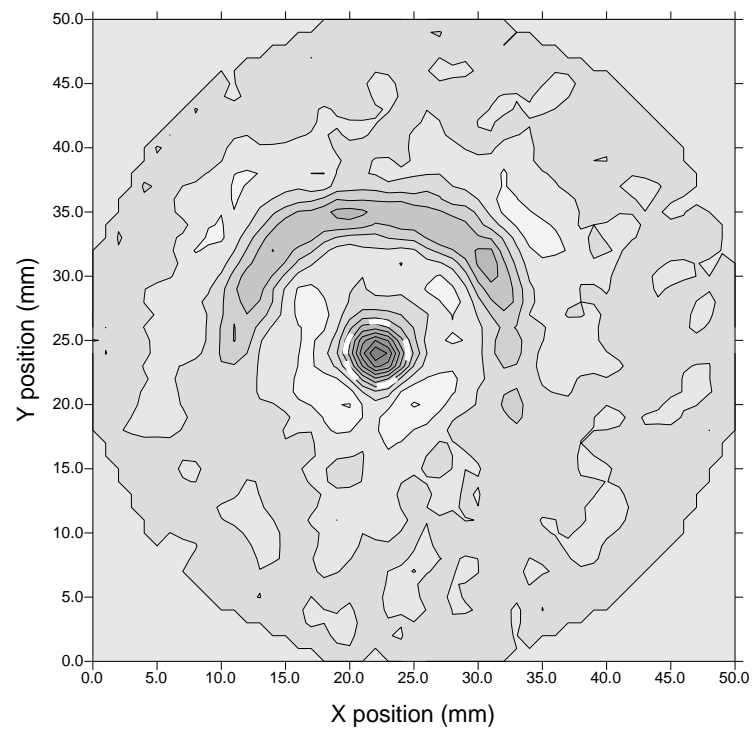


Figure 7.5(b): Image of shift in centroid frequency in kHz for the 5mm hole through a 0.69mm thick aluminium sheet.

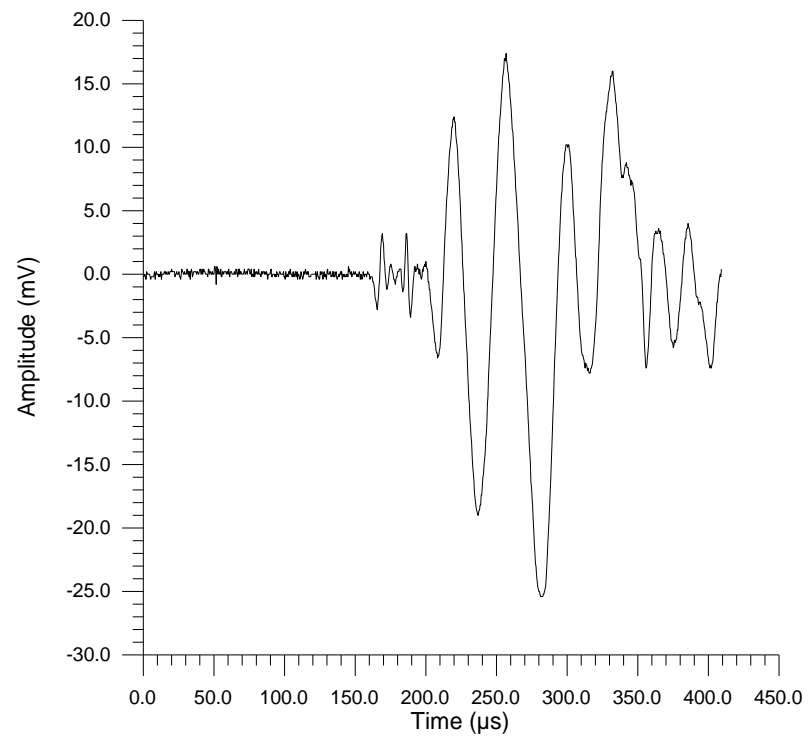


Figure 7.6(a): A typical Lamb wave in 1mm thick perspex (PMMA).

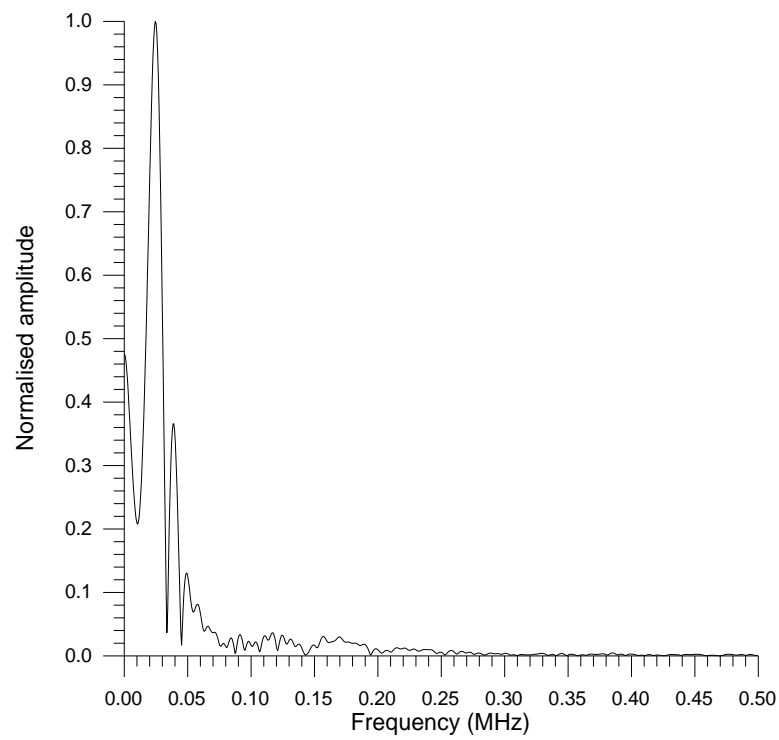


Figure 7.6(b): The frequency spectrum of Figure 7.6(a).

than for the aluminium plate, and there appears to be less dispersion. Figure 7.7 shows the images reconstructed for a 5mm hole through a 1mm thick sheet of perspex (Plexiglas). Figure 7.7(a) shows the change in signal amplitude ($\text{dB}\cdot\text{mm}^{-1}$), Figure 7.7(b) the change in slowness ($\mu\text{s}\cdot\text{mm}^{-1}$), and Figure 7.7(c) the shift in centroid frequency (Hz). The hole may be discerned in the attenuation and slowness images, but the defect size is distorted due to diffraction effects and the size of the transducer aperture. Due to the less severe dispersion, the cross-correlation was able to determine the time of flight with greater accuracy. The image of frequency shift, however, is not as clear. This was probably due to the low frequency content of the a_0 mode in this material, and the small size of the defect in relation to the wavelength which produced a subsequently tiny frequency shift.

Figure 7.8 shows the image of a 10mm diameter recess machined halfway through a 32 ply (4.4mm) cross ply carbon fibre reinforced composite (CFRP) plate, using the shift in centroid frequency in Hz. The quality of the Lamb wave signals obtained in this sample were poor, and this was attributed to the large thickness of the plate, and the interaction of more than one mode.

The filtered back projection algorithm used in this study did not allow any corrections to be made for anisotropy in the material under test. However, as a form of difference tomography was being used, it was thought that the technique may be capable of reconstructing images in anisotropic materials. The difference technique effectively removes any underlying trends due to anisotropy in the sample, as all measurements made at one angle through the object are normalised with the first ray in the projection at that angle. A 16 ply (2.2mm) unidirectional CFRP plate was available for testing, with a 1" (25.4mm) square defect formed by replacing the central 8 layers with Teflon tape during manufacture. The images reconstructed by the filtered

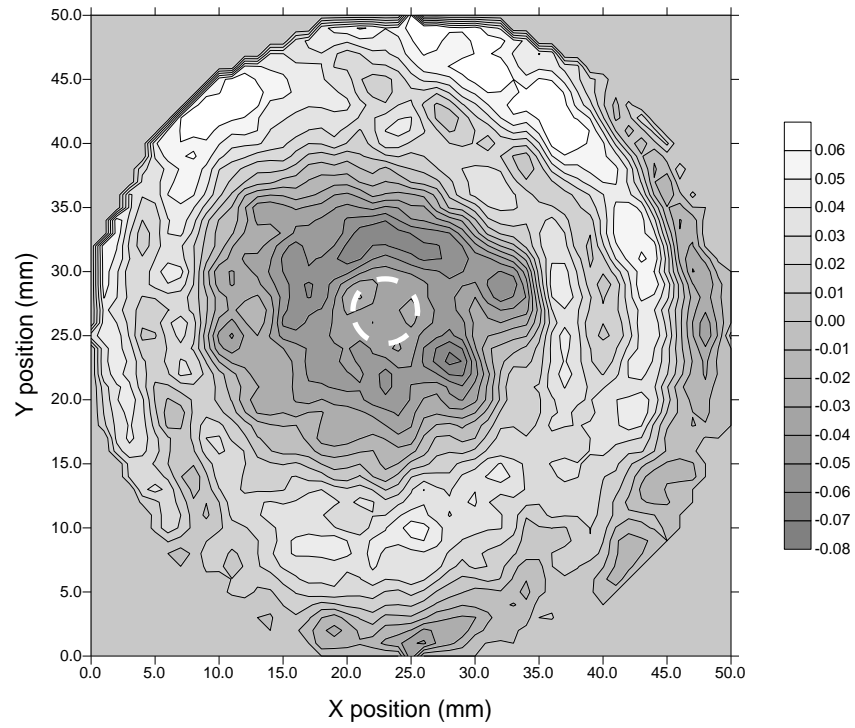


Figure 7.7(a): Attenuation image in $\text{dB} \cdot \text{mm}^{-1}$ for a 5mm hole through a 1mm thick sheet of perspex (PMMA).

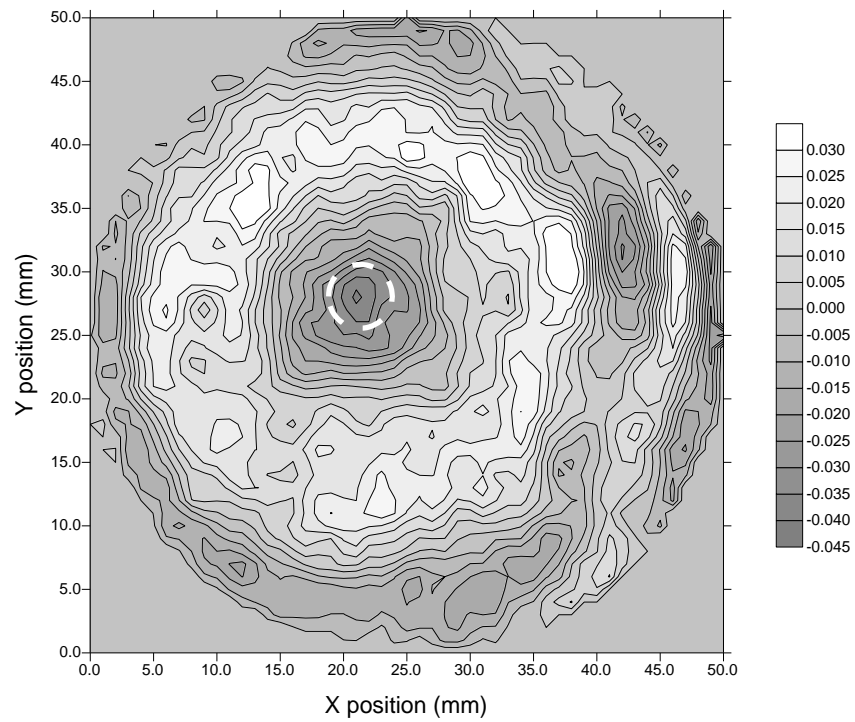


Figure 7.7(b): Slowness image in $\mu\text{s} \cdot \text{mm}^{-1}$ found using the cross correlated time of flight for a 5mm diameter hole through a 1mm sheet of perspex (PMMA).

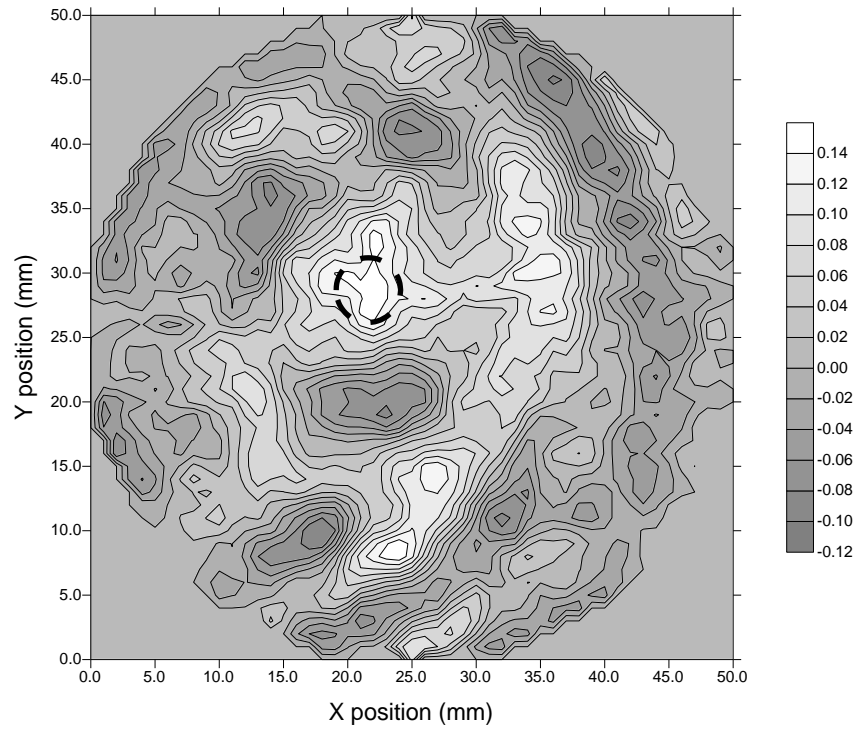


Figure 7.7(c): Image of the shift in centroid frequency in kHz of a 5mm hole through a 1mm thick sheet of perspex (PMMA).

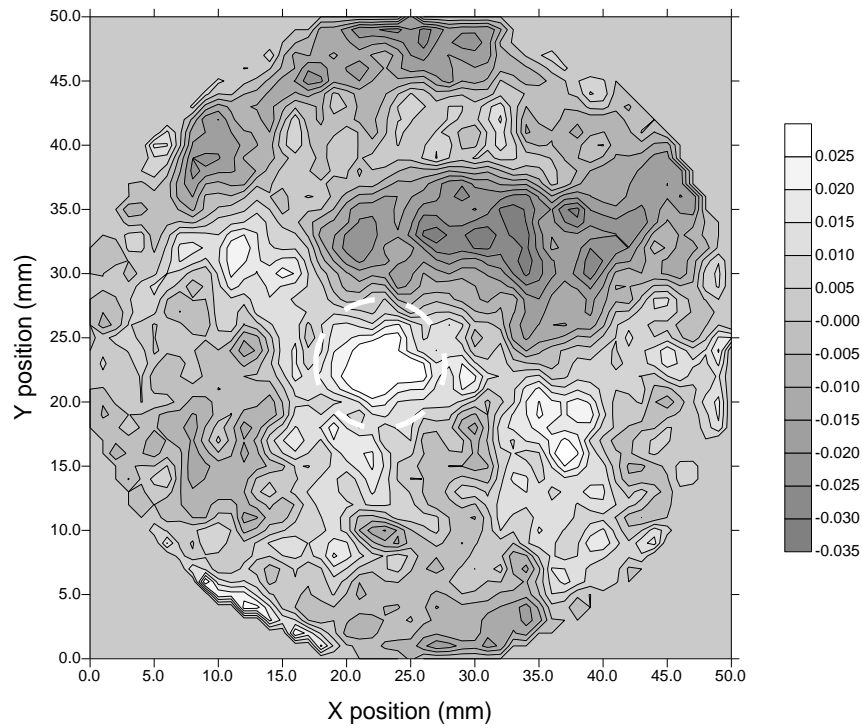


Figure 7.8: Image of the shift in centroid frequency in kHz of a 10mm diameter recess machined in a 32 ply (4.4mm) cross ply CFRP composite plate.

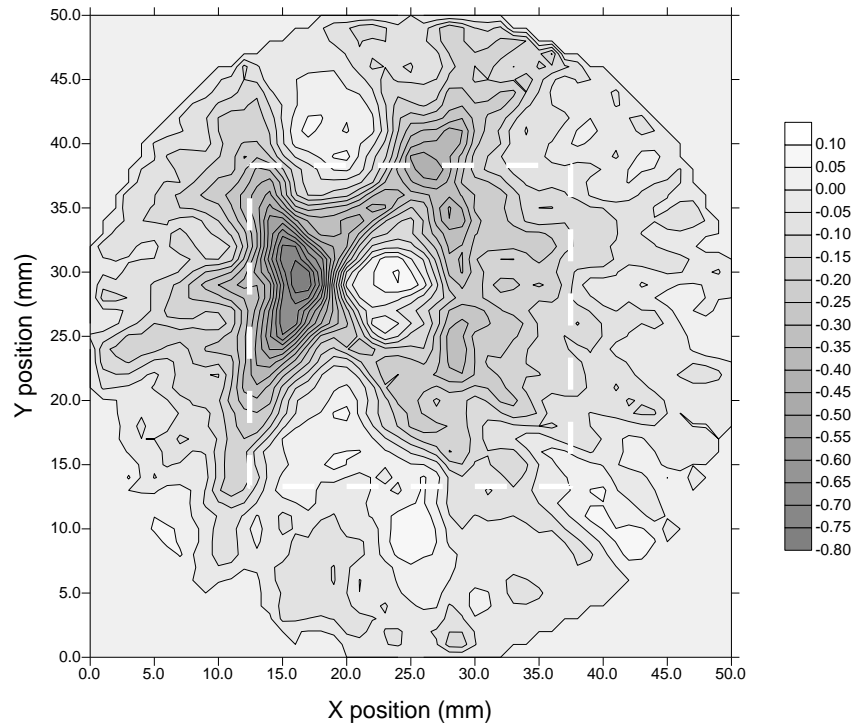


Figure 7.9(a): Attenuation image in $\text{dB} \cdot \text{mm}^{-1}$ of a 1'' (25.4mm) square delamination in a 16 ply (2.2mm) unidirectional CFRP composite plate.

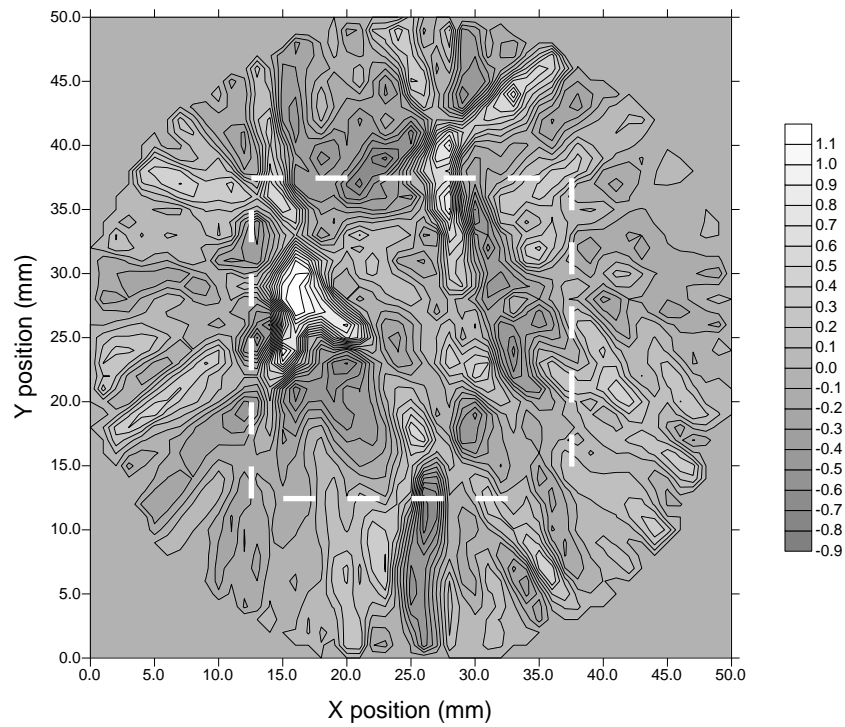


Figure 7.9(b): Slowness image in $\mu\text{s} \cdot \text{mm}^{-1}$ of a 1'' (25.4mm) square delamination in a 16 ply (2.2mm) unidirectional CFRP composite plate.

back projection algorithm are shown in Figure 7.9(a) for attenuation ($\text{dB}\cdot\text{mm}^{-1}$) and Figure 7.9(b) for slowness ($\mu\text{s}\cdot\text{mm}^{-1}$). The approximate size, location and shape of the defect is heavily distorted in both images, although the reconstruction appears to have highlighted one of the edges of the delamination. However, given the limited success with which the algorithm imaged such a gross defect, the remainder of the study concentrated on isotropic materials. The other iterative reconstruction techniques such as ART and SIRT would be more suitable for this type of material, as corrections for anisotropy may be incorporated into the reconstruction algorithms.

7.5 Results using the air-coupled capacitance transducer source

A typical Lamb wave obtained using the pair of air-coupled capacitance transducers is shown in Figure 7.10(a) for the 0.69mm aluminium sheet, with the frequency spectrum of the signal in Figure 7.10(b). The waveform is the result of 128 averages to improve the signal to noise ratio, and again the characteristic a_0 dispersion is visible before the larger direct wave through the air. The images shown in Figure 7.11 are for a 8mm diameter recess machined halfway through a 0.69mm thick aluminium sheet, formed from (a) the signal amplitude ($\text{dB}\cdot\text{mm}^{-1}$), and good results were also acquired using (b) the time of flight (slowness image in $\mu\text{s}\cdot\text{mm}^{-1}$) and (c) the shift in centroid frequency (Hz) as the measured parameter. As with the laser source, the defect is clearly resolved despite the diffraction effects. Figure 7.12(a) shows the Lamb wave obtained in the 1mm thick perspex sheet, with the corresponding FFT in Figure 7.12(b). The entirely air-coupled waveform is much simpler than the laser generated signal in the same sample, shown previously in Figure 7.6(a). This may be attributed to the more complex laser generated source, where more than one mode is

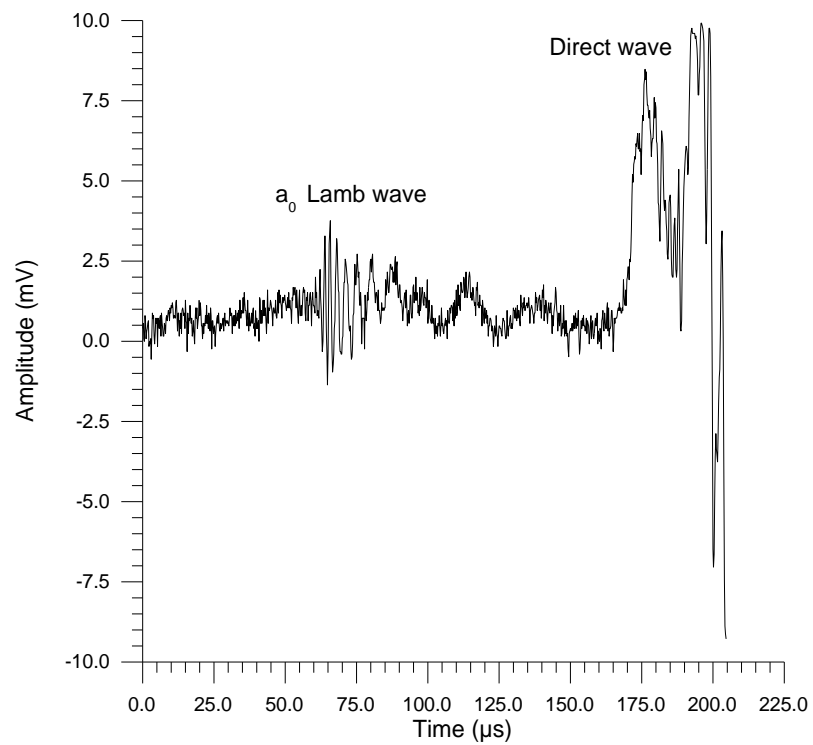


Figure 7.10(a): A typical Lamb wave in a 0.69mm aluminium sheet, obtained using the pair of air-coupled transducers.

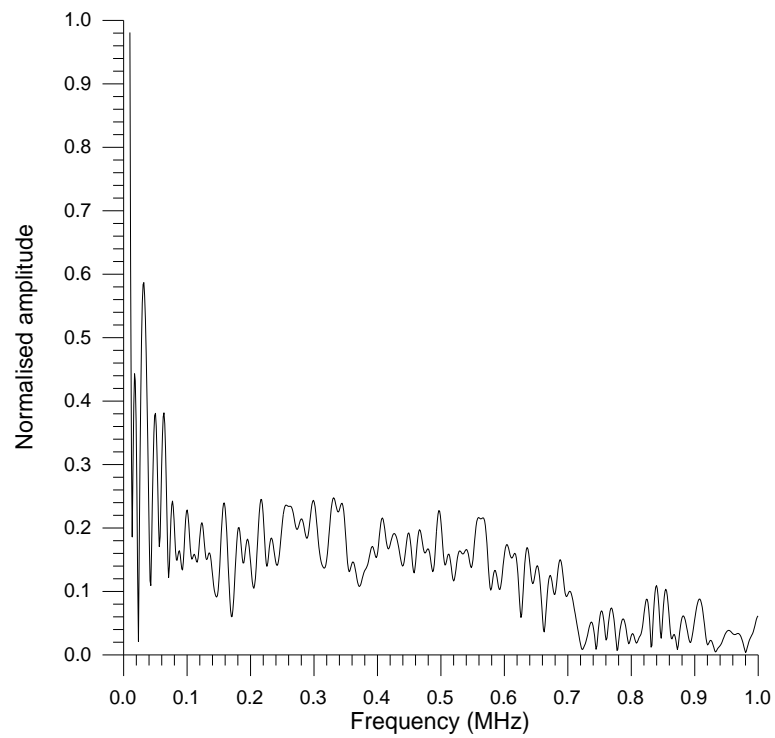


Figure 7.10(b): The frequency spectrum of Figure 7.10(a).

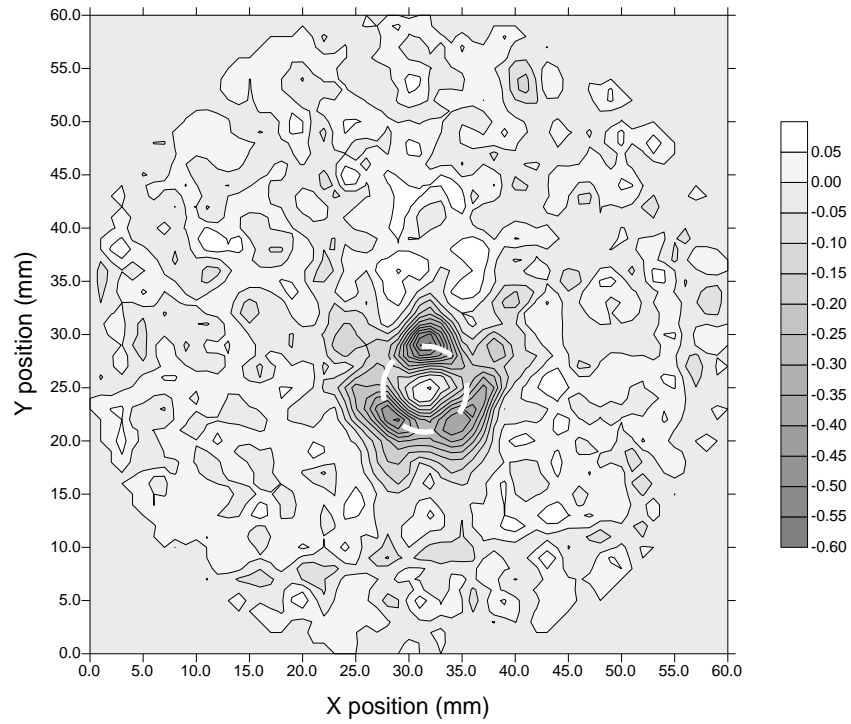


Figure 7.11(a): Attenuation image in $\text{dB} \cdot \text{mm}^{-1}$ of an 8mm diameter recess machined halfway through a 0.69mm thick aluminium sheet.

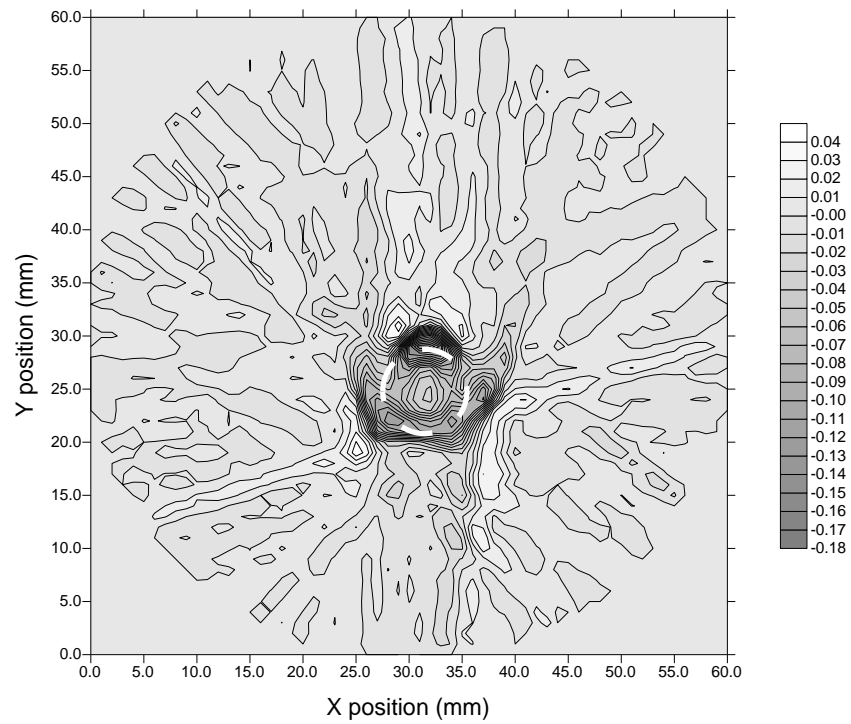


Figure 7.11(b): Slowness image in $\mu\text{s} \cdot \text{mm}^{-1}$ for an 8mm diameter recess machined halfway through a 0.69mm thick aluminium plate.

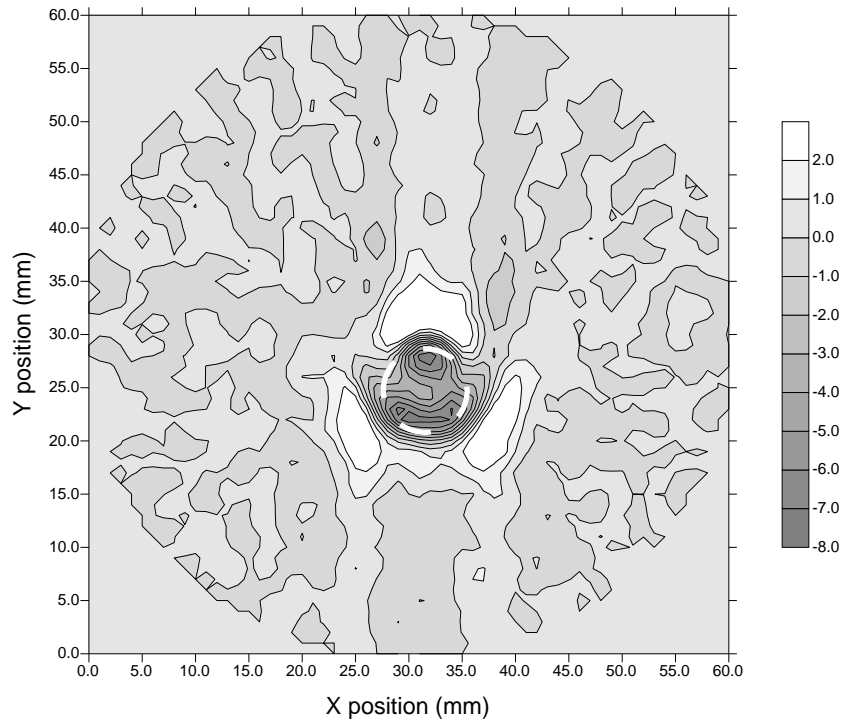


Figure 7.11(c): Image of the shift in centroid frequency in kHz for an 8mm diameter recess machined halfway through a 0.69mm thick aluminium plate.

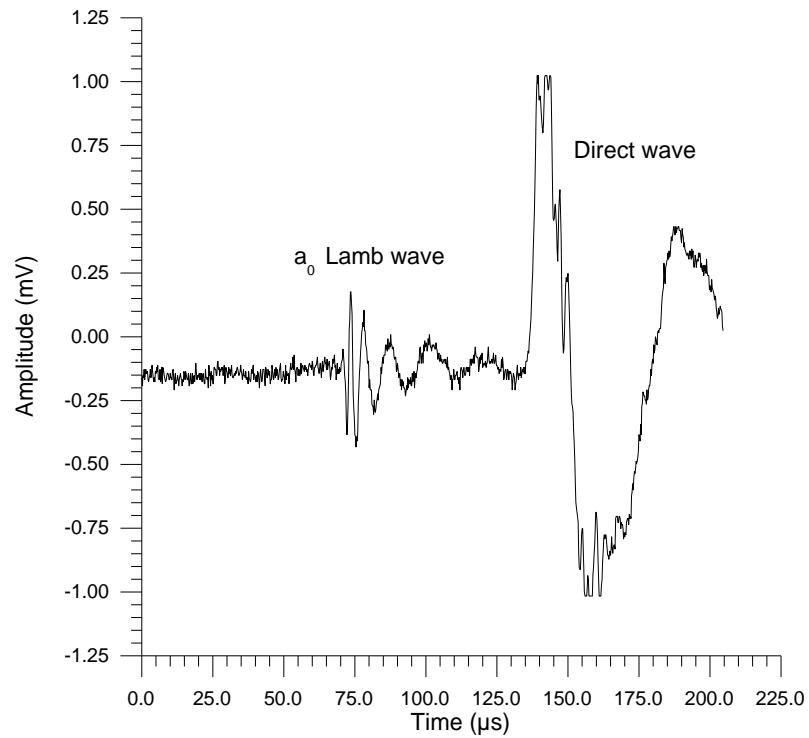


Figure 7.12(a): A typical Lamb wave in 1mm perspex (PMMA), obtained using the pair of air-coupled transducers.

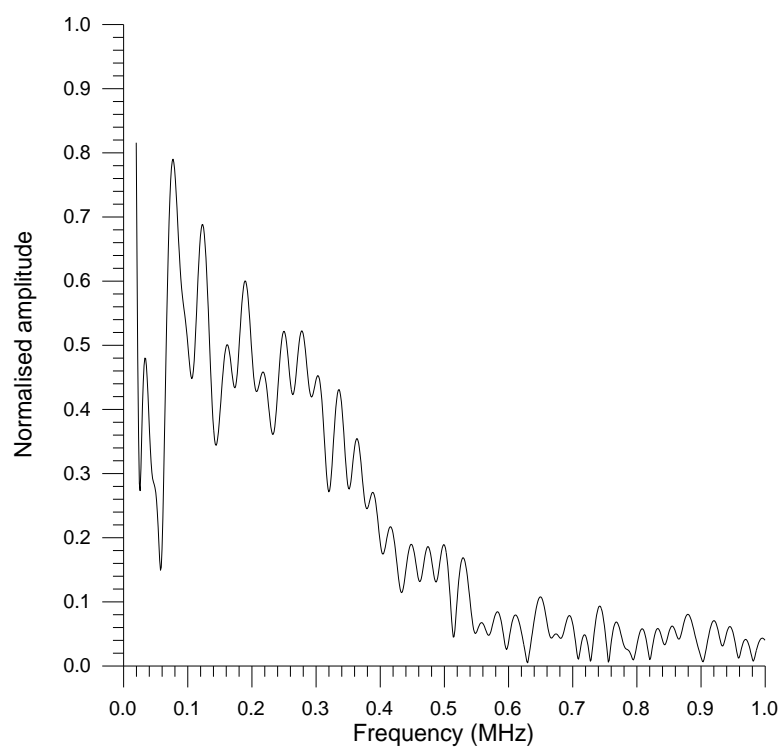


Figure 7.12(b): The frequency spectrum of Figure 7.12(a).

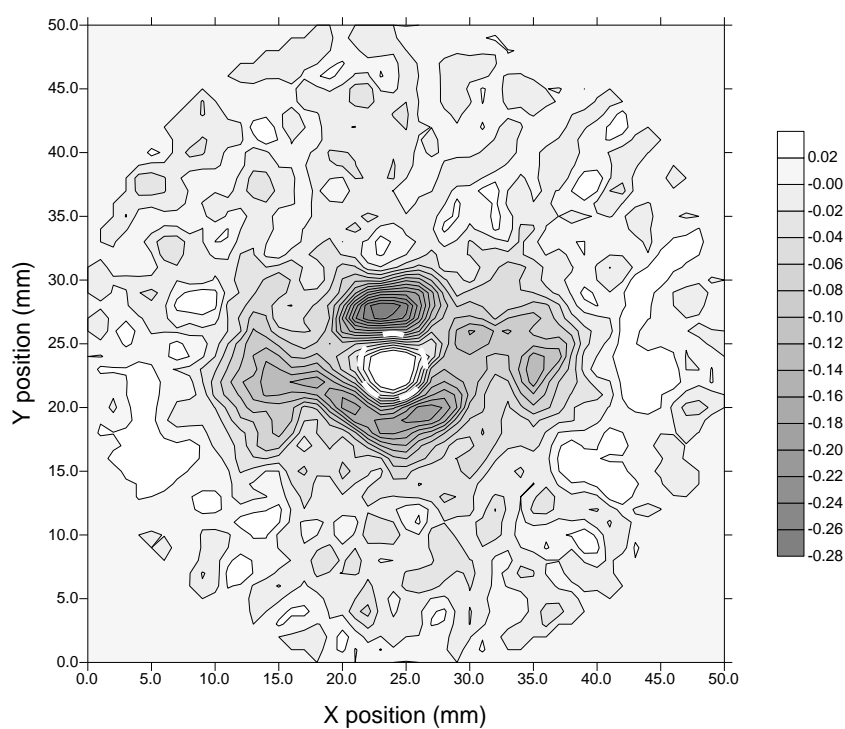


Figure 7.13(a): Attenuation image in $\text{dB} \cdot \text{mm}^{-1}$ of a 5mm hole through a 1mm thick sheet of perspex (PMMA).

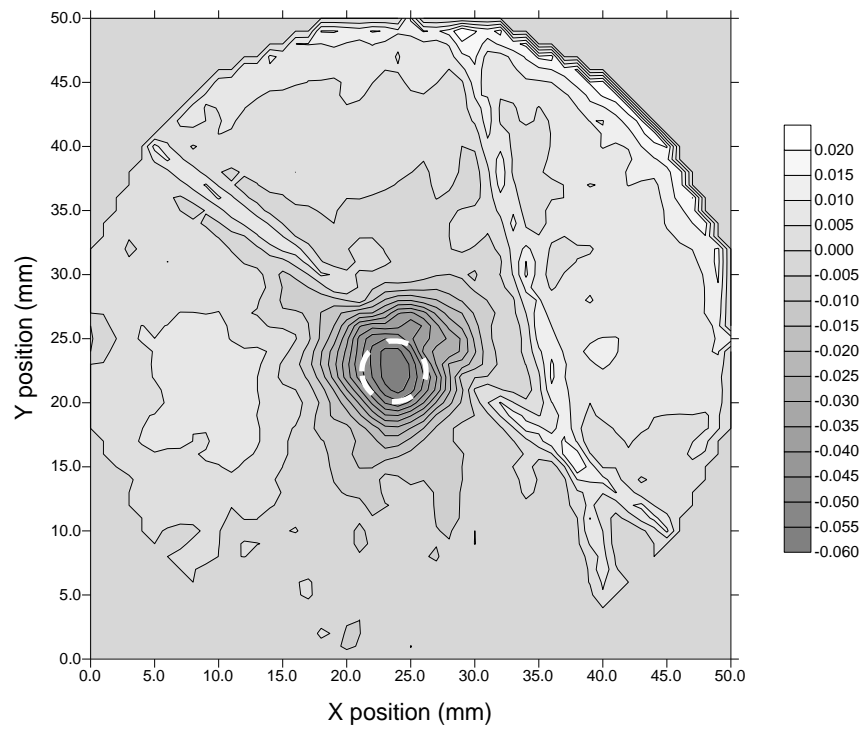


Figure 7.13(b): Slowness image in $\mu\text{s}.\text{mm}^{-1}$ of the 5mm hole through a 1mm thick sheet of perspex (PMMA).

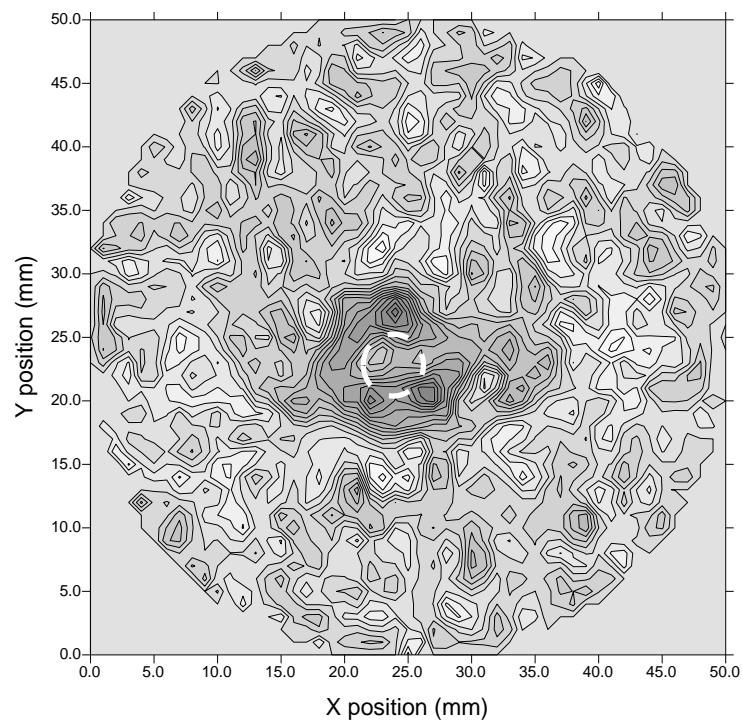


Figure 7.13(c): Image of shift in centroid frequency in kHz of the 5mm hole through a 1mm thick sheet of perspex (PMMA).

generated simultaneously. Images were also obtained for the 5mm diameter hole in a 1mm thick sheet of perspex (Plexiglas), shown in Figure 7.13 for (a) attenuation (dB.mm^{-1}), (b) for slowness ($\mu\text{s.mm}^{-1}$) and (c) for shift in centroid frequency (Hz). Note that despite the two distorted projections in the slowness image in Figure 7.13(b), the image was still clearly reconstructed, with some distortion of defect size.

The image of a 10mm diameter recess machined halfway through a 16 ply (2.2mm thick) CFRP composite plate is shown in Figure 7.14(a) using the shift in centroid frequency (Hz), with the defect offset by 10mm from the centre of the scan in each direction. This was to show that the technique could resolve non central defects, as the data points were more widely separated towards the edge of the scan area.

To see if the technique could resolve strongly non circular defects, a 1mm by 10mm slot was machined through a 0.69mm thick sheet of aluminium, and offset from the centre by 10mm in one direction. The scan size was increased to 60mm in 1mm steps to give 61 rays per projection. The resultant tomographic reconstruction is shown in Figure 7.14(b) using the signal amplitude (dB.mm^{-1}), and similar results were obtained using the shift in centroid frequency. The algorithm did not reproduce the slot shape accurately, possibly due to the size of the defect in relation to the scan resolution and the ultrasonic wavelengths available, but it has clearly picked out the diffraction at the ends of the slot. To see if the technique could resolve more than one defect in the scan area, a 0.69mm aluminium plate was machined with a 10mm diameter hole in the centre and a 5mm diameter hole offset from the centre by 20mm in both X and Y directions. The resulting tomographic images are shown in Figure 7.15(a) for the change in signal amplitude (dB.mm^{-1}), and Figure 7.15(b) for the shift in centroid frequency (Hz). In both cases, the two defects are clearly resolved, with a greater

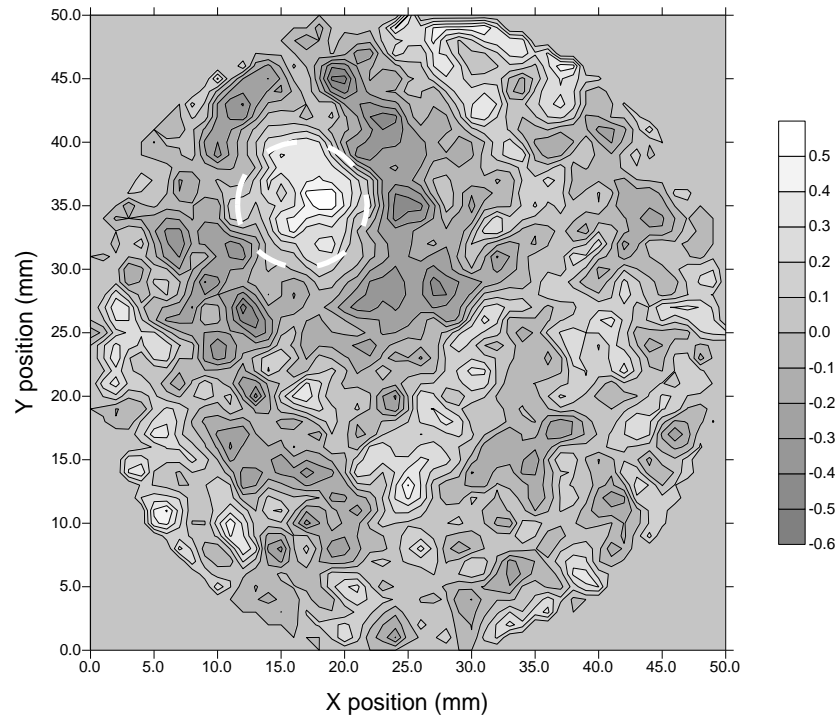


Figure 7.14(a): Image of the shift in centroid frequency in kHz for a 10mm diameter recess in a 16 ply (2.2mm) cross ply CFRP plate.

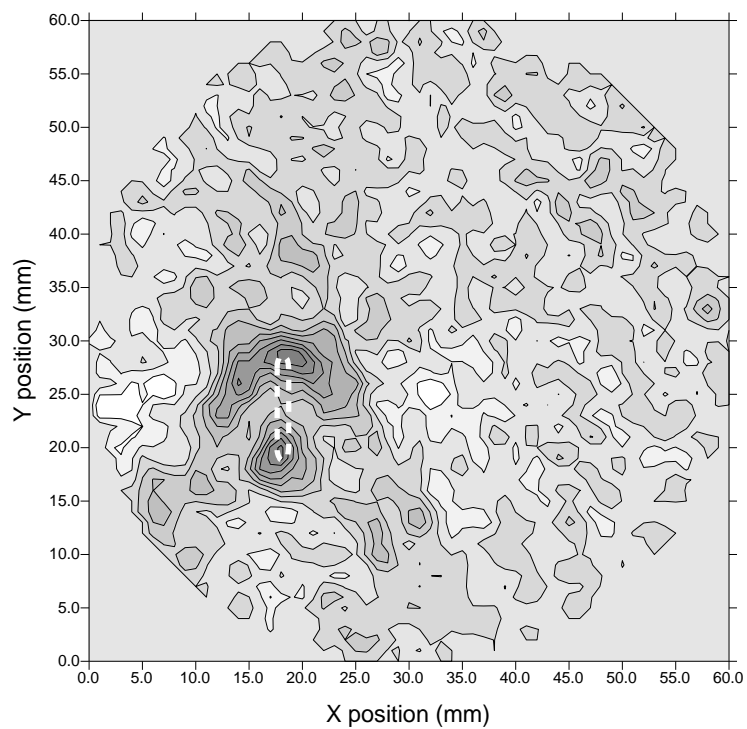


Figure 7.14(b): Attenuation image in $\text{dB}\cdot\text{mm}^{-1}$ of a 1mm by 10mm slot in a 0.69mm thick aluminium sheet, off centre by 10mm in the horizontal direction.

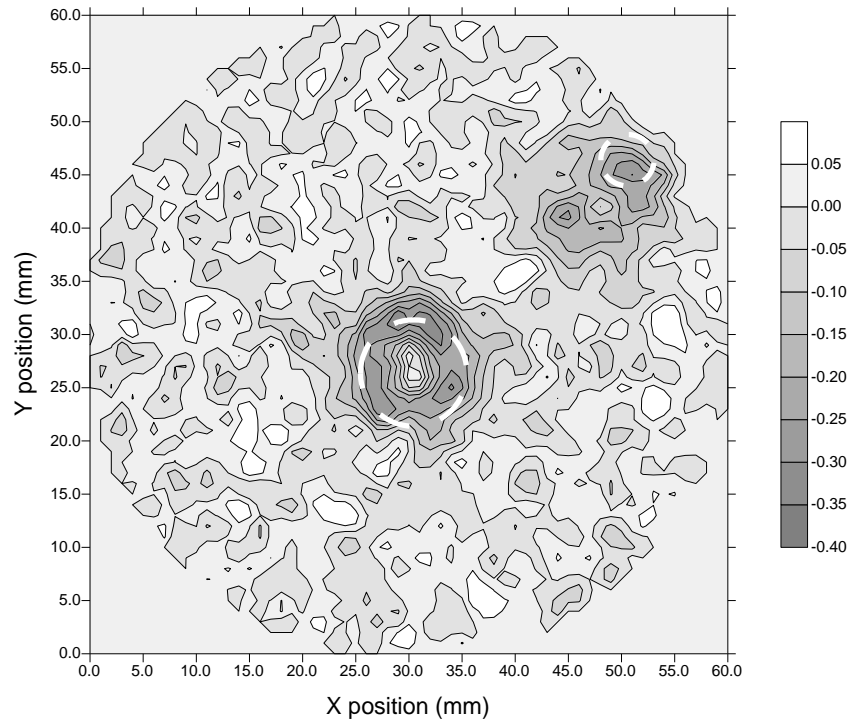


Figure 7.15(a): Attenuation image in dB.mm⁻¹ of a 10mm hole (centre) and a 5mm hole (offset by 20mm in both directions) through a 0.69mm thick aluminium sheet.

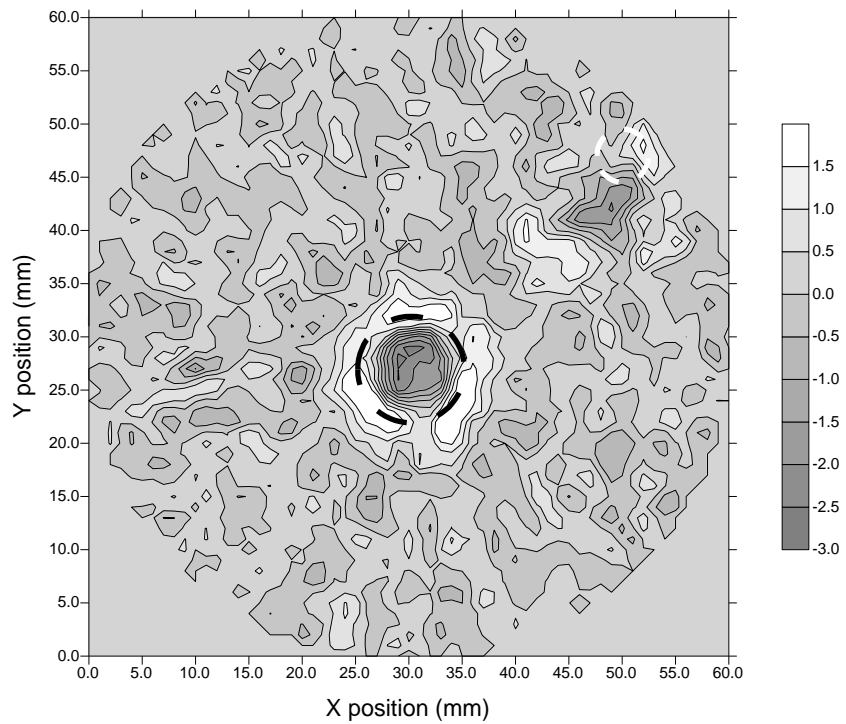


Figure 7.15(b): Image of shift in centroid frequency in kHz of a 10mm hole (centre) and a 5mm hole (offset by 20mm in both directions) through a 0.69mm thick aluminium sheet.

change in signal amplitude or frequency shift associated with the larger defect in the centre of the scan. However, the location of the 5mm defect has been distorted due to the wide spacing of the projections at the scan edges.

7.6 Conclusions

Ultrasonic tomographic imaging was performed using air-coupled Lamb waves and a filtered back projection algorithm. A difference technique was employed, to remove the unknown air gap delay, by normalising the data each projection to that obtained from the first waveform taken at each angle. In a first set of experiments, a pulsed laser was used as a source of ultrasound, with a micromachined capacitance air-coupled transducer as a receiver. Images were obtained for various defects in thin plates of aluminium, perspex (or Plexiglas) and carbon fibre reinforced polymer composite (CFRP). The laser was then replaced with another capacitance transducer to give an entirely air-coupled system. This was then successfully used to image defects in aluminium, perspex and CFRP plates, and included off centre, non-circular and multiple defects within the scan area. This flexible system produced images of the change in a variety of acoustic variables from one set of experimental data, and it is hoped will be suitable for many non destructive testing applications. It is limited in its current form to isotropic materials due to the back projection algorithm, although iterative reconstruction techniques such as ART and SIRT may be modified to compensate for anisotropy. This could be a study for future work, using higher frequency and broader bandwidth transducers and more rays per projection to increase the scan resolution.

7.7 References

- [1] A.C. Kak and M. Slaney, *Principles of computerized tomographic imaging*, IEEE Press, New York (1988)
- [2] J. Radon, 'Über die Bestimmung von Funktionen durch ihre Integralwerte lange gewisser Mannigfaltigkeiten', *Ber. Sach. Akad. Wiss.* **29**, 262-277 (1917)
- [3] J. Greenleaf, S. Johnson, S. Lee, G. Heuman and E. Wood, 'Algebraic reconstruction of spatial distributions of acoustic absorption within tissue from their two-dimensional acoustic projections', *Acoust. Hologr.* **5**, 591-603 (1974)
- [4] J. Greenleaf, S. Johnson, W. Wamoya and F. Duck, 'Algebraic reconstruction of spatial distributions of acoustic velocities in tissue from their time-of-flight profiles', *Acoust. Hologr.* **6**, 71-90 (1975)
- [5] P.N.T. Wells, 'The present status of ultrasonic imaging in medicine', *Ultrasonics* **31**, 345-352 (1993)
- [6] H.W. Jones, 'Recent activity in ultrasonic tomography', *Ultrasonics* **31**, 353-360 (1993)
- [7] A.L. Virovlyanskii, 'Use of ocean acoustic tomography for average temperature measurement', *Acoustical Physics* **40**, 671-675 (1994)
- [8] B.F. Kuryanof, 'Passive acoustic tomography of bottom sediments on a sea shelf', *Acoustical Physics* **40**, 769-771 (1994)
- [9] H. Yamada, 'Application of ultrasonic computed tomography to non-destructive inspection of SiO₂ ingot', *J. Acoust. Soc. Am.* **69**, 571-572 (1978)
- [10] A.M.H. Satti and J. Szilard, 'Computerised ultrasonic tomography for testing solid propellant rocket motors', *Ultrasonics* **21**, 162-166 (1983)

- [11] Y. Tomikawa, 'Non-destructive inspection of wooden poles using ultrasonic computed tomography', *IEEE Trans. Ultrason., Ferroelec., Freq. Contr.* **UFFC-33**, 354-358 (1986)
- [12] D.P. Jansen, D.A. Hutchins and R.P. Young, 'Ultrasonic tomography using scanned contact transducers', *J. Acoust. Soc. Am.* **93**, 3242-3249 (1993)
- [13] T.M. Chow, D.A. Hutchins and J.T. Mottram, 'Simultaneous acoustic emission and ultrasonic tomographic imaging in anisotropic polymer composite material', *J. Acoust. Soc. Am.* **94**, 944-953 (1993)
- [14] T. Chow, D.A. Hutchins, M.D.C. Moles and R.P. Young, 'Stress dependence of the acoustic properties of Zr-2.5 wt% Nb alloy', *Ultrasonics* **31**, 183-192 (1993)
- [15] D.A. Hutchins, J.K. Hu, R.P. Young, R. Stoner, D. Jansen and Q.L. Zhang, 'Ultrasonic tomography of metals using non-contact transduction', *J. Acoust. Soc. Am.* **85**, 747-752 (1989)
- [16] D.A. Hutchins, D.P. Jansen and C. Edwards, 'Lamb-wave tomography using non-contact transduction', *Ultrasonics* **31**, 97-103 (1993)
- [17] J.K. Hu, D.A. Hutchins, J. Ungar, Q.L. Zang and D.K. Mak, 'Non-contact ultrasonic reflection tomography', *Mat. Eval.* **47**, 736-740 (1987)
- [18] D.P. Jansen, D.A. Hutchins and J.T. Mottram, 'Lamb wave tomography of advanced composite laminates containing damage', *Ultrasonics* **32**, 83-89 (1994)
- [19] Y. Censor, 'Finite series expansion reconstruction techniques', *Proc. IEEE* **71**, 409-419 (1984)
- [20] R.A. Kline and Y.Q. Wang, 'A technique for ultrasonic tomography in anisotropic media', *J. Acoust. Soc. Am.* **91**, 878-884 (1992)

- [21] R. Gordon, R. Bender and G.T. Herman, 'Algebraic reconstruction techniques for three-dimensional electron microscopy and X-ray photography', *J. Theor. Biol.* **29**, 471-481 (1970)
- [22] P. Gilbert, 'Iterative methods for the three-dimensional reconstruction of an object from projections', *J. Theor. Biol.* **29**, 105-117 (1972)
- [23] R.M. Lewitt, 'Reconstruction algorithms: transform methods', *Proc. IEEE* **71**, 390-408 (1984)
- [24] H.H. Stark, J.W. Woods, I. Paul and R. Hingorani, 'Direct Fourier reconstruction in computer tomography', *IEEE Trans. Acoust., Speech, Sig. Proc.* **ASSP-29**, 237-245 (1981)
- [25] G.T. Herman, *Image reconstruction from projections: The fundamentals of computerized tomography*, Academic Press, New York (1980)
- [26] D.P. Jansen and D.A. Hutchins, 'Immersion tomography using Rayleigh and Lamb waves', *Ultrason.* **30**, 245-254 (1992)
- [27] L. Capineri, H.G. Tattersall, J.A.G. Temple and M.G. Silk, 'Time of flight diffraction tomography for NDT applications', *Ultrasonics* **30**, 275-288 (1992)
- [28] A. Witten, J. Tuggle and R.C. Waag, 'A practical approach to ultrasonic imaging using diffraction tomography', *J. Acoust. Soc. Am.* **83**, 1645-1652 (1988)
- [29] A.J. Devaney, 'A fast filtered backpropagation algorithm for ultrasound tomography', *IEEE Trans. Ultrason., Ferroelec., Freq. Contr.* **UFFC-34**, 330-340 (1987)
- [30] L.S. Koo, H.R. Shafiee, D.K. Hsu, S.J. Wormley and D.O. Thompson, 'Two-dimensional ultrasonic tomography in non-destructive evaluation by using area functions', *IEEE Trans. Ultrason., Ferroelec., Freq. Contr.* **UFFC-37**, 148-158 (1990)

- [31] D.P. Jansen, *Acoustic tomographic imaging of solid media*, Ph.D. thesis, Queens University, Canada (1992)

Chapter 8: Conclusions

8.1 Conclusions

This thesis has described how air-coupled transducers were successfully used in a variety of different ultrasonic non-destructive testing techniques.

In Chapter 2, a capacitance air-coupled transducer with a micromachined silicon backplate was characterised using laser-generated ultrasonic waves, and its response compared to that of a contact capacitance device which used the sample itself as one electrode. The air-coupled transducer was shown to be broadband up to approximately 2MHz, and gave a good representation of the displacement of the sample surface. The device was then used to study laser-generated bulk waves, Rayleigh waves travelling along a surface, and Lamb waves travelling in thin plates of material. Due to the present lack of a suitable well calibrated microphone or air-coupled transducer operating at these frequencies, a full calibration of this etched silicon device should form part of any future work.

In Chapter 3, an alternative design of air-coupled transducer was evaluated. A pair of prototype 1-3 connectivity piezocomposite devices with impedance matching layers were tested using laser-generated ultrasound as before, and found to be narrowband and resonant receivers, operating at 494kHz and 627kHz. Another high frequency prototype was found to resonate at 1.6MHz. A more advanced transducer operating at 1.2MHz used an inter-pillar resonance in the piezocomposite element to extend the bandwidth of the device to more than 1.6MHz. This device did not require an impedance matching layer, and when compared to the air-coupled capacitance device evaluated in Chapter2, was found to have a broader bandwidth but a reduced sensitivity. The broadband piezocomposite transducer was then used to test various samples of pultruded glass reinforced polymer (GRP) and carbon-fibre reinforced

polymer (CFRP) composite up to 10mm thick, and to calculate material velocities using the half wavelength resonant frequency of the longitudinal wave. The laser/air-coupled transducer system was then used successfully to C-scan various delaminations from 6mm to 25mm square, and machined defects up to 10mm in diameter in plates of composite material, in both the time and frequency domain.

In Chapter 4, a series of air-coupled capacitance transducers were manufactured with metallic backplates. Several devices were constructed using backplates of roughened and polished brass, and the effects of the surface properties on the frequency response of the device was studied. Linear relationships between sensitivity and bandwidth, and the inverse square root of surface roughness and the frequency response were observed, which was consistent with previous work by other authors on this subject. The effects of different polymer film thickness and applied bias voltage (up to 1000V) were also investigated. The expected linear fit between film thickness and device sensitivity was not observed, and there appeared to be an optimum thickness for the backplate used in these experiments. There also appeared to be an optimum bias voltage for both maximum sensitivity and bandwidth for the different thicknesses of film used. Three transducers were made in an identical fashion to test reproducibility between devices, and were found to have very similar responses. The final part of this chapter looked at devices constructed from a series of polished copper backplates into which a regular array of pits had been chemically etched, in conjunction with photolithographic techniques. Although no conclusive link between hole dimensions and frequency response was seen, the addition of holes did improve the sensitivity of the devices. Further work using a statistically large number of transducers would help to confirm these relationships, as would the use of more precise backplate machining techniques such as laser or ion beam machining.

Chapter 5 investigated the use of air-coupled Lamb waves to estimate the thickness of thin metal plates. Using a pulsed laser source and an air-coupled capacitance receiver, the group and phase velocity dispersion relations for the asymmetric zero order mode were extracted and compared to theoretical curves calculated using a FORTRAN program. A difference technique was employed to compensate for the unknown air gaps. Using a zero crossing technique to determine the group velocity curve, the sheet thickness was then estimated to within 11% for plates of aluminium and steel up to 1.2mm thick, and to a lesser accuracy in brass. A method of extracting the phase velocity dispersion from the FFT of a Lamb wave was able to estimate the thickness of steel shims between 0.07mm and 0.4mm thick to within 5%. Limited success was also achieved when the laser source was replaced with another air-coupled capacitance device, and this could be improved in future work by using more sensitive, wider bandwidth transducers.

In Chapter 6, entirely air-coupled ultrasonic testing was achieved using a pair of air-coupled capacitance transducers with micromachined silicon backplates. The longitudinal velocity of through-thickness waveforms was measured in a variety of materials including CFRP and GRP up to 10mm thick, perspex and expanded polyurethane foam up to 25mm thick, and even aluminium up to 12mm thick. Lamb waves were also detected in thin plates of different materials. The pair of transducers was then used in an entirely air-coupled C-scanning system, and images of the delaminations and machined defects in CFRP, GRP and aluminium were obtained. This entirely air-coupled system is extremely versatile, and could be applied to virtually any ultrasonic non-destructive testing application, provided that sufficiently sensitive and wideband transducers are available.

In the final chapter, a tomographic imaging technique which used a filtered back projection algorithm and a difference method was used to reconstruct images in thin plates. An air-coupled capacitance transducer was used to detect Lamb waves generated first by a pulsed laser, and then by another air-coupled device. The reconstruction technique was able to form images of delaminations and machined defects in CFRP, perspex and aluminium plates, and to resolve the shape and locations of non-circular defects and multiple anomalies within the scan area. Although limited in this study to isotropic materials because of the back projection algorithm, iterative reconstruction techniques can compensate for anisotropy and this would form a solid basis for any future work.

It is felt that the present work has added to the knowledge and the characterisation of air-coupled capacitance devices, and their application to the measurement and inspection of solid materials in air. Completely air-coupled systems, and those using a laser source, have both been shown to be suitable for these purposes. In particular, it has been demonstrated that such measurements can be obtained using various wave modes, including Lamb waves in thin sheets, and that imaging is possible in both thickness through-transmission, and using tomography. This demonstrates that a system using such devices is extremely versatile and has a future in materials testing applications. When more sensitive, broader bandwidth and higher frequency transducers are developed, many other testing applications such as pipe wall thickness measurement could be made more rapidly and at low cost due to the entirely non-contact nature of air-coupled ultrasonics.

Bibliography and publications

Bibliography

‘Guide to examinations for higher degrees by research’, The University of Warwick Graduate School, September 1995

Publications arising from the work in this thesis

- [1] D.A. Hutchins, W.M.D. Wright, L.P. Scudder, J.T. Mottram and D.W. Schindel, ‘Air-coupled ultrasonic testing of composites’, *Proc. 1994 Conference on the Inspection of Structural Composites* **Ch. 17**, 99-113 (Bentham Press, London, 1994)
- [2] W.M.D. Wright, D.A. Hutchins and D.W. Schindel, ‘Ultrasonics evaluation of polymers and composites using air-coupled capacitance transducers’, *Rev. Prog. Quant. Nondest. Eval.* **14A&B** Ch. 312, 1399-1406 (1995)
- [3] W.M.D. Wright, D.A. Hutchins, A. Gachagan and G. Hayward, ‘Evaluation of fiber-reinforced composites using a noncontact laser/air-transducer system’, *Rev. Prog. Quant. Nondest. Eval.* **14A&B** Ch. 312, 1333-1340 (1995)
- [4] D.A. Hutchins, A.G. Bashford, W.M.D. Wright and D.W. Schindel, ‘Characterization of the field of an air-coupled ultrasonic silicon capacitance transducer’, *Rev. Prog. Quant. Nondest. Eval.* **14A&B** Ch. 312, 945-950 (1995)
- [5] G. Hayward, A. Gachagan, R. Hamilton, D.A. Hutchins and W.M.D. Wright, ‘Ceramic-epoxy composite transducers for non-contact ultrasonic applications’, *SPIE Symp. 1992*, Vol. 1733, 49-56 (1992)

- [6] A. Gachagan, G. Hayward, W.M.D. Wright and D.A. Hutchins, 'Air-coupled piezoelectric detection of laser-generated ultrasound', *Proc. IEEE 1993 Ultrason. Symp.* Ch. 259, 651-654 (1993)
- [7] D.A. Hutchins, W.M.D. Wright, G. Hayward and A. Gachagan, 'Air-coupled piezoelectric detection of laser-generated ultrasound', *IEEE Trans. Ultrason. Ferroelec. Freq. Contr.* **UFFC-41**, 796-805 (1994)
- [8] W.M.D. Wright, D.A. Hutchins, A. Gachagan and G. Hayward, 'Polymer composite material characterisation using a laser/air-transducer system', accepted for publication in *Ultrasonics*
- [9] D.A. Hutchins, W.M.D. Wright and D.W. Schindel, 'Ultrasonic measurements in polymeric materials using air-coupled capacitance transducers', *J. Acoust. Soc. Am.* **96**, 1634-1642 (1994)
- [10] W.M.D. Wright, D.W. Schindel and D.A. Hutchins, 'Studies of laser-generated ultrasound using a micromachined silicon electrostatic transducer in air', *J. Acoust. Soc. Am.* **95**, 2567-2575 (1994)
- [11] W.M.D. Wright, D.A. Hutchins, D.P. Jansen and D.W. Schindel, 'Air-coupled Lamb wave tomography', submitted for publication in *IEEE Trans. Ultrason. Ferroelec. Freq. Contr.*

Appendix A: Equipment specifications

Panametrics 5055PR Pulser-Receiver

PULSER

Maximum pulse amplitude	-250V into 50 Ω -350V into 250 Ω
Pulse repetition rate (internal)	100-2000 Hz
Damping range	10 to 250 Ω
Minimum rise time	10ns
Available pulse energy	18-110 μ J in 4 steps

RECEIVER

Voltage gain	40dB (x100) or 60dB (x1000) selectable
Input impedance	500 Ω
Output impedance	50 Ω and 50 μ F in series
Noise levels	50 μ V peak-peak referred to the input
Bandwidth	10kHz-10MHz
Maximum	\pm 1V (open circuit) or \pm 0.5V into 50 Ω

Cooknell CA6/C charge amplifier

Input impedance	100 Ω above 10kHz
Sensitivity	250mV per pico-coulomb
Series noise voltage generator	0.6nV//Hz typical
Parallel noise current generator	4x10 ⁻¹⁴ A//Hz typical
Bandwidth	<10kHz to >10MHz
Max output level	1V rms into 50 Ω

Daedal linear stages

Maximum travel	150mm
Maximum load	50kg
Straight line accuracy	\pm 0.01mm/50mm of travel
Positional accuracy	\pm 0.01mm/50mm of travel
Repeatability	Bi-directional 0.01mm

Daedal rotary stage

Runout	\pm 0.07mm
Accuracy	10 Arc min.
Concentricity	\pm 0.02mm
Repeatability	0.5 Arc min. - unidirectional
Gear ratio	90:1

Appendix B: FORTRAN program listings


```

*
call eqns(slo,clo)
call eqns(shi,chi)
*
if(v.ne.ct.AND.v.cstep.ne.ct) then
if(slo*shi.lt.0) then
if(smode.le.order) then
call sroot(clo,chi,dec,cps)
dks=(f/cps)-((f-fstep)/cpsold(smode))
cgs=fstep/dks

print*, f, ' MODE s'//chr2(smode)//' ',cps,cgs
if(phgr.eq.'P'.OR.phgr.eq.'p') then
write((30+smode),*) f,cps
else
write((30+smode),*) f,cgs
endif
cpsold(smode)=cps
smode=smode+1
endif
endif
endif
*
500 continue
*
100 continue
*
print*, 'Done'
*
goto 9999
*
* File error handling
*
9000 print*, char(7)
if(ernum.eq.2015) then
print*, 'LAMBCURV.IN not found'
else
print*, 'Error '//chr4(ernum)//' opening
LAMBCURV.IN'
endif
*
9999 end
*****
*****
subroutine eqna(a0,cp)
*
implicit none
real
a0,d,a2,b,b2,ALHS,ATOPRHS,ABOTRHS,cp,cL,ct
common /const/pi,cL,ct,d
*
a2=(ct*ct)/(cp*cp)
b=ct/cL
b2=(ct*ct)/(cL*cL)
*
* There are three conditions which require different
equations:-
* (1) When a2 < b2
* (2) When a2 > b2 and a2 < 1
* (3) When a2 > 1
* There is also a fourth condition caused by FORTRAN!!
* (4) When a2 = 1
* This gives rise to sqrt(0) and therefore division by 0
*
* For s modes
*
if(a2.le.b2) then
*
SLHS=tan(sqrt(1-a2)*d)/sqrt(1-a2)
STOPRHS=-4*a2*sqrt(b2-a2)*tanh(sqrt(b2-a2)*d)
SBOTRHS=((2*a2)-1)*((2*a2)-1)
*
elseif(a2.gt.b2.and.a2.lt.1.00000000) then
*
SLHS=tan(sqrt(1-a2)*d)/sqrt(1-a2)
STOPRHS=4*a2*sqrt(a2-b2)*tanh(sqrt(a2-b2)*d)
SBOTRHS=((2*a2)-1)*((2*a2)-1)
*
elseif(a2.gt.1.00000000) then
*
SLHS=tanh(sqrt(a2-1)*d)/sqrt(a2-1)
STOPRHS=4*a2*sqrt(a2-b2)*tanh(sqrt(a2-b2)*d)

```



```

      SBOTRHS=((2*a2)-1)*((2*a2)-1)
*
*   endif
*
*   The equations have an infinite number of roots,
corresponding
*   to different order modes.
*
*   When:      LHS - (TOP / BOT) = 0
*
*   Then a root exists. So by fixing f and scanning through
values
*   of cp until the above expression changes sign will give
an
*   approximate value of cp at a root.
*
      s0=SLHS-(STOPRHS/SBOTRHS)
*
*   Now check for condition (4) when a2=1 exactly
*
      if(a2.eq.1.00000000) then
        s0=0
      endif
*
      return
*
      end
*****
*****
      subroutine aroot(clo,chi,dec,cp)
*
      implicit none
*
      integer power,dec
      real step,vel,clo,chi,alo,ahi,cp
*
*   Starting values
*
      do 50 power=1,dec
        step=1.0/10**power
*
        do 10 vel=clo,chi+step,step
          call eqna(alo,vel-step)
          call eqna(ahi,vel)
*
          if(alo*ahi.lt.0) then
            cp=vel
            clo=vel-step
            chi=vel
            goto 50
          endif
*
        10 continue
*
      50 continue
*
      return
*
      end
*****
*****
      subroutine sroot(clo,chi,dec,cp)
*
      implicit none
*
      integer power,dec
      real step,vel,clo,chi,slo,shi,cp
*
*   Starting values
*
      do 50 power=1,dec
        step=1.0/10**power
*
        do 10 vel=clo,chi+step,step

```

```

      call eqns(slo,vel-step)
      call eqns(shi,vel)
*
      if(slo*shi.lt.0) then
        cp=vel
        clo=vel-step
        chi=vel
        goto 50
      endif
*
      10 continue
*
      50 continue
*
      return
*
      end
*****
*****
      character*4 function chr4(i)
*
*   This function converts the number passed to a 4
character string.
*
      integer hund,i,ones,tens,thou
*
      thou=int(i/1000)
      hund=int((i-thou*1000)/100)
      tens=int((i-thou*1000-hund*100)/10)
      ones=(i-thou*1000-hund*100-tens*10)

chr4=char(thou+48)//char(hund+48)//char(tens+48)//char(
ones+48)
*
      return
*
      end
*****
*****
      character*2 function chr2(i)
*
*   This function converts the number passed to a 2
character
*   string and is a modification of one of Dion's functions.
*
      integer i,ones,tens
*
      tens=int(i/10)
      ones=(i-tens*10)
      chr2=char(tens+48)//char(ones+48)
*
      return
*
      end
*****
*****

```